Measurement of the J/ψ production in p-Pb collisions at the LHC with the ALICE muon spectrometer

Igor Lakomov

Institut de Physique Nucléaire

CNRS - UNIVERSITÉ PARIS SUD

IPN
INSTITUT DE PHYSIQUE NUCLÉAIRE
ORSAY

19 septembre 2014 IPNO-14-02

Thèse
Présentée par

LAKOMOV Igor

Pour obtenir le grade de Docteur ès Sciences
De l'Université Paris Sud

Mesure de la production de J/ψ en collisions p-Pb au LHC avec le spectromètre à muons d'ALICE

cnrs
UNIVERSITÉ PARIS SUD
Comprendre le monde, construire l'avenir®

UNIVERSITÉ PARIS SUD
Comprendre le monde, construire l'avenir®

IPN
INSTITUT DE PHYSIQUE NUCLÉAIRE
ORSAY

Université Paris-Sud 11
ED MIPEGE
Modélisation et Instrumentation en Physique, Energies, Geosciences et Environnement

Université Paris-Sud

École Doctorale 534 : Modélisation et Instrumentation en Physique, Énergies, Géosciences et Environnement

Laboratoire : Institut de Physique Nucléaire d'Orsay

Discipline : Physique

Thèse de doctorat

Soutenue le 19 septembre 2014 par

Igor LAKOMOV

Measurement of the J/ψ production in p-Pb collisions at the LHC with the ALICE muon spectrometer

Composition du jury :

Président du jury :	M. Patrick ROBBE	(LAL, Orsay)
Rapporteurs :	M. Raphaël GRANIER DE CASSAGNAC	(LLR, Palaiseau)
	M. Andreas MORSCH	(CERN, Genève)
Directeur de thèse :	M. Bruno ESPAGNON	(IPNO, Orsay)
Examinateurs :	M. François GELIS	(IPhT, Saclay)
	M. Christophe SUIRE	(IPNO, Orsay)

IPNO-14-02

Hard probes represent one of the hottest topics of the modern high energy physics. The production mechanism of quarkonia (mesons composed of a charm or beauty quark and its antiquark) in hadronic collisions is of particular interest. The suppression of J/ψ and other charmonium states was predicted as one of the first signatures of the Quark Gluon Plasma (QGP) formation and was seen at RHIC and SPS. It was also studied at the LHC in Pb-Pb collisions. However, other effects can affect the charmonium production in Pb-Pb collisions without the presence of the QGP. These effects are inherent to the use of nuclei and are called "Cold Nuclear Matter" (CNM) effects. They can be studied in p-Pb collisions.

This thesis is dedicated to the studies of J/ψ production in p-Pb collisions at the LHC at a center of mass energy of 5.02 TeV per nucleon pair. J/ψ production is studied as a function of transverse momentum, rapidity and event activity. These results represent a significant step to better understanding of the CNM effects and to the establishment of a reference for J/ψ production in Pb-Pb collisions.

Key words: J/ψ, cold nuclear matter, ALICE, muon spectrometer, p-Pb.

Les sondes dures apparaissent comme l'un des sujets les plus excitant de la Physique des hautes énergies. Les mécanismes de production des quarkonia (mésons formés par l'état lié quark-antiquark charmé ou beau) dans les collisions hadroniques sont particulièrement intéressants. La suppression du J/ψ et des autres charmonia a été prédites comme l'une des signatures de la formation du Plasma de Quark et de Gluons (PQG), suppression déjà observée au SPS et au RHIC. De nombreuses études de la suppression des charmonia ont également été menées au LHC.

Cependant, d'autres effets sont susceptibles de modifier la production de charmonia sans requérir la formation d'un QGP. Ces effets, inhérents aux collisions impliquant des noyaux, sont appelés effects nucléaires froids ou CNM ("Cold Nuclear Matter"). Ils peuvent être étudiés dans les collisions p-Pb.

Cette thèse est dediée à l'analyse de la production de J/ψ dans les collisions p-Pb collisions à une énergie dans le centre de masse de 5.02 TeV par paire de nucléon au LHC. La production de J/ψ est étudiée en fonction de l'impulsion transverse, de la rapidité et de l'activité de la collision.

Ces résultats apportent une contribution significative dans la compréhension des effects CNM et dans l'établissement d'une référence pour l'interprétation de la production de J/ψ dans les collisions Pb-Pb.

Mots-clés: J/ψ, matière nucléaire froide, ALICE, spectromètre à muons, p-Pb.

Contents

Dedicated to my mother who was dreaming of me defending this thesis more than I was.

Посвящается моей маме, которая мечтала, чтобы я защитил эту диссертацию больше, чем я.

Acknowledgements

I would like to acknowledge all the people who contributed to my PhD thesis by their support, help, advises:

My parents who support me during all my life, and especially my mother who was dreaming of me defending this thesis more than I was.

My wife for our love which yielded during my PhD in the birth of our first son.

My son for giving me opportunity to work at home at night.

I would like also to acknowledge my grandmother who did not live to see my PhD thesis defense but I think she would be happy for me.

Vladimir Vechernin and Grigory Feofilov and all the SPbSU ALICE team for giving me opportunity to join the ALICE Collaboration, a large international collaboration.

Bruno Espagnon for being my supervisor and for correction of my thesis, Christophe Suire for valuable advises and for correction of my thesis, Cynthia Hadjidakis for being my "encandrante" and pushing me to do Physics and for correction of my thesis, Zaida Conesa Del Valle for many senior advises during my PhD. I would like to thank the Orsay group for these three great years of my life which I spent with so nice people and for all the help and supervising which I received.

Enrico Scomparin and Roberta Arnaldi for the pleasure of working together with them and for nice time which I spent during my short visit to Turin. Thanks also to Jean-Philippe Lansberg for the organisation of this visit.

ALICE Collaboration for nice data.

My friends for our friendship.

Members of my PhD thesis jury for reading the thesis and for the questions and suggestions I got from them.

Благодарности

Я хотел бы выразить благодарность всем людям, внесшим свой вклад в мою кандидатскую диссертацию своей поддержкой, помощью, советами:

Моим родителям, которые поддерживают меня всю мою жизнь и, в особенности, моей маме, которая мечтала, чтобы я защитил эту диссертацию больше, чем я.

Моей жене за нашу любовь, результатом которой во время моего обучения в аспирантуре уже стало рождение нашего первого сына.

Моему сыну за то, что дал мне возможность работать дома ночами.

Я хотел бы также поблагодарить свою бабушку, которая не дожила до защиты моей кандидатской диссертации, но я думаю, она была бы счастлива за меня.

Владимиру Викторовичу Вечернину и Григорию Александровичу Феофилову, а также всей группе СПбГУ-ALICE за предоставленную возможность присоединиться к Коллаборации ALICE, большой международной коллаборации.

Bruno Espagnon за то, что был моим научным руководителем и за редактирование моей диссертации, Christophe Suire за ценные советы и за редактирование моей диссертации, Cynthia Hadjidakis за то, что была моим соруководителем и подталкивала меня к занятию физикой, а также за редактирование моей диссертации, Zaida Conesa Del Valle за множество серьёзных советов во время моего обучения в аспирантуре. Я хотел бы поблагодарить группу в Орсэ за эти три прекрасных года, которые я провёл в окружении столь хороших людей, а также за всю помощь и руководство, которые я получил.

Enrico Scomparin и Roberta Arnaldi за удовольствие работать вместе с ними и за хорошее время, которое я провёл во время моего короткого визита в Турин. Спасибо также Jean-Philippe Lansberg за организацию этого визита.

Коллаборации ALICE за хорошие экспериментальные данные.

Моим друзьям за нашу дружбу.

Членам моего диссертационного комитета за чтение диссертации и за вопросы и предложения, которые я получил от них.

Introduction

Hard probes represent one of the hottest topic of the modern high energy physics. The production mechanism of quarkonia (mesons composed of a quark and its antiquark) in hadronic collisions is of particular interest. Various theoretical models based on Quantum Chromodynamics (QCD) were developed but still none of them can provide a full description of the measurements. This thesis is devoted to the studies of the charmonium (quarkonia of charm quarks $c\bar{c}$) production in p-Pb collisions at the Large Hadron Collider (LHC) with the muon spectrometer of A Large Ion Collider Experiment (ALICE).

Chapter 1 presents the history of the charmonium production studies in pp collisions, which started from the J/ψ meson discovery in November 1974. This chapter also describes three theoretical models of charmonium production: the Color Evaporation Model (CEM), the Color-Singlet Model (CSM) and the Non-Relativistic QCD approach. Success and failures of these models are also discussed when they are compared to the pp experimental measurements.

In nucleus-nucleus collisions where a higher energy density is created, a new state of matter is believed to be formed: the Quark Gluon Plasma (QGP). It affects charmonium production which can be considered as a "QGP thermometer". Chapter 2 discusses charmonium production in hot medium of nucleus-nucleus collisions, comparing also experimental measurements from heavy-ion colliders: Super Proton Synchrotron (SPS), Relativistic Heavy Ion Collider (RHIC) and LHC.

Chapter 3 is devoted to the description of the nuclear matter effects that are not related to the QGP. They are called Cold Nuclear Matter (CNM) effects. CNM effects are relevant both in nucleus-nucleus and in nucleon-nucleus collisions. While in nucleus-nucleus collisions they are combined with the QGP effects, it is generally assumed that in nucleon-nucleus collisions there are no effects related to QGP. In this chapter, several theoretical approaches are presented: gluon shadowing, gluon saturation, nuclear absorption and coherent parton energy loss. These theoretical approaches are confronted to the RHIC measurements for the J/ψ production in d-Au collisions at $\sqrt{s_{\rm NN}} = 200$ GeV.

Chapter 4 briefly introduces the LHC and provides an overview of the ALICE detector. ALICE is dedicated to the study of heavy-ion collisions but also

includes in its physical program pp and p-Pb collisions. Thanks to its detection capabilities ALICE allows one to measure quarkonium production over a large rapidity range and down to zero transverse momentum p_{T}. ALICE can be divided into two main parts: central and forward detectors. The latter includes the muon spectrometer - the main detector used for the analysis presented in this thesis. The muon spectrometer is designed for quarkonium production studies in the dimuon decay channel at forward rapidity ($2.5 < y < 4$).

Chapter 5 presents my personal work related to the tuning of the corresponding Monte Carlo generator, used for the trigger rate estimations for the p-Pb collisions at ALICE. This generator, based on the Glauber model, allows to study the centrality dependence of quarkonium production in p-Pb collisions. This chapter also provides the results of comparison of this generator with the data from the pilot p-Pb run performed in September 2012.

Chapters 6 and 7 describe the two main analyses with my personal contribution. The first one is devoted to the study of p_{T} and y dependence of the J/ψ production in p-Pb collisions while the second one is dedicated to the studies of the J/ψ production in p-Pb collisions as a function of the event activity.

Chapter 8 presents the results of the analyses described in the two previous chapters. These results include the J/ψ nuclear modification factor as a function of rapidity, as a function of the event activity and as a function of both p_{T} and the event activity, as well as the forward-to-backward ratio as a function of rapidity and p_{T} in p-Pb collisions. From the p_{T} and event activity dependence, I also extracted the $\langle p_{\mathrm{T}} \rangle$ and $\langle p_{\mathrm{T}}^2 \rangle$ as a function of the event activity. Results of other ALICE analyses, where I was involved, are also presented in this chapter: the p_{T} dependence of the J/ψ nuclear modification factor and the ψ(2S) production measurements in p-Pb collisions. The results are compared to the theoretical models described in Chapter 3.

Finally the p-Pb measurements allow an estimation of the contribution of the CNM to the Pb-Pb measurements and this is also discussed.

N.B.! It is important to mention that the ALICE figures presented in this thesis are mostly the official ALICE plots. They are marked with the ALICE logo or with the phrase "ALICE Preliminary" or "ALICE performance" and/or has a link to the public source (article, proceedings, etc.). All the other figures not fulfilling these requirements should be considered as the result of this thesis and are not the official figures of the ALICE collaboration.

Chapter 1

History of the charmonium production studies in pp

This chapter describes the history of the discovery of the J/ψ meson and introduces charmonium states ($c\bar{c}$ bound states) in general. It also presents the main theoretical models of the charmonium production and experimental measurements of the charmonium production in pp collisions.

1.1 Discovery of J/ψ

The history of the charmonium production studies started in November 1974 when two independent groups working in two different experiments in the USA discovered a new particle — a resonance with a mass of 3.1 GeV (three times higher than a proton mass). One of the most curious properties of this resonance was its very narrow width of 70 keV, which corresponds to the life time of 10^{-23} seconds. The Alternating Gradient Synchrotron (AGS) group from the Brookhaven National Laboratory (BNL) found it from the reaction $p+Be \rightarrow e^+ + e^- + x$ measuring the e^+e^- invariant mass spectrum (see Fig.1.1(a)) and called it a "J" particle [1]. The Stanford Positron Electron Asymmetric Ring (SPEAR) group from the Stanford Linear Accelerator Center (SLAC) observed it in the e^+e^- annihilation reaction in both e^+e^- and $\mu^+\mu^-$ invariant mass spectra and called it "$\psi(3105)$" [2]. This name was motivated by the event display of the decay of the excited state of $\psi(3105)$, i.e. $\psi(2S) \rightarrow \psi(3105) + \pi^+ + \pi^-$ followed by $\psi(3105) \rightarrow e^+ + e^-$ (see Fig.1.1(b)).

In 1976 Ting and Richter (leaders of the two groups mentioned above) were awarded the Nobel Prize in physics for the simultaneous discovery of a new particle which was, consequently, renamed to "J/ψ". It shows the importance of that particle in this era where it was believed that only three elementary quarks (u, d, s) exist. The SLAC group wrote in their paper: "The large mass, large cross section, and narrow width of this structure is entirely unexpected." [2]

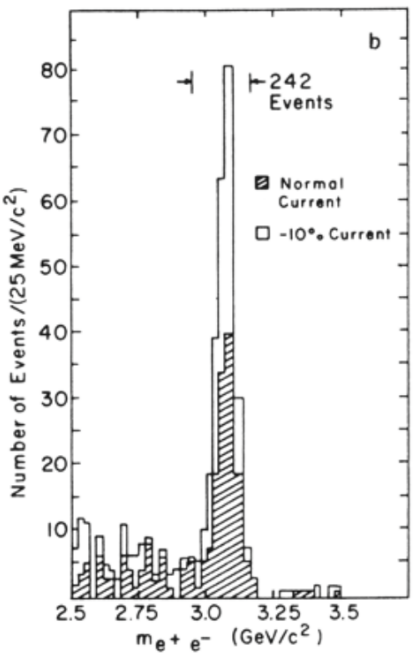

(a) Dielectron invariant mass spectrum from 20 GeV/c protons on fixed target.

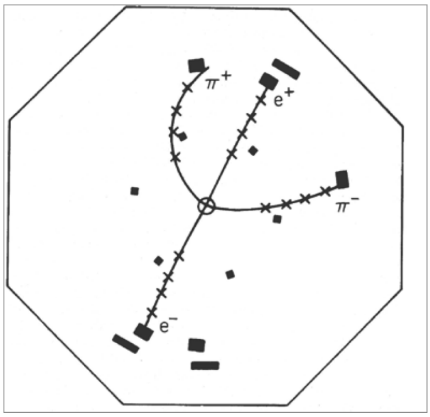

(b) Mark I (SPEAR) Event Display.

Figure 1.1. Discovery of the J/ψ particle by BNL (a) and SLAC (b).

However first ideas of the J/ψ as a charmed particle were announced in the paper of the BNL group with a citation to the private communication with S.L. Glashow [1]. A 4th quark was also expected from the GIM mechanism (Glashow, Iliopoulos and Maiani). In fact it was still disputed whether quarks exist at all and the discovery of calculable spectrum of charmonium states was convincing evidence for many (the November revolution). The J/ψ discovery resulted in a public resonance. It led to an increase of interest in studies in the c quark sector.

1.2 Charmonium states

The bound states of heavy quark q and its anti-quark $\bar{q}$ are referred to as quarkonia. The quarkonia of charm quarks $c\bar{c}$ are, consequently called "charmonia" and of bottom quarks $b\bar{b}$ "bottomonia". In this section we will mainly focus on the charmonium states since they represent the main topic of this thesis.

The most famous charmonium state is, for sure, the J/ψ meson whose discovery was described in the previous section. However besides the initially found J/ψ there is a number of other bound states of $c\bar{c}$ with different quantum

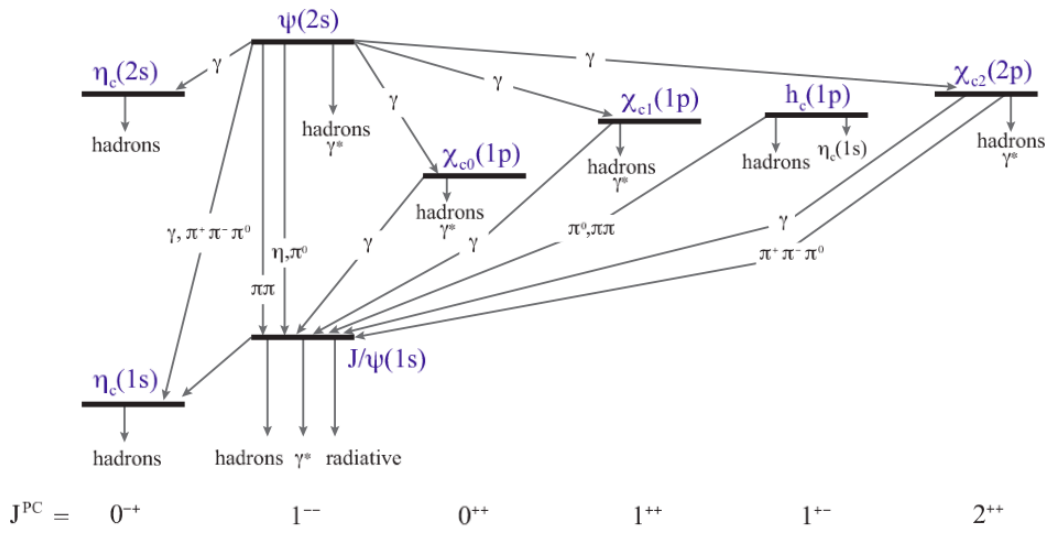

Figure 1.2. Charmonium family. The bottom row shows the spin, parity, and the charge conjugation quantum numbers associated with the states above it [3].

numbers. In Fig. 1.2 one can see all the charmonium states as well as the transitions between them. These transitions are responsible for the so-called "feed down" effect: in the final state, an experiment detecting only leptons would be unable to separate a process J/$\psi\rightarrow l^+l^-$ from the process ψ(2S)$\rightarrow$ $\pi^+\pi^-$J/ψ followed by the consequent decay of the J/ψ : J/$\psi\rightarrow l^+l^-$. As a result it will detect two J/ψ instead of one ψ(2S) and one J/ψ. They are stable in the sense that their mass is less than twice the mass of the lightest heavy meson which leads to the exclusion of the strong decays [4]. The main characteristics of the charmonia, the mass and the binding energy which is defined as the difference between the quarkonium mass and the open charm threshold, are summarized in Table 1.1.

Table 1.1. Mass and binding energy (ΔE) of charmonium states.

State	η_c	J/ψ	χ_{c0}	χ_{c1}	χ_{c2}	ψ(2S)
Mass, GeV/c^2	2.98	3.10	3.42	3.51	3.56	3.69
ΔE, GeV	0.75	0.64	0.32	0.22	0.18	0.05

The reason why the J/ψ was discovered first with respect to the other charmonium states arises mainly from the high Branching Ratio (BR) of its decay to dileptons, $BR_{J/\psi\rightarrow l^+l^-} = 5.9\%$. This can be explained by the OZI

(Okubo, Zweig, Iizuka) rule [5–7] which leads to a strong suppression of the J/ψ hadronic decays: this effect increases the lifetime of the particle and thereby gives its narrow decay width of 93.2 ± 2.1 keV/c^2. Due to this strong suppression, electromagnetic decays begin competing with hadronic decays which leads to the significant branching ratio of the dileptons decays, and in particular dimuon decays. Dimuon decays are rather easy to detect in high-energy colliders in the sense that they give rather high signal-to-background ratio since the muons, are not stopped when going through detectors and are then detected by dedicated spectrometers.

A significant effect from the feed down decays from higher charmonium states, as illustrated in Fig.1.2, and from open heavy flavour[1] should be taken into account. The J/ψ meson can be produced not only via the direct hadronization of the $c\bar{c}$ pair ("direct" J/ψ). It can be also produced via the radiative feed down decay of ψ(2S) and of $\chi_{cJ}(1P)$ (these J/ψ form with the direct J/ψ the "prompt" J/ψ sample) or via the weak decays of the bottomed mesons (B^0, B_s^0, $B^{\pm}$ and $B_c^{\pm}$) decaying into J/ψ or ψ(2S) with forming one or more additional hadrons. The J/ψ from these weak decays are called "non-prompt" J/ψ and constitute with prompt J/ψ an "inclusive" J/ψ sample usually measured in the experiment. Knowing the fractions of prompt and non-prompt J/ψ contributions to the inclusive J/ψ yield one could easily compare the experimental data with theoretical predictions since the three types of the J/ψ production involve different physics.

1.3 Theoretical description of charmonium production

There are a number of models on the market offering theoretical description of charmonium production. In the following, we will briefly describe the Color Evaporation Model, the Color-Singlet Model and the Non-relativistic Quantum Chromodynamics factorization approach.

1.3.1 Color Evaporation Model

The Color Evaporation Model (CEM) was first suggested three years after the J/ψ discovery in 1977 [8,9]. Quarkonium production in the CEM is treated identically to the open heavy quark production [10]. The only difference for quarkonium is that the heavy quark pair invariant mass is restricted to be less than twice the mass of the lowest mass meson that can be formed with

[1]Hadrons which consist of a heavy quark-antiquark pair (e.g. J/$\psi = c\bar{c}$) are called heavy quarkonia, or hidden heavy flavour. Hadrons containing a light quark and a heavy quark (e.g. D and B mesons: $D^0 = c\bar{u}$, $B^+ = u\bar{b}$) are referred to as open heavy flavour.

the heavy quark. The upper limit on the $c\bar{c}$ pair for charmonium is $2m_D = 3.74$ GeV. The CEM assumes the identity of the quarkonium dynamics to low invariant mass $c\bar{c}$ pairs although they are typically produced in different color, angular momentum, and spin states than the final charmonium states. The hadronization of the charmonium states from the $c\bar{c}$ pairs is non-perturbative and usually involves the emission of one or more soft gluons. Then different non-perturbative matrix elements depending on the quantum numbers of the initial $c\bar{c}$ pair and the final-state charmonium, should be considered. The average of these elements are combined into the universal factor F which depends on the parton densities, the c-quark mass and the scale α_s. It represents the fraction of the charmonium cross section that produces a given $c\bar{c}$ resonance in the final state. Fixing F for the different charmonium states allows the CEM to make successful predictions about energy and momentum dependencies.

Since at Leading Order (LO) the transverse momentum p_{T} of the $c\bar{c}$ pair is zero, the Next-to-Leading Order (NLO) corrections can be considered to perform the calculations of the p_{T} dependence.

However CEM has some weak points. One of them is in the fact that the CEM gives a simple qualitative prediction of the independence of the ratio of the cross sections for any two quarkonium states from the process and kinematical region while some variations in these ratios were already observed. For example, the cross sections ratio for χ_c and J/ψ are quite different in hadroproduction and photoproduction [11]. This fact presents a serious challenge to the CEM.

1.3.2 Color-Singlet Model

The Color-Singlet Model (CSM) was proposed shortly after the J/ψ discovery [12–16]. It assumes that the $c\bar{c}$ pair evolving into the charmonium is in a color-singlet state and has the same spin and angular-momentum quantum numbers as the charmonium [17]. The production rate for each charmonium state in the CSM is related to the absolute values of the $c\bar{c}$ wave function and its derivatives. They can be extracted from the experimental data. Once this extraction is done CSM has no free parameters.

The CSM was successful in prediction of production cross sections at low energy [18]. However it under-predicted the prompt charmonium production cross section in $p\bar{p}$ collisions, measured at Tevatron, by more than an order of magnitude. Recently it was shown that, at high energies, NLO and next-to-next-to-leading order (NNLO) give very large corrections in α_S to the CSM [19–21]. These higher order calculations re-emerged the possibility of the CSM to embody an important production mechanism at high energies. However it is not clear that the perturbative expansion in α_S is convergent.

1.3.3 NRQCD factorization approach

One of the most successful models for the charmonium production is the Non-relativistic Quantum Chromodynamics (NRQCD) factorization approach [22]. It makes use of perturbative methods by separating the short-distance/high-momentum, perturbative effects from the long-distance/low-momentum, non-perturbative effects. This process is called "factorization". It could be done in terms of the effective field theory NRQCD. The latter reproduces full QCD accurately at momentum scales of order mv and smaller, where v is the typical heavy-quark velocity in the bound state in the center-of-mass frame ($v^2 \approx 0.3c^2$ for charmonium) [11]. The inclusive cross section for the direct production of a charmonium state H at large transverse momentum ($p_{\mathrm{T}} \gtrsim m$) in hadron or ep colliders or at large momentum in the center-of-mass frame ($p^\star \gtrsim m$) in e^+e^- colliders can be written as a sum of products of NRQCD matrix elements and short-distance coefficients:

$$\sigma(H) = \sum_n \sigma_n(\Lambda)\langle \mathcal{O}_n^H(\Lambda)\rangle, \tag{1.1}$$

where Λ is the ultraviolet cutoff of the effective theory and the σ_n are the short-distance coefficients representing expansions in powers of v of the cross sections to produce a $c\bar{c}$ pair in a state n which is determined by its color, spin and orbital-angular momentum. Finally, the matrix elements $\langle \mathcal{O}_n^H(\Lambda)\rangle$ are the vacuum-expectation values of four-fermion operators in NRQCD.

In contrast to the CSM and CEM production cross section expressions, the NRQCD factorization formula for the production of heavy-quarkonium depends on an infinite number of unknown matrix elements. However reorganization of the sum in (1.1) as an expansion in powers of v results in the formulating of the NRQCD factorization formula as a double expansion in powers of v and powers of α_S. In phenomenological applications it is usually truncated at a fixed order in v and considers only a few matrix elements. The validity of this truncation as well as the universality of the long-distance matrix elements and the perturbative calculability of the $c\bar{c}$ cross sections define the predictive power of the NRQCD factorization approach.

It should be noted that by dropping all of the color-octet terms and all but one of the color-singlet terms in (1.1) one obtains the CSM [11]. However such an omission of color-octet contributions leads to inconsistencies because of uncanceled infrared divergences in the production rates of P-wave (see Fig.1.2) and high orbital-angular momentum quarkonium states.

Assuming certain relationships between the NRQCD long-distance matrix-elements then the CEM is obtained [23]. These relationships however are inconsistent with the scaling of the matrix elements with v predicted by NRQCD.

The NRQCD factorization approach successfully described many observables. However there are still some open issues, both from the purely theoret-

ical and from the phenomenological point of view. One of them is the validity of the factorization formula (1.1) which was proven for the calculation of two exclusive amplitudes [24, 25]: exclusive production of quarkonium + light meson in B-meson decays and exclusive production of two quarkonium states in e^+e^- annihilation, but not for the inclusive production. Moreover, this formula breaks down when an additional heavy quark is produced in close proximity to a $q\bar{q}$ pair that evolves into a quarkonium. Experimental results on quarkonium + heavy-quark production should help in understanding the magnitude of this process. It should be also mentioned that LO NRQCD had problems in describing polarization results on prompt J/ψ production at Tevatron and this was the reason for a revival of the CSM in the last years [19–21].

1.4 Experimental results on charmonia in pp

As it was already discussed above charmonia represent one of the most exciting areas of the modern physics. This explains a large amount of experimental data on charmonium production in various collision systems at the wide range of energies. In this section we provide some highlights of the measurements of charmonium production in high energy elementary collisions performed by Tevatron, Relativistic Heavy Ion Collider (RHIC) and the Large Hadron Collider (LHC).

1.4.1 Tevatron results

The Collider Detector at Fermilab (CDF) collaboration [26] was the main player in charmonium production studies at Tevatron [27]. In Run I (the first period of the data taking) of the Tevatron, CDF performed measurements of the direct production cross sections of J/ψ and ψ(2S) in p$\bar{\text{p}}$ collisions at $\sqrt{s}$ =1.8 TeV [28, 29]. A striking discrepancy was found with the existing theoretical predictions: CSM at LO in α_S predicted more than an order of magnitude lower rates than those observed in the experiment (See Section 1.3.2). The dotted curves in Fig.1.3 show this discrepancy. Including the color-singlet fragmentation increases the cross section values by more than an order of magnitude at large p_{T}. However it still falls below the data. To explain the CDF results on J/ψ and ψ(2S) production, the leading color-octet contributions $\langle \mathcal{O}_8^H(^3S_1)\rangle$, $\langle \mathcal{O}_8^H(^3P_0)\rangle$ and $\langle \mathcal{O}_8^H(^1S_0)\rangle$ have to be included, adjusting the corresponding non-perturbative parameters to fit the data. For the χ_{cJ} states production the most important matrix element is $\langle \mathcal{O}_8^H(^3S_1)\rangle$. Therefore to fit the prompt J/ψ production from decay of χ_c the $\langle \mathcal{O}_8^{\chi_{c0}}(^3S_1)\rangle$ contribution should be adjusted [30].

The shape and the normalization of the prompt charmonium cross section at the Tevatron can be also well described by the CEM. The normalization

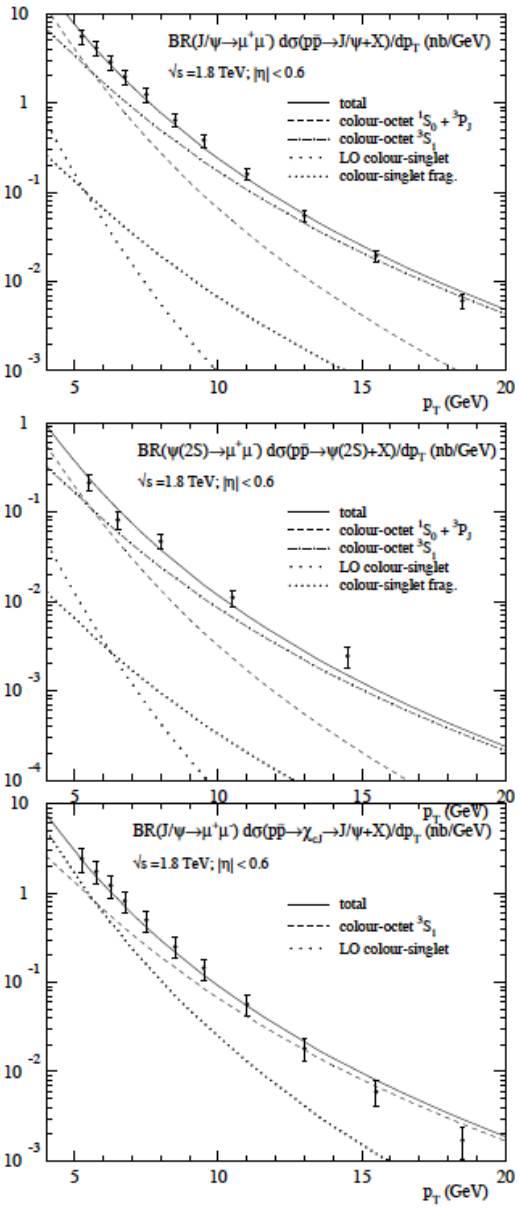

Figure 1.3. Top panel: Differential cross sections for the direct J/ψ production in $p\bar{p} \to J/\psi + X$ at the Tevatron ($\sqrt{s} = 1.8$ TeV, pseudorapidity cut $|\eta| < 0.6$) compared to experimental data from CDF as a function of p_T. Middle panel: the same for the prompt ψ(2S). Bottom panel: the same for the prompt J/ψ from decay of χ_c. Dotted lines are the CSM contributions, the solid lines are the NRQCD factorization fits, other lines represent individual color-octet contributions to the fits. p_T is given in natural units. From [30].

of the prompt J/ψ production cross section predicted by CEM at NLO are in reasonable agreement with the CDF data from Run I.

A simple phenomenological model for the effects of multiple gluon emission on the theoretical predictions is k_{T} smearing [23]. In k_{T} smearing, the colliding partons are given Gaussian distributions in the intrinsic transverse momentum, with a width that is treated as a phenomenological parameter. A particular version of this model that has been used in comparing the CEM predictions with the CDF data attempts to account for multiple gluon emission from the two initial-state partons by adding two transverse momentum "kicks" to the quarkonium momentum. The direction of each momentum kick is symmetrically distributed over the 4π solid angle, and the magnitude k_{T} of each momentum kick distributed as

$$g(k_{\mathrm{T}}) = \frac{1}{\pi\langle k_{\mathrm{T}}^2\rangle}\exp(-k_{\mathrm{T}}^2/\langle k_{\mathrm{T}}^2\rangle), \tag{1.2}$$

where $\langle k_{\mathrm{T}}^2\rangle$ is a phenomenological parameter. Adding k_{T} smearing, with $\langle k_{\mathrm{T}}^2\rangle = 2.5$ (GeV/c)^2, improves the agreement with the data for the J/ψ cross sections (see Fig.1.4).

Other interesting result by the CDF is the polarization variables which can be defined as ratios of cross sections for the production of different spin states of the same charmonium. The models seen above give very different predictions for the polarizations. In addition, many uncertainties cancel out in this variables which makes it a powerful tool. The angular distribution of the charmonium decay products depends on the spin state of the charmonium. The polarization of a 1^{--} state (like J/ψ) can be measured from the angular distribution of its decay into leptons pairs, taking θ as the angle in the J/ψ rest frame between positive lepton momentum and the chosen polarization axis. The choice of the axis depends on the process (see e.g. [31]). The differential cross section has the form [11]:

$$\frac{\mathrm{d}\sigma}{\mathrm{d}(\cos\theta)} \propto 1 + \alpha\cos^2\theta, \tag{1.3}$$

where polarization variable α varies from -1 to $+1$. One can define longitudinal and transverse polarization of J/ψ as a function of its spin components along the polarization axis: $\alpha = 1$ for the 100% transverse polarized J/ψ, while $\alpha = -1$ for the 100% longitudinal polarized J/ψ. Fig.1.5 shows the striking disagreement between the NRQCD prediction and the experimentally observed polarization. The k_{T} factorization approach prediction [32], including only color-singlet contributions is also shown. In this approach one takes into account that gluons generated in the parton evolution cascade do carry non-negligible transverse momentum (k_{T}) and are off mass shell. This approach also has a visible disagreement with the data but seems to describe the shape

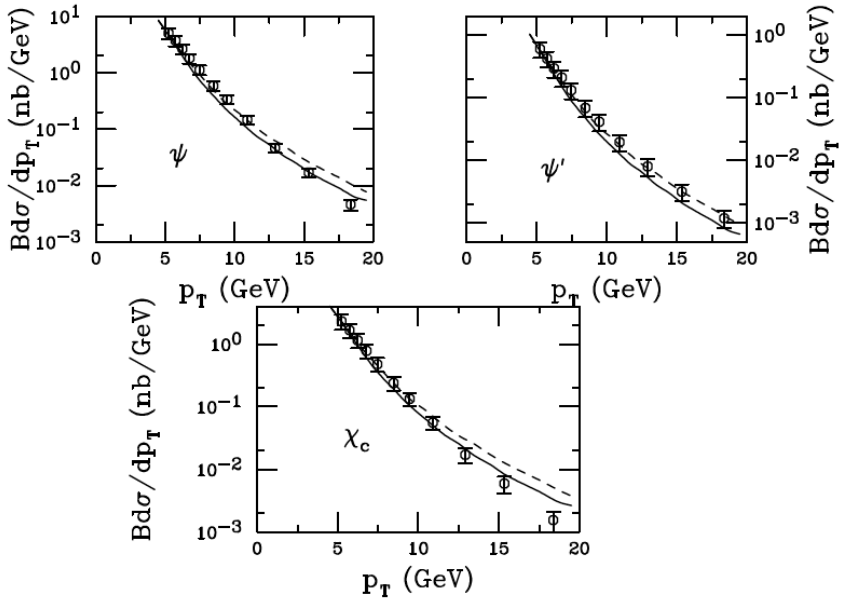

Figure 1.4. p_{T} dependence of the differential cross sections for the production of direct J/ψ (top left panel), prompt ψ(2S) (top right panel), and prompt J/ψ from decays of χ_c (bottom panel) at the Tevatron. CDF data points are taken from [28,29]. The dotted and solid lines are the CEM predictions at NLO with $\langle k_{\mathrm{T}}^2 \rangle = 2.5$ (GeV/c)^2, using different sets of charmonium parameters. p_{T} is given in natural units. From [11].

of the experimental measurements better.

The failure of NRQCD, which was successful in describing the J/ψ production cross sections, lead to many theoretical efforts in the CSM framework.

1.4.2 RHIC results

Four experiments are hosted at RHIC (Relativistic Heavy Ion Collider) [35]. Two of them, PHENIX (Pioneering High Energy Nuclear Interaction eXperiment) Collaboration [36] and STAR (Solenoidal Tracker at RHIC) Collaboration [37] still continue operating. In 2009 results on the prompt J/ψ production for p_{T} up to 12 GeV/c in pp collisions at $\sqrt{s} = 200$ GeV have been released [38]. The p_{T}-dependence of the measured production rate was compared to predictions based on NRQCD factorization at LO [39] and the CSM up to NNLO* accuracy [21]. NNLO* corresponds to the yield at the NNLO accuracy (at α_S^5) from gg and gq fusion. The calculations do not include feeddown from the ψ(2S) and the χ_c states. The NRQCD factorization prediction is favored by the data over the CSM prediction. No strong conclusions can be made since the feeddown effect was not taken into account. In fig.1.6 calculations of the

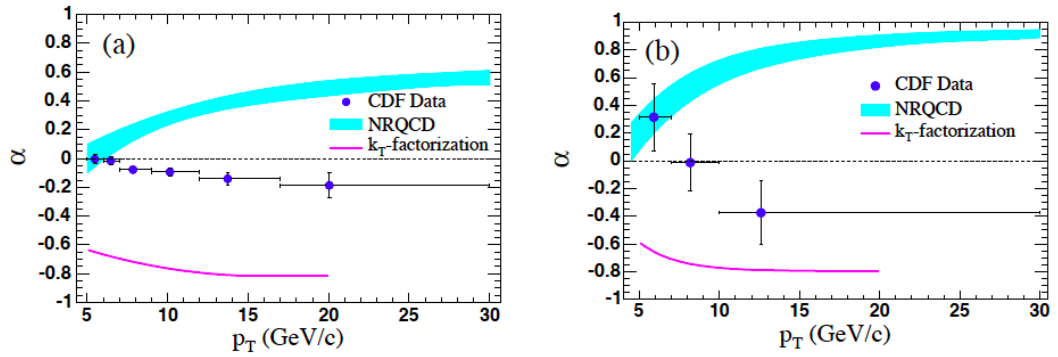

Figure 1.5. p_{T} dependence of the prompt polarizations in $\mathrm{p\bar{p}}$ collisions at $\sqrt{s}$ =1.96 TeV for (a) J/ψ and (b) ψ(2S). The band correspond to the LO NRQCD prediction [33], while the line represent the k_{T} factorization model [32]. From [34].

prompt J/ψ production at RHIC including the feeddown from the ψ(2S) and the χ_c states were performed in the CSM and the NRQCD factorization formalism at LO [40]. The NRQCD predictions are again favored over the CSM predictions.

Higher-order corrections to the color-singlet contribution to J/ψ production were found to be large [42]. In Fig.1.7 the comparison between the CSM prediction for the J/ψ cross section and the prompt J/ψ data from STAR [38] and PHENIX [43] is shown. NLO$^+$ stands for the yield at NLO accuracy (up to α_S^4) from gg (gluon-gluon) and gq (gluon-quark) fusion added to the yield from cg (charm-gluon) fusion at LO accuracy (at α_S^3). See [42] for more details. The color-singlet contributions through NLO$^+$ agree with the PHENIX prompt data at low p_{T} but go below the data at $p_{\mathrm{T}} > 2$ GeV/c. The NNLO* color-singlet contribution can be computed reliably only for $p_{\mathrm{T}} > 5$ GeV/c and shows a good agreement with the data but has very large theoretical uncertainties.

PHENIX also measure a p_{T}-dependence for the prompt J/ψ polarization. In Fig.1.8 it is compared in the helicity frame[1] to NRQCD LO and CSM LO (left panel) and CSM NLO (right panel). The data indicate a polarization compatible with zero, with a trend towards longitudinal polarization with increasing p_{T}. NRQCD LO and CSM NLO are favored by the data, while CSM LO shows disagreement with the experimental measurements.

Thus, comparison of the J/ψ polarization in the experimental data to those calculated by NRQCD LO leads to different conclusions at RHIC energies with respect to those at the Tevatron energies.

[1]The most common polarization frame used in analyses performed at collider experiments is where z axis is chosen as quarkonium momentum. Polarization measured in this manner is referred to as being in the helicity frame [44].

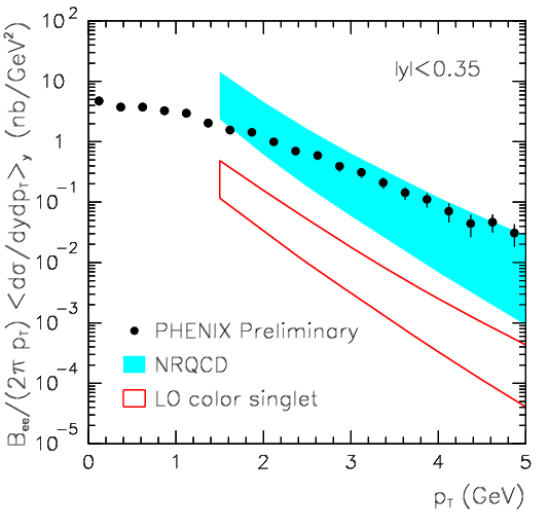

Figure 1.6. The p_T dependence of the differential cross section for the inclusive J/ψ measured by PHENIX in pp collisions at $\sqrt{s}$ = 200 GeV [41]. The shaded band represents the NRQCD prediction, while the band surrounded by a solid line is the color-singlet contribution at LO in α_s. Theoretical predictions are made for the prompt J/ψ. From [40].

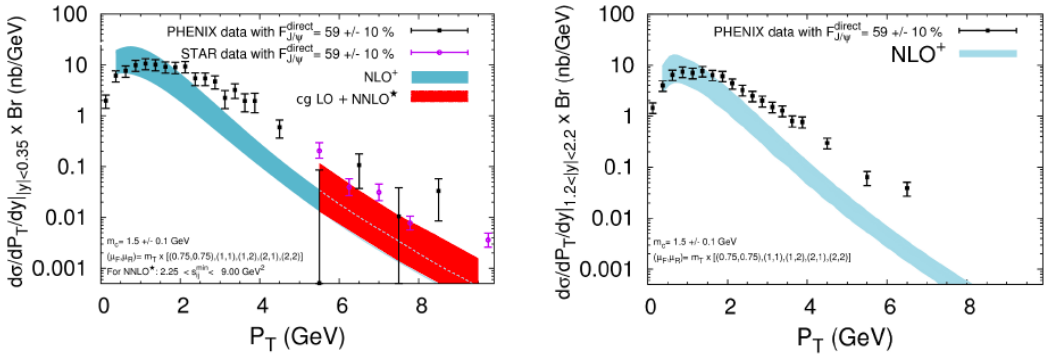

Figure 1.7. p_T dependence of the differential cross sections for the prompt J/ψ in pp collisions at $\sqrt{s}$ = 200 GeV from STAR [38] and PHENIX [43] in two rapidity regions at NLO$^+$ (and *cg* LO + NNLO* for the left panel) compared. Left panel: central ($|y| < 0.35$) region, right panel: forward (1.2<|y|<2.2) region. p_T is given in natural units. From [42].

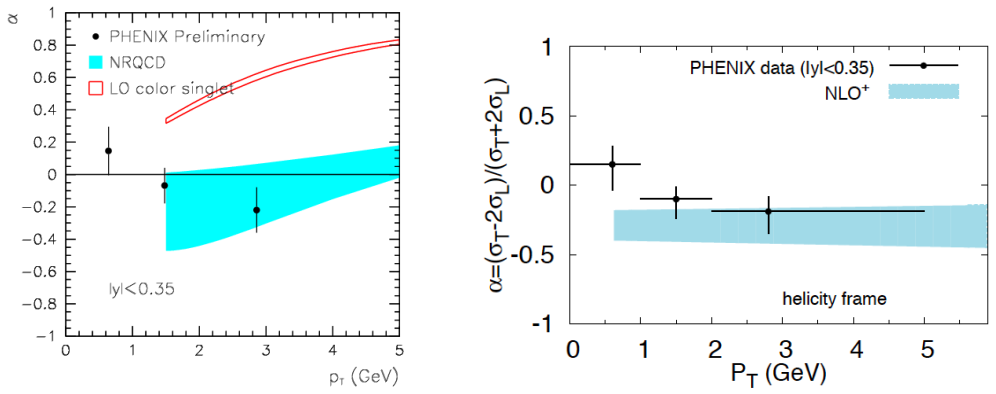

(a) From [40]. (b) From [42].

Figure 1.8. Prompt J/ψ polarization in pp collisions at RHIC at $\sqrt{s}$ = 200 GeV in the helicity frame compared to theoretical models: (a) to NRQCD LO and CSM LO predictions; (b) to CSM NLO. p_{T} is given in natural units.

1.4.3 LHC results

The LHC [45–47], situated at CERN (European Organization for Nuclear Research), is the highest-energy particle collider in the world. The four largest detectors at the LHC are the following: ATLAS (A Toroidal LHC Apparatus) [48], CMS (Compact Muon Solenoid) [49], ALICE (A Large Ion Collider Experiment) [50] and LHCb (Large Hadron Collider beauty) [51]. The ALICE detector will be described in more details in Sect.4.2. First beams were circulated through the LHC in September 2008. The full operation started in November 2009.

Fig.1.9 shows the comparison of the prompt J/ψ production in pp collisions at the LHC experiments at different collision energies. ALICE results are shown for the inclusive J/ψ production at $\sqrt{s}$ = 2.76 TeV and 7 TeV, while CMS and ATLAS results are presented for the prompt J/ψ at 7 TeV and the those of LHCb for the prompt J/ψ at 8 TeV. CMS and ATLAS are focused mainly on the high-p_{T} J/ψ while ALICE and LHCb study lower p_{T} J/ψ. Both NRQCD NLO and CSM with high order corrections describe the data rather well in the wide p_{T} range. One should mention however, that CMS can also provide measurements for low p_{T} J/ψ(see Fig.1.10).

Fig.1.11 shows the p_{T} dependence of the fraction of prompt J/ψ produced in χ_c decays measured by ATLAS and LHCb at high p_{T} ($p_{\mathrm{T}} > 10$ GeV/c). Comparison with NRQCD NLO shows a good agreement between theory and experiment. Total amount of the prompt J/ψ from χ_c is about 20-30%. Fig.1.12 presents another interesting observable measured by ATLAS and CMS: the

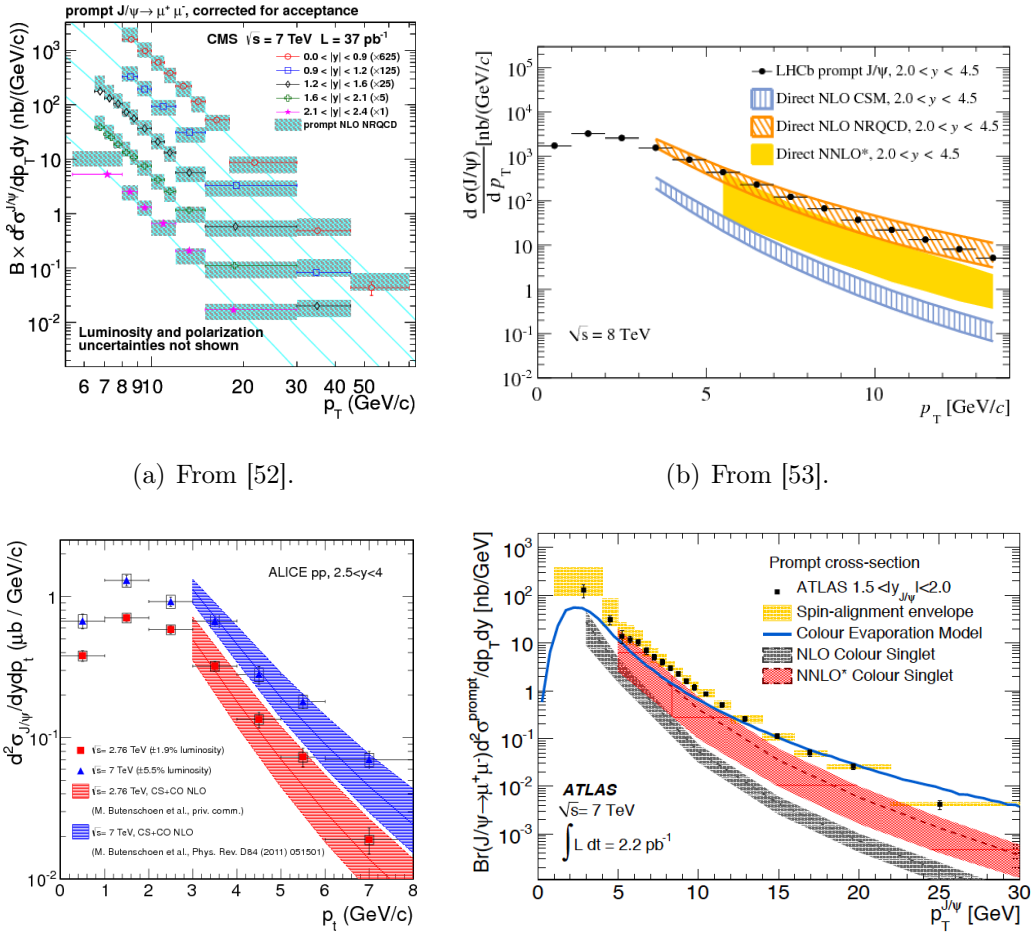

(a) From [52].

(b) From [53].

(c) From [54].

(d) From [55].

Figure 1.9. J/ψ production cross sections in pp collisions at the LHC experiments at $\sqrt{s} = 2.76$ TeV, 7 TeV and 8 TeV: (a) CMS, prompt J/ψ; (b) LHCb, prompt J/ψ; (c) ALICE, inclusive J/ψ; (d) ATLAS, prompt J/ψ. p_{T} is given in natural units.

ratio of production cross sections of prompt J/ψ from χ_{c2} to those from χ_{c1} at high p_{T} ($p_{\mathrm{T}} > 10$ GeV/c). It is compared to NRQCD NLO and to CSM LO. As in the previous case, NRQCD NLO fits the data rather well while the CSM LO is unable to describe the experimental measurements.

Fig.1.13 shows the ALICE results on the inclusive J/ψ polarization in pp collisions at $\sqrt{s} = 7$ TeV [60], compared to theoretical models. Only the results for $p_{\mathrm{T}} > 3$ GeV/c are shown in this plot while ALICE also performed measurements in the p_{T} range [2; 3] GeV/c. The two points presented in the plot correspond to the p_{T} ranges [3; 4] GeV/c and [4; 8] GeV/c. The CSM NLO model is in agreement with the data in the p_{T} range [3; 4] GeV/c, but does not get the trend of the data and underestimates the J/ψ polarization

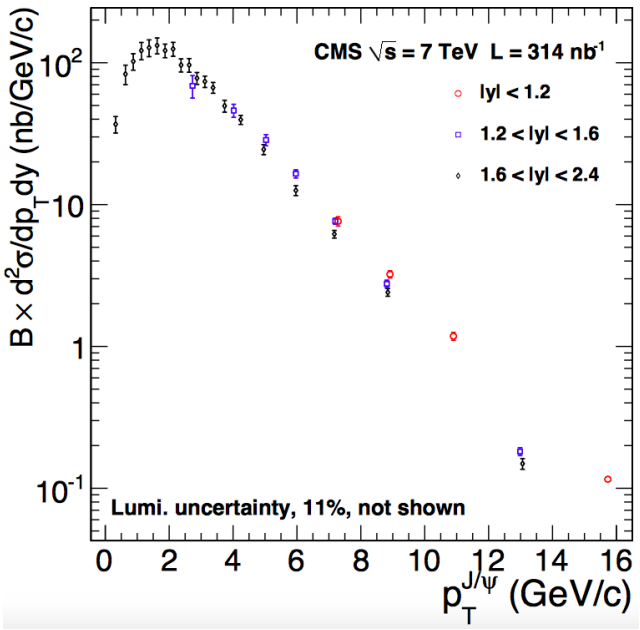

Figure 1.10. p_{T} dependence of the inclusive J/ψ cross section in pp at $\sqrt{s}$ =7 TeV measured by CMS. From [56].

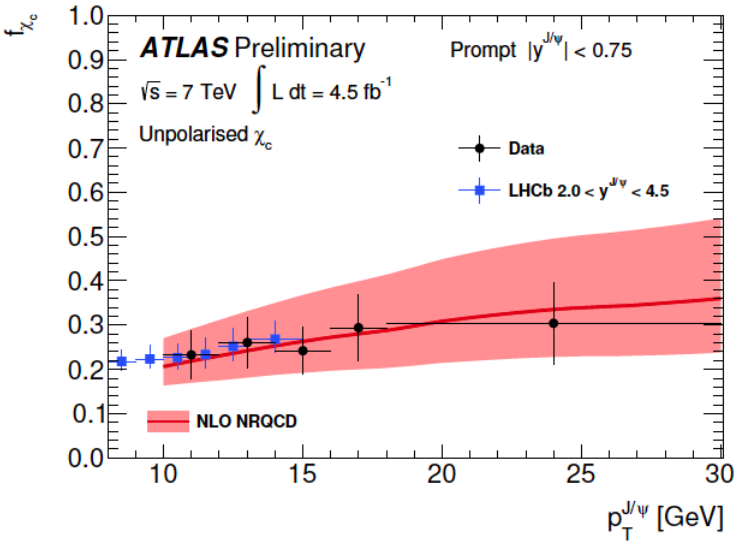

Figure 1.11. p_{T} dependence of the fraction of prompt J/ψ produced in χ_c decays. The error bars represent the total uncertainty on the measurement, assuming unpolarised production. LHCb points are from [57]. p_{T} is given in natural units. From [58].

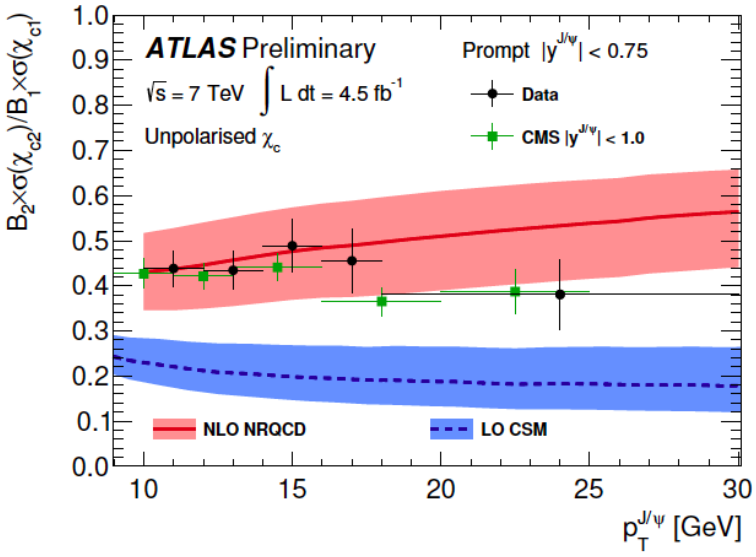

Figure 1.12. Ratio of production cross sections of prompt J/ψ from χ_{c2} to those from χ_{c1}. The error bars represent the total uncertainty on the measurement, assuming the unpolarized production. The factors B_1 and B_2 denote the branching ratios $B_1 = \mathcal{B}(\chi_{c1} \to J/\psi\gamma)$ and $B_2 = \mathcal{B}(\chi_{c2} \to J/\psi\gamma)$. CMS points are from [59]. p_T is given in natural units. From [58].

in the p_T range [4; 8] GeV/c. The CSM LO model reproduces correctly the trend of the data but strongly overestimate the measured J/ψ polarization. The NRQCD approach gives a fair agreement with the data at both LO and NLO.

Thus, NRQCD NLO provides a fair description of both the J/ψ cross section and the J/ψ polarizaton in the helicity frame for pp collisions at $\sqrt{s} = 7$ TeV. However the ALICE results represent the inclusive J/ψ production, while the theoretical prediction are made for the prompt J/ψ. NRQCD NLO also shows a good agreement with the J/ψ pp cross section at 2.76 TeV and with the fraction of the J/ψ produced in χ_c decays in pp collisions at 7 TeV. Therefore, NRQCD NLO can be indeed considered as a very successful model for the J/ψ production at the LHC energies.

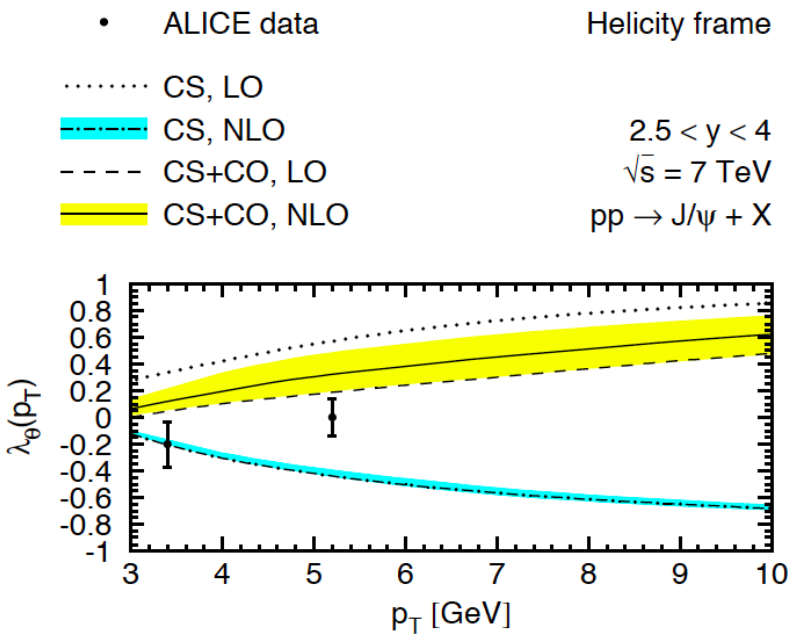

Figure 1.13. Polarization of the inclusive J/ψ in the helicity frame in pp collisions at $\sqrt{s} = 7$ TeV compared to theoretical models. Dotted line is the CSM LO calculation. Dot-dashed line corresponds to the CSM NLO predictions including theoretical uncertainties (hatched/blue band). Dashed line represents the NRQCD LO. Solid line denotes the NRQCD NLO prediction including theoretical uncertainties (shaded/yellow band). p_{T} is given in natural units. From [61].

Chapter 2

The QGP and charmonium production in A-A

In the previous chapter the charmonium production in elementary pp and $p\bar{p}$ collisions was described. In this chapter we will discuss charmonium production in A-A collisions where a higher energy density is created over larger volume.

2.1 QGP as a new state of matter

Lattice gauge theory shows that quarks inside the hadron interact with an effective strength which grows approximately linearly with the spatial distance. This leads to the effect of confinement where the quarks cannot quit the hadron due to the strong force binding them. However, in a system with high energy density ($\sim 0.6-1$ GeV/fm^3), the hadrons start overlapping each other and their constituents are no longer confined inside baryons and mesons. The interaction between the elementary constituents becomes weak and a system of deconfined quarks and gluons is formed. This new state of matter is called Quark-Gluon Plasma (QGP) [62] and is believed to be formed at a critical temperature where the phase transition occurs [63]. In the big bang cosmological scenario [64], the early Universe may have gone through a QGP state at a very early time. The QGP can be also obtained in laboratories in heavy-ion collisions. In Fig.2.1 the space-time evolution of a heavy-ion collision is shown schematically. It can be described as follows[1]:

- *Pre-equilibrium* phase can be divided in two phases:

[1]The time given for each of these phases is not a result of experimental measurements but represents some possible values. Indeed t-values depend on $\sqrt{s_{\rm NN}}$ (the center-of-mass energy per nucleon pair) of the collision.

  - · *Initial hards scatterings* at $t \approx 0$ fm/c where heavy quarks, jets and direct photons are created.
  - · *Thermalization* phase at $t \approx 1 - 2$ fm/c is a result of multiple scatterings of partons and a rapid increase of entropy caused by the produced particles.

- *QGP* phase is a phase where the quarks and gluons are deconfined. The system reaches it at $t \approx 2 - 10$ fm/c.
- *Mixed phase* corresponds to an intermediate state between the QGP and the hadronic gas when the system is cooling down. It takes place at $t \approx 10 - 15$ fm/c
- *Hadronic gas* phase starts at $t \approx 20$ fm/c when the expanding system cools down below a critical temperature and a hadronization of quarks and gluons starts.
- *Freeze-out* phase can be also divided in two phases:
  - · *Chemical freeze-out* occurs when the inelastic processes are reduced until the relative abundance of hadrons is fixed.
  - · *Kinetic freeze-out* takes place when all the interactions cease and created hadrons stream out.

There are two ways to extract precise information about the initial processes in the system. First is to study the observables which are related to the early stage of the collision and are not affected by rescattering and system expansion. Second is to make extrapolations to the earlier stages of the evolution of the heavy-ion collision. This extrapolation is performed based on the information, carried by the produced particles, about the final state of the fireball. Depending on the choice of the way to proceed, two classes of observables can be distinguished: early and late signatures [62]. The hadrons made of light quarks (u and d) contribute to the late signature group and can provide useful information about the hadronization and the freeze-out of the collision. Thermal photons produced in the plasma, heavy flavors and quarkonia represent the early probes group. Charmonia as a signature of the QGP is of particular interest in this work.

2.2 Quarkonium suppression as a signature of the QGP

Almost thirty years ago, in 1986, T. Matsui and H. Satz proposed to study the J/ψ suppression as one of the signatures of the QGP formation [63]. It was

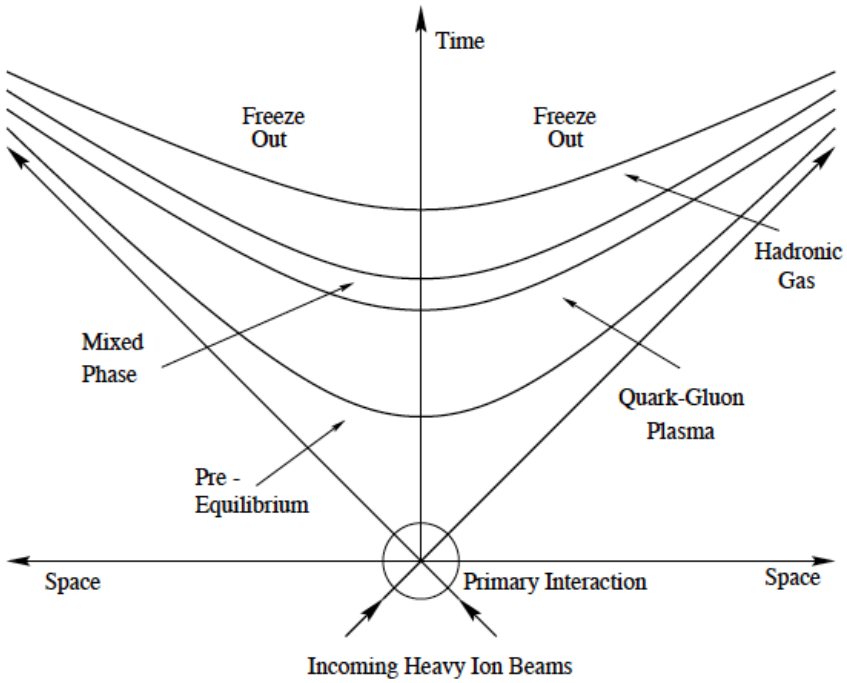

Figure 2.1. The space-time evolution of a heavy-ion collision, describing the formation of a QGP and the phase transition to ordinary matter. From [65].

argued that at sufficiently high temperatures all quark-antiquark bound states will be destroyed by the color screening in the deconfined medium. According to lattice calculations at zero net-baryon density [66–75], deconfinement occurs at a critical temperature $T_c \sim$ 165-195 MeV. Due to color screening, the interaction range between heavy quarks becomes proportional to the inverse temperature $(1/T)$. Consequently, at sufficiently high temperatures the bound state of a heavy quark and its antiquark cannot be produced. The heavy-quark interaction range becomes comparable to the charmonium radius and continue to decrease at temperatures higher than T_c. Thus, charmonium states are not expected to be bound after some temperature T_d. This effect is usually referred to as "dissociation" or "melting". Different charmonium states fully dissociate at different dissociation temperatures. For example, J/ψ is expected to dissociate at a temperature two times higher than the critical temperature, while ψ(2S) is believed to dissociate already at a temperature of the order of critical temperature. This leads to a sequential suppression of different charmonium states. This is the reason why the charmonia are sometimes called a "QGP thermometer". In Table 2.1 dissociation temperatures of different charmonium and bottomonium states are shown.

There are also other effects seen in the hot medium which may significantly

Table 2.1. Quarkonium dissociation temperatures, as a function of T_c. From [76].

State	J/ψ(1S)	χ_c(1P)	ψ(2S)	Υ(1S)	χ_b(1P)	Υ(2S)	χ_b(2P)	Υ(3S)
T_d/T_c	2.10	1.16	1.12	> 4.0	1.76	1.60	1.19	1.17

affect the charmonium production at high energy densities. One of them is "regeneration" [77–81]. The main idea of this effect may be described as follows: at sufficiently high energy densities in the hot medium the quarks and the anti-quarks from two different $c\bar{c}$ pairs may be located quite close to each other to be able to recombine and to form a new state. This is possible since the number of charm quarks (and $c\bar{c}$ pairs) increases with the energy of collisions (see Fig.2.2). Thus, the regeneration effect will compete with the dissociation effect, since they affect the charmonium production in the opposite ways, and should be taken into account when interpreting the data. A schematic illustration for J/ψ production by regeneration is compared in Fig.2.3 to that from sequential suppression. It is shown that at high energy densities the J/ψ production will not be suppressed anymore but is expected to increase due to the regeneration.

2.3 Experimental measurements

The charmonium production can be studied at different temperatures of the medium experimentally, varying $\sqrt{s_{\rm NN}}$ and centrality of the collision (see Section 5.1). In the absence of any medium effects its production in heavy-ion collisions is scaled with the binary nucleon-nucleon collisions. For quantitative studies, an observable called the Nuclear Modification Factor $R_{\rm AA}$ is defined as:

$$R_{\rm AA} = \frac{d^2N_{\rm AA}/dp_{\rm T}d\eta}{< N_{\rm coll} > d^2N_{\rm pp}/dp_{\rm T}d\eta}, \tag{2.1}$$

where η is the pseudorapidity (which is defined as $\eta = -\ \ln \tan \theta/2$ with θ the polar angle relative to the beam axis), $< N_{\rm coll} >$ is the mean number of binary nucleon-nucleon collisions. The terms $d^2N_{\rm AA}/dp_{\rm T}d\eta$ and $d^2N_{\rm pp}/dp_{\rm T}d\eta$ are the yields differential in transverse momentum $p_{\rm T}$ and pseudo-rapidity η produced in A-A and in pp collisions, respectively. If $R_{\rm AA}$ is different from unity it indicates that some medium effects affect the assumption on the binary scaling.

It should be mentioned that medium effects occur not only in heavy-ion

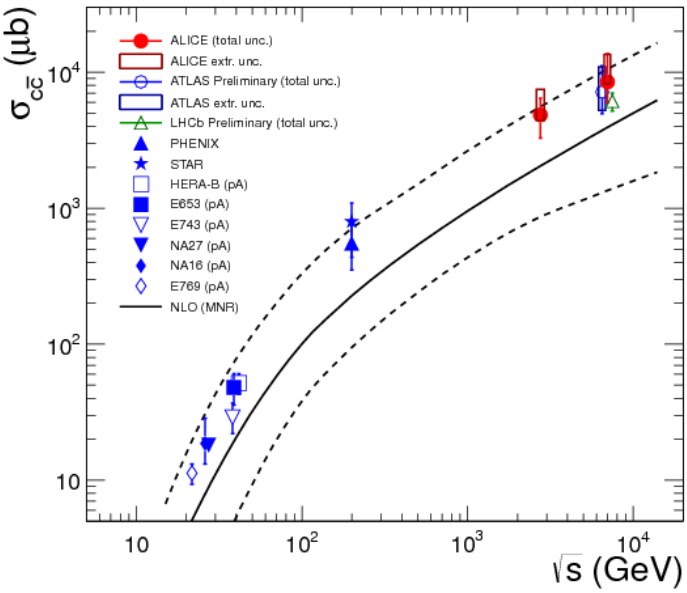

Figure 2.2. Energy dependence of the total charm production cross section in pp collisions. In case of proton–nucleus (pA) or deuteron–nucleus (dA) collisions, the measured cross sections have been scaled down by the number of binary nucleon–nucleon collisions calculated in a Glauber model of the proton–nucleus or deuteron–nucleus collision geometry. The NLO MNR (Mangano, Nason, Ridolfi) calculation [82] and its uncertainties are represented by solid and dashed lines, respectively. From [83].

collisions. Some of them take place even in a "cold" medium where the energy densities are not high enough to create QGP. These "Cold Nuclear Matter" (CNM) effects are studied in p(d)-A collisions. A description of the CNM effects is given in Chapter 3. The CNM effects most widely used to describe the data are shadowing, nuclear absorption and coherent parton energy loss. Shadowing takes place before the $c\bar{c}$ pair formation and is related to the overlapping of the color fields of the gluons and to a respective modification of the parton distribution functions. Nuclear absorption affects the formed $c\bar{c}$ pairs and is related to the absorption of $c\bar{c}$ pair by the nucleus while crossing the nuclear matter. Coherent parton energy loss is related to the multiple parton scatterings resulting in a gluon radiation and corresponding radiative energy loss. This effect can be seen before and after the $c\bar{c}$ pair formation.

In order to draw conclusion from theory/data comparison of medium effects in heavy-ion collisions, elementary pp collisions and in p(d)-A collisions should be also studied (in the same kinematical domain and at the same $\sqrt{s_{\mathrm{NN}}}$).

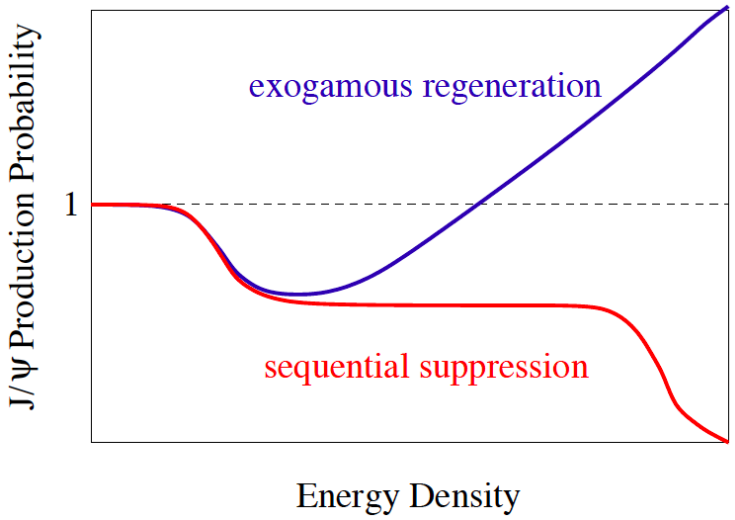

Figure 2.3. Statistical J/ψ regeneration vs sequential suppression. From [80].

2.3.1 SPS and RHIC results

In 1997 a fixed target experiment NA50 at SPS (Super Proton Synchrotron) at CERN discovered an anomalous J/ψ suppression in Pb-Pb collisions at the energy $\sqrt{s_{\rm NN}}$ = 17.3 GeV [84]. It was shown that integrated over the impact parameter, the ratio of the J/ψ to the Drell-Yan cross section[1] was a factor 0.71 ± 0.03 below the value expected from nuclear absorption as extrapolated from the previous experimental results. The same ratio for the most central collisions were 0.62 ± 0.04 below the expected value. Fig.2.4 illustrates this anomalous suppression for the J/ψ (left) and ψ(2S) (right) as a function of L, the distance of nuclear matter traversed by the charmonium. Large L values correspond to the most central collisions. The data are compared to the nuclear absorption derived from the fit to p-A data [85, 86] based on the Glauber formalism [87]. The p-A, S-U data points and the curves have been rescaled to the conditions (energy and rapidity window) of the Pb-Pb data.

PHENIX measured J/ψ suppression in Au-Au collisions at ~10 times higher energy ($\sqrt{s_{\rm NN}}$ = 200 GeV) as a function of $N_{\rm part}$, the number of participant nucleons [89]. These measurements were performed in two rapidity domains: mid and forward y with $|y| < 0.35$ and $1.2 < |y| < 2.2$, respectively. Fig.2.5 presents the RHIC results compared to theoretical predictions. Model calculations by Zhao and Rapp from [79, 90] are presented for two rapidity intervals, incorporating cold and hot nuclear matter suppression as well as coalescence

[1] the Drell-Yan cross section was corrected for the "isospin effect" by the correction factor $\mathrm{AB} \cdot \sigma_{pp}^{DY\,calc}/\sigma_{\rm AB}^{DY\,calc}$ where A and B are the colliding nuclei atomic numbers, $\sigma_{pp}^{DY\,calc}$ and $\sigma_{\rm AB}^{DY\,calc}$ the theoretical calculations of the Drell-Yan cross sections in pp and A-B collisions.

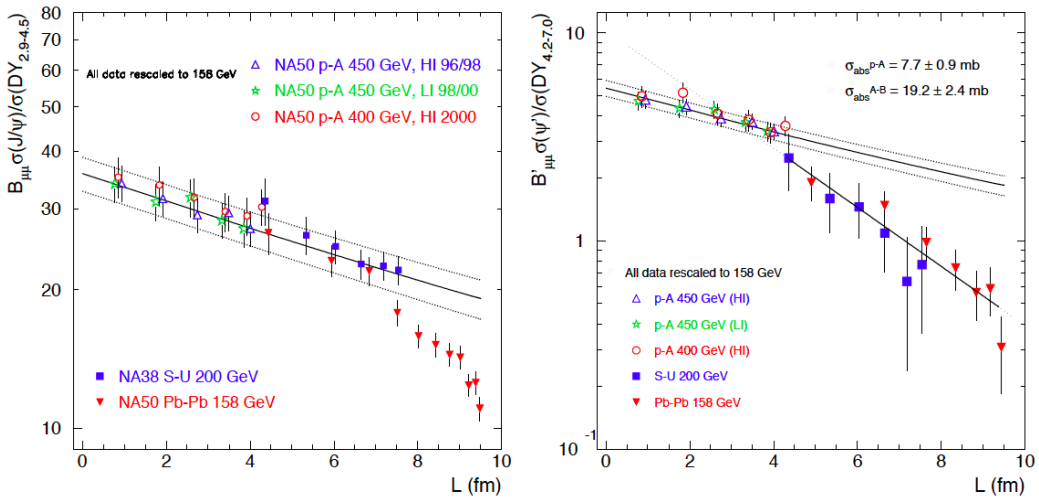

Figure 2.4. Anomalous suppression of J/ψ (left) and ψ(2S) (right) measured by NA38 and NA50, in p-A, S-U and Pb-Pb collisions, as a function of L. The data are compared to the nuclear absorption predictions (black solid line) with the corresponding uncertainties (dashed lines). See text for details. From [88].

of $c\bar{c}$ pairs. The various line styles represent the different contributions to the total as laid out in the legend, while the two colors represent the two rapidity ranges: blue for midrapidity and red for forward rapidity. The lower panel shows the ratio of forward rapidity to midrapidity nuclear modification factors. The J/ψ suppression is systematically higher at forward rapidity than at midrapidity except for the very low $N_{\rm part}$. A strong J/ψ suppression is seen at the most central events (high values of $N_{\rm part}$), while at the most peripheral events (small values of $N_{\rm part}$) the data are consistent with no J/ψ suppression. The model can catch the main features of the J/ψ suppression at RHIC. However it slightly underestimates the measured J/ψ suppression at forward y in the most central collisions. It also overestimates the J/ψ suppression at mid rapidity. Finally, ratio of forward to mid rapidity nuclear modification factors is described by the model only in the most central or in the most peripheral events. This may indicate that the model shares the J/ψ production between hot and cold nuclear matter effects not in the fully correct way.

In Fig.2.6 both SPS and RHIC results on the J/ψ suppression as a function of the charged particle multiplicity at mid-rapidity, after having accounted for estimated CNM effects, are compared. The highest charged particles multiplicity corresponds to the most central collisions. A similar behaviour can be seen for different systems. The magnitude of the anomalous J/ψ suppression is almost system- and $\sqrt{s}$ -independent when expressed as a function of $\mathrm{d}N_{\rm ch}/d\eta|_{\eta=0}$. It was not expected to observe the same suppression at the energy ∼10 times

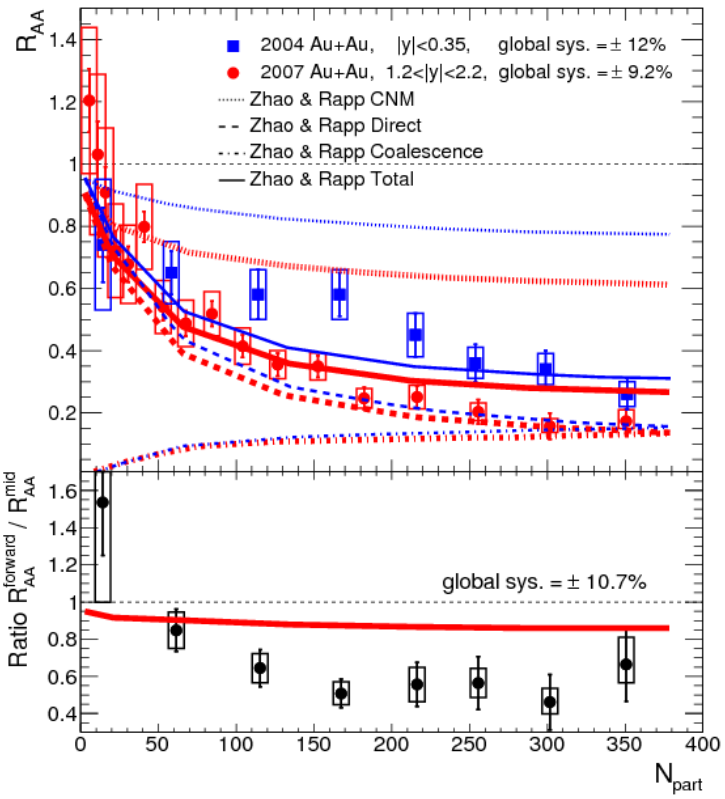

Figure 2.5. J/ψ R_{AA} as a function of N_{part}. Model calculations by Zhao and Rapp from [79, 90] are presented for two rapidity intervals. The lower panel shows the ratio of forward rapidity to midrapidity nuclear modification factors. See text for details. From [89].

higher than the one at SPS.

While trying to deeper understand charmonium production in heavy-ion collisions, more puzzles arised from the heavy-ion measurements by RHIC and SPS. Larger suppression of J/ψ at forward compared to midrapidity, combined with the similar suppression of J/ψ at midrapidity between RHIC and lower energy experiments created an outstanding puzzle in terms of a full theoretical description of the J/ψ production. Higher energy LHC results were strongly anticipated.

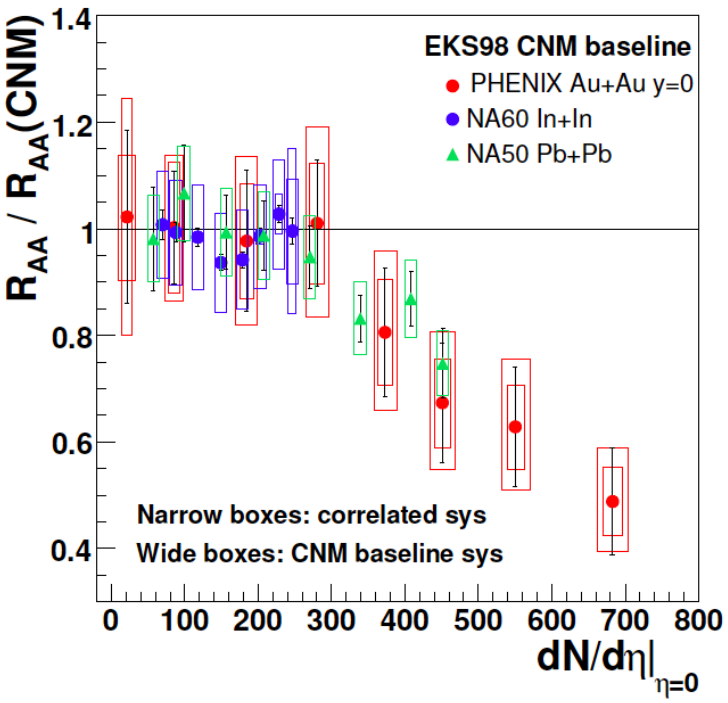

Figure 2.6. Comparison of the anomalous J/ψ suppression at the SPS and RHIC as a function of $\mathrm{d}N_{\mathrm{ch}}/d\eta$ at $\eta = 0$. From [17].

2.3.2 LHC results

The LHC results were expected to confirm the recombination scenario since at the LHC energies the number of the produced $c\bar{c}$ pairs was expected to be high enough to see the enhancement of the J/ψ production due to recombination.

ALICE collaboration published results of differential studies of the J/ψ production in Pb–Pb collisions at $\sqrt{s_{\rm NN}} = 2.76$ TeV in the forward rapidity region $2.5 < y < 4$ [91]. In Fig.2.7, the centrality dependence of the nuclear modification factor $R_{\rm AA}$ is shown. A much lower J/ψ suppression at the LHC energy with respect to that at RHIC energy is seen for $\langle N_{\rm part}\rangle \gtrsim 100$ (top panel). This effect is well described by models which include a recombination scenario (bottom panel). However some of them fail to describe quantitatively the lower $N_{\rm part}$ region ($\langle N_{\rm part}\rangle < 50$).

Fig.2.8 shows the inclusive J/ψ $R_{\rm AA}$ as a function of $N_{\rm part}$ in Pb-Pb collisions at $\sqrt{s_{\rm NN}} = 2.76$ TeV for different ranges in $p_{\rm T}$. The results are compared to two transport models and to a comover interaction model. Two transport models from Zhao et al. [92] and from Liu et al. [93] differ in the rate equation describing the J/ψ dissociation and recombination. Both models are shown with the uncertainty bands which cover results with shadowing included (lower limit) and without shadowing (upper limit). The comover interaction model or CIM [94] combines shadowing, interaction with co-moving medium and recombination effects. The uncertainty band of the model is related to the variation of the charm cross-section dσ/dy from 0.4 to 0.6 mb. For the 30% most central collisions ($\langle N_{\rm part}\rangle \gtrsim 150$), the low $p_{\rm T}$ J/ψ $R_{\rm AA}$ is significantly larger than the mid and high $p_{\rm T}$ ones. This is consistent with the expectation from the recombination hypothesis. The comparison to theoretical model leads to the same conclusions as in the $p_{\rm T}$-integrated case: the models reasonably well describe the data for $\langle N_{\rm part}\rangle \gtrsim 100$ but fail to describe precisely the shape at low $\langle N_{\rm part}\rangle$.

CMS collaboration measured J/ψ $R_{\rm AA}$ at high $p_{\rm T}$ in Pb-Pb collisions at $\sqrt{s_{\rm NN}} = 2.76$ TeV at central rapidities $|y| < 2.4$ [95]. Fig.2.9 shows the comparison of these results to those from the STAR collaboration for Au-Au collisions at $\sqrt{s_{\rm NN}} = 0.2$ TeV at midrapidity $|y| < 1$. Recombination effects are expected to be negligible at high $p_{\rm T}$ and the dissociation of the J/ψ should play a more significant role. This is confirmed by the data: at high $p_{\rm T}$ less J/ψ suppression is seen at RHIC than at the LHC.

The prediction of the charmonium suppression is complicated by various factors: feed-down contributions from higher-mass resonances into the observed charmonium yields, as well as several competing nuclear and medium effects. The bottomonium family is expected to provide additional and theoretically cleaner probes of the deconfined medium. The three $\Upsilon(nS)$ states, characterized by similar decay kinematics but different binding energies, allow

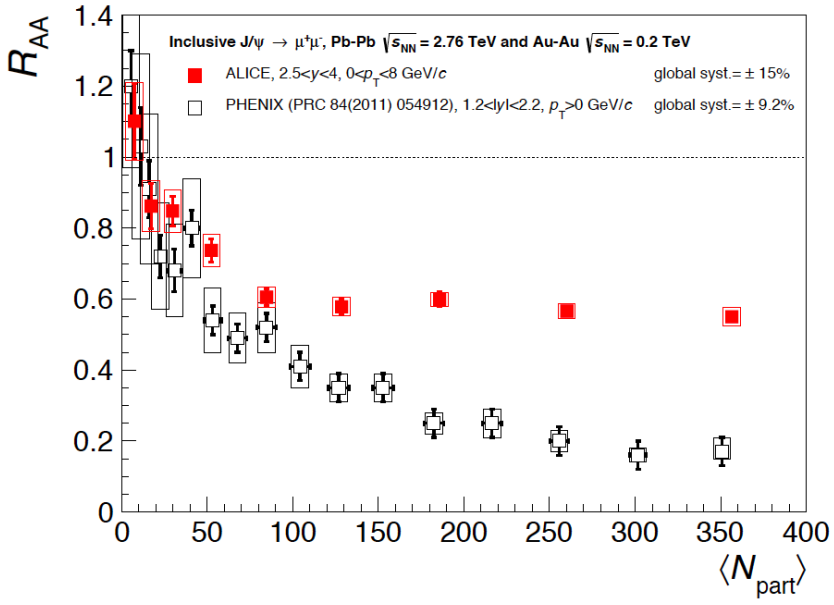

(a)

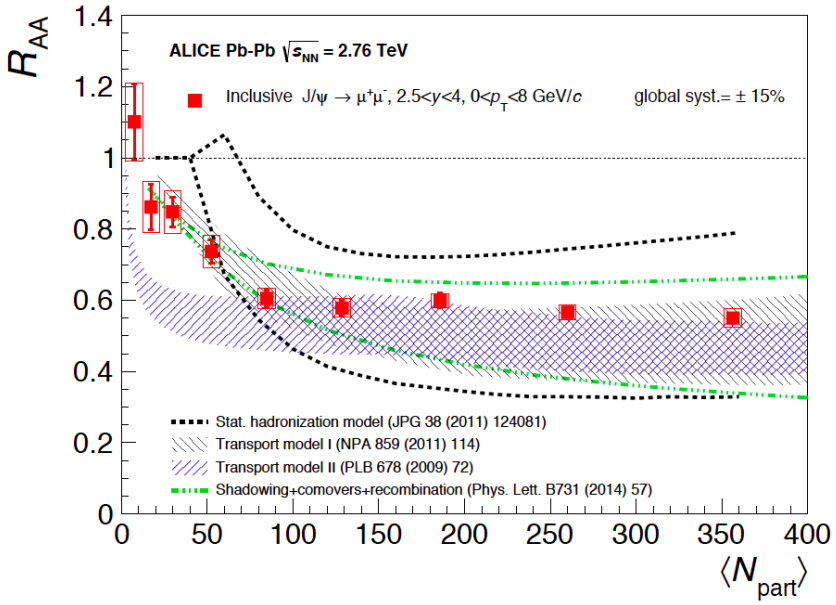

(b)

Figure 2.7. Inclusive J/ψ $R_{\rm AA}$ as a function of $N_{\rm part}$ in Pb-Pb collisions at $\sqrt{s_{\rm NN}} = 2.76$ TeV, compared to the PHENIX measurements in Au-Au collisions at $\sqrt{s_{\rm NN}} = 0.2$ TeV (a) and to theoretical models including in various ways a J/ψ (re)combination component (b). From [91].

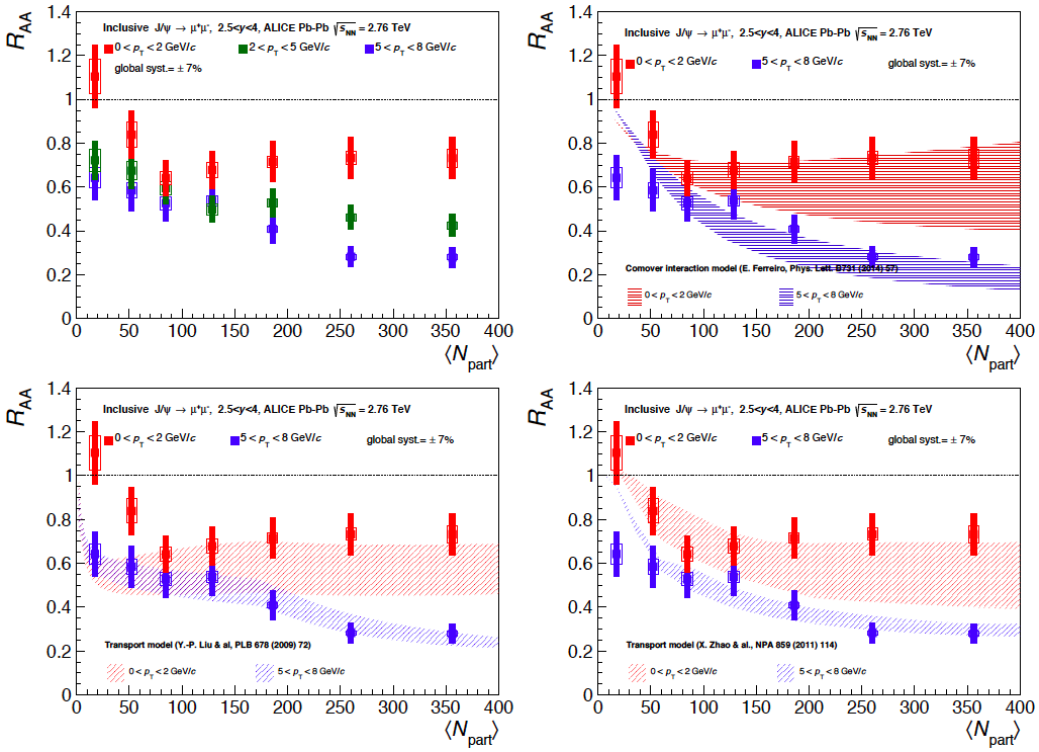

Figure 2.8. Inclusive J/ψ $R_{\rm AA}$ as a function of $N_{\rm part}$ in Pb-Pb collisions at $\sqrt{s_{\rm NN}} = 2.76$ TeV for different ranges in $p_{\rm T}$, compared to transport models and to comover interaction model. From [91].

the measurement of relative state suppression, where common experimental and theoretical factors, and respective uncertainties, cancel. CMS collaboration performed studies of sequential suppression of $\Upsilon(nS)$ states in Pb-Pb collision [96, 97]. Fig.2.10 shows dimuon invariant mass distributions in pp (left) and Pb-Pb (right) collisions at $\sqrt{s_{\rm NN}} = 2.76$ TeV measured by CMS. The three $\Upsilon(nS)$ peaks are clearly visible in the pp case. In the Pb-Pb case the $\Upsilon(3S)$ peak is less evident. More quantitative picture is presented in Fig.2.11.

The following double ratios were estimated directly from the distributions in Fig.2.10:

$$\begin{aligned} \frac{\Upsilon(2S)/\Upsilon(1S)|_{PbPb}}{\Upsilon(2S)/\Upsilon(1S)|_{pp}} &= 0.21 \pm 0.07\,(stat.) \pm 0.02\,(syst.), \\ \frac{\Upsilon(3S)/\Upsilon(1S)|_{PbPb}}{\Upsilon(3S)/\Upsilon(1S)|_{pp}} &= 0.06 \pm 0.06\,(stat.) \pm 0.06\,(syst.) < 0.17\,(95\%\,\mathrm{CL}) \end{aligned} \tag{2.2}$$

These double ratios are expected to be compatible with unity in the absence of suppression of the excited states relative to the $\Upsilon(1S)$ state. The measured values are considerably smaller, indicating a significant suppression

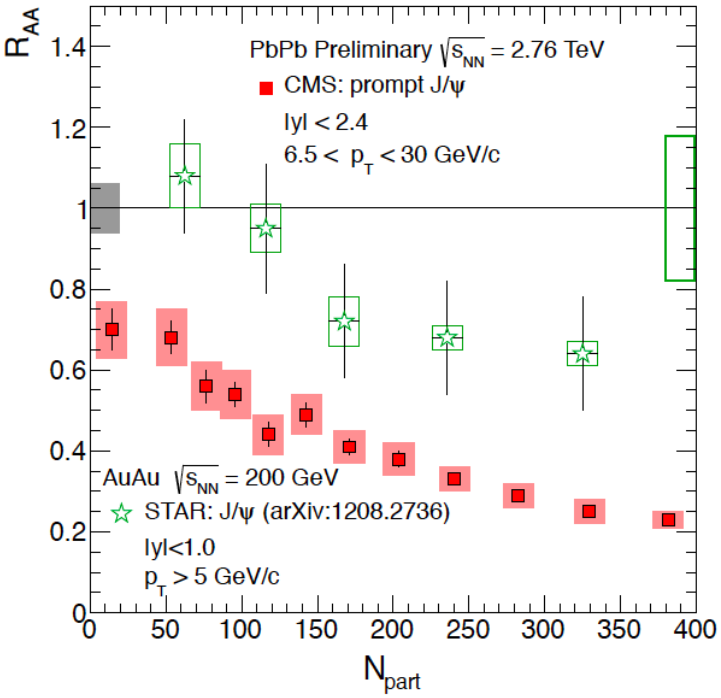

Figure 2.9. Prompt J/ψ R_{AA} as a function of N_{part} in Pb-Pb collisions at $\sqrt{s_{\mathrm{NN}}}$ = 2.76 TeV measured by CMS, compared to Au-Au results from the STAR collaboration. From [95].

of the $\Upsilon(nS)$ states in Pb-Pb collisions compared to pp collisions. This result supports the hypothesis of increased suppression of less strongly bound state: the $\Upsilon(1S)$ is the least suppressed, while the $\Upsilon(3S)$ is the most suppressed of the three states. The measured difference in the production yields in Pb-Pb and in pp can be also partly ascribed to CNM effects.

Thus, the LHC results show a different behaviour of the J/ψ production compared to the lower energy experiments. A hypothesis of the pure melting of different charmonium states explains some part of the J/ψ suppression but cannot fully describe the J/ψ suppression in heavy-ion collisions at high energies. Other effects like recombination and the CNM effects complement the J/ψ melting effects. In order to quantify the hot nuclear matter effects it is, therefore, necessary to know the CNM effects which can be studied in p(d)-A collisions. It is also shown that quantifying the CNM effects is important not only for J/ψ measurements but for other quarkonia, in particular for $\Upsilon(nS)$ family.

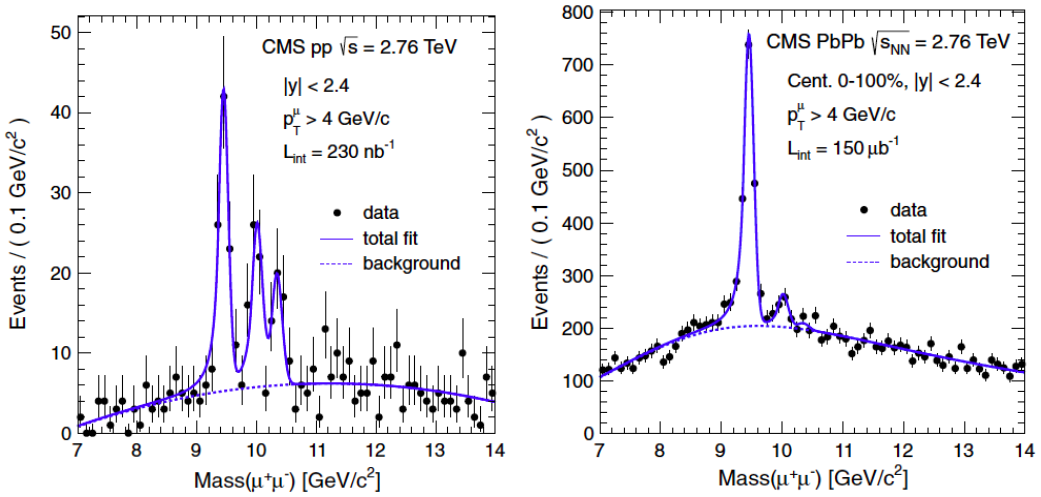

Figure 2.10. Dimuon invariant mass distributions in pp (left) and Pb-Pb (right) collisions at $\sqrt{s_{\mathrm{NN}}} = 2.76$ TeV measured by CMS. From [97]. Solid (signal+background) and dashed (background-only) curves represent the results of the simultaneous fit to the two data sets.

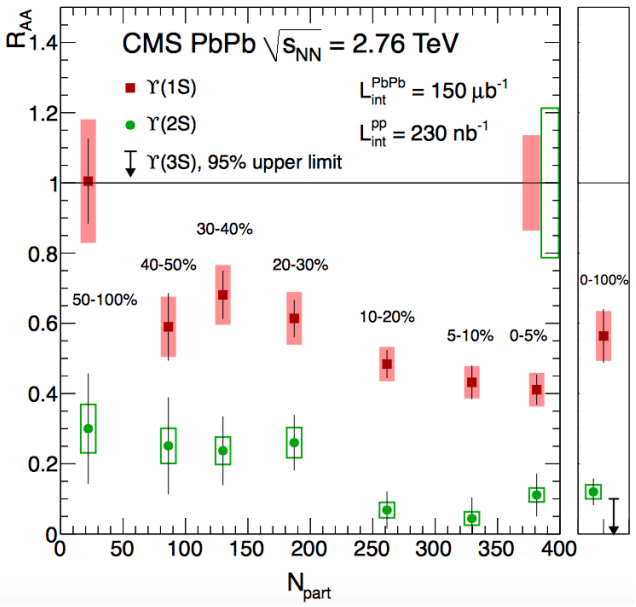

Figure 2.11. Centrality dependence of the nuclear modification factor for the $\Upsilon(1S)$ and $\Upsilon(2S)$ states measured by CMS in Pb-Pb collisions at $\sqrt{s_{\mathrm{NN}}} = 2.76$ TeV. The event centrality bins used are indicated by percentage intervals. From [97].

Chapter 3

Cold Nuclear Matter Effects

In the previous chapter charmonium production in heavy-ion collisions was described. It was explained that at high energy densities of the collision a state of matter, referred to as QGP, is created. The presence of hot nuclear matter affects the charmonium production. However hot nuclear matter effects in heavy-ion collisions cannot be easily distinguished from the additional effects arising from "cold" nuclear matter (CNM). These effects can in principle modify the charmonium production both in nucleus-nucleus and nucleon-nucleus collisions. A schematic classification of nuclear matter effects taking place in different collision systems is shown in Fig.3.1. From this scheme, nucleon-nucleus collision can be considered as the reference collision to study CNM effects that affect Pb-Pb collision.

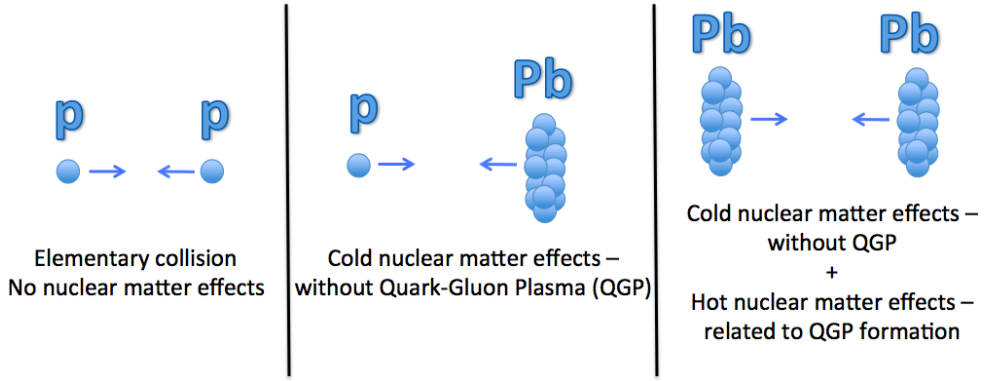

Figure 3.1. Schematic classification of nuclear matter effects taking place in different collision systems.

CNM effects can be divided into three main groups, depending on the time when they take place, with respect to the time of the $c\bar{c}$ pair formation:

- Initial state effects: they take place in the first moments of the collision

before the $c\bar{c}$ pair formation. The initial state effects group the following effects: multiple scattering, the radiative energy loss, gluon shadowing and gluon saturation.

- Final state effects: they occur after the production of a pre-resonant state ($c\bar{c}$ pair). The final state effects includes the nuclear absorption effect.

- Initial and final state coherent effects. These effects cannot be considered neither as pure initial state effects nor as final state effects. This group is represented by the coherent parton energy loss effect

In the following we will not discuss all possible cold nuclear matter effects but we will focus only on few of them: gluon shadowing, gluon saturation, nuclear absorption and coherent parton energy loss effects.

3.1 Definition of the kinematic variables

In this section, we will first review the kinematics of the deep inelastic scattering (DIS) to introduce the kinematic variables and their meaning. Then we will present the other variables, and their meaning, more specific to hadron hadron collisions.

Let us consider a process $l + N \to l + X$, where a charged lepton scatters inelastically off a nucleon at rest; the final state contains the scattered lepton and the debris of the nucleon. A Feynman diagram of such DIS is shown in Fig.3.2, assuming exchange of only one virtual photon [98] (this assumption is valid at the leading order of QCD). Let E and E' be the energies of the incident and scattered lepton, k and k' their four-momenta, and θ is the lepton scattering angle, in the laboratory frame for the energies and the angles. Then, neglecting the lepton mass, the following variables can be introduced:

- $q = k - k'$, the four-momentum of the virtual photon,
- $Q^2 = -q^2 = -(k - k')^2 \simeq 4EE'\sin^2(\theta/2)$, where q^2 is the square of the four-momentum transferred from the lepton to the target nucleon,
- $\nu = P \cdot q/M = E - E'$, the virtual photon energy,
- $s = W^2 = (P + q)^2 = M^2 - Q^2 + 2M\nu$, the square of the total energy released in the interaction of the nucleon with the virtual photon,
- $x = Q^2/(2P \cdot q) = Q^2/(2M\nu)$, the Bjorken scaling variable,
- $y = P \cdot q/(P \cdot k) = \nu/E$, the fraction of energy transferred in the scattering,

where P is the four-momentum of the target nucleon and the rightmost expressions for Q^2, ν, x, y are valid in the laboratory frame, where the target nucleon is at rest. The mass M is taken as the proton mass.

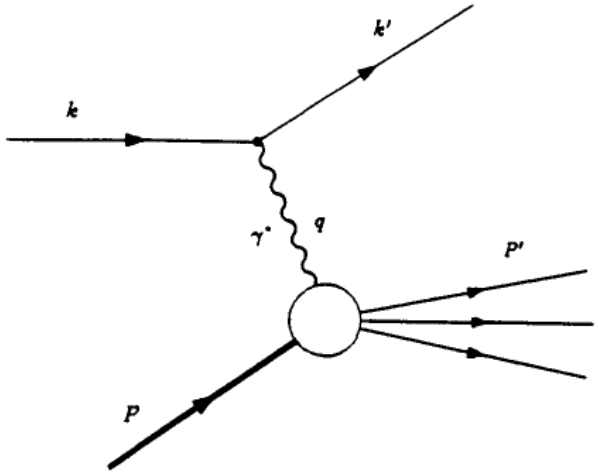

Figure 3.2. Deep inelastic lepton-nucleon scattering. From [98].

The original DIS definition of x is not very enlightening if hadron-hadron collisions are studied. More interesting is the interpretation of x as a momentum fraction. If a DIS event is considered in a frame where the proton is very highly boosted (such as the electron rest frame, also called the "infinite momentum frame") then it turns out that kinematically the x of the event is the fraction of the proton total momentum involved in the scattering. If the electron had a hard interaction with an object within the proton, a "parton", then x can be considered as the fraction of the total proton momentum carried by the parton that interact with the virtual photon.

This leads to the interpretation of the x-dependence of DIS spectra as a probability of finding a parton with momentum fraction x within the proton. Thus, the distribution of partons over x is an intrinsic property of the proton which explains why it is a good scaling variable independent of the energy of the electron.

The x-dependence of parton distributions is the most fundamental description of the nucleon as seen in high-energy interactions. The momentum distribution functions of the partons within the nucleon are called Parton Distribution Functions (PDFs). They represent the probability densities[1] to find a parton carrying a momentum fraction x at a squared energy scale Q^2. DIS

[1]Strictly speaking they rather represent number densities as they are normalised to the number of partons.

experiments showed that the number of partons increases at low x and large Q^2, and decreases at high x. At $x \sim 1/3$ there are three valence quarks sharing the nucleon momentum. They are more dominant at low Q^2 (the resolution of the probe). And at low x, there is an increase of the sea quarks and gluon component that rises with Q^2. An example of the PDFs measured by H1 [99] and ZEUS [100] collaborations is shown in Fig.3.3 for different Q^2. The PDFs are shown in form $xf(x)$, where f denotes a PDF of flavour f. For example, the PDFs for u valence are denoted as $u_v(x)$, d valence, $d_v(x)$, total sea, $S(x)$, the gluon, $g(x)$.

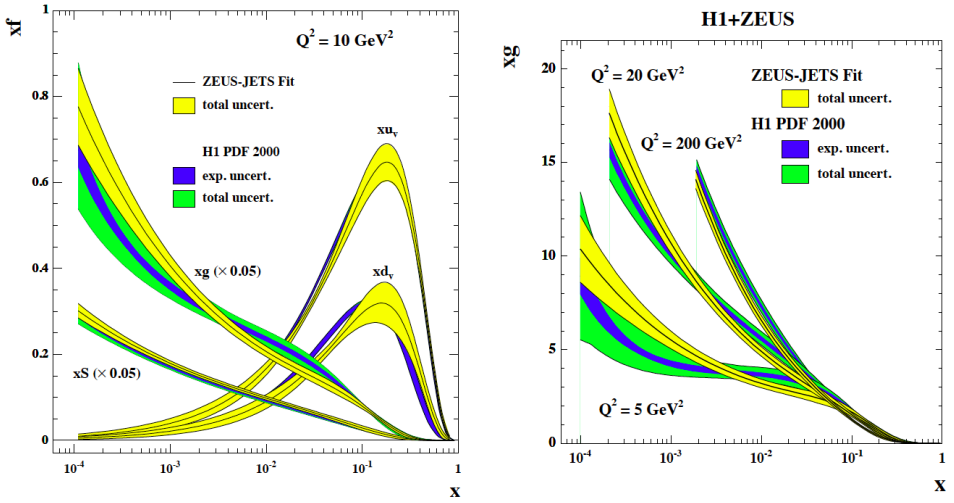

Figure 3.3. *Left*: Comparison of PDFs for different flavours measured by ZEUS and H1 at $Q^2 = 10$ GeV^2. *Right*: Comparison of gluon PDFs from ZEUS and H1 analyses, at various Q^2. From [101].

When studying hadron-hadron collisions, it is possible to describe the interaction as the following elementary process: a parton of the first hadron (beam 1) with momentum fraction x_1 interacts with a parton of the second hadron (beam 2) with a momentum fraction x_2. Since the momenta of nucleons in the beams are known, x_1 and x_2 can be immediately related to the total energy and total momentum of the parton-parton system ($x_1 \cdot x_2 \cdot \sqrt{s_{\mathrm{NN}}}$).

In a "2 $\rightarrow$ 1 process", two partons with x_1 and x_2 combine to form a single particle with the longitudinal momentum p_{L} in the final state. Let both hadron beams have the same energy. Total momentum conservation implies $p_{\mathrm{L}} = (x_1 - x_2) \cdot \sqrt{s}/2$, where p_{L} is the longitudinal momentum in the center of mass frame of the two incident hadrons. If the mass of the final state particle is small compared to $\sqrt{s}$, then the maximum p_L the particle can have, is essentially $\sqrt{s}/2$. Then one more widely-used variable x_F — Feynman x can

be defined as:

$$x_{\mathrm{F}} = p_{\mathrm{L}}/p_{\mathrm{L}}^{\mathrm{max}} = \frac{2p_{\mathrm{L}}}{\sqrt{s}} = x_1 - x_2. \tag{3.1}$$

Rapidity y is an alternative way to study the p_{L}-dependence:

$$y = \frac{1}{2} \cdot \ln\frac{E + p_{\mathrm{L}}}{E - p_{\mathrm{L}}}. \tag{3.2}$$

Longitudinal momentum p_{L} can be also defined through the scattering angle θ: $p_{\mathrm{L}} = p \cdot \cos\theta$. Then a variable $p_{\mathrm{T}} = \sqrt{p_{\mathrm{L}}^2 - p^2} = p \cdot \sin\theta$ can be defined. p_{T} is the transverse momentum in the center-of-mass frame.

Another observable measured in the experiment is "pseudorapidity":

$$\eta = \frac{1}{2} \cdot \ln\frac{1 + \cos\theta}{1 - \cos\theta} = \frac{1}{2} \cdot \ln\frac{\cos\theta/2}{\cos\theta/2} = \frac{1}{2} \cdot \ln\left(\tan\frac{\theta}{2}\right). \tag{3.3}$$

The pseudorapidity η is a good approximation of the true relativistic rapidity y, when a particle is "relativistic" (i.e. $p \approx E$).

3.2 Gluon shadowing

At high parton density the gluons interact (recombine) actively. It also leads to a modification of PDFs of bound nucleons (in nucleus) to those of the free nucleons. Such a modification is defined as follows:

$$R_i^{\mathrm{A}}(x, Q^2) = \frac{f_i^{\mathrm{A}}(x, Q^2)}{f_i^{\mathrm{free}}(x, Q^2)}, \tag{3.4}$$

where $R_i^{\mathrm{A}}(x, Q^2)$ denotes a nuclear modification to the free nucleon PDF $f_i^{\mathrm{free}}(x, Q^2)$. The $f_i^{\mathrm{A}}(x, Q^2)$ represents the bound nucleon PDF and i stays for the different parton flavours: $i = V, S, G$ for valence quark distributions, for all sea quarks and for gluons, respectively [102].

Nuclear effects are usually divided in the following four categories (Fig.3.4) depending on the value of $R_i^{\mathrm{A}}(x, Q^2)$ [103]:

- shadowing, a depletion at small x,
- antishadowing, an excess at intermediate x,
- EMC effect, a depletion at higher x,
- Fermi motion, an excess at x close to 1.

The $R_i^{\mathrm{A}}(x, Q^2)$ function is then parametrized by piecewize functions to cover all the four effects. An illustration of such fitting function is shown in Fig.3.4.

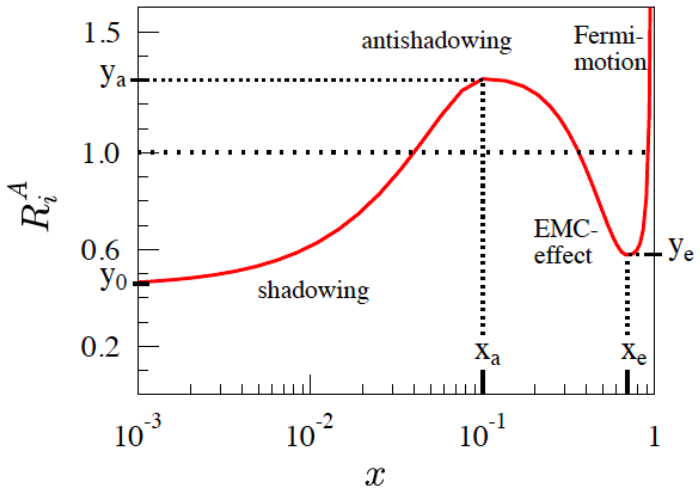

Figure 3.4. An illustration of $R_i^{\mathrm{A}}(x)$ fitting function and its parameters. From [102].

There are various models using different experimental datasets for constraining the fitting function parameters. A review of the current status of PDF studies is given in [104]. In this chapter only EPS09 (Eskola, Paukkunen, Salgado, 2009) parametrization is considered as an example of one of the latest successful variants [102]. The main experimental data used in EPS09 are l–A deep inelastic scatterings (DIS) measurements. Drell-Yan production from fixed target p–A collisions at Fermilab, inclusive neutral-pion production measured in d–Au and pp collisions at RHIC were also used.

The parametrization of the nuclear modifications $R_i^{\mathrm{A}}(x, Q^2)$ is performed at the charm quark mass threshold $Q_0^2 \equiv m_c^2 = 1.69$ GeV^2 imposing the momentum and baryon number sum rules for each nucleus A separately. At higher scales $Q^2 > Q_0^2$, the nuclear PDFs (nPDFs) are obtained by solving DGLAP (Dokshitzer-Gribov-Lipatov-Altarelli-Parisi) QCD evolution equations for parton densities [105–107] with NLO splitting functions [108–110]. These equations are then solved numerically. The uncertainties for the model originate from the experimental uncertainties of the fitted data. DGLAP and BFKL (Balitsky-Fadin-Kuraev-Lipatov) [111–113] equations are the evolution equations of parton densities. DGLAP evolution equations are used to describe hadron interactions at short distances. DGLAP approach sums up higher order α_{s} contributions enhanced by $\ln Q^2$. In case of high-energy scattering, the contributions enhanced by $\ln \frac{1}{x}$ become important. BFKL approach sums up the leading-log contributions of the type $(\alpha_{\mathrm{s}} \ln \frac{1}{x})^{\mathrm{n}}$.

In Fig.3.5 nuclear modification functions of lead nucleus are shown for three parton flavours: valence, sea quarks and gluons. The production cross section

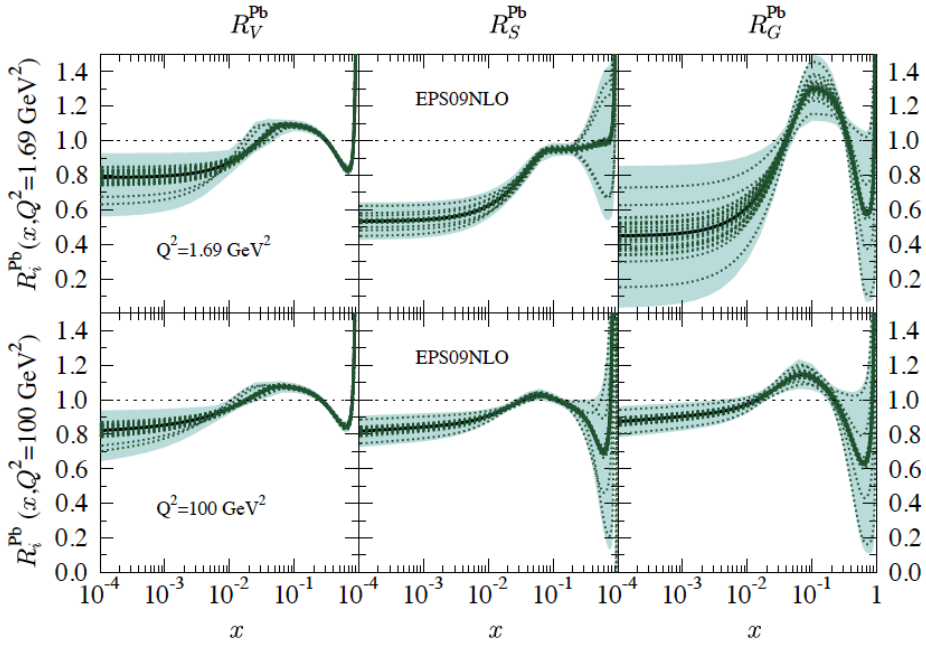

Figure 3.5. The nuclear modifications R_V, R_S, R_G for lead at the initial scale $Q_0^2 = 1.69$ GeV^2 and $Q_0^2 = 100$ GeV^2. The thick black lines indicate the best-fit results, while the dotted green curves denote the error sets. The shaded bands are estimated from the experimental uncertainties of the fitted data. From [102].

of the $c\bar{c}$ pair at high energies is affected by the gluon PDFs. Thus, the large uncertainty band for gluons in the top right panel shows the importance of experimental studies using nuclear target at high energy (to probe the low x) and charmonia (to probe the low Q^2) to better constrain the model. Other probes could be open charm and π_0, both at low p_{T}.

3.3 Gluon saturation

Collisions of any particles at high energy (DIS, hadron-hadron collisions etc.) can be described within the Color Glass Condensate (CGC) model [114]. J/ψ production in proton-nucleus collisions at high energies can be also described basing on the CGC picture of the nuclear wavefunction at small x [115]. The size of the gluon wavefunction depends on both x and Q^2. At low x and finite Q^2, the gluon density increases as shown by the gluon PDF. Then at sufficiently low x, the gluon densitiy is expected to reach a maximum and should saturate. The condition for observing CGC requires small x and Q^2 values (Fig. 3.6).

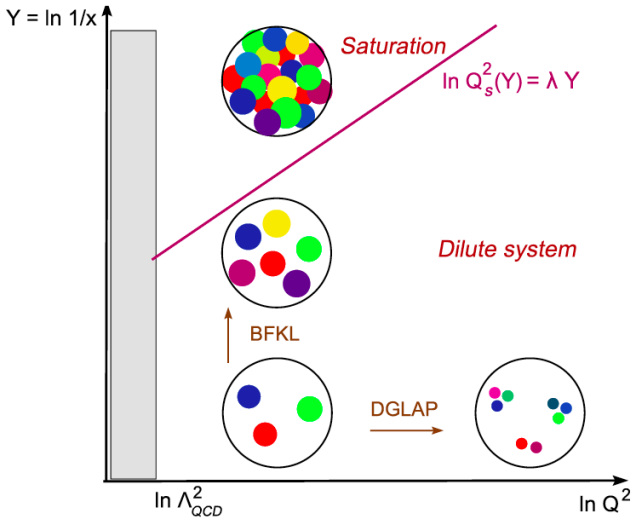

Figure 3.6. The partonic phase diagram. Evolution of parton densities can be considered in energy/rapidity y (BFKL equation) or in Q^2 (DGLAP equation). From large x to low x, the dilute system becomes dense and undergoes a transition to a saturation region which is characterized by saturation scale $Q_s^2(Y)$. From [116].

This condition can be formulated in terms of characteristic scale for gluon saturation named the *saturation scale*, $Q_s(x)$. It describes the Q^2 boundary of the saturation regime that evolves with x [117]. A "pocket formula" used for the energy and nuclear dependence estimation of the saturation scale is $Q_s^2 \sim A^{1/3}x^{-0.3}$: nonlinear high gluon density effects are enhanced at smaller x and for larger A nuclei (A is the atomic number of the nucleus) [118].

The meaning of the CGC model name comes from:

- **Color** refers to the color charges of gluons.
- **Glass** represent a disordered system which can be considered as a solid on short timescales and a liquid on long timescales. The partons color fields are frozen at short timescales while on long timescales they can fluctuate.
- **Condensate** refers to the very high density of gluons at their saturation scale Q_s.

In the CGC approach, the strength of the color field inside the nucleus is proportional to the saturation scale $Q_s^2(x)$ determined by the density of partons in the transverse plane. It is a growing function of the collision energy and the atomic number of the nucleus. At RHIC kinematics, $Q_s \gg \Lambda_{\mathrm{QCD}}$ which

implies that the inter-nucleon interactions play a little role in pA collisions at high energies. In that case a nuclear color field at high energies can be described by only one universal (process independent) dimensional scale $Q_s(x)$ where x refers to the Bjorken variable corresponding to the nuclear parton distribution. It was argued [119, 120] that at high energies there are two different dynamical regimes of the heavy quark production depending on the relation between the quark mass m and the saturation scale:

- $Q_s \ll m$: the heavy quark production is *incoherent*, i.e. produced in a single sub-collision of a proton with a nucleon, and can be treated within a conventional perturbative approach;
- $Q_s \gg m$: the heavy quark production is *coherent* (since the whole nucleus takes part in the process) and is sensitive to the strong color field [119, 121]. This regime is favoured at the LHC and at sufficiently small x at RHIC.

An elementary process contributing to the J/ψ production in pA collisions in the nucleus rest frame is the scattering of a gluon from the proton wave function on the nucleus. Calculating properly all the contributions to the J/ψ production, the gluon saturation effects can then be estimated and compared to the data. It should be mentioned that the hadronization mechanisms of the $c\bar{c}$ pair also play an important role within the framework of this model. There are various approaches describing the gluon saturation effects on the J/ψ production, depending on the J/ψ production model used in each approach: CSM [115, 119–123], CEM [124, 125], NRQCD [126]. All these J/ψ production models with their advantages and disadvantages were discussed in Section 1.3. It should be mentioned that some work is still needed to calculate the J/ψ cross section within the NRQCD framework combined with CGC.

3.4 Nuclear absorption

Interactions between the pre-resonant or fully formed $c\bar{c}$ pair state and the nucleus can cause the $c\bar{c}$ pair dissociation. This effect is called "nuclear absorption". It can be studied using the Glauber model described in more details in Section 5.1. This model describes the collision of two nuclei in terms of independent interactions of the constituent nucleons. It assumes that at sufficiently high energies, the nucleons carry sufficiently large momentum to be essentially undeflected as the nuclei pass through each other. It also assumes that the nucleons move independently in the nucleus and that the size of the nucleus is large as compared to the extent of the nucleon-nucleon force. The

Glauber formalism allows to integrate the nuclear absorption effect and to calculate the observed charmonium production cross sections [127]:

$$\sigma_{\mathrm{pA}} = \frac{\sigma_0}{\sigma_{\mathrm{abs}}^{\mathrm{G}}} \int \mathrm{d}\vec{b} \left[1 - \left(1 - T_{\mathrm{A}}(\vec{b}) \sigma_{\mathrm{abs}}^{\mathrm{G}} \right)^A \right], \tag{3.5}$$

where $\sigma_{\mathrm{abs}}^{\mathrm{G}}$ represents the break-up cross section of an "object" going through the nuclear matter. The nuclear thickness is represented by $T_{\mathrm{A}}(\vec{b})$, where b is the impact parameter in-between the produced $c\bar{c}$ pair and the nuclear matter. Nuclear thickness function T_{A} represents the nuclear density per unit of surface and is usually calculated for a heavy nucleus using Woods-Saxon parametrization of the nuclear density profile. σ_0 denotes the elementary nucleon-nucleon charmonium production cross section [128]. It should be underlined that $\sigma_{\mathrm{abs}}^{\mathrm{G}}$ is not simply an interaction cross section of the produced $c\bar{c}$ pair with nucleons. $c\bar{c}$ pair needs some time to cross the entire nucleus (crossing time). If the crossing time is larger than the formation time of the charmonium bound state, then the absorption will occur on the pre-resonant and fully formed state. If the crossing time is lower than the formation time, then the absorption will occur only on the pre-resonant state. Thus, the produced $c\bar{c}$ pair may break up even before forming the physical charmonium bound state. This is particularly true for the charmonium production through a spatially extended and strongly interacting $c\bar{c} - g$ colour dipole state. The "formation time" argumentation emphasizes the importance of studying the charmonium production as a function of y, and at different collision energies.

A much simpler "$\langle \rho \mathrm{L} \rangle$ parametrization" is often used:

$$\sigma_{\mathrm{pA}} = \sigma_0 \cdot A \, \exp\left(\sigma_{\mathrm{abs}}^{\rho \mathrm{L}} \langle \rho \mathrm{L} \rangle \right), \tag{3.6}$$

where $\langle \rho \mathrm{L} \rangle$ denotes the average amount of matter crossed by the $c\bar{c}$ pair from its production point till its escape from the nucleus. The formula (3.6) is an approximation of the Glauber formula, which can be found from (3.5) by expanding the term in square parentheses in powers of σ_{abs}. It can be shown that

$$\langle \rho \mathrm{L} \rangle = \frac{A-1}{2} \int \mathrm{d}\vec{b} \left[T_{\mathrm{A}}(\vec{b}) \right]^2. \tag{3.7}$$

There is also a third way to describe nuclear absorption, the so-called "α parametrization":

$$\sigma_{\mathrm{pA}} = \sigma_0 \cdot A^{\alpha}, \tag{3.8}$$

which is equivalent to the previous approach for small enough absorption cross section, if $\alpha = 1 - \sigma_{\mathrm{abs}} \frac{\langle \rho \mathrm{L} \rangle}{\ln A}$. This parametrization is widely-used, though

it is very rough. In particular, the value of α extracted from a fit to a given data set depends on the nucleus used as the lightest target. In that case, experiments comparing heavy targets with Deuterium systematically derive artificially high values of α.

Nuclear absorption was used, for example, in Fig.2.4 to estimate the CNM contribution to the J/ψ suppression. At high energy, nuclear absorption is not expected to give a large effect since it is expected to decrease with collision energy (since the crossing time decreases). Fig.3.7 shows the dependence of the nuclear absorption cross section on the collision energy. Thus, at the LHC energies it is expected to be a negligible effect.

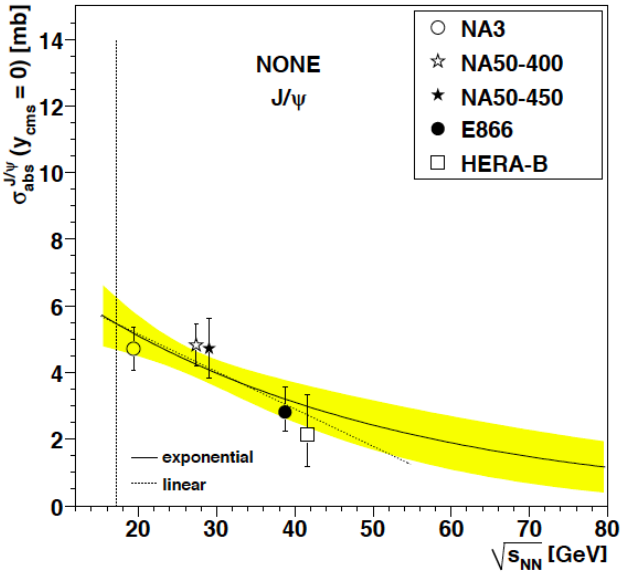

Figure 3.7. The collision energy dependence of the nuclear absorption cross section. Lines are the fits with exponential (solid line with error band) and linear (dotted line) functions. From [129].

3.5 Coherent parton energy loss effect

An energetic parton travelling in a large nuclear medium undergoes multiple elastic scatterings, which induce gluon radiation. The amount of such gluon radiation is usually referred to as the (radiative) *energy loss* of the fast parton. The notion of parton energy loss is widely used in phenomenological studies of nuclear effects. The suppression of production rates in A-A and pA compared to pp collisions (after an adequate normalization) observed for various processes in some kinematical regions was attributed, at least partly,

to parton energy loss [130, 131]. New scaling properties were identified in [132] for the induced gluon radiation spectrum and associated energy loss of hard processes where color charge undergoes small angle scattering through a static medium (cold matter or QGP).

In the model from [132], the following assumption is made. The heavy-quark $q\bar{q}$ pair of mass M is assumed to be produced, within the perturbative proper time[1] scale $\tau_{q\bar{q}} \sim 1/M$, in a compact *color octet state*, and remains color octet for a time $\tau_{\rm octet} \gg \tau_{q\bar{q}}$.

In quarkonium production models where color neutralization is a soft, non-perturbative process, $\tau_{\rm octet}$ coincides with the quarkonium hadronization time[2] $\tau_{{\rm J}/\psi}$ in the nucleus rest frame. In the CSM the gluon emission required for color neutralization of the $q\bar{q}$ pair is constrained by energy conservation at rather large x_F. Thus it becomes softer and occurs late, leading to $\tau_{q\bar{q}} \ll \tau_{\rm octet} \lesssim \tau_{{\rm J}/\psi}$ [133].

Therefore, the assumption of a color octet $q\bar{q}$ pair living longer than the perturbative time scale $\sim 1/M$ holds quite independently of the quarkonium production model [133]. This assumption allows, at sufficiently large quarkonium energy E in the target rest frame, to consider quarkonium as a small angle scattering of a color charge. Then the associated soft gluon radiation spectrum depends on the amount of transverse momentum kick $q_\perp$ to the charge.

The typical $q_\perp$ is expected to be larger in pA than in pp collisions due to the transverse momentum *nuclear broadening* $\Delta q_\perp^2$. An average medium-induced radiative loss is scaled with the quarkonium energy, $\Delta E \propto E$ [134]. It should be underlined that the medium-induced radiation spectrum is coherent. It indeed arises from the interference between the initial and final state emission amplitudes. The energy loss ΔE is thus neither a pure initial nor final state effect.

The amount of medium-induced gluon radiation, and hence the strength of J/ψ suppression in pA collisions, is controlled by $\Delta q_\perp^2$ mentioned above. For a path length L travelled across the target (proton or nucleus), it is given by the following equation:

$$\Delta q_\perp^2(L) = \hat{q}_{\rm A} L - \hat{q}_{\rm p} L_{\rm p}, \tag{3.9}$$

where the average path length is given by $L = \frac{3}{2} r_0 A^{1/3}$ with $r_0 = 1.12$ fm, assuming the hard process to occur uniformly in the nuclear volume [134]. Transport coefficients $\hat{q}_{\rm A}$ ($\hat{q}_{\rm p}$) in the nucleus (proton) are related to the gluon distribution $G(x)$ in a target nucleon [135].

The L-dependence of $\hat{q}$ enters mainly via the typical x at which $xG(x)$

[1] Usually proper time is the formation time in the $c\bar{c}$ rest frame.

[2] The J/ψ case is considered as an example but the argumentation is valid for all quarkonium states.

should be evaluated. If the hard production time in the nucleus rest frame $t_{\rm h} \ll L$, then $x \simeq (2m_{\rm p}L)^{-1} \equiv x_0$ [135]. If $t_{\rm h} \gg L$, the hard subprocess is coherent over the whole nucleus, and, assuming a $2 \to 1$ subprocess kinematics, $x \sim x_2$ where x_2 is the nucleus parton momentum fraction (see (3.1)). Using power-law behaviour $xG(x) \sim x^{-0.3}$ suggested by fits to HERA data [136], $\hat{q}$ is thus given by[1]

$$\hat{q}(x) = \hat{q}_0 \left(\frac{10^{-2}}{x}\right)^{0.3} ; \quad x = min(x_0, x_2). \tag{3.10}$$

The transport coefficient $\hat{q}_0 \equiv \hat{q}(x = 10^{-2})$ is the only free parameter of the model. It is determined by fitting the J/ψ suppression measured by E866 [137] in p-W over p-Be collisions at $\sqrt{s} = 38.7$ GeV in the [0.2-0.8] x_F-range. The data from E866 are used to determine $\hat{q}_0$ since they are the most precise and cover a wide x_F-range[2]. The fit provides $\hat{q}_0 = 0.09$ GeV^2/fm assuming energy loss effects only. Including saturation effects into the model[3] results in a lower value [134]: $\hat{q}_0 = 0.05$ GeV^2/fm.

Since the model has only one free parameter, it makes it predictive for various collision energy.

3.6 Experimental results

In order to understand if the J/ψ suppression discovered by SPS with respect to nuclear absorption (Fig.2.4) is anomalous or not, more accurate studies on CNM effects were required. Afterwards PHENIX published a lot of interesting results for J/ψ production in d-Au collisions at $\sqrt{s_{\rm NN}} = 200$ GeV in different rapidity domains: $|y| < 0.35, 1.2 < |y| < 2.2$, measured via dielectron and dimuon decay channels, respectively [138, 139].

In Fig.3.8 J/ψ nuclear modification factors $R_{\rm dAu}$ are shown as a function of rapidity for peripheral (a) and central (b) collisions. In (c) their ratio is shown and is referred to as $R_{\rm CP}$. The most central collisions correspond to cases where nucleons in deuteron strike closer to the middle of the gold nucleus, and thus nuclear effects are expected to be enhanced. This behavior is confirmed by the data [138]. Peripheral $R_{\rm dAu}$ measurements is compatible with a constant suppression as a function of rapidity. However, the large uncertainty of the order of 15% does not allow to make a strong conclusion. Central $R_{\rm dAu}$ results

[1] x-dependence of $\hat{q}$ is not essential. Similar results would be obtained using constant $\hat{q}(x) = \hat{q}$ [134].

[2] The resulting uncertainty on $\hat{q}_0$ is found to be of the order of 20%, depending on the x_F range used for the fit [134].

[3] It should be noted that the phenomenological way of the inclusion of the saturation effects is not fully correct. It was confirmed in the private discussion with the authors of the model.

show a significant J/ψ suppression at forward rapidity. The $R_{\rm CP}$ ratio allows to better constrain the models since some part of systematic uncertainties cancel out. In Fig.3.8(c) a dramatic suppression of forward rapidity J/ψ yields for central d-Au events with respect to peripheral events is shown. At backward rapidity, $R_{\rm CP}$ becomes compatible with unity.

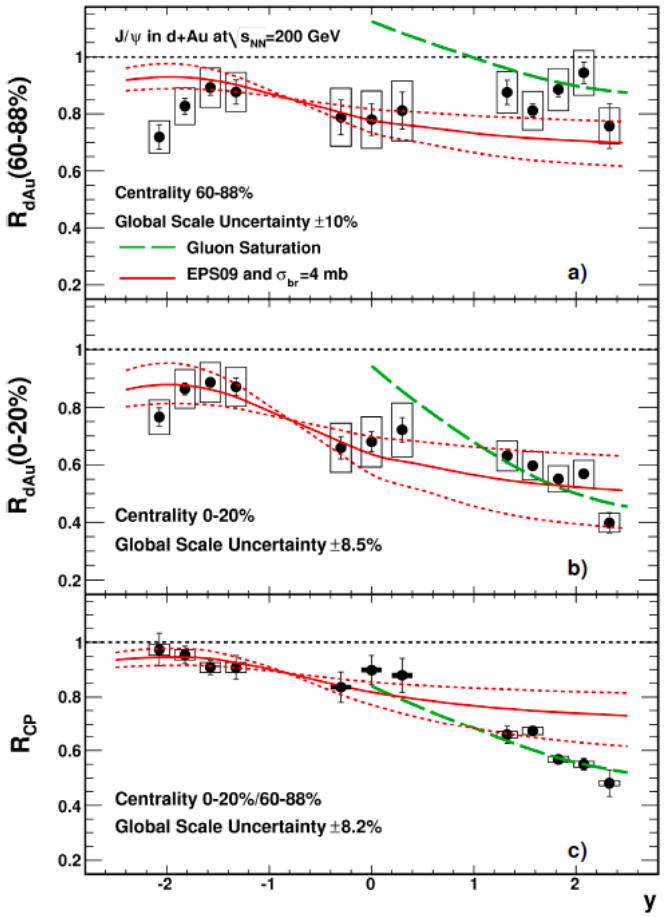

Figure 3.8. The J/ψ nuclear modification factor $R_{\rm dAu}$ for (a) peripheral and (b) central collisions. In (c) their ratio $R_{\rm CP}$ is shown. From [138].

The data in Fig.3.8 are compared to theoretical predictions of gluon saturation model [115, 119] and gluon shadowing model with EPS09 parametrization [102] combined with a nuclear break-up cross section $\sigma_{\rm br} = 4$ mb [140]. Within uncertainties, shadowing model shows a reasonable agreement with the data for the most central events. In the most peripheral events it shows an agreement at midrapidity while at backward and forward rapidity it overestimates and underestimates the suppression, respectively. Shadowing predictions for $R_{\rm CP}$ are in fair agreement with the data for the most central events

in the full rapidity range except the largest forward rapidity. Gluon saturation model predicts a modest J/ψ enhancement at midrapidity due to double-gluon exchange processes (not seen in the data). A stronger suppression at forward rapidity, especially in the most central d-Au events (due to saturation effects) predicted by the model are in a good agreement with the data. The R_{CP} ratio however is well described by this model both at forward and midrapidity, showing the main disadvantage of such a variable: R_{CP} can be well described by the model even if it simultaneously fails to describe R_{dAu} both in most central and most peripheral events.

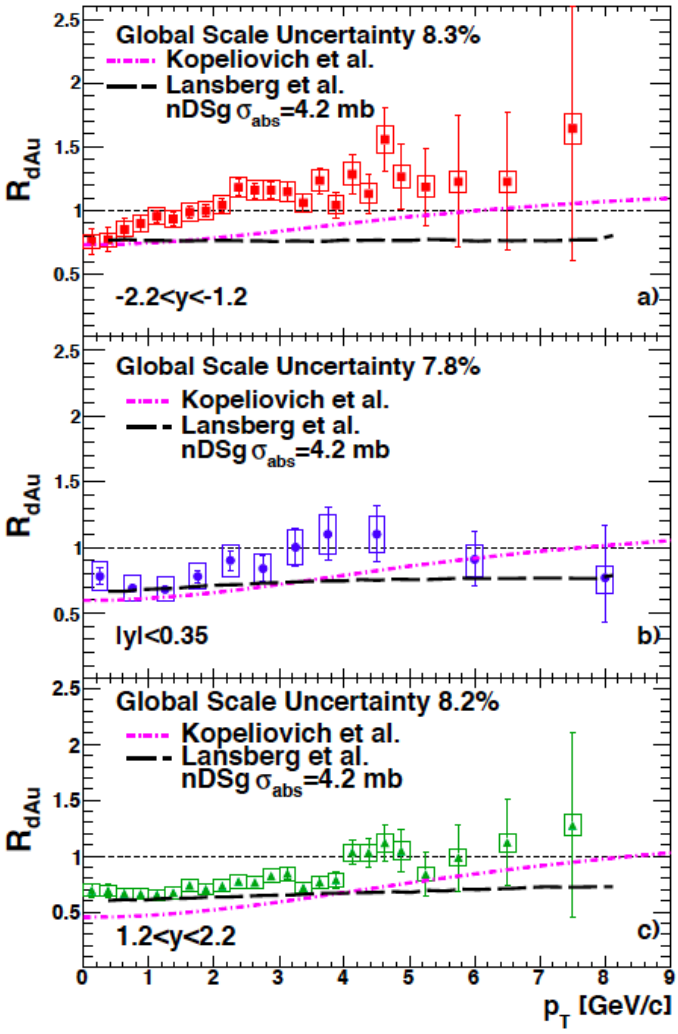

Figure 3.9. The J/ψ nuclear modification factor R_{dAu} for (a) backward, (b) midrapidity, (c) forward rapidity, integrated over centrality. From [139].

PHENIX also performed multidifferential studies of R_{dAu} as a function of

mean transverse momentum and rapidity (see Fig.3.9). Results were compared to two models: a shadowing model with a nDSg parametrization [141] of nuclear PDFs, combined with a nuclear break-up cross section $\sigma_{\rm br} = 4.2$ mb, proposed by Lansberg et al. [142], and a model of Kopeliovich et al. [143, 144] combining shadowing with a nDSg parametrization of nuclear PDFs, nuclear break-up cross section and a Cronin effect. Cronin effect, or $p_{\rm T}$ broadening, is usually related to multiple elastic scattering of the incoming parton before the hard collision that produces the J/ψ [145]. Both Lansberg and Kopeliovich models use CSM as a J/ψ production model. Fig.3.9 shows a different behaviour of $R_{\rm dAu}$ at backward ($-2.2 < y < -1.2$) compared to mid ($|y| < 0.35$) and forward ($1.2 < y < 2.2$) rapidities. At backward rapidity, the $R_{\rm dAu}$ is suppressed only at the lowest $p_{\rm T}$ with a rapid increase to $R_{\rm dAu} = 1$ at $p_{\rm T} \approx 1.5$ GeV/c. The mid and forward rapidity data show a similar level of suppression at the lowest $p_{\rm T}$ but a much slower increase of $R_{\rm dAu}$ with $p_{\rm T}$, reaching unity only at $p_{\rm T} \approx 4.0$ GeV/c. The shape and absolute scale for the mid and forward rapidity data is almost consistent for all $p_{\rm T}$ measured by PHENIX.

The results shows a good agreement with the Lansberg model calculations at low $p_{\rm T}$ for mid and forward rapidity while the model has a flatter $p_{\rm T}$ dependence than the one seen in the data. The shape of the distribution at backward rapidity in data shows a strong $p_{\rm T}$ dependence with respect to the model's prediction. As for the Kopeliovich model, the $p_{\rm T}$ shape is in good agreement with the data at mid and forward rapidity but predicts a larger suppression than the one seen in the data. At backward rapidity, the model shows a $p_{\rm T}$ shape different from the one measured in the experiment. The difference in the two models results mainly from the Cronin effect used in the model of Kopeliovich et al. The Cronin effect causes a suppression of the J/ψ production at low $p_{\rm T}$ and an increase at higher $p_{\rm T}$.

The coherent parton energy loss model [133] was very successful in description of both low (HERA) and high (PHENIX) energy experimental data as it can be seen in Fig.3.10. As for the PHENIX results (Fig.3.10(b)), the comparison is made with the model including (dashed line) or not (solid line) saturation effects. The suppression at the most forward rapidity is often attributed to gluon saturation effects or strong small-x shadowing [115, 140]. However energy loss effects alone might be responsible for the observed suppression, although initial state effects such as gluon shadowing and saturation might also play a role. The agreement is indeed better when saturation is included. A disagreement is seen at negative rapidity where nuclear absorption might also play a role (at least for $y < -1.1$).

It was shown in this chapter that various models can fair describe different experimental data. More experimental measurements at different energy, with different nuclei, are needed to constrain better the models. At

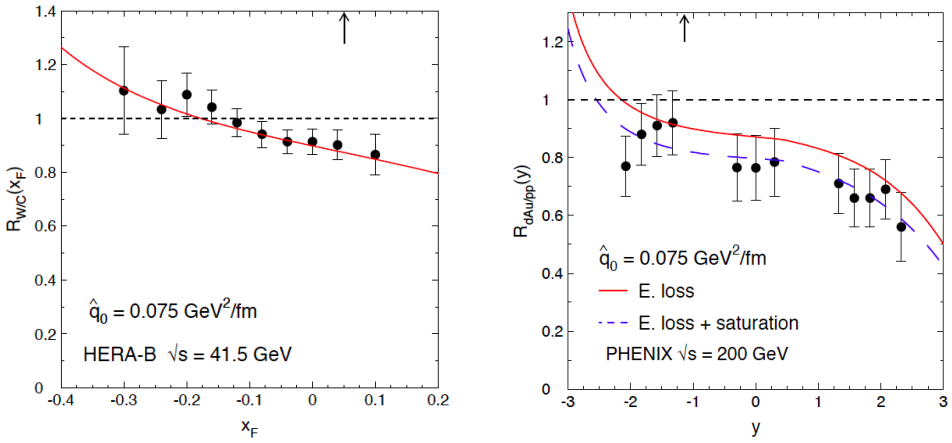

(a) HERA-B J/ψ suppression in p-A [146]. (b) PHENIX results on J/ψ R_{dAu} [138].

Figure 3.10. Coherent parton energy loss model compared to experimental data. From [133].

$\sqrt{s_{\mathrm{NN}}} = 5.02$ TeV, the LHC measurements allow to probe a very low-x region where different nuclear effects are expected: shadowing, saturation, coherent energy loss or, less pronounced, nuclear absorption.

Chapter 4

ALICE in the LHC wonderland

This chapter briefly describes the LHC and its goals and gives a detailed description of the ALICE apparatus, which was used for the main results presented in this thesis.

4.1 The LHC and its physics goals

The Large Hadron Collider (LHC) is the world largest and most powerful particle accelerator [45–47]. It remains the latest edition of CERN's accelerator complex. The LHC consists of a 27-kilometer ring of superconducting magnets with numerous accelerating structures to boost energy of the particles along their way. The LHC has the following physics goals:

- **The search of the Higgs boson.** The Standard Model (SM) does not explain the origin of mass and the difference of mass for different particles. The so-called "Higgs mechanism" could be the answer to this question. According to the theory of the Higgs mechanism, particles acquire their masses by interacting with a "Higgs field" which is believed to fill the whole space. The more intensively particles interact with this field the larger mass they acquire. The Higgs field has at least one associated particle, the Higgs boson. If it exists, it should be detected at the LHC. Finally, it was discovered by the CMS and ATLAS collaborations in 2012 [147–149].

- **Supersymmetry (SUSY) existence checks and searches for the SUSY particles responsible for dark matter and dark energy.** The SM is not able to provide a unified description of all the fundamental forces since it is difficult to describe the gravity in the same way as the other forces. The SUSY suggests the existence of more massive partners of the standard particles which could facilitate the unification of funda-

mental forces. If it is correct, the lightest of SUSY particles should be found at the LHC.

Cosmological and astrophysical observation showed that the visible matter contributes only to 4% of the Universe while the other part consists of the dark matter (23%) and dark energy (73%). No particles or phenomena responsible for it have been found yet. SUSY particles could be good candidates.

- **Matter/antimatter asymmetry.** The present Universe is made only of matter. CP violation may describe some excess of matter with respect to antimatter, but it is estimated to be far too small with respect to what we currently observe in the Universe. The LHC could help to understand matter/antimatter asymmetry.

- **QGP studies** The LHC allows to reach very high energy densities in ultrarelativistic heavy ion collisions. This makes it a powerful tool for studying the properties of the QGP which was defined in Section 2.1.

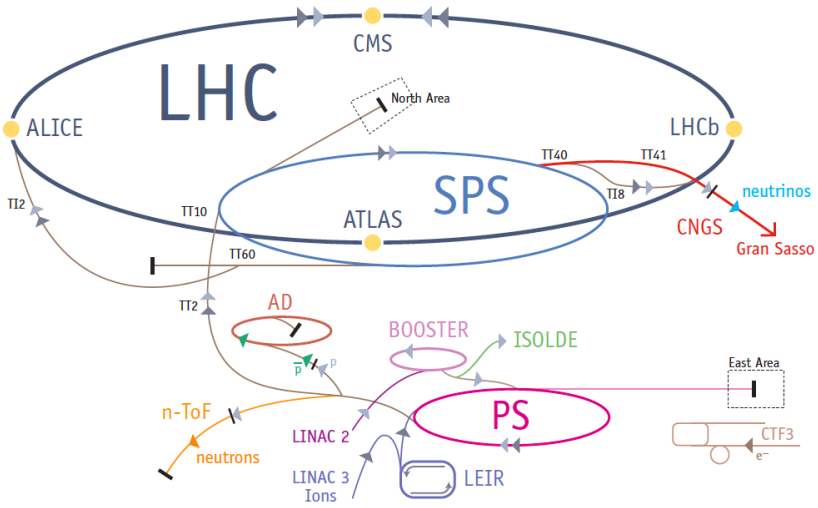

Figure 4.1. Scheme of the CERN accelerator complex. Protons after an acceleration in the linear accelerator (LINAC) and the Proton Synchrotron Booster, are injected in the Proton Synchrotron (PS) to be accelerated up to a momentum of 25 GeV/c. The next step is the Super Proton Synchrotron (SPS), where the protons reach a momentum of 450 GeV/c and are injected in the LHC ring. The ions acceleration is more complex since it includes additional stripping and accumulation phases at the very beginning. From [150].

The particles collide at four locations inside the accelerator ring (Fig.4.1). These colliding points correspond to the positions of the four experiments mentioned in Section 1.4.3:

- ATLAS [48] is a general-purpose detector. It covers wide range of physics at the LHC, from the search of the Higgs boson to SUSY and extra dimensions. Its main feature is a large superconducting toroidal magnet. ATLAS is the largest-volume collider-detector ever constructed.
- CMS [49] is also a general-purpose detector with the same physics goals as ATLAS. However it has different technical solutions and design. It is built around a huge superconducting solenoid.
- LHCb [51] was designed to study the slight asymmetry between matter and antimatter present in interactions of B-particles (particles containing b quark). Instead of surrounding the entire collision point with an enclosed detector, LHCb uses a series of sub-detectors to detect mainly forward particles.
- ALICE [50] is a detector specialized in analyzing heavy-ion collisions. It is dedicated to the study of the QGP properties. ALICE will be discussed in details in the following section.

The first proton beams were circulated in the LHC in the end of 2008. However a serious accident [151] delayed the LHC operations for one year. In November 2009 the first pp collisions were performed at $\sqrt{s} = 900$ GeV.

4.2 ALICE subsystems

As it was already mentioned before, ALICE was designed for studying the properties of the QGP in heavy-ion collisions. pp and p-Pb collisions are already extensively studied and are fully included in the ALICE physics program. ALICE covers a wide range of observables [152, 153]: global event characteristics, heavy flavour production and jet fragmentation, elliptic flow, quarkonium production, particle interferometry etc. It also has an excellent particle identification employing different techniques and is able to track the identified particles in a wide momentum range (from less than 0.1 up to 100 GeV/c). ALICE consists of two main parts: central barrel (which covers mid-rapidity ($|\eta| < 0.9$) over the full azimuth) and several forward systems (see Fig.4.2). The coordinate system of ALICE is defined as follows: origin of the system is located in the interaction point (IP), x-axis is perpendicular to the beam line and points to the center of the LHC ring in the horizontal plane, y-axis points upwards and the z-axis is collinear with the beam line and is

positive in the counter-clockwise direction. As it can be seen from Fig.4.2, the central part of the ALICE detector is inside a solenoid magnet. Maximum magnetic field of 0.5 T allows to track low momentum particles. Central barrel includes detectors for tracking and identification of produced particles. The muon spectrometer dedicated to quarkonia and HF studies is located in the forward region.

The ALICE detector subsystems are detailed below. Section 4.4 is devoted to the ALICE muon spectrometer.

4.2.1 Inner Tracking System (ITS)

The ITS [155] consists of six cylindrical layers of silicon detectors, with a radius from 4 to 44 cm. The two innermost layers are Silicon Pixel Detectors (SPD), the following two layers are Silicon Drift Detectors (SDD) and the two outer layers include double-sided Silicon micro-Strip Detectors (SSD) as it is shown in Fig.4.2.

The outer radius is determined to match tracks with those from Time Projection Chamber (TPC) while the inner radius corresponds to the minimum allowed by the beam pipe. The first layer has an extended pseudo-rapidity acceptance to provide, with the FMD (Forward Multiplicity Detector), a continuous coverage for the charged particle multiplicity measurements.

ITS allows to localize primary vertex with a resolution better than 100 μm, to reconstruct secondary vertices from decays of hyperons, B and D mesons, to track and identify particles with a low momentum ($p < 100$ MeV/c) and to complement the informations from the TPC.

4.2.2 Time Projection Chamber (TPC)

The TPC [156] is the main tracking detector of central barrel allowing charged-particle measurements with p_{T} from 0.1 up to 100 GeV/c, with a good particle identification and vertex determination even in the high multiplicity environment of Pb-Pb collisions. The TPC has an inner radius of 85 cm and outer radius of 250 cm (see Fig.4.3). The length of the TPC is 500 cm. Such a size results in a 88 μs drift time. Low magnetic field ($\lesssim 0.5T$) and a large detector size allow to detect simultaneously high and low momentum particles since a large section of the track is registered. Combined with the Time Of Flight (TOF) system, the Transition Radiation Detector (TRD) and the ITS, the TPC allows identifying particles by $\mathrm{d}E/\mathrm{d}x$.

4.2.3 Transition Radiation Detector (TRD)

The TRD [158] allows the identification of the electrons with momenta higher than 1 GeV/c, where the pion rejection through the energy loss mea-

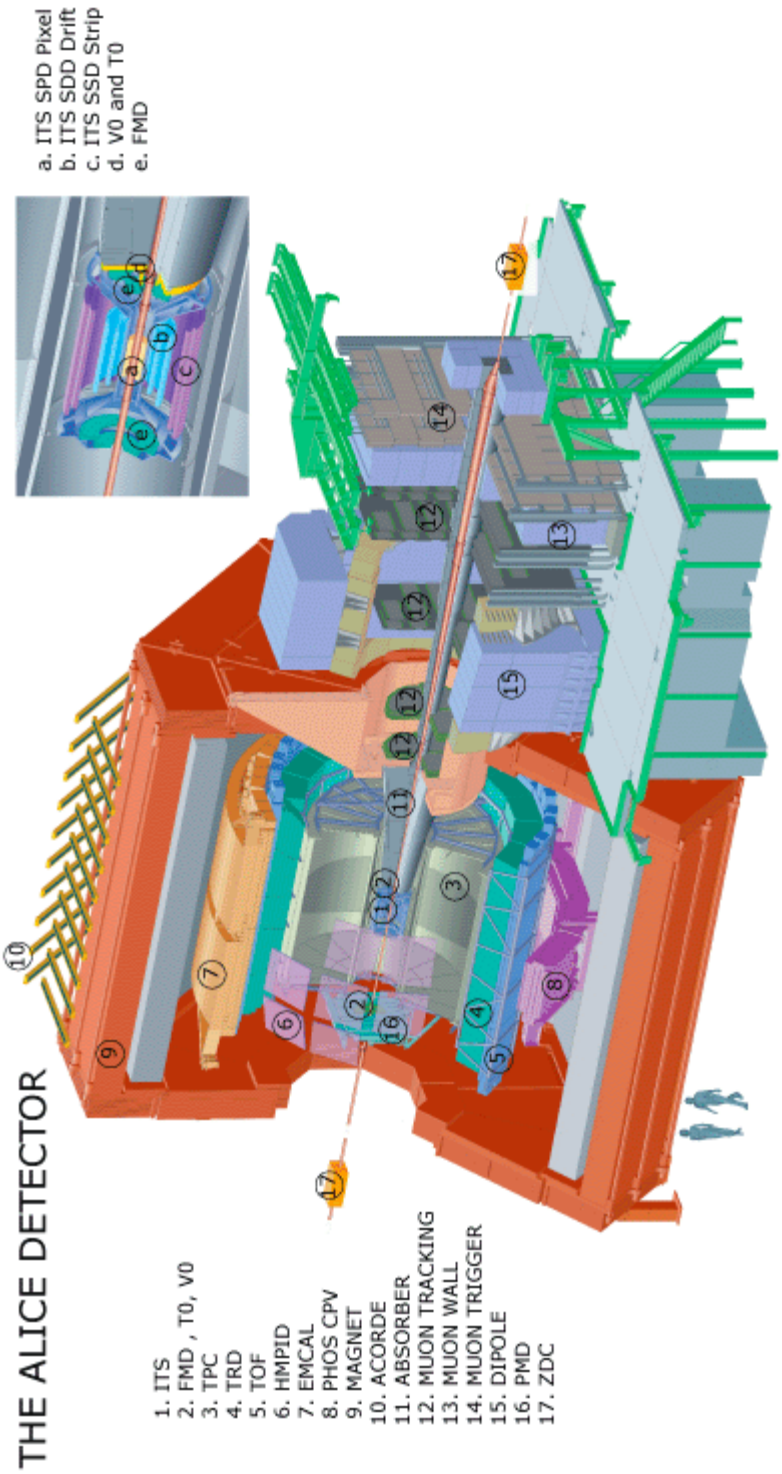

Figure 4.2. ALICE detector. From the official ALICE web-page [154].

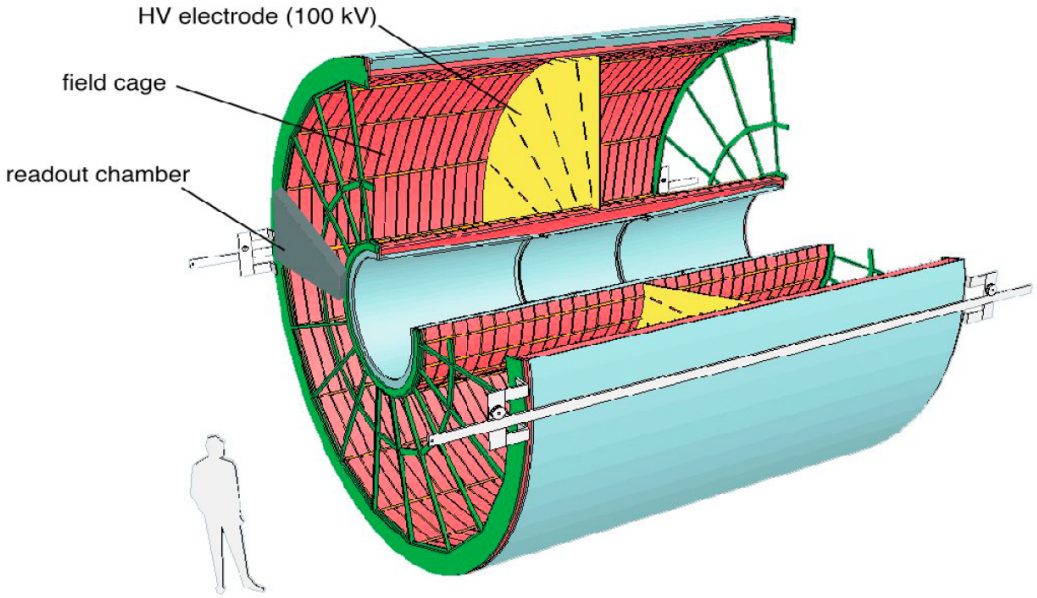

Figure 4.3. The TPC layout. From [157].

surement in the TPC is not sufficient anymore. The TRD increases the ALICE pion rejection capabilities by a factor of 100 for electron momenta above 3 GeV/c. Used together with the TPC and the ITS, the TRD allows to measure light and heavy meson resonances production. With the impact parameter determination of the ITS it is also possible to identify open charm and beauty.

4.2.4 Time Of Flight (TOF)

The TOF system [160, 161] allows the particle identification (PID) in a large momentum range from 0.2 up to 2.5 GeV/c for pions and kaons, up to 4 GeV/c for protons. For such a wide p_{T} range covered by the TOF, gaseous detector is used which consists of Multi-gap Resistive Plate Chambers (MRPC) providing an intrinsic time resolution better than 40 ps and almost 100% efficiency (see Fig4.4). The π/K and K/p separation in the TOF system is better than 3σ. Combined with the ITS and the TPC it allows an event-by-event identification of pions, kaons and protons.

4.2.5 High-Momentum Particle Identification Detector (HMPID)

The HMPID [162] is a single-arm array with an acceptance in pseudorapidity of $|\eta| < 0.6$ and an azimuthal coverage of 56° which correspond to the 5%

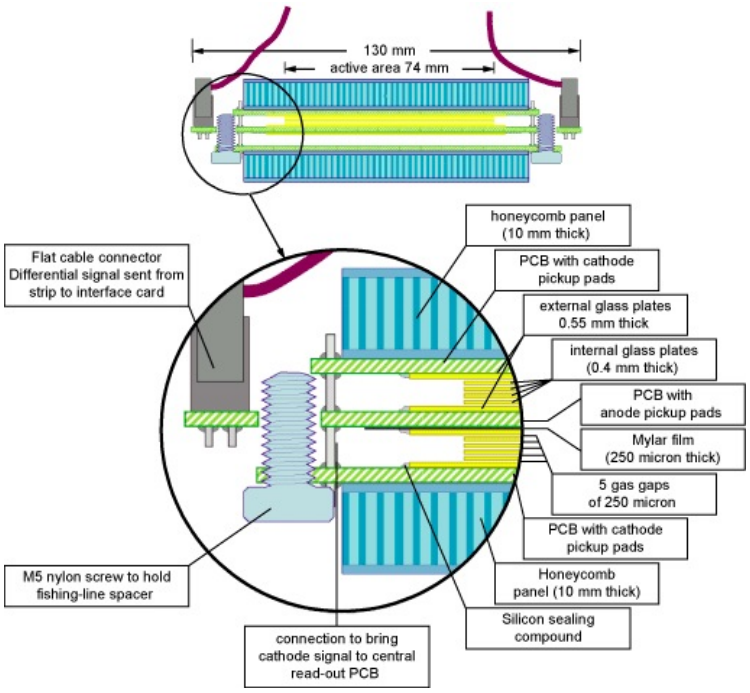

Figure 4.4. The TOF view with a zoom into the MRPC. From the official ALICE web-page [159].

of phase space in the central barrel. Based on proximity-focusing Ring Imaging Cherenkov counters, the HMPID identifies hadrons with $p_{\mathrm{T}} > 1$ GeV/c. It enhances the ALICE PID capability by enabling the identification of particles beyond the momentum interval accessible through energy loss (in ITS and TPC) and TOF measurements. The HMPID extends the range for π/K and K/p discrimination, on a track-by-track basis, up to 3 GeV/c and 5 GeV/c.

4.2.6 PHOton Spectrometer (PHOS)

The PHOS [164] is a single-arm spectrometer including a highly segmented electromagnetic calorimeter made of lead-tungstate crystals and a charged particle veto detector consisting of a Multi-Wire Proportional Chamber with cathode-pad readout. It covers a pseudo-rapidity range of $|\eta| < 0.12$ and azimuthal angle of 100°. This electromagnetic spectrometer is aimed to identify photons and neutral mesons through the two-photons decay channel. The properties of the initial phase of the heavy-ion collisions can be tested through the measurements of single photon or di-photon spectra and Bose-Einstein correlations of direct photons. Detection of high p_{T} π^0 allows also to study jet quenching as a deconfinement probe.

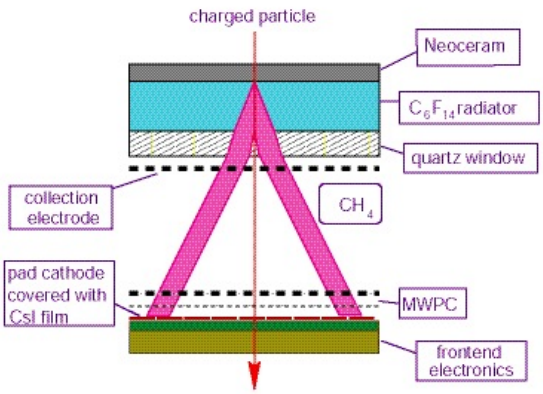

Figure 4.5. The HMPID view. From the official HMPID web-page [163].

4.2.7 ElectroMagnetic CALorimeter (EMCAL)

The EMCAL [165] is large lead-scintillator calorimeter with alternating layers of 1.44 mm of lead and 1.76 mm of polystyrene scintillator. It is located between the ALICE spaceframe, supporting the central detectors and the magnet coils. The covered azimuthal acceptance of 107° is limited by the HMPID and the PHOS. EMCAL improves the ALICE capabilities of jet studies and provides trigger signals on hard jets, photons and electrons.

4.2.8 ALICE COsmic Ray DEtector (ACORDE)

The ACORDE [166] is an array of plastic scintillator counters placed on the upper surface of the three upper faces of the ALICE magnet. The ACORDE provides a fast trigger signal, for the commissioning, calibration and alignment procedures of some of the tracking detectors. In combination with the TPC, TRD and TOF, ACORDE detects single atmospheric muons allowing to study high-energy cosmic rays.

4.2.9 Photon Multiplicity Detector (PMD)

The PMD [167, 168] is a preshower detector with a thick converter sandwiched between two planes of highly granular gas proportional counters. It measures the multiplicity and spatial distribution of photons on an event-by-event basis, in the forward region ($2.3 < \eta < 3.7$). It is placed in the side opposite to the muon spectrometer, with respect to the IP. The PMD estimates the transverse energy and the reaction plane on an even-by-event basis.

4.2.10 Forward Multiplicity Detector (FMD)

The FMD [169] is a silicon strip detector. It consists of seven disks perpendicular to the beam pipe. The FMD provides a charged particle multiplicity information complementary to the SPD, covering $-3.4 < \eta < -1.7$ and $1.7 < \eta < 5.1$. High radial detector segmentation allows the FMD to measure multiplicity fluctuations on an event-by-event basis, while azimuthal segmentation allows the determination of the reaction plane for each event and the flow analysis within the FMD's pseudo-rapidity coverage.

4.2.11 V0

The V0 (or VZERO) [169] is a small angle detector consisting of two arrays of scintillator counter, placed in the two opposite sides with respect to the IP: V0A in the side of the PMD and V0C in the muon spectrometer side, having pseudo-rapidity coverage of $2.8 < \eta < 5.1$ and $-3.8 < \eta < -1.7$, respectively. The V0 allows to identify and reject beam-gas events by measuring the difference of the time-of-flight between the two parts of the detector. Thus the V0 provides a minimum bias trigger for the central barrel detectors, a validation signal for the muon trigger and allows the luminosity studies. The V0 also measures the charged particle multiplicity allowing to determine centrality in Pb-Pb and to estimate it in p-Pb collisions.

4.2.12 T0

The T0 [169] consists of two arrays of Cherenkov quartz counters, based on a photomultiplier tube. The two array are installed in both sides of the IP and have 12 counters each. The pseudo-rapidity coverage of these arrays are $-3.28 < \eta < -2.97$ and $4.61 < \eta < 4.92$, respectively. The T0 provides for the TOF system a start time with a precision better than 50 ps. It also measures the vertex position and allows to identify and reject beam-gas events, providing additional checks to V0.

4.2.13 Zero Degree Calorimeter (ZDC)

The ZDC [170] consists of two pairs of quartz-fiber hadronic calorimeters (ZN for neutrons and ZP for protons) installed close to the beam pipe, on both sides of the IP, at a distance of 116 m from it. The ZDC is used to provide a centrality estimation and a trigger in Pb-Pb and p-Pb collisions by measuring the energy carried by non-interacting (spectator) nucleons in the forward direction, and to estimate the reaction plane of the collision. The ZDC system also has two electromagnetic calorimeters (ZEM), placed at about 7 m from IP, on both sides of the LHC beam pipe along the positive z axis.

The ZEM measures the energy of particles emitted at forward rapidity ($4.8 < \eta < 5.7$), mainly photons generated from π^0 decays. It allows to discriminate between central and peripheral collisions.

4.3 ALICE trigger and Data Acquisition

The ALICE Central Trigger Processor (CTP) collects the trigger signals from the detectors. It selects events with various options and rates and allows to perform a down-scaling of these rates in order to fit the bandwidth requirements of the acquisition system. In order to select/reject an event as fast as possible the triggers form 3 groups of the trigger levels depending on their response time:

- L0 (Level-0): these trigger signals arrive to the CTP first. They are sent by the fastest detectors, such as the SPD, V0, T0 and the muon trigger system. In order to select a certain class of events, a logic AND and OR is used when combining these signals in the CTP.
- L1 (Level-1): these trigger signals are sent from slower detectors and must be delivered to the detectors in 6.5 μs after the collision took place.
- L2 (Level-2): the last trigger level. The time of arrival of ~ 100 μs after the collision is constrained by the TPC drift time and by the past-future protection circuit. The latter looks for other events of a certain type in time windows before and after the considered collision, thus helping the rejection of the pile-up events and the read out of the detectors.

The ALICE Data AcQuisition (DAQ) system copes with both pp collisions with high rates and relatively small event sizes, on the one hand, and with Pb-Pb collisions with lower rates but larger event sizes (up to 1.25 GB/s sent to the storage elements), on the other hand. After the CTP selects an event, the trigger signal is sent to the FERO (Front-End Read-Out) electronics of the involved detectors. The data are then transmitted to the computer farms LDCs (Local Data Concentrator) which build the event fragments from the front-end electronics into sub-events. Those sub-events are then transferred to the GDC (Global Data Collectors) which build the whole event combining all the sub-events from various LDCs. The whole event is then sent by the GDC to the storage facilities.

4.4 ALICE muon spectrometer

The ALICE muon spectrometer [171, 172] is the main forward detector with full tracking, identification and triggering capabilities. It is aimed to

study open heavy flavours (D and B mesons), quarkonium (charmonium and bottomonium) and low-mass vector mesons (ϕ, ω, ρ) production via their muonic decay channels in a wide transverse momentum range in the pseudo-rapidity range $-4.0 < \eta < -2.5$. Two main conditions were required for the muon spectrometer: to perform charmonium detection down to zero transverse momentum and to have a high enough mass resolution to separate the bottomonium states ($\Upsilon, \Upsilon', \Upsilon''$) in the large-background environment of central Pb-Pb collisions. The layout of the muon spectrometer is shown in Fig.4.6. It consists of the system of absorbers, five tracking stations (TRK1-TRK5), a dipole magnet and two trigger chambers shielded by an iron wall. The total length of the spectrometer is about 17 m, it covers a polar angular range from 171° to 178° with respect to the ALICE reference frame.

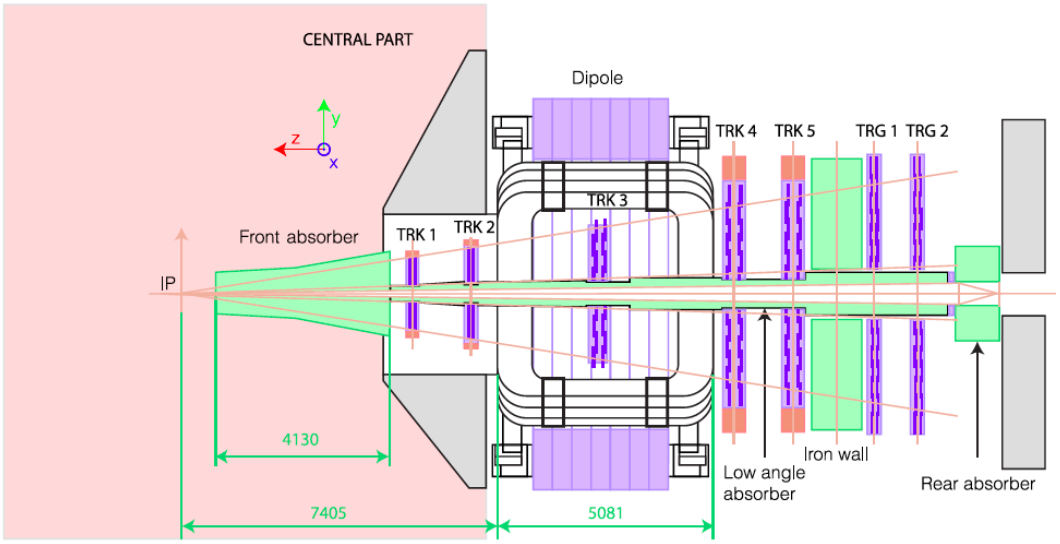

Figure 4.6. ALICE muon spectrometer layout. From [60].

4.4.1 System of absorbers

The main goal of the absorbers in the muon spectrometer is to protect it from the high background produced in the central Pb-Pb collisions. Four absorbers are used for this purpose: the front absorber, the beam shield, the iron wall and the rear absorber.

4.4.1.1 Front absorber

The front absorber (see Fig.4.7) has two main functions:

- A significant reduction of the charged particles flux and of background of muons from pions and kaons decays. This can be achieved by limiting the free path of primary pions and kaons via minimizing the distance between the absorber and the IP and by using materials with low nuclear interaction length λ_i[1]. Constrains with the ITS length along the beam pipe line give the minimum value of 90 cm for such distance. The external part of the absorber is made of lead and tungsten to protect the detectors from the particle flux originated by particles crossing the absorber.

- Limitation of the multiple scattering which could affect the spectrometer mass resolution. This is achieved using materials with high radiation length X_0[2] in the absorber layer close to the IP and with high atomic number at the rear end. The central part, near the IP, is made of carbon (a low Z material), to reduce muon multiple scattering effects. The rear region is made of concrete, lead, tungsten and boronated polyethylene to absorb the secondary particles produced in the absorber, low energy neutrons and protons. The lead layer wrapping the whole absorber is aimed to avoid the back-scattering particles into the TPC.

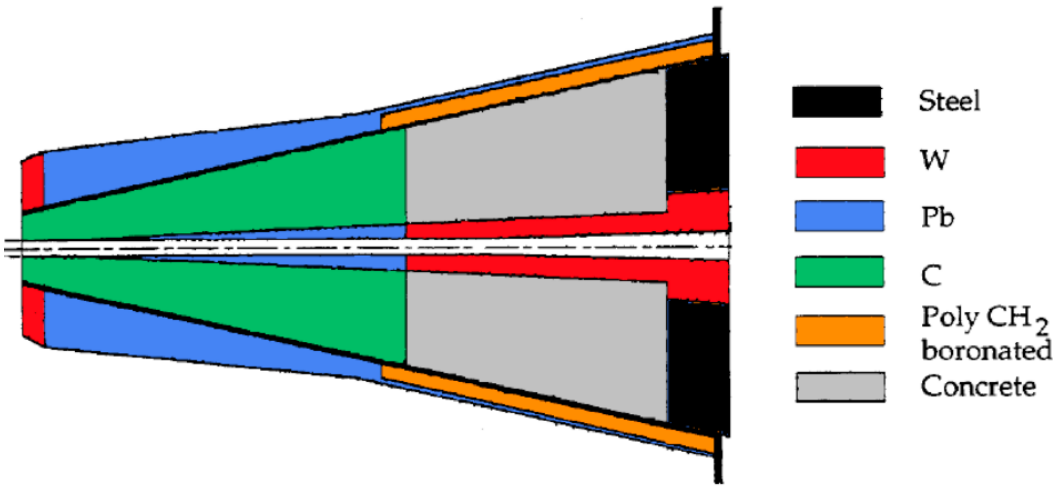

Figure 4.7. The layout of the front absorber of the ALICE muon spectrometer. From [173].

[1]The nuclear interaction length λ_i is the mean path length required to reduce the numbers of relativistic charged particles by the factor $1/e$, or 0.368, as they pass through matter.

[2]The radiation length X_0 is a characteristic of material representing a distance travelled by a charged particle before losing $1/e$ of its energy.

4.4.1.2 Beam shield

The low angle absorber is aimed to minimize the high background produced by the interactions with the beam pipe of particles with low angle (up to 2°), mainly pions and kaons. This shield, made of tungsten and lead is covered by a stainless steel layer [174].

4.4.1.3 Iron wall

The iron wall is installed between the last tracking station and the first trigger chamber. It stops hadrons and secondary particles that punch through the absorber. Since the wall is located after the tracking stations on the way of particles, it does not affect the mass resolution of the detector. The front absorber and the iron wall introduce a cut on the momentum of 4 GeV/c for the muons.

4.4.1.4 Rear absorber

The trigger chamber must be protected from the background generated by the accelerator (beam-gas residual interaction). This background is proportional to the luminosity of the beam and, therefore, is very high during the pp collisions data taking period. The rear absorber has recently been extended to fully cover the tunnel aperture.

4.4.2 Dipole magnet

The warm dipole magnet of the ALICE muon spectrometer generates a maximum central field of 0.67 T and an integral field of 3 Tm. It has an angular acceptance of $171° < \theta < 178°$. The direction of the magnetic field generated by the dipole magnet lays in the horizontal plane, perpendicular to the beam pipe line, defining a bending plane (zy plane) and a non bending plane (xz plane). The polarity of the magnet can be reverted within a short time. The magnet deflects muons according to their electric charge (allowing to separate positive and negative muons) and transverse momentum. Thus, the goal of the magnet is to allow the p_{T} determination.

4.4.3 The tracking system

The tracking system is employed for the reconstruction of muon trajectories inside the muon spectrometer. It consists of five tracking stations with two chambers in each of them. The first two stations are installed right after the front absorber, the third one is located inside the dipole and the last two are placed between the magnet and the iron wall. The active area of each station increases along the z axis going from the front absorber towards the

trigger chambers, from 2.5 to 20 m^2. The total area covered by the tracking stations is about 100 m^2. The active area of the first two stations is equal to the geometrical projection of the front absorber, the third stations dimensions are limited by the magnet, the last two stations are the largest ones and are aimed to detect muons deflected by the dipole. The main constraints to the performance of the tracking system are the following:

- a spacial resolution better than 100 μm in order to disentangle the Υ mass with a mass resolution of 100 MeV/c^2, and to operate in a maximum hit density of about $5 \cdot 10^{-2}$cm^{-2}, the rate expected in central Pb-Pb collisions;

- the resolution along the non-bending plane (parallel to the magnetic field) better than about 2 mm to allow an efficient track finding.

Multi-Wire Proportional Chambers (MWPC) with cathode readout are used to fulfill these requirements. Thus, each chamber in all five tracking stations consists of a central anode plane with wires equally spaced parallel to the y axis and sandwiched between two cathode planes. The wires have a high voltage of ∼1600 V, while the cathode planes are grounded. It allows to generate an electric field with its maximum value at the wire surface, decreasing as $1/r$ near the wires. The segmentation of the cathode pads was designed to keep the occupancy at a 5% level: the size of the pads increases with the radius since the hit density decreases with the distance from the beam pipe. In total there are $1.1 \cdot 10^6$ channels.

The chamber thickness is limited to $0.03 \cdot X_0$ in order to minimize multiple scattering of the muons in the chamber. This is achieved by using composite material, such as carbon fibres. The individual chambers were designed based on standard MWPC technology taking into account the particular constraints on the different tracking stations. The first two of them (TRK1 and TRK2) are based on a quadrant structure, while the others have a slat structure. A layout of the cathode plane for a quadrant of Station 1 is shown in Fig.4.8(a). Fig. 4.8(c) shows a photography of TRK2. Figures 4.8(b) and 4.8(d) show the same for the stations with a slat architecture. Within a tracker chamber the quadrants (or slats) overlap to avoid dead zones, i.e. zones without active detection area.

The front-end electronics based on a 64 channels board MANU (NUmerical MAnas) is used for all the stations (Fig.4.9). The signals of four 16-channel charge amplifier chips MANAS (Multiplexed ANAlogic Signal processor) located on this board, are sent to two 12-bits ADCs (Analog-to-Digital Converter) and to a readout chip MARC (Muon Arm Readout Chip). The MARC controls the functioning of the MANAS and the zero suppression. The digital signal is then transmitted to the CROCUS (Concentrator ReadOut Cluster)

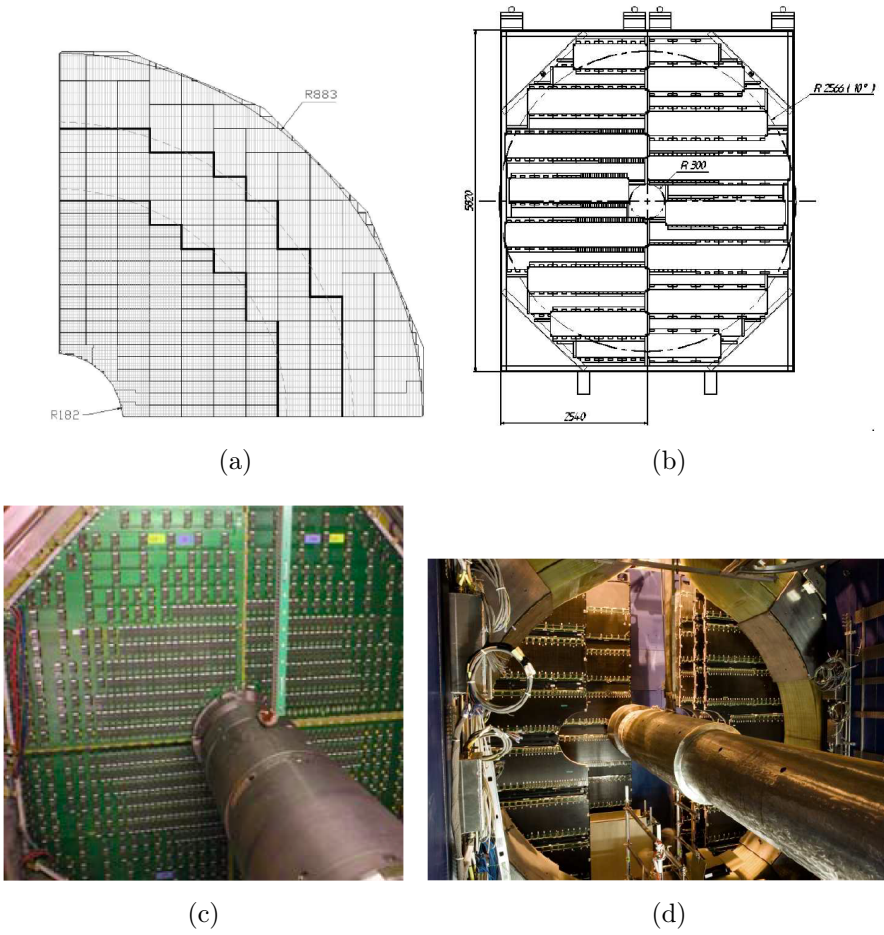

(a) (b)

(c) (d)

Figure 4.8. (a): The cathode plane layout of Station 1. From [50]. (b): Segmentation of a station with a slat architecture. From [60]. (c): A photography of TRK2. From [175]. (d): An overview of a station with a slat architecture. From [50].

which dispatches the trigger signal from the CTP to each half plane. The CROCUS performs the calibration of the MANU and gathers data through specific buses PATCH (Protocol for the ALICE Tracking CHamber) sending them further to the DAQ.

In order to estimate p_{T} and y resolution of single muons or dimuons, the following procedure can be done. p_{T} and y distributions of muons (dimuons) are generated in simulations. These distributions are then reconstructed in the same way as the data. Furthermore, the difference between generated and reconstructed p_{T} and y is calculated providing corresponding p_{T} and y distributions. These distributions are then fitted with gaussian. The corresponding gaussian width and/or RMS of the distributions are used to quantify the re-

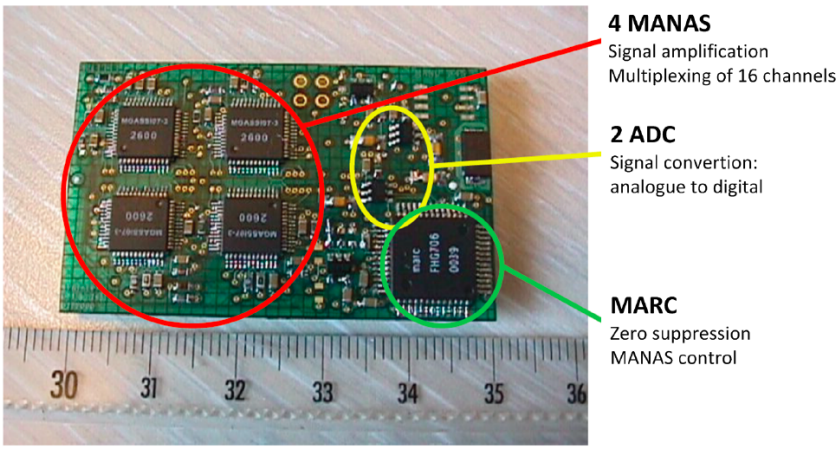

Figure 4.9. An example of a MANU including 4 MANAS, 2 ADC and 1 MARC. See text for details. From [173].

quired resolution. An example of such studies is presented in Fig. 4.10 where J/ψ p_{T} (left panel) and y (right panel) resolution in p-Pb collisions are shown. Black points denote the RMS mentioned above, while white points represent the corresponding gaussian widths.

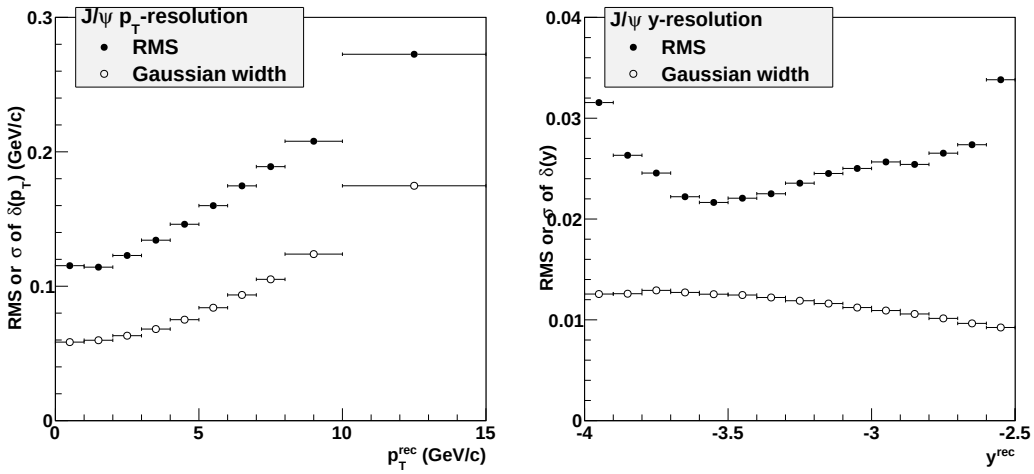

Figure 4.10. J/ψ p_{T} (left) and y (right) resolution in p-Pb collisions. See text for details. From [176].

4.4.4 The trigger system

The trigger system was designed to select events with a high probability to contain heavy quark or quarkonia decay muons. The selection is made on the transverse momentum p_{T} of each individual muons. The four planes of RPCs (Resistive Plate Chamber) are arranged in two trigger stations (MT1 and MT2) and are installed behind the iron muon filter. The spatial resolution should be better than 1 cm. The time resolution of 2 ns required for the bunch crossing identification is obtained by using a special Front-End Electronics (FEE) [177, 178].

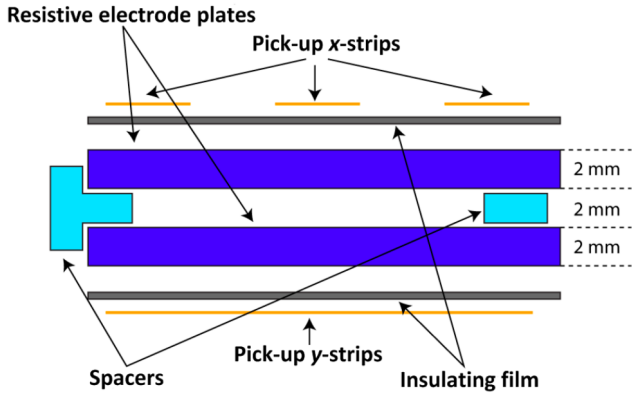

Figure 4.11. Schematic view of a Resistive Plate Chamber. From [173].

The RPCs (Fig.4.11) are based on the traditional spark chambers, where a spark is created by a charged particle crossing a gas placed in an electric field between two metallic parallel plates. In a following multiplication process created after that, electrons are driven to the anode while the ions move towards the cathode. Due to the planar geometry of the RPC, its electric field does not decrease with a distance from the anode which yield to the fact that multiplication process occurs in the whole gas volume. The main difference of RPC from the standard spark chambers is the resistive materials used in RPC for the electrodes. They prevent the signal propagation beyond the small region, thus allowing to control the sparks under consideration.

It should be also emphasized that RPC can be used in two regimes, depending on the gas mixtures and the high voltage values [179]:

- The streamer mode is used in high multiplicity A-A collisions. It allows a large signal amplification in the detector and therefore is less sensitive to electronics noise. However it leads to a fast ageing.

- The avalanche mode has a very good time resolution and slower ageing. It is employed during high luminosity pp runs with a high collision rate.

The signal generated in the RPC is sent to conductive strips electrically insulated from the electrodes. The strips are placed in both sides of the chambers, in the front face and in the rear, orthogonally to each other, providing a two-dimensional tracks reconstruction. The horizontal strips aligned with the x axis, measure the bending deviation due to the dipole magnetic field, while the vertical strips aligned with the y axis, measure the non-bending direction. The two corresponding read-out strip layers are called bending and non-bending planes.

The read-out strips described above are connected with the FEE. The signals coming from the FEE consist in the x and y fired strip patterns of the four detection planes, and are sent to the local trigger electronics. The whole system is divided in 234 detection areas, each of them associated with a local trigger board. The density of the local board reflects the segmentation of the strip: it is finer in the region close to the beam pipe, where particle multiplicity is expected to be high. The local electronics is aimed to perform the local trigger algorithm, deliver the trigger decision on single tracks and to backup strip patterns and trigger decision in a pipeline memory which is read-out on occurrence of an ALICE trigger sequence.

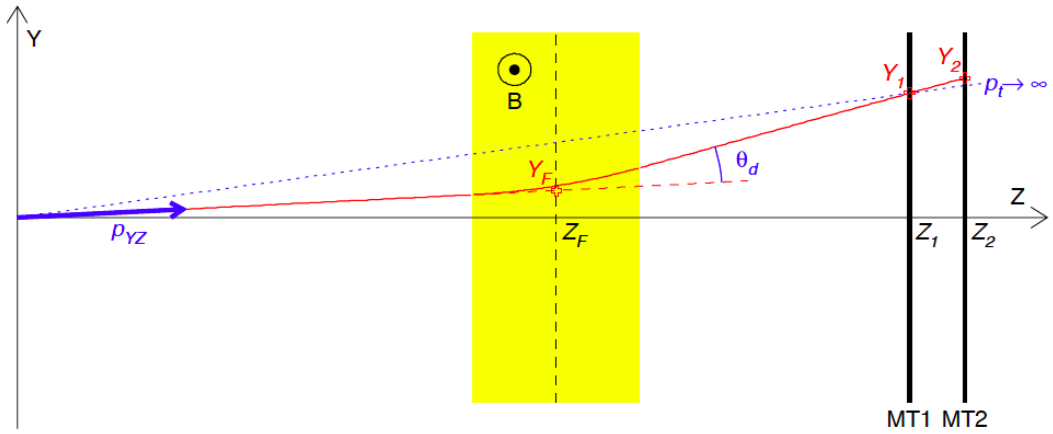

Figure 4.12. The muon spectrometer trigger principle. See text for details.

The muons coming from the IP, depending on their momentum, are deviated by a giving angle due to the magnetic field of the dipole magnet (Fig.4.12). The muons spectrometer principle of the mean transverse momentum p_{T} cut is based on the estimation of the p_{T} track: the larger the distance between Y_F and the $p_{\mathrm{T}} \to \infty$ straight line, the lower the p_{T} of the track . The estimation is made by the local boards. The maximum measurable deflection is fixed to ± 1 strip in the horizontal and ± 8 strips in the vertical direction.

The main features of the ALICE muon trigger system are the following:

- It is able to provide trigger inputs at the L0 level.
- it selects muon candidates with p_{T} of a muon track larger than a given programmable threshold.

Chapter 5

p-Pb physics program preparation

For the preparation of the 2013 p-Pb physics run at the LHC, a Monte-Carlo (MC) generator for quarkonia and open HF production was developed, based on the ALICE software. The main motivation for its development was the absence of a generator for p(A)-A collisions including an underlying event (UE) and a realistic production of heavy-flavour (HF) hadrons and quarkonia. PYTHIA [180] does not provide a realistic description of the quarkonia and open HF production in pp collisions. This led us to use PYTHIA without HF, combined with NLO pQCD and the CDF-data inputs for the HF description. When precise measurements became available at the LHC at $\sqrt{s_{\rm NN}}$ = 7 TeV, an extrapolation of pp cross-section to other LHC collision energies (2.76 and 5 TeV) became achievable, using CDF and LHC data [181]. The idea was to build a cocktail generator for p(A)-A in analogy to the pp case, with Glauber scaling of pp cross sections, centrality dependence of the quarkonia cross-sections and the CNM effects. The goal of this generator was to provide estimations for the trigger rate and for the "signal-to–background" ratio.

In this chapter I will first describe the Glauber model, then the generator for the J/ψ production. After that the pilot p-Pb run performed at the LHC in September 2012 is described. Finally, a comparison of the generator with the data from the pilot p-Pb run is given.

5.1 Glauber model

The high energy scattering with composite particles was of great interest in 1950's to both nuclear and particle physicists. In his lectures in 1958, Glauber was first to present the systematic calculations treating the many-body nuclear system either as a projectile or target. His work put the quantum theory of collisions on a firm basis, providing a consistent description of the experimental data for protons colliding with deuterons and light nuclei [182,183]. This model

was then further improved by other authors. In 1967 Czyz and Lesniak, using the Glauber model, correctly predicted position and magnitude of the dips observed later in the elastic peaks [184]. In 1976 Bialas, Bleszynski and Czyz applied their model, the "wounded nucleon model" to hadron-nucleus collision and then the Glauber approach to inelastic nuclear collisions [185]. Their approach introduced the thickness function and a prototype of the nuclear overlap function T_{AB}. They also defined a convention allowing to use the optical limit for analytical and numerical calculations.

The estimation of the collision properties from the measured distributions is the main feature of the Glauber model. A collision can be defined by the impact parameter b, the number of participating nucleons N_{part}, the number of the binary nucleon-nucleon collisions N_{coll}. The model describes the collision of two nuclei in terms of independent interactions of the constituent nucleons. It assumes that at sufficiently high energies, the nucleons carry sufficiently large momentum to be essentially undeflected as the nuclei pass through each other. It also assumes that the nucleons move independently in the nucleus and that the size of the nucleus is large as compared to the extent of the nucleon-nucleon force.

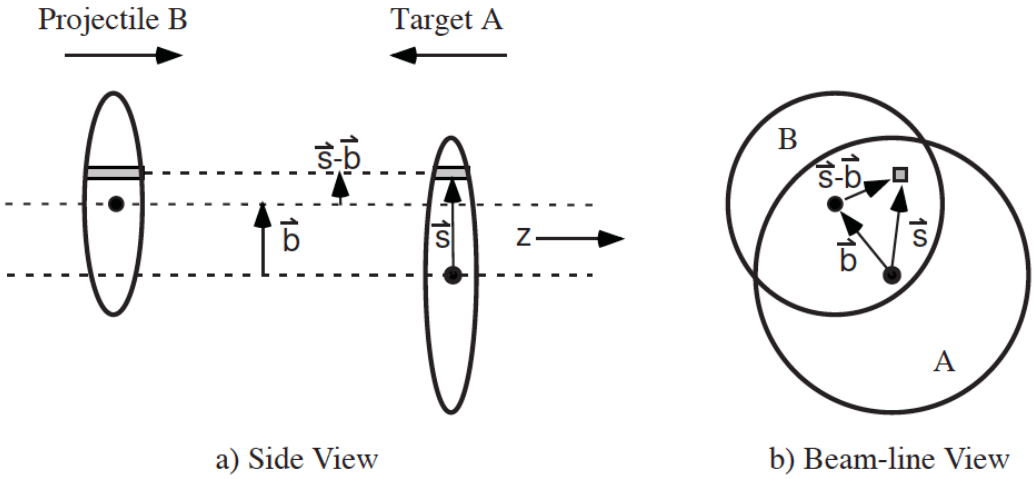

Figure 5.1. Schematic view of a nucleus-nucleus collision in the Glauber model in two projections: (a) transverse and (b) longitudinal. From [186].

Fig.5.1 shows in a transverse (a) and longitudinal (b) projection a schematic view of a heavy-ion collision with a projectile B and a target A colliding at the relativistic speed with an impact parameter **b**. The two flux tubes located at a displacement **s** from the center of the target nucleus and a distance **s-b** from the center of the projectile, overlap during the collision. The probability per unit of transverse area of a given nucleon to be located in a target flux tube is $T_A(\mathbf{s}) = \int \mathrm{d}z_A \rho_A(\mathbf{s}, z_A)$, where $\rho_A(\mathbf{s}, z_A)$ is the probability per unit volume, normalized

to unity, to find the nucleon at a position ($\mathbf{s}$,z_A). The same expression is given for the projectile nucleon. Then, the joint probability per unit area of nucleons to be located in the overlapping target and projectile flux tubes of differential area d^2s can be derived from the product $T_A(\mathbf{s})T_B(\mathbf{s}-\mathbf{b})\mathrm{d}^2s$. Integrating this value over $\mathbf{s}$ defines the "thickness function" [186]:

$$T_{AB}(\boldsymbol{b}) = \int T_A(\mathbf{s})T_B(\mathbf{s}-\mathbf{b})\mathrm{d}^2s. \tag{5.1}$$

In the following, the Glauber model will be applied to pA collisions which can be considered as a simplified version of nucleus-nucleus collisions. It should be mentioned that N_{part} in pA can be easily derived from N_{coll} from the expression: $N_{\mathrm{part}}^{pA} = N_{\mathrm{coll}}^{pA} + 1$.

5.1.1 Inelastic cross section

The inelastic cross section in pA collisions for a given collision energy $\sqrt{s}$ is usually given in the optical-limit in the eikonal form [187]:

$$\sigma_{pA}(s) = \int \mathrm{d}^2b \left[1 - \exp\left(-\sigma_{NN}(s)T_A(b)\right)\right], \tag{5.2}$$

where $\sigma_{NN}(s)$ is nucleon-nucleon inelastic cross section for the energy $\sqrt{s}$ and $T_A(b) = \int \mathrm{d}z\rho_A(b,z)$ the nuclear thickness function (nuclear profile function). The latter gives the number of nucleons in the nucleus A per unit area along the direction z separated from the center of the nucleus by an impact parameter b. The nuclear density $\rho_A(b,z)$ is usually parametrized by a three-parameters Woods-Saxon distribution:

$$\rho_A(r) = \rho_0 \frac{1 + \omega\left(r/R_A\right)^2}{1 + \exp\left(\left(r - R_A\right)/z\right)} \tag{5.3}$$

where R_A is the nuclear radius and $R_A = 1.19 \cdot A^{\frac{1}{3}} - 1.61 \cdot A^{-\frac{1}{3}}$ fm, α is the surface thickness and $\alpha = 0.54$, and ω is a parameter taken equal to zero for Pb nuclei [187, 188]. The central density ρ_0 is found from the normalization

$$\int \mathrm{d}^3r\, \rho_A(r) = \int \mathrm{d}^2b\, T_A(b) = A. \tag{5.4}$$

The inelastic cross section (5.2) is also called geometrical cross section σ_{geo}. In the following, the energy dependence will be omitted.

5.1.2 Hard processes

The expression (5.2) for the cross section can be applied to the inclusive process $p + A \to h + X$, where h is a given particle.

If the corresponding cross section $\sigma_{NN}^{hard} \ll 1$ then in the first approximation:

$$\sigma_{pA}^{hard} \approx \int \mathrm{d}^2 b \; \sigma_{NN}^{hard} \, T_A(b), \tag{5.5}$$

from which using (5.4) and assuming that σ_{NN}^{hard} does not depend on b:

$$\sigma_{pA}^{hard} = \sigma_{NN}^{hard} \cdot A. \tag{5.6}$$

In that case the average number of hard scattering collisions for a given impact parameter b can be found as:

$$\left\langle N_{pA}^{hard} \right\rangle (b) = \sigma_{NN}^{hard} \cdot T_A(b), \tag{5.7}$$

and the same for the average number of binary inelastic collisions in a nucleon-nucleus reaction with impact parameter b:

$$\left\langle N_{coll} \right\rangle (b) = \sigma_{NN} \cdot T_A(b). \tag{5.8}$$

5.1.3 Centrality dependence

Let's introduce the centrality dependence by defining C, the centrality bin, corresponding to the range of impact parameter b in $[b_1; b_2]$. Using (5.4) and (5.5), the fraction of the total cross section for hard processes occurring in a given centrality bin C can be defined as:

$$f_C^{hard} = \frac{\sigma_{pA\,C}^{hard}}{\sigma_{pA}^{hard}} = \frac{\int\limits_{b1}^{b2} \mathrm{d}^2 b \, \sigma_{NN}^{hard} \, T_A(b)}{\int \mathrm{d}^2 b \, \sigma_{NN}^{hard} \, T_A(b)} = \frac{\int\limits_{b1}^{b2} 2\pi b \, \mathrm{d}b \, T_A(b)}{A} = \frac{2\pi}{A} \int\limits_{b1}^{b2} b \, \mathrm{d}b \, T_A(b). \tag{5.9}$$

Similarly, using (5.2), the fraction of the geometric cross section in a centrality bin C can be found as follows:

$$\sigma_{pA\,C} = \frac{2\pi \int\limits_{b1}^{b2} b \, \mathrm{d}b \left[1 - \exp\left(-\sigma_{NN}(s) T_A(b)\right)\right]}{\sigma_{geo}}. \tag{5.10}$$

Then the relation between $\langle N_{coll} \rangle_C$ and $\left\langle N_{pA}^{hard} \right\rangle_C$ can be also found by

using (5.8) and (5.7).:

$$\begin{aligned}\langle N_{coll}\rangle_C &= \frac{\int_{b1}^{b2} 2\pi b\,\mathrm{d}b\,\langle N_{coll}\rangle\,(b)}{\sigma_{geo\,C}} = \\ &= \frac{\sigma_{NN}\cdot\frac{1}{\sigma_{NN}^{hard}}\int_{b1}^{b2} 2\pi b\,\mathrm{d}b\,\sigma_{NN}^{hard}T_A(b)}{\sigma_{geo\,C}} = \frac{\sigma_{NN}}{\sigma_{NN}^{hard}}\cdot\left\langle N_{pA}^{hard}\right\rangle_C.\end{aligned} \tag{5.11}$$

From (5.11) and (5.5) one obtains:

$$\langle N_{coll}\rangle_C = \frac{\sigma_{NN}}{\sigma_{NN}^{hard}}\cdot\frac{\sigma_{pA\,C}^{hard}}{\sigma_{geo\,C}}. \tag{5.12}$$

The $< N_{coll} >_{MB}$ can be calculated from (5.6):

$$\langle N_{coll}\rangle_{MB} = \frac{\sigma_{NN}}{\sigma_{NN}^{hard}}\cdot\frac{\sigma_{pA}^{hard}}{\sigma_{geo}} = \frac{\sigma_{NN}}{\sigma_{geo}}\cdot A, \tag{5.13}$$

where "MB" stands for minimum bias, i.e. a centrality range of [0;100%]. If the hard cross section fraction is defined for a given centrality bin C as

$$\begin{aligned} r_C &= \frac{\sigma_{pA\,C}^{hard}}{\sigma_{geo\,C}} \\ \text{and consequently}\quad r_{MB} &= \frac{\sigma_{pA}^{hard}}{\sigma_{geo}}, \end{aligned} \tag{5.14}$$

the ratio between $\langle N_{coll}\rangle_C$ and $\langle N_{coll}\rangle_{MB}$ can be calculated in terms of these hard cross section fractions:

$$\frac{\langle N_{coll}\rangle_C}{\langle N_{coll}\rangle_{MB}} = \frac{\sigma_{NN}}{\sigma_{NN}^{hard}}\cdot\frac{\sigma_{NN}^{hard}}{\sigma_{NN}}\cdot\frac{\sigma_{pA\,C}^{hard}}{\sigma_{geo\,C}}\cdot\frac{\sigma_{geo}}{\sigma_{pA}^{hard}} = \frac{r_C}{r_{MB}}, \tag{5.15}$$

5.2 MC generator for the J/ψ production

As mentioned above a MC generator was developed to study the J/ψ production in p-Pb collisions. It was built in two steps:

- HIJING (Heavy-Ion Jet Interaction Generator) [189] is used to generate an UE, in particular the background from the pions/kaons decays. It simulates the event centrality according to the Glauber model.

- Open HF and quarkonium generation. A p_{T} and y dependence for HF are generated according to the perturbative QCD calculations at fixed order with next-to leading order resummation (FONLL) [190]. A p_{T}, y and b-dependent production of quarkonia are simulated according to a parametrization on real data and the following assumptions:

  · factorization for p_{T} and y-dependence of pp cross section $\frac{\mathrm{d}^2\sigma_{pp}}{\mathrm{d}p_{\mathrm{T}}\mathrm{d}y}$ is assumed;

  · y-dependence is taken from CEM;

  · p_{T}-dependence is extrapolated from the world data [191].

A scheme of this MC generator is shown in Fig.5.2. The generation of event starts with HIJING which generates an impact parameter b based on the Glauber model in an optical limit (see (5.2)). In that case the cross sections of hard processes are found using (5.5) and (5.6). Then open HF are generated taking into account shadowing calculations performed for the centrality-integrated case. Afterwards quarkonium family is generated, depending on the impact parameter b, according to the cross sections corrected by the shadowing calculations from the EPS09 LO parametrization. In order to increase the quarkonium statistics for some specific needs, a factor may be used to scale the quarkonium production cross sections. HIJING provides the dimuon background from π/K meson decays. Generation of HF hadrons is used for the main dimuon background from HF as well as to reproduce the J/ψ and ψ(2S) from B-hadron decays.

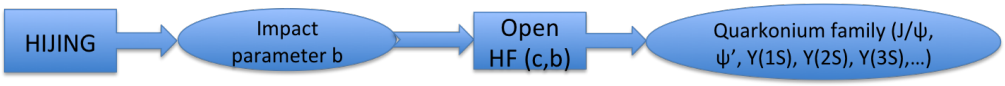

Figure 5.2. A scheme of a MC generator for the J/ψ production in p-Pb.

It should be mentioned that the impact parameter b was used to define a corresponding centrality bin for each event. The number of centrality bins in the MC generator was fixed to four: 0-20%, 20-40%, 40-60%, 60-100% of the geometric cross section (see (5.10)). The number and the ranges of centrality bins can be defined differently. However the choice of centrality ranges for the most peripheral centrality bins is limited due to small N_{coll} (and N_{part}) and consequently, a low charged particle multiplicity, used for centrality determination with V0A detector. The centrality determination in ALICE will be detailed in Chapter 7.

5.3 The Glauber model inputs to the generator

The main inputs of the generator are the definition of the centrality bins, the nucleon-nucleon and p-Pb cross section and the quarkonium cross sections. The impact parameter distribution provided by HIJING is shown in Fig.5.3. First, this generator was mainly used for studying J/ψ production. The fol-

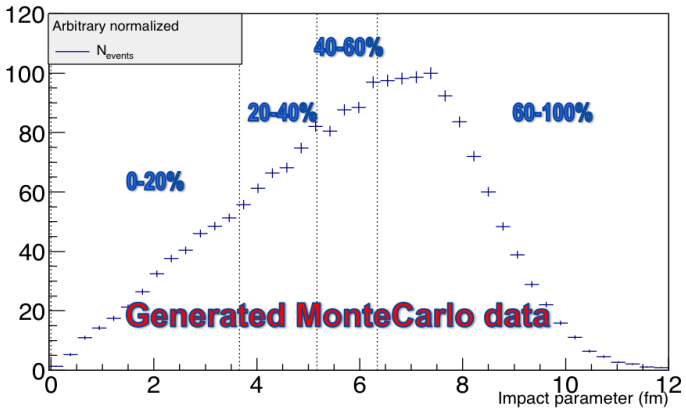

Figure 5.3. Impact parameter distribution provided by HIJING.

lowing values were fixed in the code from the Glauber MC calculations [192] and private discussions with Smbat Grigoryan (one of the co-authors of [181]): $\sigma_{\rm pPb} = 2100\,{\rm mb}$, $\sigma_{\rm NN} = 70\,{\rm mb}$ and $\sigma_{\rm J/\psi} = 5.5\,{\rm mb}$. Using (5.13), one can obtain the value $\langle N_{coll}\rangle_{MB} = 6.93$. First row of Table 5.1 represents the fraction of the p-Pb cross section, related to the centrality bin determination. Second row shows the values of the impact parameter b_{up} corresponding to b_2 from (5.10). The corresponding mean values of the impact parameter in each centrality bin are denoted as $\langle b\rangle$. Third row provides $\langle N_{\rm coll}\rangle_C$. Finally, fourth row shows the shadowing factors calculated for each centrality bin according to the EPS09-LO parametrization.

Table 5.1. Main inputs to the MC generator.

Fraction of the $\sigma_{\rm pPb}$	0-20%	20-40%	40-60%	60-100%	0-100%
b_{up}, $\langle b\rangle$ fm	3.66, 2.44	5.17, 4.46	6.34, 5.77	10, 7.50	10, 5.53
$\langle N_{coll}\rangle_C$	13.4	10.2	6.34	2.31	6.93
EPS09-LO shadowing factor	0.715	0.775	0.856	0.951	0.785

5.4 p-Pb run set-up

A short pilot p-Pb run was performed at the LHC in September 2012 at the energy $\sqrt{s_{\mathrm{NN}}} = 5.02$ TeV in preparation of the p-Pb physics run scheduled for the beginning of 2013. Beam 1 consisted of protons at 4 TeV energy circulating in the negative z-direction of the ALICE laboratory frame. Beam 2 consisted of fully stripped $^{208}_{82}$Pb ions at $82 \cdot 4 = 328$ TeV energy. Due to the low luminosity only Minimum Bias (MB) triggers were recorded. The ALICE detector collected two million MB events during 10 hours of data taking, including 3 hours with the ALICE muon spectrometer (Fig.5.4). During the run, beams consisting of 13 bunches were circulating, with about 10^{10} protons and 6×10^7 Pb ions per bunch. In the ALICE interaction region, 8 pairs of bunches were colliding, leading to a luminosity $L \sim 8 \cdot 10^{25} cm^{-2} s^{-1}$ [193]. During this short data taking period it was expected to see approximately 8 J/ψ in the muon spectrometer rapidity range ($2.5 < y < 4$ in the ALICE laboratory system).

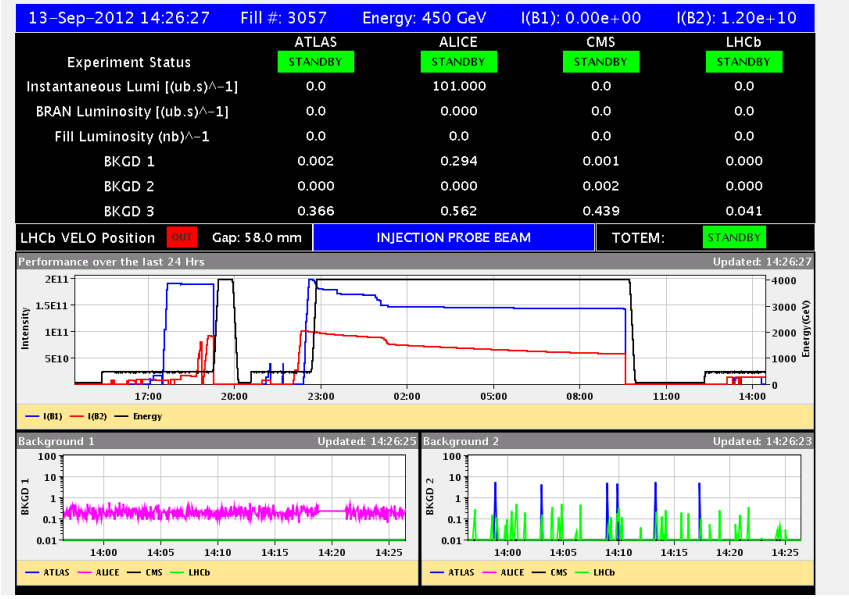

Figure 5.4. Online monitor during the pilot p-Pb run in 2012.

In Fig.5.5 the dimuon invariant mass distribution from the pilot run analysis is shown. Analysis details are discussed in Chapter 6 dedicated to the p-Pb physics run and to this kind of analysis. In this plot a J/ψ signal is seen around the mass value of 3.1 GeV/c^2. Assuming no background, 8 events are counted within the mass window [3; 3.2] GeV/c^2. This rough estimation of the number of J/ψ corresponds well to the expected J/ψ yield mentioned above.

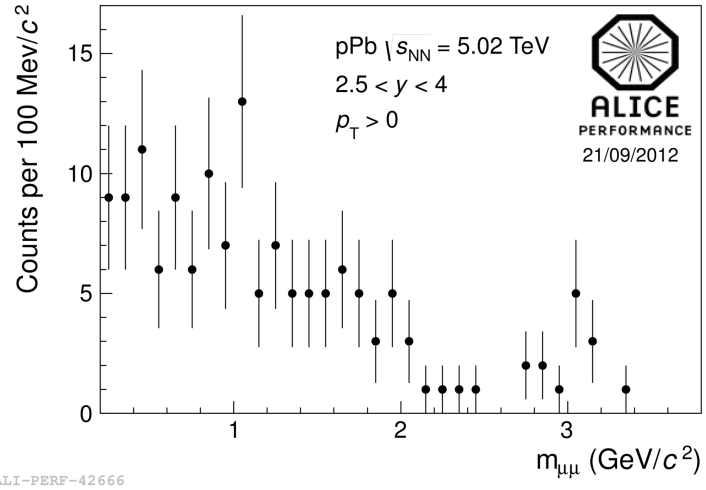

Figure 5.5. Invariant mass distribution of the opposite-sign dimuons reconstructed during the pilot p-Pb run in the muon spectrometer rapidity range.

5.5 Comparison of MC simulations to the pilot p-Pb run

To validate the MC generator, it was compared to the data from the pilot p-Pb run. In Fig. 5.6 a comparison of the pseudorapidity η distribution[1] of single muons matching the all-p_{T} (Apt) single muon trigger[2] is shown. The pseudorapidity is multiplied by the sign of the muons to distinguish μ^+ from μ^-, and is normalized by the total number of MB events. Thus, negative pseudorapidity corresponds to μ^+, positive to μ^-. In the bottom part of the figure the ratio of the data to the MC distribution is shown for a quantitative comparison. A discrepancy is seen both in the shape and in the magnitude reaching a ratio data/MC of 2 at $\eta = -2.5$ for both μ^+ and μ^-.

The p_{T} distribution of the single muons matching an Apt trigger, presented in Fig. 5.7 also shows a discrepancy between the data and the MC. The distribution from the data is always higher than the MC one. At low p_{T}, where the spectrum is dominated by secondary muons, the data and simulations disagree in shape. In the region dominated by open HF (at p_{T} >2 GeV/c) similar shape in data and MC is seen, but simulations underestimate the data by a factor of 2.5.

[1]Pseudorapidity η is defined as $\eta = -\ln\tan(\theta/2)$, where θ is the polar angle between the charged particle direction and the beam axis z.

[2]ALICE muon spectrometer provides different trigger options, allowing to trigger muons with different p_{T} thresholds. All-p_{T} trigger indicates that the muons with the lowest p_{T} trigger threshold are triggered (0.5 GeV/c). More triggers are presented in Section 6.2.

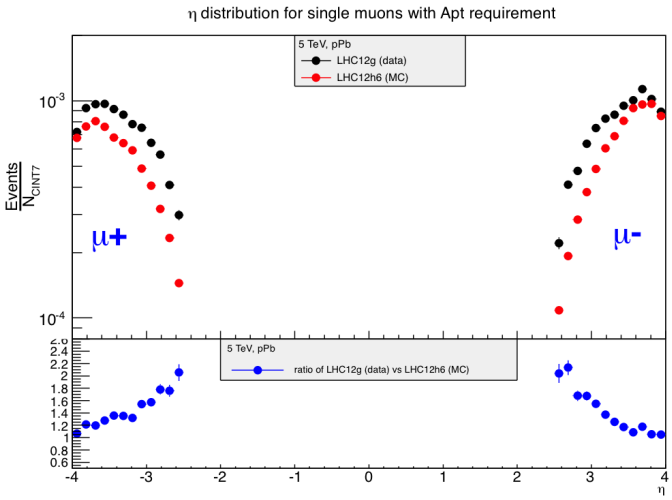

Figure 5.6. Comparison of the pseudorapidity distribution of the single muons. The distribution from the simulation is shown in red, while the data are shown in black, and in blue their ratio is presented. The pseudorapidity is multiplied by the sign of the muons to distinguish μ^+ from μ^-, and is normalized by the total number of the MB events.

The discrepancies between the MC generator results and the pilot p-Pb run data demonstrated that further studies are needed for this MC generator. One of the possibilities to improve this generator is to tune some numbers fixed in it, using the real data. It is important to note that this MC was used to define the trigger strategy. The comparison with the data was sufficiently good to estimate the rate of trigger with different p_{T} threshold (in the pilot run, only one trigger threshold of 0.5 GeV/c could be tested).

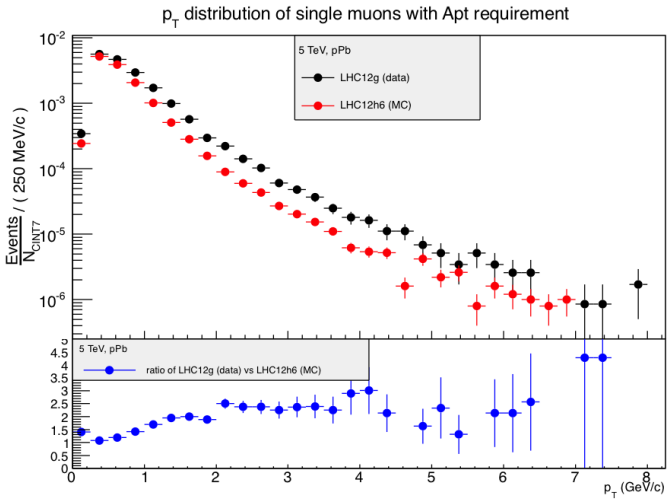

Figure 5.7. A comparison of the p_{T} distribution of the single muons measured in the described MC generator (red points) and in the pilot p-Pb run data (black points), and their ratio (blue points). No separation is made between μ^+ and μ^-. Both p_{T} distributions are normalized by the total number of the corresponding MB events.

Chapter 6

p_{T} and y dependence of the J/ψ production in p-Pb

This chapter describes the analysis of the J/ψ production in p-Pb collisions integrated over the event activity. This chapter describes the event and muon track selection criteria, the related acceptance and efficiency corrections, the raw J/ψ yield extraction, the event normalization, the pp reference estimation and the evaluation of the systematic uncertainties.

6.1 Main observables

The main observables of this analysis are the inclusive J/ψ cross section, the nuclear modification factor and the Forward-to-Backward ratio. The definition of these observables is presented below.

The inclusive J/ψ cross section is computed as:

$$\frac{\mathrm{d}\sigma}{\mathrm{d}y\mathrm{d}p_{\mathrm{T}}}(p_{\mathrm{T}}, y) = \frac{Y_{\mathrm{J}/\psi\to\mu^+\mu^-}(\Delta p_{\mathrm{T}}, \Delta y)}{BR \times \Delta p_{\mathrm{T}} \times \Delta y} \times \sigma_{\mathrm{MB}}, \tag{6.1}$$

where BR is the J/$\psi \to \mu^+\mu^-$ branching ratio equal to (5.93$\pm$0.06)% [194], σ_{MB} is the MB cross section determined from van der Meer scans [195]. Finally, $Y_{\mathrm{J}/\psi\to\mu^+\mu^-}(\Delta p_{\mathrm{T}}, \Delta y)$ is the inclusive J/ψ invariant yield for a given range in p_{T} and y, Δp_{T} and Δy respectively. It can be written as:

$$Y_{\mathrm{J}/\psi\to\mu^+\mu^-}(\Delta p_{\mathrm{T}}, \Delta y) = \frac{N_{\mathrm{J}/\psi\to\mu^+\mu^-}(\Delta p_{\mathrm{T}}, \Delta y)}{N_{MB} \times A\epsilon(\Delta p_{\mathrm{T}}, \Delta y)}, \tag{6.2}$$

where N_{MB} is the number of equivalent MB events and $A\epsilon(\Delta p_{\mathrm{T}}, \Delta y)$ is the acceptance times efficiency of the detector.

The inclusive J/ψ yield cross section in p-Pb collisions is compared to the inclusive J/ψ cross section in pp collisions $\sigma^{\mathrm{pp}}_{\mathrm{J}/\psi\to\mu^+\mu^-}$ at the same energy to

extract the nuclear modification factor R_{pPb} defined as:

$$R_{\mathrm{pPb}}(p_{\mathrm{T}}, y) = \frac{Y_{\mathrm{J}/\psi\to\mu^+\mu^-}(\Delta p_{\mathrm{T}}, \Delta y)}{\langle T_{\mathrm{pPb}}\rangle \times \Delta p_{\mathrm{T}} \times \Delta y \times \frac{BR\times \mathrm{d}\sigma^{\mathrm{pp}}_{\mathrm{J}/\psi\to\mu^+\mu^-}}{\mathrm{d}y\mathrm{d}p_{\mathrm{T}}}(p_{\mathrm{T}}, y)}, \tag{6.3}$$

where $\langle T_{\mathrm{pPb}}\rangle = 0.0983 \pm 0.0035\mathrm{mb}^{-1}$, the nuclear overlap function, is determined using the Glauber model [196].

In order to exclude the systematic uncertainty from the pp cross section and the nuclear overlap function, a Forward-to-Backward ratio R_{FB} is defined as follows:

$$R_{\mathrm{FB}}(y) = \frac{R_{\mathrm{pPb}}(|y|)}{R_{\mathrm{pPb}}(-|y|)}. \tag{6.4}$$

6.2 Data samples

The present analysis is based on the data collected by ALICE in January and February 2013 in p-Pb collisions at $\sqrt{s_{\mathrm{NN}}} = 5.02$ TeV. ALICE allows to study the J/ψ production down to zero transverse momentum p_{T} in two dilepton decay channels: dimuon at forward and dielectron at mid-rapidity (see more details in Section 4.2). This analysis is based on the dimuons measured by the ALICE muon spectrometer with an acceptance of $-4 < \eta_{\mathrm{lab}} < -2.5$ in the ALICE coordinate system (defined in Section 4.2). Two p-Pb beam configurations were provided by the LHC and analyzed. In the first configuration (p-Pb), beam 1 of protons was circulated towards the Muon spectrometer in the negative z direction (clockwise in LHC) while beam 2 of Pb ions was circulated in the positive z direction (counter clockwise). The second configuration (Pb-p) was obtained by inverting the beams 1 and 2. The first configuration allows to probe the forward rapidity region while the second one the backward rapidity region. Due to the beam energy asymmetry there is a shift in rapidity of $\Delta y = 0.465$ in the laboratory system towards the proton beam direction, leading to two asymmetric rapidity ranges of the muon spectrometer in the center-of-mass system: forward ($2.03 < y_{\mathrm{cms}} < 3.53$) and backward ($-4.46 < y_{\mathrm{cms}} < -2.96$)[1]. The following periods of data taking took place:

- MB trigger periods (LHC13b,c for p-Pb only) collecting MB data;
- Rare trigger periods (LHC13d,e for p-Pb and LHC13f for Pb-p) aiming to collect the rare events (e.g. events where a J/ψ is produced and decays into two muons).

[1]The sign of y in two beam configurations is defined with respect to the proton beam direction and is aimed to show that the two beam configurations probe different physics.

Standard quality checks for the detectors considered in the analysis (V0, SPD, ZDC, muon tracking and trigger chambers) have been applied to select the data.

Different triggers were activated during data taking. The Minimum Bias (MB) trigger is called CINT7. It is defined as the coincidence of a signal in VZERO-A and VZERO-C detectors synchronized with the passage of the colliding lead and proton bunches. During the rare trigger periods the MB trigger was downscaled at the L0 level of dimuon trigger to allow more DAQ bandwidth for rare triggers. For the muon part, the following triggers were used:

- Single muon low-p_{T} (where the p_{T} of a single muon ${p_{\mathrm{T}}}^{\mu} \geq 0.5$ GeV/c) or CMSL
- Single muon higt-p_{T} (${p_{\mathrm{T}}}^{\mu} \geq 4$ GeV/c) or CMSH
- Unlike sign dimuon low-p_{T} (${p_{\mathrm{T}}}^{\mu} \geq 0.5$ GeV/c on each muon) or CMUL
- Like sign dimuon low-p_{T} (${p_{\mathrm{T}}}^{\mu} \geq 0.5$ GeV/c on each muon) or CMLL

We define the corresponding L0 trigger inputs by replacing "C" with "0" in the beginning of the trigger name (i.e. 0MSL, 0MSH, 0MUL, 0MLL). The CMUL7 trigger used in the analysis is defined as the coincidence of 0MUL and CINT7. Timing cuts on the signals from the VZERO and from the ZDC were used to reduce the beam induced background. This physics selection (PS) removes from few percent up to 10% of the events depending on the run (and the beam configuration). In total, after applying the event physics selection, a data sample of 9.27 M collisions in p-Pb and 20.9 M collisions in Pb-p triggered by CMUL7 trigger were collected. The data sample comes only from the rare trigger samples since the luminosity was low in the MB sample resulting to a low number of J/ψ. The V0AND cross section (corresponding to the coincidence of V0A and V0C signals) is measured in van der Meer scans [195]: 2.09 b $\pm$ 3.2% (2.12 b $\pm$ 3.0%) in p-Pb (Pb-p). The normalization factors between CMUL7 and CINT7 trigger described in Section 6.6 allow to compute the total integrated luminosities of 5.01 ± 0.17 nb^{-1} in p-Pb and 5.81 ± 0.18 nb^{-1} in Pb-p. The two periods LHC13d and LHC13e with p-Pb configuration were considered together.

6.3 Event and track selection

In order to select a clean data sample, only events passing the physics selection cuts were kept. The analysis of the J/ψ decaying into two unlike sign muons required to select only CMUL7 triggered events. The standard

J/ψ analysis cuts on single muons and on the opposite-sign dimuons were applied:

- $2.5 < \eta_{\mu} < 4$ on both muons, to reject tracks at the edges of the spectrometer acceptance. An additional geometrical cut was added at the dimuon level: $2.5 < y_{\mu\mu} < 4$.
- both muon tracks reconstructed in the tracking chambers should match a trigger track reconstructed in the trigger system, above the low p_{T} threshold.
- $17.6 < R_{\mathrm{abs}} < 89.5$ cm, where R_{abs} is the radial transverse position of the muon tracks at the end of the absorber. This cut removes the tracks at the edge of the absorber.

6.4 Signal extraction

J/ψ candidates are obtained combining pairs of muons of opposite charge reconstructed within the geometrical acceptance of the spectrometer. Most of the hadrons escaping or produced in the front absorber, single muons, low p_{T} muons from pions and kaons decays, secondary muons produced in the front absorber and fake tracks are removed by the cuts described above.

The J/ψ raw yield is then extracted using a fit to the invariant mass spectrum. The fitting function is a superposition of a signal and a background shapes. Three functions were used for modeling the signal shape: an extended Crystal Ball (CB2) function (allowing a non gaussian tail both on the right and left side of the resonance peak), "NA60 function" (a gaussian with a fixed width core around the J/ψ pole and mass dependent widths on the right and on the left side of it) [127] and NA60CB2 function merging the left tail of NA60 and the right tail of CB2 functions. Given a poor Signal-to-Background ratio in the tail region, it is not possible to fix the tails of these signal shapes directly by fitting the data. Therefore, the signal shape parameters are tuned on the J/ψ from MC simulations and then fixed in the fit procedure to the invariant mass spectra. In particular, parameters are tuned in each kinematic interval under study. As an example, in Fig.6.1,6.2,6.3, the CB2, the NA60 and the mixed NA60CB2 fits to the MC results are shown.

Even if the region around the peak, corresponding to the core of the J/ψ statistics, is well described by all the functions, the CB2 function does not properly describe the left part of the J/ψ mass distribution. The agreement improves when the NA60 function is used. The mixed NA60CB2 function still improves the description of the right tail of the mass spectra, in particular when high-p_{T} J/ψ are studied. The only signal parameters which are kept free in the final fit are the J/ψ mass, width and absolute normalization.

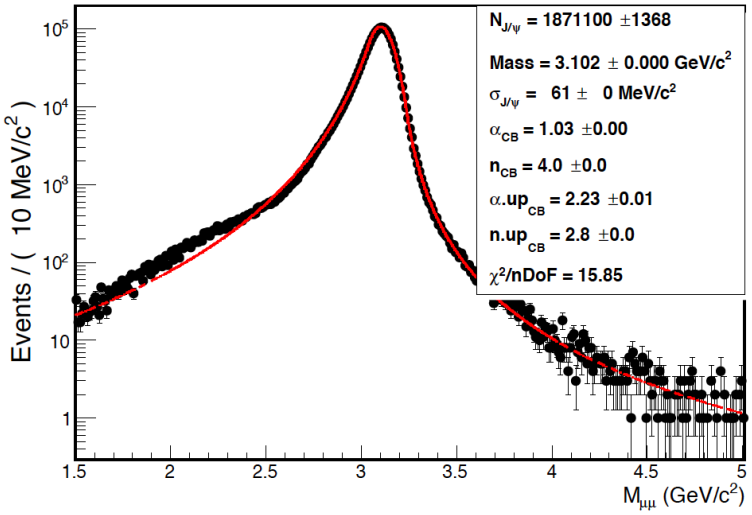

Figure 6.1. Fit to the J/ψ MC invariant mass spectra with the CB2 function.

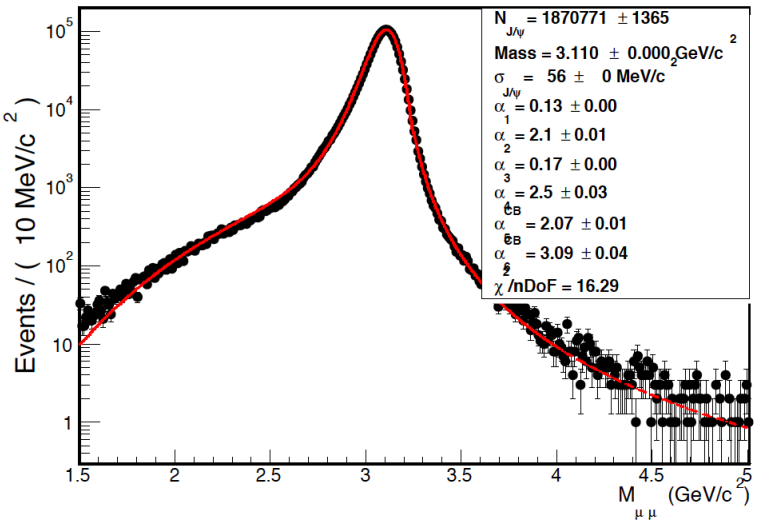

Figure 6.2. Fit to the J/ψ MC invariant mass spectra with the NA60 function.

The background is described with three functions: a variable width gaussian function (VWG) and an exponential function (Exp) multiplied by 2^{nd} or 4^{th} order polynomials (Pol2, Pol4). Background parameters are given by the fit to the invariant mass spectrum. The ψ(2S) resonance is also included in the fitting procedure. Given the low signal to background ratio for the ψ(2S) ,

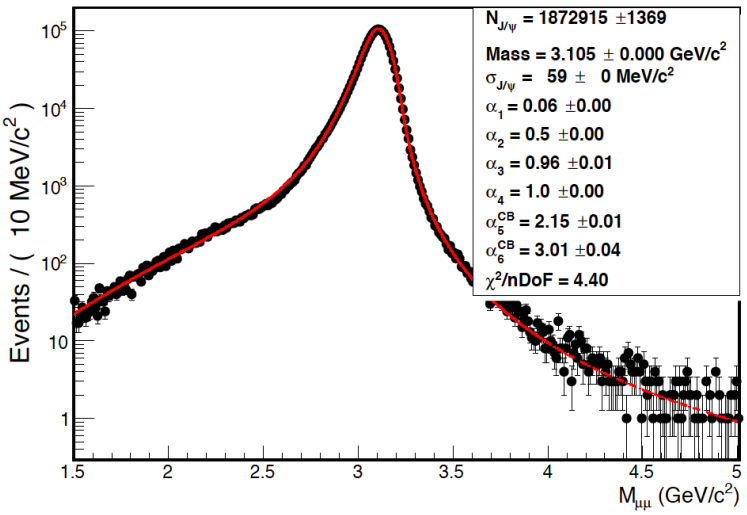

Figure 6.3. Fit to the J/ψ MC invariant mass spectra with the NA60CB2 function.

its mass $m_{\psi(2S)}$ and the width $\sigma_{\psi(2S)}$ are bound to the J/ψ ones as follows:

$$m_{\psi(2S)} = m_{\mathrm{J}/\psi} + \left(m^{\mathrm{PDG}}_{\psi(2S)} - m^{\mathrm{PDG}}_{\mathrm{J}/\psi}\right); \quad \sigma_{\psi(2S)} = \sigma_{\mathrm{J}/\psi} \times \left(\frac{m^{\mathrm{PDG}}_{\psi(2S)}}{m^{\mathrm{PDG}}_{\mathrm{J}/\psi}}\right), \qquad (6.5)$$

where PDG stands for Particle Data Group values [194]. An approach with the ψ(2S) width bound to the J/ψ one by the ratio of the σ obtained in the MC, have been tested and has shown a negligible influence on the J/ψ signal extraction. The other ψ(2S) parameters are fixed to the J/ψ ones.

Two independent analyses have been performed with the following tests:

- CB2 or NA60CB2 signal shape combined with VWG or Pol2 × Exp for the background, using a fitting range 2-5 (GeV/c)^2 or 2.3-4.7 (GeV/c)^2;
- CB2 or NA60 signal shape combined with VWG or Pol4 × Exp for the background, using a fitting range 2-5 (GeV/c)^2 or 2.2-4.5 (GeV/c)^2.

Both analyses give very similar results at each step.

For all the periods of data taking under study, the J/ψ mass position $m_{\mathrm{J}/\psi} = 3.098 \pm 0.001$(GeV/$c$)^2 is in very good agreement with the PDG value and the J/ψ width is ∼70 MeV/c^2. The signal to background ratio in the invariant mass range of $m_{\mathrm{J}/\psi} \pm 3\sigma$ is ≥2 for all the periods, for the p_{T} and y integrated spectrum. The invariant mass spectra, corresponding to the total statistics collected in the Pb-p and p-Pb, are shown in Fig.6.4.

As it was mentioned above, the J/ψ raw yields have been extracted by varying the signal and background shape as well as the fitting range. The

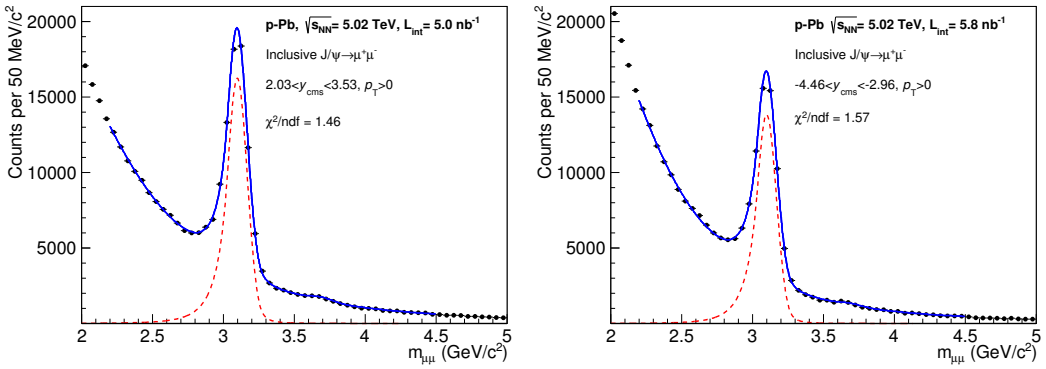

Figure 6.4. An example of a fit to the invariant mass spectra corresponding to LHC13d+e (left) and LHC13f (right) periods. The invariant mass spectra correspond to the total collected statistics (integrated over p_{T} and rapidity).

weighted average of all the obtained results provide the final results. The RMS of the raw yield distributions provides the systematic uncertainty on the signal extraction. In Fig. 6.5 an example of the J/ψ raw yields extraction for the LHC13d+e and LHC13f periods as a function of the tests is shown.

The average J/ψ raw yields obtained for the two periods are reported in Table 6.1, together with the statistical and systematic uncertainties. The procedure is repeated to extract the J/ψ yield in each kinematic range under study, tuning the tails of the signal function on the corresponding MC simulations.

Table 6.1. J/ψ raw yields for the total collected statistics of the LHC13d+e and LHC13f periods. The first uncertainty represents the statistical one, while the second denotes the systematic one. The quoted systematic uncertainty is related only to the signal extraction.

Period	J/ψ raw yield
LHC13d+e	$66948 \pm 486 \pm 844$
LHC13f	$56749 \pm 451 \pm 662$

For the rapidity dependence measurements, 6 intervals are considered in the $2.5 \leq y_{\mathrm{lab}} \leq 4$ range. Signal-to-background ratio estimated in a 3σ interval around the J/ψ mass peak does not go below 1.4, providing a clear visible J/ψ signal in all the intervals under study. The number of J/ψ varies from ∼2000-4000 at the edges of the y range to ∼15000 at $|y| \sim 3.25$. See Appendix A for details.

In order to study the Forward-to-Backward ratio R_{FB}, the J/ψ raw yields are extracted in the y range common to p-Pb and Pb-p, i.e. $2.96 \leq y_{\mathrm{cms}} \leq 3.53$.

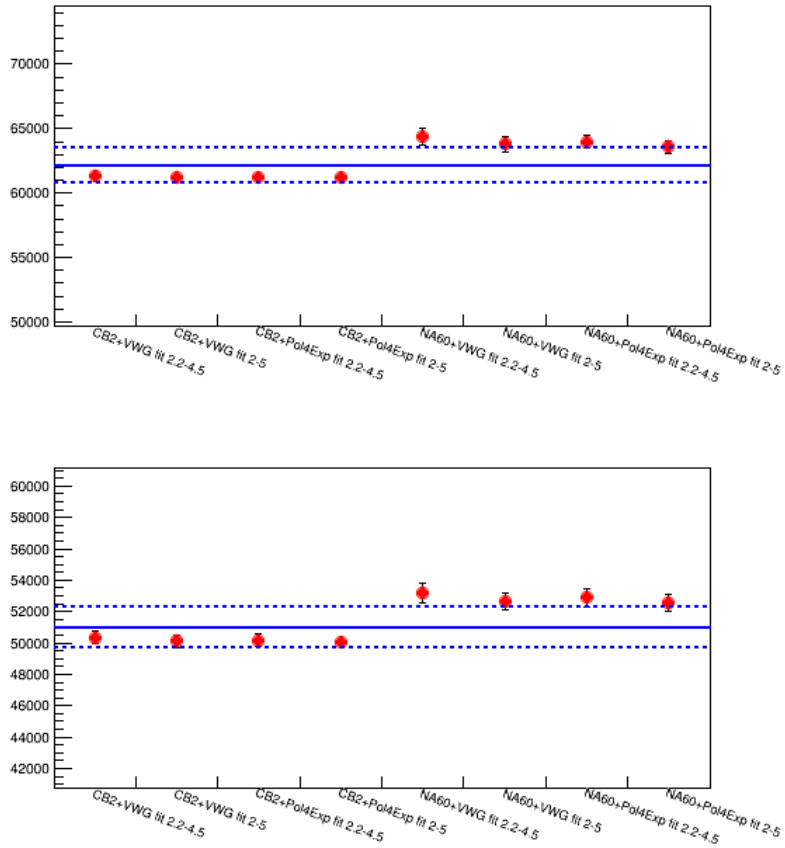

Figure 6.5. J/ψ raw yield as a function of the signal extraction tests for LHC13d+e (top panel) and LHC13f (bottom panel).

The average raw yields, obtained for the LHC13d+e and LHC13f periods, and the associated uncertainties are reported in Table 6.2.

The systematic uncertainty on the signal extraction is computed directly on the ratio of the forward to backward raw yields. The same tests as mentioned above have been performed. The signal function was assumed to be the same for both p-Pb and Pb-p. The fitting range was also varied for forward and backward data simultaneously. The only independently varied option in those tests was the background shape. An example of the raw yield ratio as a function of the tests is shown in Fig.6.6.

The R_{FB} ratio is studied in y and p_{T} intervals. In this case the tail parameters of the fit are also tuned in each kinematic bin. For the differential study versus p_{T}, 15 intervals were analyzed in the $0 \leq p_{\mathrm{T}} \leq 15$ GeV/c range. The number of J/ψ varies between 4000-5000 around $p_{\mathrm{T}}\sim$ 2 GeV, where the

Table 6.2. J/ψ raw yields (LHC13d+LHC13e and LHC13f periods) with statistical (first) and systematic (second) uncertainties corresponding to the y range used for the R_{FB} study, i.e. 2.96$\leq y_{\rm cms} \leq$3.53

Period	J/ψ yield
LHC13d+e	$17913 \pm 216 \pm 203$
LHC13f	$22411 \pm 312 \pm 361$

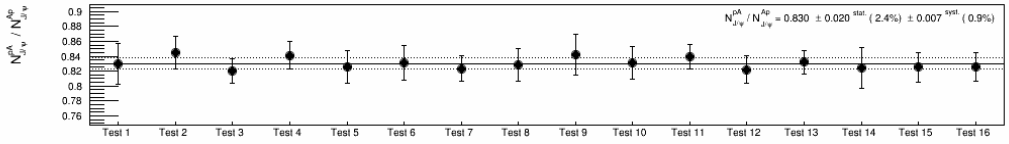

Figure 6.6. Forward to backward ratio of the J/ψ raw yields as a function of the signal extraction tests.

bulk of the J/ψ production is, to $\sim$ 150 in the highest $p_{\rm T}$ bin. In the last bin ($10 \leq p_{\rm T} \leq 15$ GeV/c) where the statistics is low, the J/ψ peak is clearly visible thanks to the higher signal to background ratio. For the study of $R_{\rm FB}$ versus y (where three intervals were analyzed), the average J/ψ raw yield decreases from $\sim$10000 to $\sim$2000 moving towards the edges of the muon spectrometer acceptance.

6.5 Acceptance and efficiency corrections

In order to estimate the invariant yields, the raw yields have to be corrected by the detector acceptance and efficiency ($A\epsilon$). A run-per-run simulation was performed using a pure signal parametrization reproducing the measured J/ψ kinematical $p_{\rm T}$ and y distributions. A small or zero J/ψ polarization is suggested by the recent measurement at the LHC [197–199].

In the p-Pb and Pb-p data taking periods, occupancy in the detector was small and no deterioration of the muon tracking chamber efficiency was observed even for the most central events, justifying the use of pure signal simulations [200].

The simulations were performed in a run-per-run basis with a number of events generated proportional to the number of unlike-sign dimuon triggers after the physics selection. Fig. 6.7 shows the $A\epsilon$ correction as a function of the run number for LHC13d+e (left plot) and LHC13f (right plot). At the end of each period, an increasing number of hardware issues in the tracking

chambers (mainly HV trips) lead to a decrease of the tracking efficiency. As a consequence, lower $A\epsilon$ are obtained.

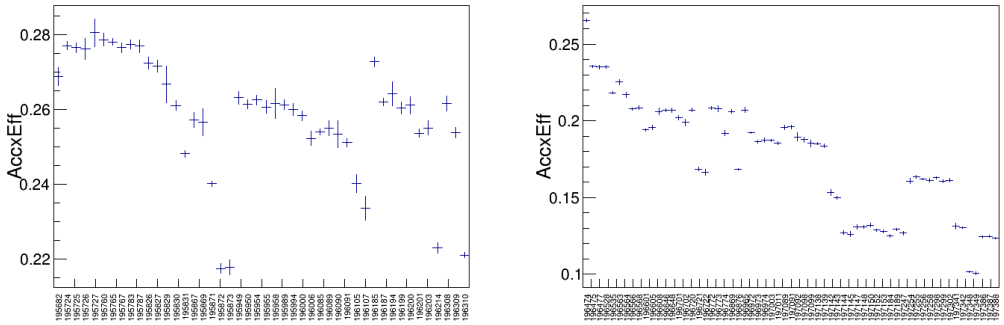

Figure 6.7. Integrated $A\epsilon$ (Acc×Eff) correction as a function of the run number in p-Pb (left) and Pb-p (right).

The p_{T} and y input distributions of the generated J/ψ were tuned directly on the J/ψ raw yield extracted from the data. Starting from a generator based on a parametrization of the J/ψ production in pp collisions at $\sqrt{s} = 5.02$ TeV, a single iteration over the corrected data allowed to describe the measured p_{T} and y distribution within 10% accuracy as shown in Fig. 6.8 for LHC13d+e.

The integrated $A\epsilon$ is approximately $(25.4 \pm 1.3)\%$ and $(17.1 \pm 1.2)\%$ for the periods LHC13de and LHC13f, respectively. The quoted uncertainty is systematic (see Section 6.8.3). The lower value for LHC13f is mainly due to a smaller detector efficiency. Fig.6.9 shows the y (left panel) and p_{T} (right panel) dependences of $A\epsilon$ for the two periods of data taking.

6.6 Dimuon trigger event normalization

In order to estimate the invariant yields, the number of MB events is needed. There are three methods to estimate the equivalent number of MB events from the measured number of opposite-sign dimuon triggers in the rare trigger periods. We will discuss them below, but first we define pile-up effect which is common to all the three methods.

6.6.1 Pile-up effect

The pile-up (PU) events are the events with more than one inelastic collision. PU effect, denoted as $\mathrm{F}_{\mathrm{pile-up}}$, is defined as the ratio of number of real MB events to the number of triggered MB events.

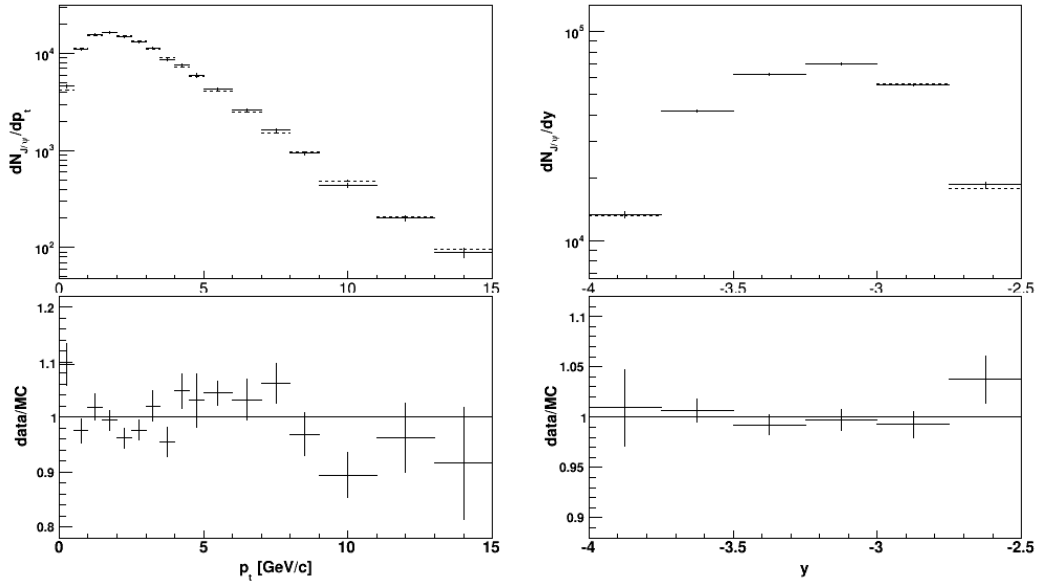

Figure 6.8. Raw distributions for extracted J/ψ as a function of p_{T} (left panel) and rapidity (right panel) for data (full line) and simulation (dashed line) in LHC13de.

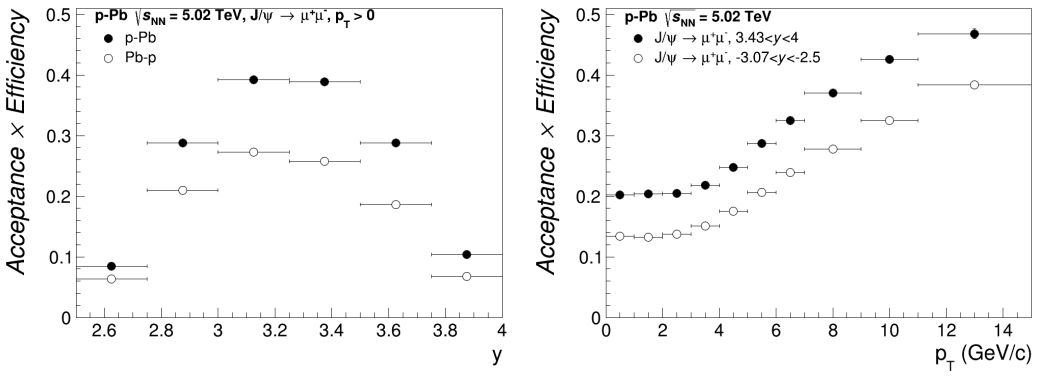

Figure 6.9. Differential $A\epsilon$ correction as a function of y and integrated over p_{T} (left panel) and as a function of p_{T} for different y range (right panel) for p-Pb (full points) and Pb-p (open points).

Assuming that the number of inelastic collisions per bunch crossing follows a Poisson distribution, the probability of an event with N inelastic collisions is found as:

$$P^i(N) = \frac{(\mu^i)^N e^{-\mu^i}}{N!}, \tag{6.6}$$

with μ as the mean number of collisions per bunch crossing:

$$\mu^i = -ln\left(1 - \frac{\mathrm{PS}^i_{\mathrm{CINT7}} \times L0bRate^i_{\mathrm{CINT7}}}{N^i_{\mathrm{colliding}} \times f_{\mathrm{LHC}}}\right), \tag{6.7}$$

where $\mathrm{PS}_{\mathrm{CINT7}}$ denotes the fraction of good MB events selected by the physics selection on recorded events, $N_{\mathrm{colliding}}$ is the number of colliding bunches and $f_{\mathrm{LHC}} = 11245$ Hz, the LHC revolution frequency. It was assumed that the physics selection effect, i.e. the fraction of good MB events does not depend on the trigger veto at the L0 level.

Then the MB event correspond to the probability of having at least one collision in run i is equal to:

$$P^i(N \geq 1) = 1 - P^i(0) = 1 - e^{-\mu^i}, \tag{6.8}$$

and the pile-up probability is found as:

$$P^i(N \geq 2) = P^i(N \geq 1) - P^i(1) = 1 - e^{-\mu^i} - \mu^i e^{-\mu^i}. \tag{6.9}$$

The pile-up correction factor $\mathrm{F}_{\mathrm{pile-up}}$ defined above is obtained as follows:

$$F^i_{pile-up} = \frac{\mu^i}{P^i(N \geq 1)} = \frac{\mu^i}{1 - e^{-\mu^i}} \tag{6.10}$$

6.6.2 1st method ("naive offline method")

The equivalent number of MB (CINT7) events can be estimated from the number of dimuon (CMUL7) triggered events for each run, i, through the normalization factor F^i_{norm}:

$$F^i_{\mathrm{norm}} = \frac{\mathrm{MB}^i}{\mathrm{MB}^i\&0\mathrm{MUL}} \times \mathrm{F}^i_{\mathrm{pile-up}} \tag{6.11}$$

where for each run i, MB is the number of good (i.e. physics selected) MB events, MB&0MUL the number of MB events which have in addition the 0MUL L0 trigger input present. The ratio F^i_{norm} is computed offline.

The CMUL trigger, as well as CINT7, is affected by beam-gas tracks, whose amount varies from run to run. The F_{norm} ratio thus should be computed run by run. However the limited CINT7 statistics due to the downscaling of this trigger in the rare trigger periods results in a non-negligible statistical uncertainty for the ratio (FnormOffline1PUPS in Fig. 6.10).

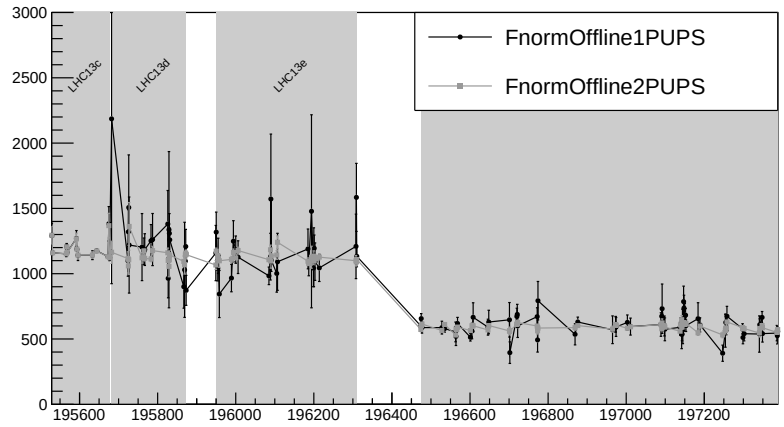

Figure 6.10. Evolution of F_{norm} computed using the two offline methods (FnormOffline1PUPS for the 1st method and FnormOffline2PUPS for the 2nd method). The two-steps method (FnormOffline2PUPS) decreases the statistical uncertainty.

6.6.3 2nd method ("offline method")

To improve the statistical uncertainty on the ratio F_{norm} a two steps method can be applied, using a trigger condition that has a large statistic within the cluster CINT7. The single low p_{T} muon trigger input (0MSL) can be used for that:

$$F^{i}_{\text{norm}} = \frac{\text{CMSL}^{i}}{(\text{CMSL\&0MUL})^{i}} \times \frac{\text{CINT7}^{i}}{(\text{CINT7\&0MSL})^{i}} \times \text{F}^{i}_{\text{pile-up}} \tag{6.12}$$

It allows to decrease the statistical uncertainty (Fig. 6.10), but it is still not optimal.

6.6.4 3rd method ("scalers method")

Another way to calculate F_{norm} is based on the L0b trigger scalers[1] where the statistics is huge. In that case, at first order :

$$F^i_{\mathrm{norm}} = \frac{\mathrm{L0b(CINT7)}^i}{\mathrm{L0b(CMUL7)}^i} \tag{6.13}$$

This factor is corrected by the physics selection (PS) on both triggers (CINT7 and CMUL) and by the PU effect $\mathrm{F_{pile-up}}$ (Fig. 6.11):

$$F^i_{\mathrm{norm}} = \frac{\mathrm{L0b(CINT7)}^i \times \mathrm{PS}^i_{\mathrm{CINT7}} \times \mathrm{F}^i_{\mathrm{pile-up}}}{\mathrm{L0b(CMUL7)}^i \times \mathrm{PS}^i_{\mathrm{CMUL7}}}. \tag{6.14}$$

The corrections due to PS and PU are small (Tab.6.3). The PS effect is very similar for both CINT7 and CMUL7 triggers resulting in a small ratio $\frac{\mathrm{PS_{CINT7}}}{\mathrm{PS_{CMUL7}}}$. The PU factor has a slightly bigger effect. The global correction factor is then 1.02 for p-Pb and 1.04 for Pb-p.

Period	$\mathrm{PS_{CINT7}}$	$\mathrm{PS_{CMUL7}}$	$\frac{\mathrm{PS_{CINT7}}}{\mathrm{PS_{CMUL7}}}$	$\mathrm{F_{pile-up}}$	$\frac{\mathrm{PS_{CINT7}}}{\mathrm{PS_{CMUL7}}}\mathrm{F_{pile-up}}$
LHC13de	0.997±0.001	0.996±0.001	1.001±0.001	1.020±0.001	1.022 ± 0.001
LHC13f	0.999±0.001	0.981±0.001	1.017±0.001	1.023±0.001	1.041 ± 0.002

Table 6.3. Correction factors used in the computation of F_{norm} using the scalers method.

6.6.5 Final estimation of F_{norm}

In the previous chapter, it was shown that F_{norm} needs to be calculated run per run. When considering the whole period, F_{norm} was obtained as a weighted average of the run-by-run normalization factor, with the number of CMUL7 taken as a weight for each run:

$$F_{\mathrm{norm}} = \frac{\sum_{i=1}^{\mathrm{nruns}} F^i_{\mathrm{norm}} \times N^i_{\mathrm{CMUL7}}}{\sum_{i=1}^{nruns} N^i_{\mathrm{CMUL7}}} \tag{6.15}$$

[1]There are six trigger class counters: L0b, L0a, L1b, L1a, L2b and L2a, where "b" and "a" stand for "before" and "after" veto. In particular, L0b gives the number of times a given trigger class is fired, and L2a gives the number of times the same trigger class passes the CTP and detector dead-time, as well as any other possible veto. These counters are measured online and can be retrieved off-line for each run [201].

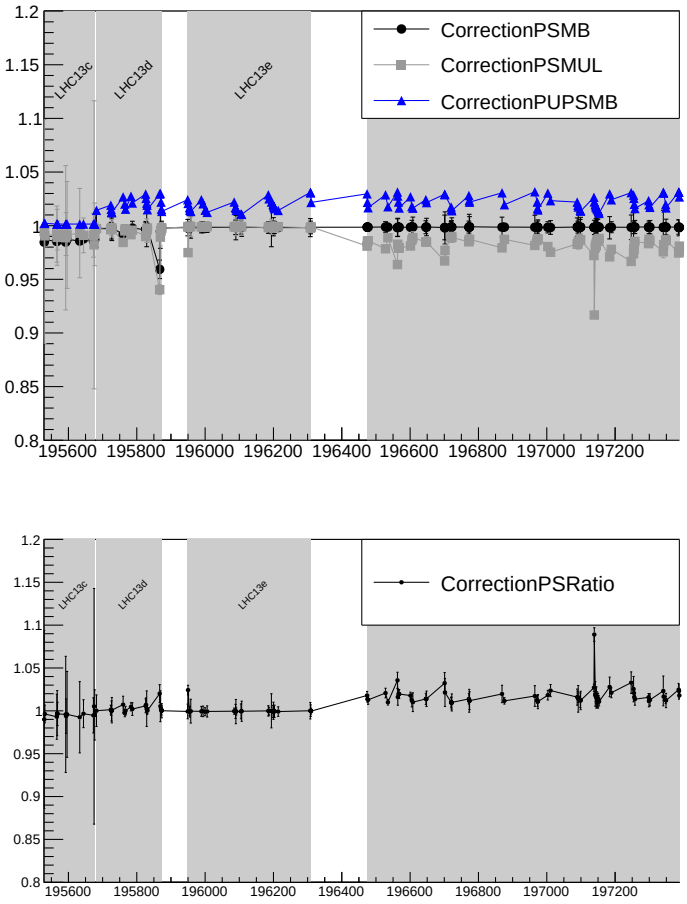

Figure 6.11. Correction factors used in the computation of F_{norm} in the scalers method. CorrectionPSMB corresponds to the factor $\text{PS}^i_{\text{CINT7}}$, CorrectionPSMUL is $\text{PS}^i_{\text{CMUL7}}$, CorrectionPUPSMB represents $\text{PS}^i_{\text{CINT7}} \times \text{F}^i_{\text{pile-up}}$ and CorrectionPSratio shows the $\frac{\text{PS}^i_{\text{CINT7}}}{\text{PS}^i_{\text{CMUL7}}}$ ratio from (6.14).

Period	$\text{F}^{\text{Offline2PUPS}}_{\text{norm}}$	$\text{F}^{\text{ScalersPUPS}}_{\text{norm}}$	Offline-Scalers relative difference (%)	F_{norm}
LHC13de	1124.00 ± 4.99	1129.33 ± 1.71	0.55 ± 0.41	1129.08 ± 1.75
LHC13f	588.52 ± 2.65	589.48 ± 2.33	0.19 ± 0.22	589.31 ± 2.34

Table 6.4. F_{norm} values for different periods and the two different methods of computation.

The run-by-run variation of the F^{i}_{norm} factor computed using the two methods (the 2nd and 3rd method described in this chapter) reaches 14% in some runs (Fig. 6.12). However these runs contribute to a small fraction of the total number of analyzed events. At the level of the global F_{norm} the difference is less than 1% (third column of Tab. 6.4). The central value is taken as the weighted (by their error) average of the two methods (last column of Tab.6.4). A systematic uncertainty of 1% is considered on the F_{norm} ratio. It includes the difference between the two methods.

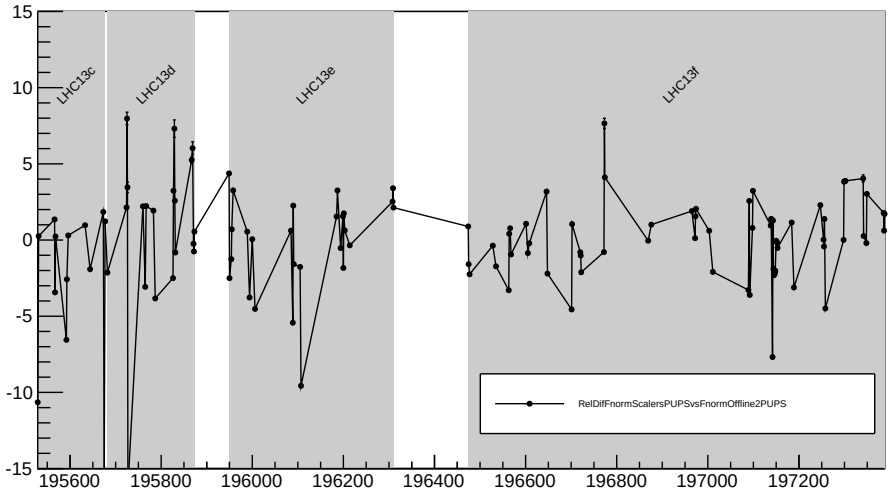

Figure 6.12. Run-by-run evolution of the relative difference (in percentage) between the offline and scalers methods.

6.7 pp reference at $\sqrt{s} = 5.02$ TeV

The pp J/ψ cross section (pp reference) at $\sqrt{s} = 5.02$ TeV is needed for the evaluation of the nuclear modification factor R_{pPb} defined in (7.1). Since $\sigma^{\mathrm{J}/\psi}_{\mathrm{pp}}$ is not measured at $\sqrt{s_{\mathrm{NN}}} = 5.02$ TeV, an energy interpolation procedure described in [202] was applied. In this approach only the pp ALICE data in the forward rapidity region $2.5 < y_{\mathrm{cms}} < 4$ have been used[1]. This is a two-step procedure:

[1]For the preliminary results [203] the pp reference was based on a different approach, where all the available results obtained at several energies and at different rapidity were used [204].

- **Energy interpolation:** existing ALICE pp results at $\sqrt{s} = 2.76$ TeV [205] and at $\sqrt{s} = 7$ TeV [206] in $2.5 < y_{\rm cms} < 4$, $0 < p_{\rm T} < 8$ GeV/c, were interpolated with empirical shapes (linear, power law and exponential) in six rapidity bins with $\Delta y = 0.25$.

- **Rapidity extrapolation:** due to the y-shift in p-Pb, the results from the previous step were fitted with empirical shapes (gaussian, polynomial) to reach the measured rapidity coverage at $\sqrt{s} = 5.02$ TeV.

6.7.1 Energy interpolation for $2.5 < y_{\rm cms} < 4$

The illustration of the energy interpolation procedure in the full rapidity range $2.5 < y_{\rm cms} < 4$ is shown in Fig.6.13. Red points corresponds to the existing pp measurements while the blue one is the interpolated value. Lines correspond to different empirical shapes used for the interpolation. A least mean squares method was used for the estimation of the uncertainties from the fit. The uncertainties in the fit procedure are the quadratic sum of statistical and uncorrelated systematic uncertainties. A 5% correlated uncertainty between the $\sqrt{s} = 2.76$ TeV and $\sqrt{s} = 7$ TeV ALICE data points was added in quadrature to the uncertainty from the interpolation result. This 5% correlated uncertainty corresponds to a combination of uncertainties on tracking and triggering efficiency, and to the uncertainty on the branching ratio of the J/ψ decay to two muons. The final value of the interpolated cross section is found as a weighted average of the interpolated results with the three different fitting functions. The weights are the inverse of the variances of the individual points. An additional 0.10 μb uncertainty corresponds to the maximum deviation of the individual fits from the average value. The uncertainty of the interpolated cross section at $\sqrt{s} = 5.02$ TeV is then 7.9%. The corresponding results are shown in Table 6.5.

Fitting function shape	Cross-section, μb
linear	5.17 ± 0.41
power law	5.26 ± 0.40
exponential	5.38 ± 0.40
weighted average	$5.28 \pm 0.40 \pm 0.10$

Table 6.5. The interpolation of cross section at $\sqrt{s} = 5.02$ TeV with empirical shapes. See text for details.

A small additional systematic uncertainty was found from the comparison of the empirical shapes to those calculated with the LO CEM [207] and

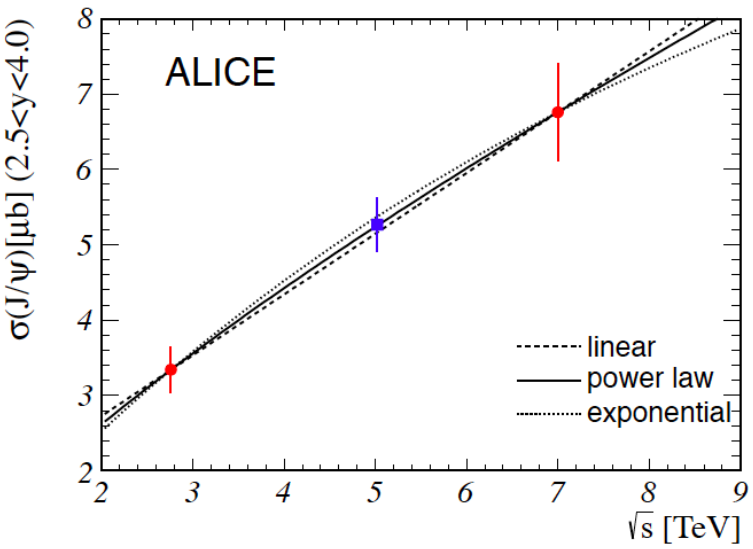

Figure 6.13. pp cross section interpolation procedure.The blue point at $\sqrt{s}$ = 5.02 TeV is the result of this procedure. The error bar represents the error propagation of the experimental uncertainties from the measurements at $\sqrt{s}$ = 2.76 TeV and $\sqrt{s}$ = 7 TeV. From [202].

FONLL[1] [190] models (Fig.6.14). The predicted cross section is taken as the average of the models that describe the data. The CEM gives $\sigma(5.02\ \mathrm{TeV}) = 5.29 \pm 0.10\ \mu$b, while FONLL provides $\sigma(5.02\ \mathrm{TeV}) = 5.32 \pm 0.02\ \mu$b, where the uncertainty corresponds to the RMS of the corresponding fit results. Both values of the cross section are in agreement with the weighted average from Table 6.5. The maximum deviation of the LO CEM and FONLL results from the weighted average in Table 6.5, was conservatively taken as an additional systematic uncertainty. Finally, the interpolated inclusive J/ψ cross section at $\sqrt{s} = 5.02$ TeV in $2.5 < y_{\mathrm{cms}} < 4$ was found as: $\sigma^{\mathrm{J}/\psi}_{\mathrm{pPb}}|_{\sqrt{s}=5.02\ \mathrm{TeV}} = 5.28 \pm 0.40(\mathrm{exp.}) \pm 0.10(\mathrm{interp.}) \pm 0.05(\mathrm{theor.})\ \mu\mathrm{b} = 5.28 \pm 0.42\ \mu\mathrm{b}$.

6.7.2 Energy interpolation for different rapidity bins

The procedure described above was repeated for smaller rapidity bins obtained by dividing the full rapidity range $2.5 < y_{\mathrm{cms}} < 4$ in six equal intervals. The result of this procedure is illustrated in Fig.6.15, and numerical values are given in Table 6.6.

[1]FONLL predicts the $c\bar{c}$ cross-sections, not the J/ψ cross-section.

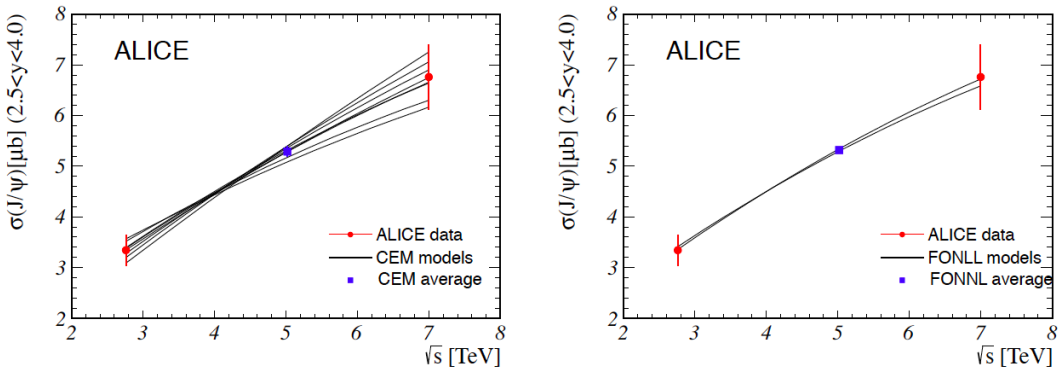

Figure 6.14. Interpolation of the J/ψ cross section at $\sqrt{s} = 5.02$ TeV using theoretical predictions of LO CEM [207] and FONLL [190]. From [202].

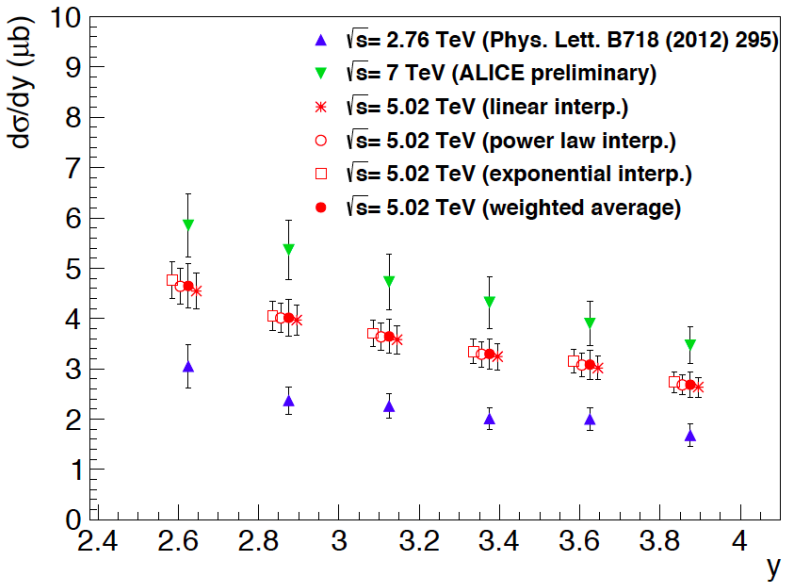

Figure 6.15. The energy interpolation of $\frac{d\sigma}{dy}|_{\sqrt{s}=5.02\ \text{TeV}}$. See text for details. From [202].

6.7.3 Rapidity extrapolation

Since the backward ($-4.46 < y_{\text{cms}} < -2.96$) and forward ($2.03 < y_{\text{cms}} < 3.53$) rapidity ranges in p-Pb collisions are not equal to the y range of the interpolated results at $2.5 < y_{\text{lab}} < 4$ (see Section 6.2) an extrapolation of the rapidity dependence of the J/ψ cross section $\frac{d\sigma}{dy}|_{\sqrt{s}=5.02\ \text{TeV}}$ is needed.

To extrapolate the J/ψ cross section to the rapidity ranges not covered by the ALICE pp measurements, three empirical shapes were used to describe

$y_{\rm cms}$ range	$\frac{{\rm d}\sigma}{{\rm d}y}\vert_{\sqrt{s}=2.76\ {\rm TeV}}$, μb	$\frac{{\rm d}\sigma}{{\rm d}y}\vert_{\sqrt{s}=7\ {\rm TeV}}$, μb	$\frac{{\rm d}\sigma}{{\rm d}y}\vert_{\sqrt{s}=5.02\ {\rm TeV}}$, μb
$2.50 < y_{\rm cms} < 3.75$	$3.05 \pm 0.35 \pm 0.25$	$5.85 \pm 0.13 \pm 0.61$	$4.65 \pm 0.43 \pm 0.12$
$2.75 < y_{\rm cms} < 3.00$	$2.37 \pm 0.19 \pm 0.19$	$5.37 \pm 0.06 \pm 0.59$	$4.01 \pm 0.36 \pm 0.04$
$3.00 < y_{\rm cms} < 3.25$	$2.26 \pm 0.15 \pm 0.18$	$4.73 \pm 0.05 \pm 0.55$	$3.64 \pm 0.33 \pm 0.06$
$3.25 < y_{\rm cms} < 3.50$	$2.01 \pm 0.14 \pm 0.16$	$4.32 \pm 0.05 \pm 0.51$	$3.29 \pm 0.30 \pm 0.05$
$3.50 < y_{\rm cms} < 3.75$	$2.00 \pm 0.16 \pm 0.16$	$3.90 \pm 0.05 \pm 0.44$	$3.08 \pm 0.28 \pm 0.07$
$3.75 < y_{\rm cms} < 4.00$	$1.68 \pm 0.19 \pm 0.13$	$3.47 \pm 0.08 \pm 0.35$	$2.68 \pm 0.24 \pm 0.05$

Table 6.6. The interpolation of $\frac{{\rm d}\sigma}{{\rm d}y}\vert_{\sqrt{s}=5.02\ {\rm TeV}}$ in six rapidity intervals in the range $2.5 < y_{\rm cms} < 4$. See text for details.

Table 6.7. ${\rm d}\sigma/dy$ in the p-Pb y-range. The 1$^{\rm st}$ uncertainty is uncorrelated in rapidity and comes from the first step of the interpolation procedure; the 2$^{\rm nd}$ one is the y-correlated uncertainty, the 3$^{\rm rd}$ one is related to the maximum spread between results obtained with the three interpolating functions. The 4$^{\rm th}$ uncertainty represents the theory-related contribution.

$y_{\rm cms}$ range	${\rm d}\sigma/dy$ (μb)
$2.03 < y_{\rm cms} < 2.28$	$4.72 \pm 0.28 \pm 0.26 \pm 0.42 \pm 0.12$
$2.28 < y_{\rm cms} < 2.53$	$4.53 \pm 0.25 \pm 0.25 \pm 0.24 \pm 0.11$
$2.53 < y_{\rm cms} < 2.78$	$4.30 \pm 0.20 \pm 0.23 \pm 0.11 \pm 0.04$
$2.78 < y_{\rm cms} < 3.03$	$4.02 \pm 0.16 \pm 0.22 \pm 0.01 \pm 0.11$
$3.03 < y_{\rm cms} < 3.28$	$3.70 \pm 0.12 \pm 0.20 \pm 0.04 \pm 0.09$
$3.28 < y_{\rm cms} < 3.53$	$3.36 \pm 0.10 \pm 0.18 \pm 0.06 \pm 0.08$
$2.03 < y_{\rm cms} < 3.53$	$4.12 \pm 0.18 \pm 0.23 \pm 0.11 \pm 0.10$
$-3.21 < y_{\rm cms} < -2.96$	$3.81 \pm 0.13 \pm 0.21 \pm 0.03 \pm 0.09$
$-3.46 < y_{\rm cms} < -3.21$	$3.47 \pm 0.11 \pm 0.19 \pm 0.06 \pm 0.09$
$-3.71 < y_{\rm cms} < -3.46$	$3.11 \pm 0.11 \pm 0.17 \pm 0.04 \pm 0.03$
$-3.96 < y_{\rm cms} < -3.71$	$2.70 \pm 0.15 \pm 0.15 \pm 0.02 \pm 0.03$
$-4.21 < y_{\rm cms} < -3.96$	$2.30 \pm 0.21 \pm 0.13 \pm 0.10 \pm 0.06$
$-4.46 < y_{\rm cms} < -4.21$	$1.95 \pm 0.26 \pm 0.11 \pm 0.15 \pm 0.05$
$-4.46 < y_{\rm cms} < -2.96$	$2.86 \pm 0.13 \pm 0.16 \pm 0.05 \pm 0.07$

the $\frac{{\rm d}\sigma}{{\rm d}y}\vert_{\sqrt{s}=5.02\ {\rm TeV}}$ rapidity dependence: gaussian, 2$^{\rm nd}$ and 4$^{\rm th}$ order polynomial [181]. This procedure is illustrated in Fig.6.16. In these fits only the statistical and the y-uncorrelated systematic uncertainties of $\frac{{\rm d}\sigma}{{\rm d}y}\vert_{\sqrt{s}=5.02\ {\rm TeV}}$

were taken into account. A 5.4% y-correlated uncertainty[1] was then added in quadrature to the uncertainties of each fit. The final values are taken as the average of the results of the three fits. Table 6.7 gives the results for the backward ($-4.46 < y_{\rm cms} < -2.96$) and forward ($2.03 < y_{\rm cms} < 3.53$) rapidity ranges.

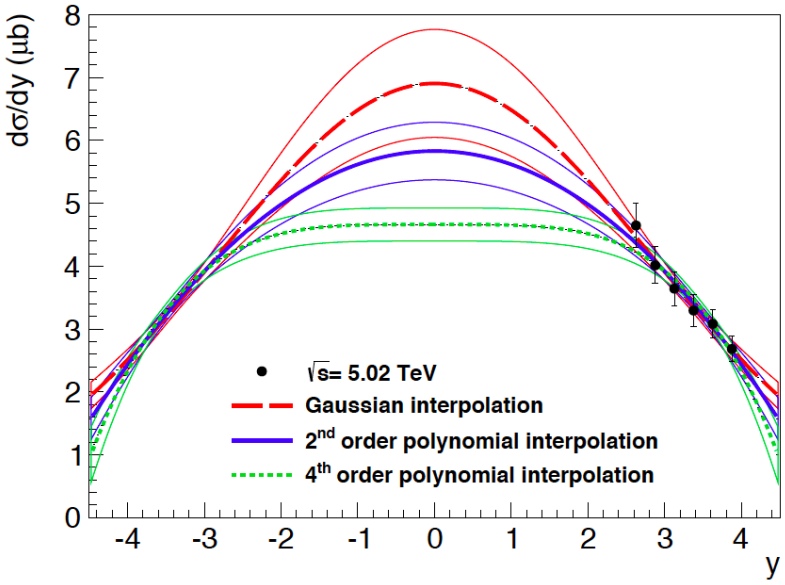

Figure 6.16. The rapidity extrapolation of $\frac{{\rm d}\sigma}{{\rm d}y}|_{\sqrt{s}=5.02\ {\rm TeV}}$. See text for details. From [202].

6.8 Systematic uncertainties

6.8.1 Signal extraction

As discussed in Section 6.4, the J/ψ raw yields have been estimated with different functions. The weighted average of the raw yields extracted in the different tests provides the final J/ψ raw yields. The RMS of the raw yield distributions gives the systematic uncertainty on the signal extraction. This systematic uncertainty is of the order of $\sim 1\%$ on the integrated J/ψ raw yields both in p-Pb and in Pb-p. When the raw yields are extracted in rapidity intervals the uncertainties reach 2-4%.

[1]This uncertainty is a quadratic sum of two sources from the first step of the interpolation procedure: 1) a 5% uncertainty corresponding to $\sqrt{s}$ -correlated uncertainty; 2) a 2% uncertainty related to the average spread of the values obtained with different fitting functions (linear, power law or exponential).

For the $R_{\rm FB}$ studies, the systematics on the signal extraction are evaluated directly on the ratio between the J/ψ collected in Pb-p and p-Pb (see an example in Fig.6.6). For the integrated $R_{\rm FB}$ the systematic uncertainty on the signal extraction is $\sim 1\%$. For the $p_{\rm T}$ dependence of $R_{\rm FB}$, this uncertainty varies from $\sim 1\%$ to $\sim 13\%$ in the less populated high $p_{\rm T}$ bin. For the y dependence of the $R_{\rm FB}$ studies, the uncertainty is in the range 1-4%.

The systematic uncertainty on the signal extraction is considered as uncorrelated in $p_{\rm T}$ and y. However when comparing the forward (p-Pb) and backward (Pb-p) rapidity results it is considered as partially correlated since the main contribution to this uncertainty is related to the choice of the signal function, i.e. CB2 or NA60 (NA60CB2). The integral of the NA60 (NA60CB2) function always gives a larger J/ψ yield with respect to the CB2 one, introducing a correlation between p-Pb and Pb-p extracted yields.

6.8.2 pp reference systematics

The systematic uncertainties on the pp reference are summarized in Section 6.7. They include uncorrelated, correlated and partially correlated contributions. They represent one of the main contributions to the systematic uncertainties of $R_{\rm pPb}$ results.

6.8.3 $A\epsilon$ systematics from the MC parametrization

The J/ψ distributions in rapidity and $p_{\rm T}$ were extracted from the data in p-Pb and Pb-p for different event activity classes and kinematic ranges:

- the event activity class $0-20\%$ of V0M multiplicity[1], $50-80\%$ of V0M multiplicity;
- low $p_{\rm T}$ events ($0 \leq p_{\rm T} \leq 2$ GeV/c), high $p_{\rm T}$ events ($5 \leq p_{\rm T} \leq 15$ GeV/c);
- low y events ($2.5 \leq y \leq 3$), high y events ($3.5 \leq y \leq 4$).

From these boundary distributions, the two extreme distributions, a softest and a hardest, were defined in $p_{\rm T}$ and y. It results in four different combinations of the $p_{\rm T}$ and y distributions corresponding to four sets of simulations. The systematic on $A\epsilon$ was estimated as the maximum difference between the values obtained with these simulations and the nominal one. Integrated over $p_{\rm T}$ and y, the systematic amounts to 1.5% both for p-Pb and Pb-p. It is almost constant as a function of $p_{\rm T}$, while it varies by $0\% - 5\%$ as a function of y. The lower and higher y ranges give the larger uncertainties. The uncertainty on $A\epsilon$ is expected to be uncorrelated with respect to $p_{\rm T}$, y and the period of

[1]The event activity estimators used in ALICE are discussed in Chapter 7

data taking (p-Pb or Pb-p). Finally the acceptance was estimated assuming unpolarized J/ψ [197–199] and no uncertainty from the unknown polarization of the J/ψ is considered.

6.8.4 Tracking efficiency

The single-muon tracking efficiencies are obtained using an algorithm based on reconstructed tracks [208]. The tracking efficiency was measured on the data and amounts to approximately 90%, 85% and 74% for LHC13d, LHC13e and LHC13f periods, respectively. It fluctuates from one run to another depending on the tracking chambers condition (Fig. 6.17). It was checked that this quantity does not depend on the event activity as shown in Fig. 6.18 where the V0M event activity estimator is used [1]. The tracking efficiency measured in the data is also compared to the one measured in the MC simulations in Fig.6.17. The difference observed between the data and the MC simulations is taken as a systematics for single muon and was found to be 2% (3%) for p-Pb (Pb-p). This uncertainty was assumed to be uncorrelated between the two detecting muons, resulting, at the dimuon level, in 4% (6%) for p-Pb (Pb-p). The uncertainty is uncorrelated with respect to p_{T}, y and the period of data taking. It represents one of the main sources of the systematic uncertainties in this analysis.

6.8.5 Trigger efficiency

The trigger efficiency was measured at sufficiently high p_{T} from the data and amounts to approximately $97 - 97.5\%$ for each chamber leading to an overall trigger efficiency above 99% [209, 210].

The systematic uncertainty arising from the intrinsic trigger efficiency was estimated by varying by 2% the efficiency of each local board in the simulation. This value corresponds to the uncertainty on the local board efficiency determined by varying the cuts on the trigger or tracker tracks used to determined the intrinsic efficiency. Using pure signal simulations, an uncertainty on dimuon trigger efficiency (extrapolated from the single muon studies) of the order of 2% was found. This uncertainty is uncorrelated as a function of p_{T}, y and the period of data taking due to possible variations from one local board to another.

The systematic uncertainty arising from the trigger p_{T} threshold is estimated by varying the p_{T} dependence of the trigger efficiency in the simulations. In previous J/ψ analyses [54, 208, 211], the trigger threshold was set

[1] This was expected since the most central (i.e. highest event activity) events in p-Pb correspond to 60%-70% centrality range in Pb-Pb where no effect from tracking chambers occupancy was measured.

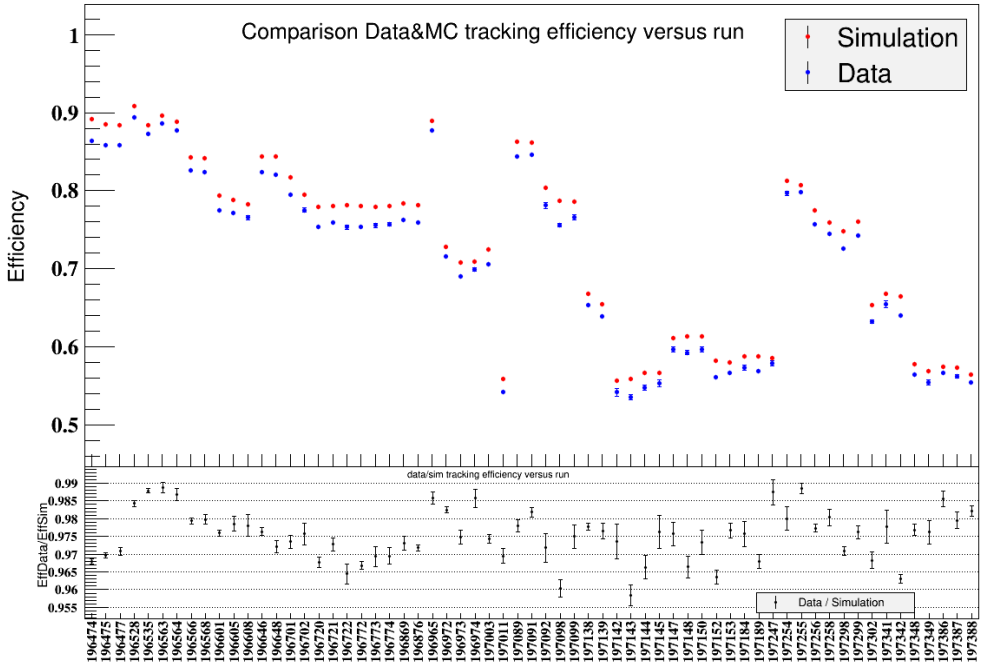

Figure 6.17. Tracking efficiency measured both in the data and in the MC simulations for Pb-p. From JavierBlanco.

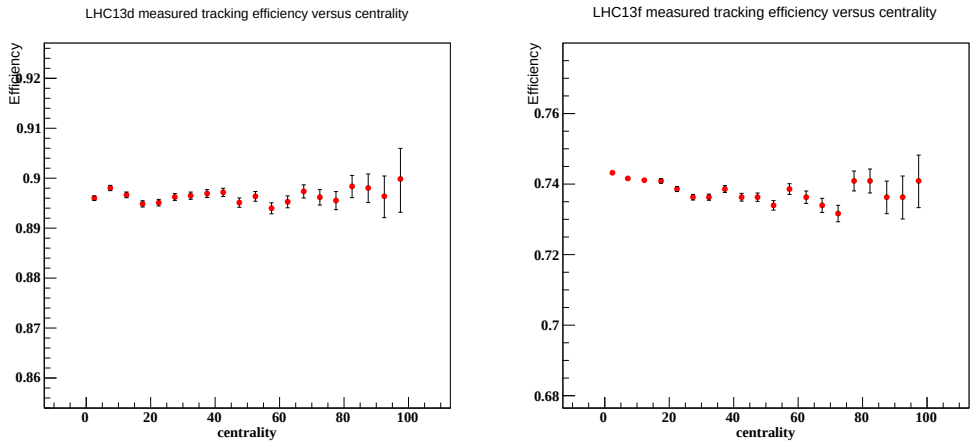

Figure 6.18. Tracking efficiency vs V0M event activity classes for LHC13d (left panel) and LHC13f (right panel). From [200].

to 1 and 4 GeV/c and the difference between the data and MC simulations in the ratio between the 0.5 and 1 GeV/c trigger thresholds was considered to estimate the systematic uncertainty on the trigger threshold. However in

2013, the trigger threshold was set to 0.5 and 4 GeV/c and it was therefore not possible to estimate the systematic uncertainty using the same method. It was assumed in the data and in the MC simulations that the variation between 0 and 0.5 GeV/c trigger threshold in 2013 is the same as between 0.5 and 1 GeV/c trigger threshold in Pb-Pb data in 2011. From this study, the systematic uncertainty is found to be of the order of 3% for the dimuons (extrapolated from the single muon studies) and decreases with higher value of p_{T}. It is an uncorrelated uncertainty with respect to p_{T}, y and the period of data taking.

6.8.6 Matching efficiency

The systematic uncertainty on the matching efficiency between the track reconstructed in the tracking chambers and the one reconstructed in the trigger chambers was found to be $0.5-1\%$ for single muons [212]. It was estimated as the difference observed in the simulations compared to the data when applying different goodness-of-fit χ^2 cuts on the matching between the trigger and tracker track. For large mass resonance as the J/ψ , this uncertainty amounts to 1%. This uncertainty is uncorrelated as a function of p_{T} , y and the period of data taking.

6.8.7 Normalization CINT7 - CMUL7

The systematic uncertainty on the normalization amounts to 1% and is described in Section 6.6. This uncertainty is correlated as a function of p_{T} and y and uncorrelated for the different collision systems. However as it is small, it is also considered as uncorrelated in p_{T} and y.

6.8.8 Other systematics

The systematic uncertainty on the nuclear thickness function T_{pPb} is taken from [196] and is equal to 0.0035 mb^{-1} (3.6%). It is correlated as a function of p_{T}, y and the period of data taking. The systematic uncertainty on the V0AND cross section $\sigma_{V0AND} \equiv \sigma^{\mathrm{MB}}_{\mathrm{pPb}}$ are described in 6.2. Finally for the J/ψ cross section studies, the branching ratio of J/ψ decay to dimuon pair is used with its 1% uncertainty taken from [194].

The summary of all the systematic uncertainties is presented in Table 7.8. The values given in parenthesis correspond to the uncertainty variation in different y bins. The uncertainties on $\sigma^{\mathrm{MB}}_{\mathrm{pPb}}$ are relevant only for the inclusive J/ψ cross section results while the uncertainties on $\sigma^{\mathrm{J}/\psi}_{\mathrm{pp}}$ and on $\langle T_{\mathrm{pPb}} \rangle$ contribute only to the nuclear modification factors measurements.

Source	LHC13d+e	LHC13f
Uncorrelated		
Tracking efficiency	4	6
Trigger efficiency	2.8	3.2
Signal extraction	1.3 (1.5-3.4)	1.2 (1.6-3.8)
MC input	1.5 (1.1-3)	1.5 (0.9-4.2)
Matching efficiency	1	1
Normalization factor F_{norm}	1	1
$\sigma_{\mathrm{pp}}^{\mathrm{J}/\psi}$	4.3 (3.1-6)	4.6 (3.1-13.4)
Partially correlated		
$\sigma_{\mathrm{pPb}}^{\mathrm{MB}}$	3.2	3
$\sigma_{\mathrm{pp}}^{\mathrm{J}/\psi}$	3.7 (2.7-9.2)	3.1 (1.2-8.3)
Correlated		
Branching ratio	1	
$\langle T_{\mathrm{pPb}} \rangle$	3.6	
$\sigma_{\mathrm{pp}}^{\mathrm{J}/\psi}$	5.5	

Table 6.8. Systematic uncertainties (given in percentage) contributing to the measurement of the inclusive J/ψ cross sections and corresponding nuclear modification factors in different data taking periods. See text for details.

Chapter 7

Event activity and p_{T} dependence analysis

This chapter describes the analysis of the J/ψ production in p-Pb collisions as a function of the event activity (centrality) of the collision. It includes also the description of the centrality determination in ALICE. This chapter also describes the extraction of the mean transverse momentum and the mean square of the transverse momentum from the measured p_{T} spectra.

7.1 Main observables

The main observables of this analysis are the inclusive J/ψ cross section, the biased nuclear modification factor and the mean transverse momentum. The definition of the inclusive J/ψ cross section is given in (6.1).

The nuclear modification factor is referred to as Q^i_{pPb} and not the usual R^i_{pPb} when evaluated in a given event activity class i, due to the possible biases (discussed in Section 7.2.1) in the determination of N_{coll} (or T_{pPb}). Q^i_{pPb} is thus not necessarily equal to unity in the absence of nuclear effects. It is defined as follows:

$$Q^i_{\mathrm{pPb}}(p_{\mathrm{T}}, y) = \frac{Y^i_{\mathrm{J}/\psi\to\mu^+\mu^-}(\Delta p_{\mathrm{T}}, \Delta y)}{\langle T_{\mathrm{pPb}}\rangle^i \times \Delta p_{\mathrm{T}} \times \Delta y \times \frac{BR\times \mathrm{d}\sigma^{\mathrm{pp}}_{\mathrm{J}/\psi\to\mu^+\mu^-}}{\mathrm{d}y\mathrm{d}p_{\mathrm{T}}}(p_{\mathrm{T}}, y)}, \tag{7.1}$$

where T^i_{pPb}, the nuclear overlap function, is determined separately for each event activity estimator (discussed in Section 7.2.1), $Y^i_{\mathrm{J}/\psi\to\mu^+\mu^-}(\Delta p_{\mathrm{T}}, \Delta y)$ is the inclusive J/ψ yield defined in (6.2).

7.2 Centrality determination in ALICE

7.2.1 Centrality estimators

In ALICE, several centrality (event activity) estimators are available [213]:

- CL1 ($|\eta| < 1.4$) denotes the number of clusters in the outer layer of the SPD;
- V0A (V0C) with η range $2.8 < \eta < 5.1$ ($-3.7 < \eta < -1.7$) is the amplitude measured by the VZERO hodoscopes on the A-side (C-side), corresponding to Pb-remnant side in p-Pb (Pb-p);
- V0M is the sum of the VZERO amplitude's hodoscopes on the A- and C-side (V0A+V0C);
- ZNA (ZNC) is the energy deposited in Zero-degree Neutron calorimeter on the A-side (C-side).

The details on the centrality determination for each of the estimators can be found in [213]. In the following, the V0A and ZN estimators are used since they are located in a region outside of the J/ψ measurement. Indeed in order to avoid situation where the centrality measurement is biased by the J/ψ muon decay itself, a large rapidity gap between the muon spectrometer and the centrality detector is required. Therefore, the V0A and ZN centrality estimators have less bias than the CL1 and the V0C for the J/ψ analysis. V0A estimator was used for both periods of data taking, p-Pb and Pb-p. The ZNA (ZNC) estimator was used for p-Pb (Pb-p).

The centrality of the collision is usually determined from a monotonic dependence of an experimental observable on the number of binary collisions N_{coll}, e.g. the particle multiplicity or the summed energy in a certain pseudo-rapidity range. The distributions of the V0A multiplicity and of the ZDC neutron energy with corresponding division into the centrality classes are illustrated in Fig.7.1. These distributions are fitted with theory-based functions: negative binomial distribution (NBD) for V0A and functions from slow-nucleon models (SNM) [214, 215] for ZN. These models are coupled to the Glauber model which provides a distribution of N_{coll} for each centrality class (see Section 5.1).

In p-Pb collisions, in contrast to Pb-Pb ones, the fluctuations of multiplicity for a fixed N_{coll} are large with respect to the relatively small range of N_{coll}. This leads to a wide correlation between N_{coll} and the particle multiplicity, introducing a dynamical bias which depends on the centrality classes determination. It should be mentioned that different centrality estimators have different level of bias in p-Pb collisions:

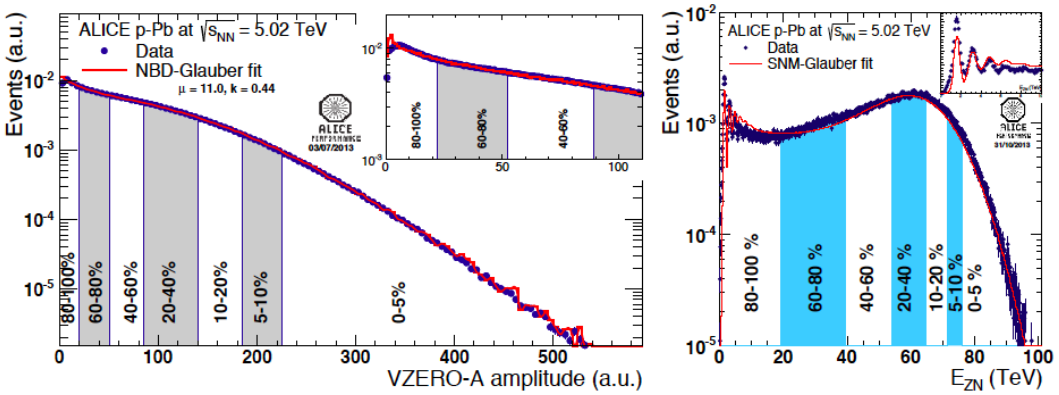

Figure 7.1. Left: Sum of amplitudes in the VZERO-A scintillators for p-Pb. Right: Neutron energy spectra measured in the ZNA calorimeter. The distributions are compared with theory-based functions from the NBD-Glauber and the SNM-Glauber fits, respectively. From [213].

- V0C: strong bias due to full overlap with the tracking region. But for Pb-p it is reduced because of the important contribution from Pb fragmentation region.
- V0M: biased since it includes V0C.
- CL1: reduced bias since it is outside of the tracking region.
- V0A: reduced bias since it is outside of the tracking region. For p-Pb it is even more reduced because of the important contribution from Pb fragmentation region.
- ZNA (ZNC): small bias since the slow nucleon[1] production is independent of hard processes.

The term "event activity" instead of "centrality" is used further in this work, drawing attention to the unknown biases in its determination.

7.2.2 T_{pPb} and N_{coll} determination

The N_{coll} and T_{pPb} values are calculated using the approach described above and in [216]. For the V0A estimator, a Glauber model (Section 5.1) was employed. For the ZN estimator, a more complicated "Hybrid" approach described

[1]Emitted nucleons are classified as "black" and "gray". This definition from emulsion experiment is related to the track grain density. Black particles are the low energy target (Pb) fragments emitted by evaporation processes with momentum $p < 250$ MeV/c. Gray particles are the soft nucleons knocked out by wounded nucleons with 250 MeV/$c < p < 1$ GeV/c. In both cases, the momentum is given in the nucleus rest frame.

in [216] is used. This approach is based on the following three assumptions, providing three slightly different sets of T_{pPb} values for the event activity classes used in the analysis:

- The multiplicity at mid-rapidity is proportional to N_{part}. Corresponding observables are denoted with a superscript "mult".
- The yield of the high-p_{T} particles is proportional to N_{coll}. Corresponding observables are denoted with a superscript "high-p_{T}".
- The Pb-going side multiplicity is proportional to N_{part}. Corresponding observables are denoted with a superscript "Pb-side".

Table 7.1 (Table 7.2) summarizes the N_{coll} (T_{pPb}) values for V0A and ZN analyses. The V0A results are given with two systematic uncertainties: the first one comes from the Glauber model and the second one from the variation between N_{coll} extracted from the fit and from the MC simulations using HIJING [189] as input. For ZN estimator, the results are given for the three cases (mult, high-p_{T}, Pb-side) and the maximum deviation is taken as a systematic uncertainty, denoted as "model uncertainty". An additional systematic uncertainty of 8.0% arising from the Glauber model ("Glauber uncertainty") should be added quadratically. The Glauber uncertainty is thus common for all the bins. For the results, the multiplicity assumption is chosen to determine N_{coll}.

Table 7.1. The N_{coll} values for V0A and ZN analyses for different event activity classes. See text for details.

Event activity class	V0A	ZN			
	$N_{\mathrm{coll}}^{\mathrm{V0A}}$	$N_{\mathrm{coll}}^{\mathrm{mult}}$	$N_{\mathrm{coll}}^{\mathrm{high-pT}}$	$N_{\mathrm{coll}}^{\mathrm{Pb-side}}$	Max. deviation
0-5%	14.8 ± 10% ± 3%	12.226	12.540	13.308	8.9%
5-10%	13.0 ± 10% ± 1%	11.625	12.076	12.280	5.6%
10-20%	11.7 ± 10% ± 2%	10.961	11.257	11.397	4.0%
20-40%	9.36 ± 8.8% ± 2%	9.551	9.694	9.603	1.5%
40-60%	6.42 ± 6.6% ± 3%	7.074	6.795	6.741	4.9%
60-80%	3.81 ± 4.3% ± 20%	4.380	4.094	4.002	9.5%
80-100%	1.94 ± 2.0% ± 23%	2.052	2.107	2.060	2.7%

7.2.3 Event activity distribution for MB events with V0A

If the centrality ranges are well calibrated run per run, the event activity distribution is expected to be flat for MB events. While in the MB

Table 7.2. The $T_{\rm pPb}$ values for V0A and ZN analyses for different event activity classes. See text for details.

Event activity class	V0A	ZN			
	$T_{\rm pPb}^{\rm V0A}$	$T_{\rm pPb}^{\rm mult}$	$T_{\rm pPb}^{\rm high-pT}$	$T_{\rm pPb}^{\rm Pb-side}$	Max. deviation
0-5%	0.211 ± 3.7% ± 3%	0.1747	0.1792	0.1901	8.9%
5-10%	0.186 ± 3.5% ± 1%	0.1661	0.1725	0.1754	5.6%
10-20%	0.167 ± 3.2% ± 2%	0.1566	0.1608	0.1628	4.0%
20-40%	0.134 ± 3.1% ± 2%	0.1364	0.1385	0.1372	1.5%
40-60%	0.0918 ± 4.3% ± 3%	0.1011	0.0971	0.0963	4.9%
60-80%	0.0544 ± 6.7% ± 20%	0.0626	0.0585	0.0572	9.5%
80-100%	0.0277 ± 9.3% ± 23%	0.0292	0.0301	0.0294	2.7%

trigger period (LHC13b,c), event activity estimators are correctly calibrated, they may suffer from miscalibration and/or pile-up in the rare trigger period (LHC13d,e,f) where the CINT7 trigger rate reaches up to 200 kHz. The event activity distribution from the V0A estimator for MB events is shown in Fig. 7.2 for p-Pb (top left) and for Pb-p (top right) data taking periods. Events are required to pass the Physics Selection. The event activity distributions are fitted by a constant value and the ratio between the distribution and the fit result is shown in the bottom plots of Fig. 7.2. Small deviations (up to 4%) from the fit result are observed in the event activity distribution.

The V0C estimator cannot be used for the J/ψ analysis due to the bias from the measurement itself. However, in the Pb-p the V0A is not located in the Pb-beam remnant side. This leads to a lower multiplicity used for the centrality determination in the Pb-p and may affect it. It was checked in Fig. 7.3 that the V0A event multiplicity in Pb-p is correlated with the V0C one for MB events. This correlation allows us to use the V0A estimator not only for p-Pb but also for Pb-p.

Since no cut was applied on the primary vertex position along z-axis in the event selection of the J/ψ analysis, it was necessary to check that the V0A event activity distribution is independent from the z vertex position. Top panels of Fig.7.4 show the V0A event activity distribution for p-Pb (left) and Pb-p (right) for different cuts on the primary vertex: no z-vertex found, $|z| < 10$ cm, $z > -10$ cm, $z \geq 10$ cm. In the bottom panels of Fig. 7.4, the ratio between the event activity distribution with a given z-vertex cut (color lines) and the one without any cut (black line "all") are shown for both periods. Using the V0A estimator, the event activity dependence is flat for the three classes of events: $|z| \leq 10$ cm, $z \leq -10$ cm, $z \geq 10$ cm. In addition, most of

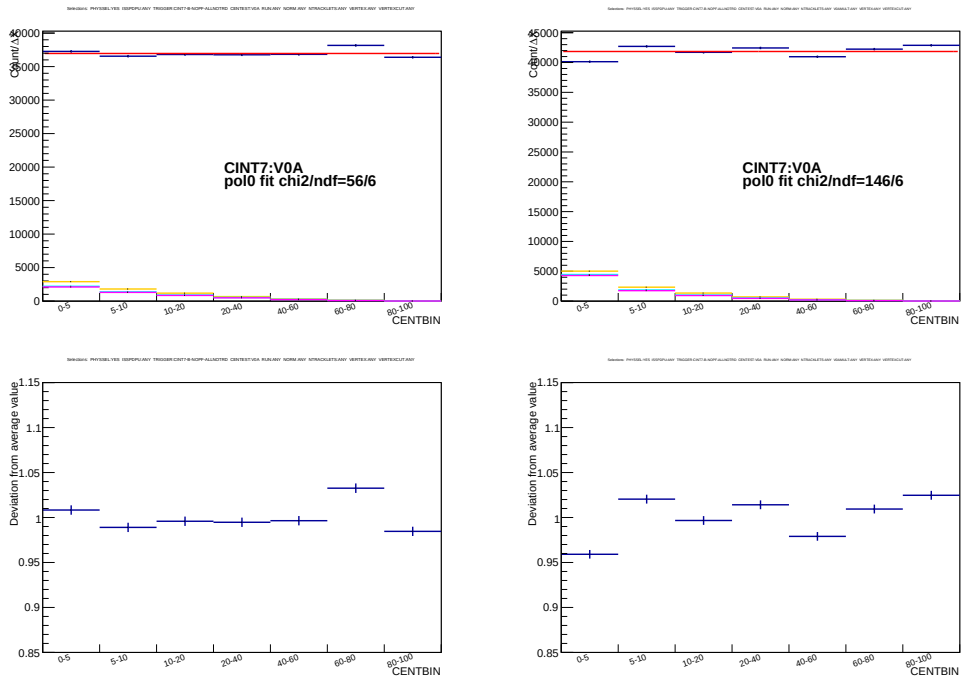

Figure 7.2. V0A event activity distribution of MB events, for p-Pb (top left) and Pb-p (top right). The event activity distributions (blue points) are normalized by the corresponding width of the event activity classes ΔX and then fitted by a constant (red line). The ratio between the event activity distribution and the fit result is shown for both periods in the bottom panels. Color lines in the top panels correspond to the pile-up events estimated with different pile-up cuts, but they are not discussed in this figure (see Section 7.3.1 for more details).

the events have a vertex except 2-3% in the lowest event activity class.

7.2.4 Event activity distribution for MB events with ZN

The event activity distribution of the ZNA(C) of the MB events is shown in Fig. 7.5 for p-Pb (Pb-p) periods in the top left (top right) panel. Events are required to pass the Physics Selection. Events with event activity higher than 100% are counted in the lowest event activity bin (80-100%). No dependence of the ZN estimator on the vertex position along z was assumed, as it was observed for the V0A estimator.

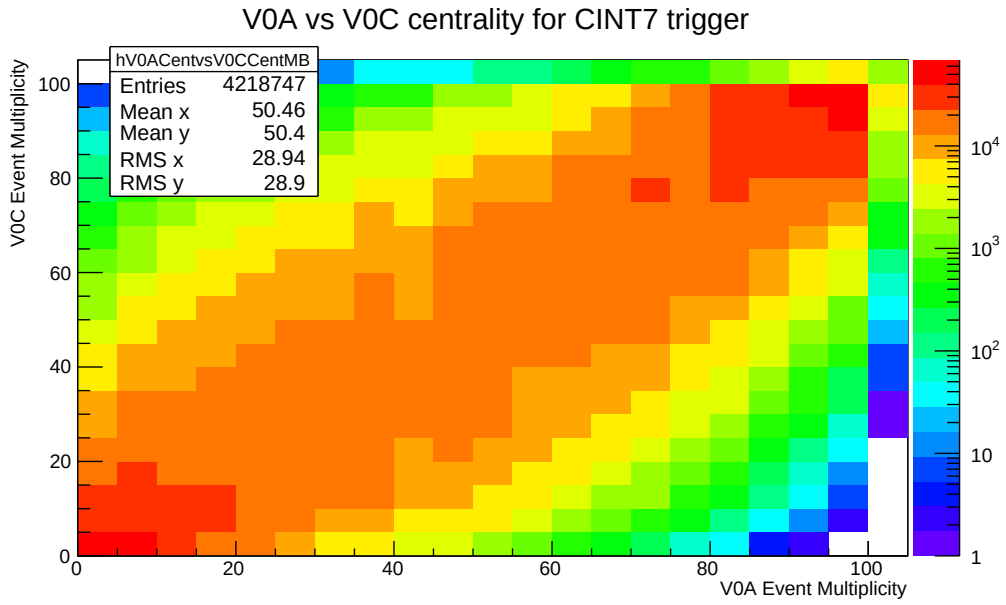

Figure 7.3. V0A vs V0C event activity distribution of the MB events in Pb-p.

7.3 Contribution from pile-up events

In p-Pb collisions data taking, the bunch spacing is 200 ns. In the data selection, the muon tracks are requested to be matched with the muon trigger which has a trigger decision time of 25 ns. This condition implies that the J/ψ events are not sensitive to pile-up from different bunches. The V0A has a very fast time ($<$ 25 ns), thus it is expected to be insensitive to pile-up from different bunches. For the ZN, the gate value was 100 ns during 2013 data taking. The ZDC signal is 60 ns long and starts around 20 ns after the arrival of the gate, so it is below the 200 ns spacing of two collisions. Therefore pile-up events from different bunches are expected to be negligible for the detectors used for this analysis. In the following, pile-up will always refer to pile-up from the same bunch crossing. Pile-up refers to MB events. Pile-up events can increase the multiplicity of the events, smearing an event from a lower event activity bin to a higher one. Different cuts were applied in order to reject pile-up events both for the V0A and the ZN estimators. An illustration of these cuts and their effect on the event activity distribution is shown for the ZN estimator in Fig. 7.5. A detailed description of these cuts is given below.

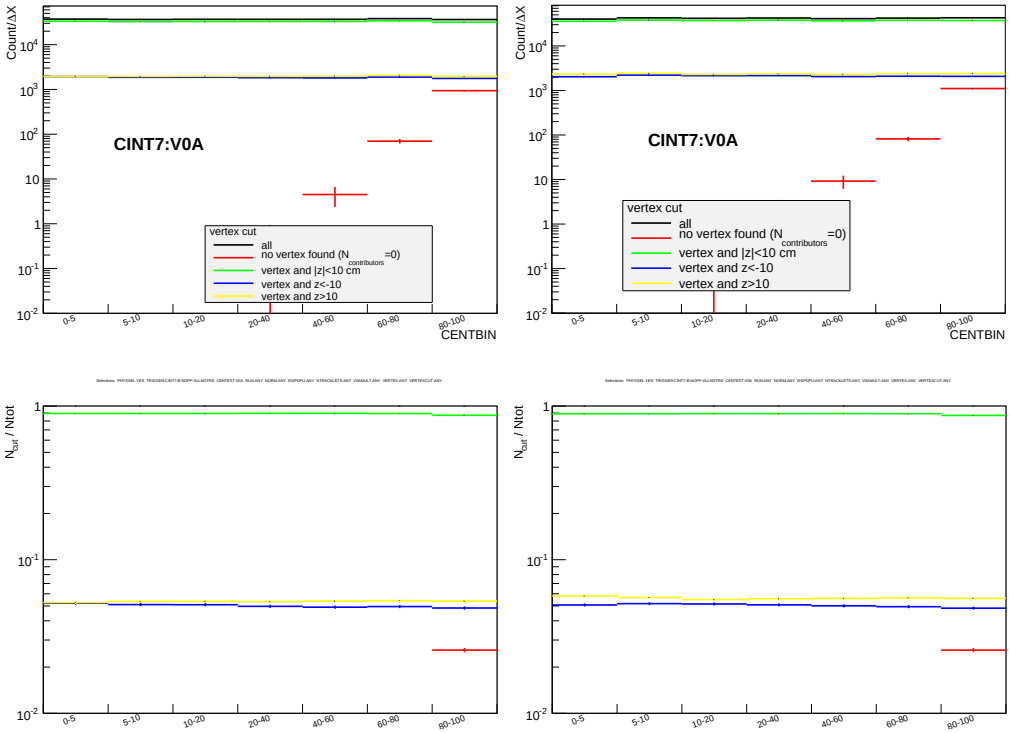

Figure 7.4. V0A event activity distribution of the MB events for p-Pb (top left) and Pb-p (top right) for different requirement on the z-vertex. The ratio between the event activity distribution with a given z-vertex cut (color lines) and the one without any cut (black line "all") is shown in the bottom panels. All the event activity distributions are normalized by the corresponding width of the event activity classes ΔX.

7.3.1 Estimation of the fraction of pile-up events

The pile-up contribution can be estimated run per run using the L0b trigger rate for CINT7 (MB) trigger ($L0bRate_{CINT7}$) and assuming that the number of collisions per bunch crossing follows a Poisson distribution (see also Section 6.6). In particular, the mean number of collisions per bunch crossing, μ, is obtained for a given run i from the following expression:

$$\mu^i = -ln\left(1 - \frac{PS^i_{CINT7} \times L0bRate^i_{CINT7}}{N^i_{colliding} \times f_{LHC}}\right) \tag{7.2}$$

where PS_{CINT7} denotes the fraction of good MB events selected by the physics selection on recorded events, $N_{colliding}$ is the number of colliding bunches and f_{LHC} = 11245 Hz, the LHC revolution frequency. It was assumed that the physics selection effect, i.e. the fraction of good MB events does not depend

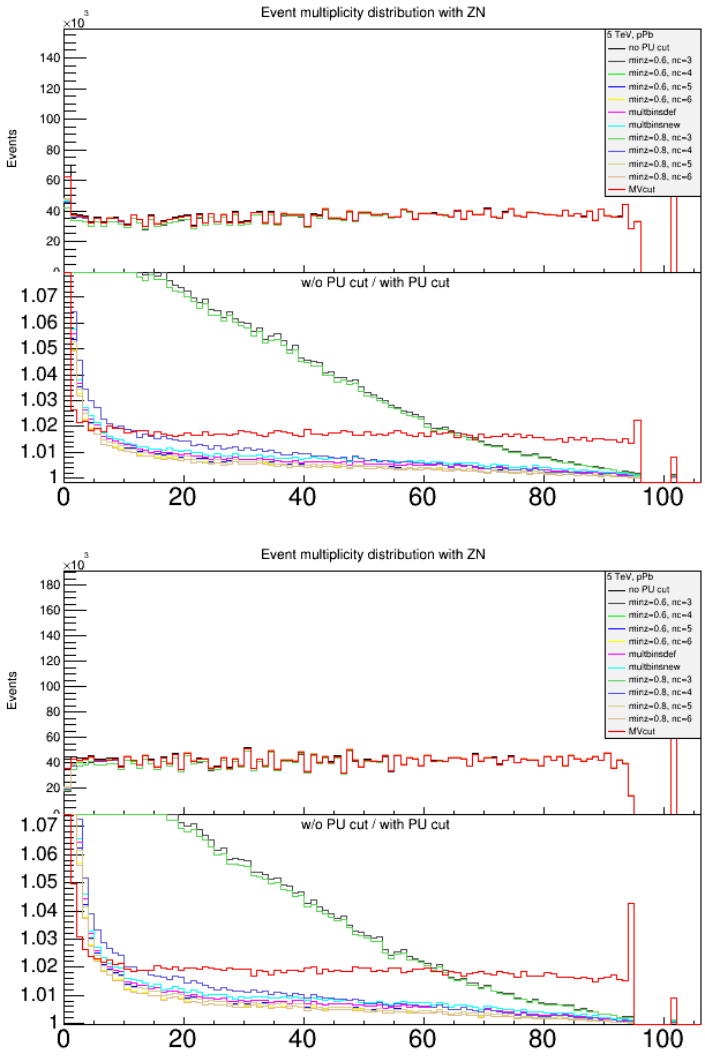

Figure 7.5. ZNA(C) event activity distribution of MB events for p-Pb (Pb-p) in the top (bottom) panel. The ratio between the event activity distribution without any pile-up cut to those with different pile-up cuts are shown in the bottom part of the plots.

on the trigger veto at the L0 level.

One can then derive the MB pile-up fraction run per run as:

$$\text{MB pile-up fraction}^i = \frac{\mathcal{P}^i(n>1)}{\mathcal{P}^i(n>0)} = 1 - \frac{\mu^i e^{-\mu^i}}{1-e^{-\mu^i}} \tag{7.3}$$

Fig. 7.6 and Fig. 7.7 show the pile-up fraction run per run for p-Pb and Pb-p for different pile-up estimators (see in Section 7.3.2 for details). The thick

black line indicates the estimation of pile-up fraction obtained from (7.3). The estimated pile-up fraction varies from 1% to 3%, with a structure corresponding to the LHC fills. A decreasing trend is observed due to the lowering of the beams intensities (in particular, the Pb beam). The method described above gives an estimation of the average pile-up fraction per run but cannot be used to identify pile-up events in different event activity classes.

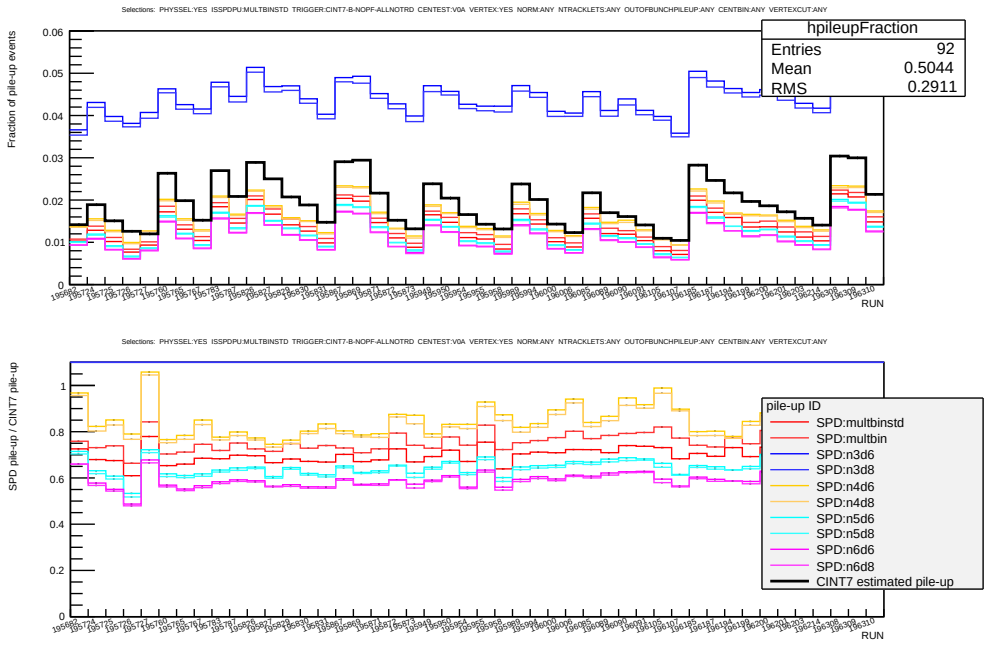

Figure 7.6. Top: pile-up fraction in p-Pb estimated run per run from the L0b CINT7 rate (black thick line) and from the SPD method using different options (see text for details). Bottom: ratio between the fraction of pile-up event using SPD tagging method and the MB pile-up fraction estimated using (7.3).

7.3.2 Tagging pile-up events with multi-vertices in SPD

The candidates to the primary vertex are found using the SPD tracklets and the distances between them. SPD tracklet is defined as a line segment built using two clusters in the inner and outer SPD layers within a small azimuthal window. The primary vertex corresponds to the candidate with the largest number of contributors (the tracklets contributing to this vertex). Pile-up events are tagged by the SPD if more than one vertex is reconstructed per event. This method has different parameters. In particular, a vertex is considered only if it has a minimum number of contributors and if the

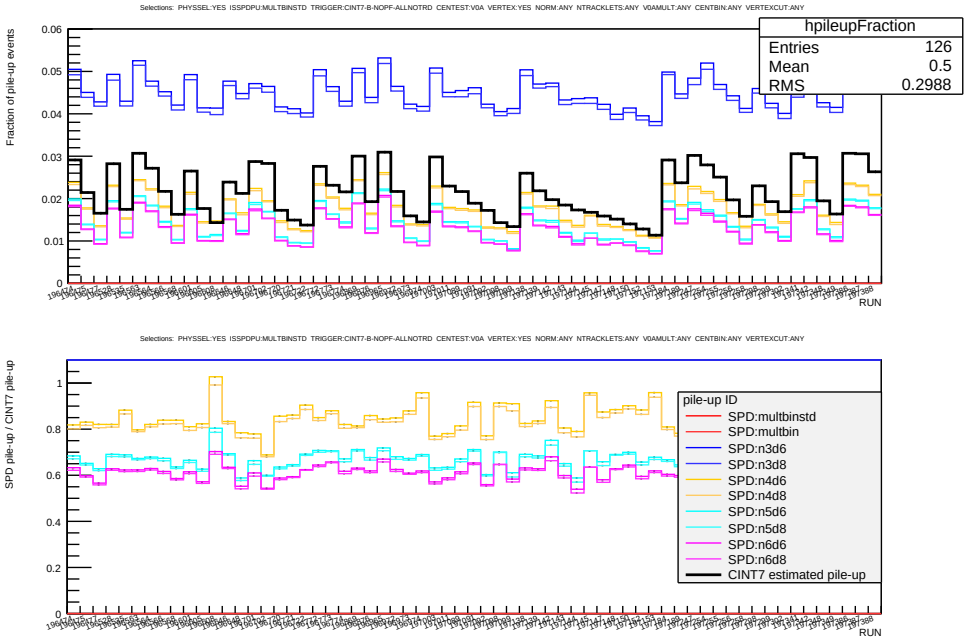

Figure 7.7. Top: pile-up fraction in Pb-p estimated run per run from the L0b CINT7 rate (black thick line) and from the SPD method using different options (see text for details). Bottom: ratio between the fraction of pile-up event using SPD tagging method and MB pile-up fraction estimated using (7.3).

distance between the pile-up and the primary vertex is higher than a given minimum distance to the primary vertex. This method suffers from inefficiency, in particular if the multiplicity of tracks in the SPD is low or if the minimum distance to the primary vertex is low. This method may also be contamined by false positive events (where the pile-up is detected in events without pile-up), in particular at high multiplicity of tracks in the SPD and/or at low minimum number of contributors.

The SPD pile-up fraction is defined as:

$$\text{SPD pile-up fraction} = \frac{N_{SPD\ pile-up}}{N_{tot}} \tag{7.4}$$

where N_{tot} is the number of events of a particular trigger that pass the PS and $N_{SPD\ pile-up}$ the number of events tagged as pile-up by the SPD.

In Fig.7.6 and 7.7, the SPD pile-up fraction is presented in the top panels as a function of the run number for MB events. Different options of the method are displayed where n refers to the minimum number of contributors and d to the minimum distance in mm to the primary vertex. The options "multbinstd"

and "multbin" were not used in the final results and are not discussed here. In the bottom panels of Fig.7.6 and 7.7, the ratio between the pile-up fraction detected by the SPD and the estimated one is shown. This comparison allows us to discard the option $n = 3$ which indicates a much larger pile-up fraction as compared to the estimated value. This is probably due to a large contamination from good events tagged as pile-up by the method, or false positive events. It also indicates that the minimum distance of 6 or 8 mm does not vary much the pile-up contribution. The options $n4d6$, $n5d6$ and $n6d6$ reproduce fairly well the trend of the estimated pile-up fraction but underestimate it by 60% to 80%. The numbers below show the total number of MB events that passed the PS and the SPD-pile-up cut. In the parenthesis the percentage of pile-up events is indicated. The mean number of collisions per bunch crossing, μ, is equal to 0.038 for p-Pb and 0.043 for Pb-p:

- p-Pb: estimated pile-up fraction with $\mu = 0.038$ is 1.89%
  - no SPD pile-up cut: 3721882
  - d = 6 mm,, n = 3: 3559243 (4.57% of pile-up)
  - d = 6 mm,, n = 4: 3663631 (1.59% of pile-up)
  - d = 6 mm,, n = 5: 3676736 (1.23% of pile-up)
  - d = 6 mm,, n = 6: 3680696 (1.12% of pile-up)
  - d = 8 mm,, n = 3: 3563426 (4.45% of pile-up)
  - d = 8 mm,, n = 4: 3664804 (1.56% of pile-up)
  - d = 8 mm,, n = 5: 3677394 (1.21% of pile-up)
  - d = 8 mm,, n = 6: 3681211 (1.10% of pile-up)
- Pb-p: estimated pile up with $\mu = 0.043$ is 2.13%
  - no SPD pile-up cut: 4217841
  - d = 6 mm,, n = 3: 4028896 (4.69% of pile-up)
  - d = 6 mm,, n = 4: 4144053 (1.78% of pile-up)
  - d = 6 mm,, n = 5: 4158719 (1.42% of pile-up)
  - d = 6 mm,, n = 6: 4163726 (1.30% of pile-up)
  - d = 8 mm,, n = 3: 4033663 (4.57% of pile-up)
  - d = 8 mm,, n = 4: 4145426 (1.75% of pile-up)
  - d = 8 mm,, n = 5: 4159556 (1.40% of pile-up)
  - d = 8 mm,, n = 6: 4164428 (1.28% of pile-up)

From these numbers, the option d = 6 mm,, n = 4 shows the best efficiency (85% of the total estimated pile-up).

7.3.3 SPD pile-up events contribution to MB events as a function of the event activity

The ratios between the distribution without any pile-up cut and those with different pile-up cuts are shown in the bottom plots of Fig.7.5 as a function of the event activity defined by the ZN estimator in p-Pb (left) and Pb-p (right). In this figure minz corresponds to $d/10$, nc stands for n, noPUcut denotes the case without any pile-up cut. The options "multbinsdef" and "multbinsnew" were not used in the final results and are not discussed here. The MultiVertexer cut (MVcut) uses a slightly different approach for the pile-up determination. However it is not discussed here since it gives a non-physical result. As shown previously in the integrated case, the option with n = 3 gives a large pile-up fraction and is not reliable. At low ZN event activity (below 2%), the fraction of pile-up events is larger than 10% for each SPD pile-up cut.

In the J/ψ analysis as a function of the ZN event activity, for the cross section and Q_{pPb} studies, it was decided to remove, for the preliminary results, the event activity class 0-5% and to quote 2% of partially correlated uncertainty for each event activity class. It was also checked with a simple toy MC that the pile-up does not exceed this limit of 2% in each ZN event activity class except the event activity class 0-5%.

Fig.7.8 shows the SPD pile-up fraction for MB events as function of the V0A event activity in p-Pb (left) and Pb-p (right). The pile-up fraction increases with the event activity. It reaches, for the $0-5\%$ V0A event activity class, 6-8% in p-Pb and 11-12% in Pb-p, depending on the SPD pile-up cut options.

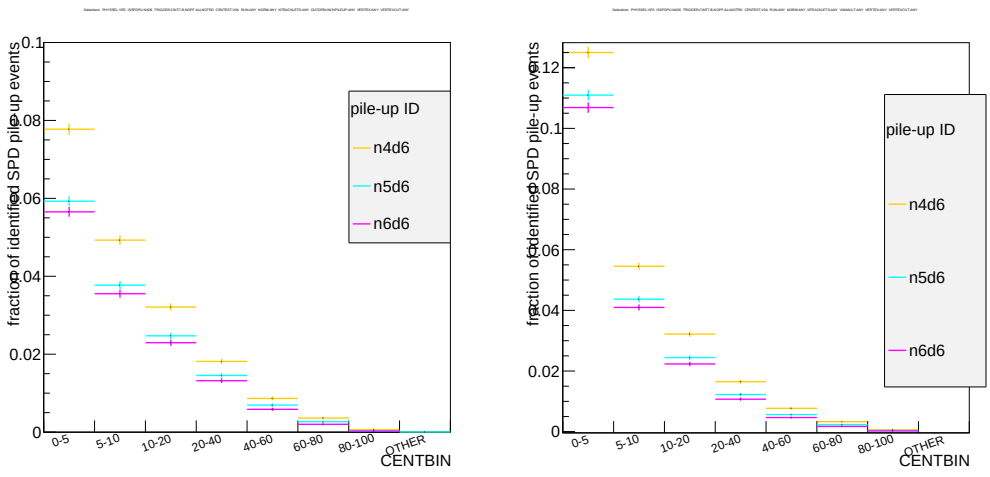

Figure 7.8. SPD pile-up fraction for MB events as a function of the V0A event activity for p-Pb (left) and Pb-p (right).

7.3.4 SPD pile-up events contribution to Dimuon triggered events as a function of the event activity

Fig. 7.9 shows the SPD pile-up fraction for dimuon triggered events as function of the V0A event activity in p-Pb (left panel) and Pb-p (right panel). The pile-up fraction increases with the event activity. It reaches, for the $0-5\%$ V0A event activity class, 9-11% in p-Pb and 12-14% in Pb-p. Integrated over the event activity, the fraction of the dimuon triggered events tagged as pile-up with the SPD pile-up cut $n5d6$ amounts to 3.6% in p-Pb and to 3.5% in Pb-p.

These values of the SPD pile-up fraction for dimuon triggered events are different to those for MB events. The dimuon triggered events are affected by the pile-up in MB interaction, i.e. no additional pile-up contribution is expected in the dimuon triggered events. Therefore, a difference in the pile-up fraction in the dimuon triggered events and the pile-up fraction in the MB events is a priori not expected. However the efficiency of the SPD tagging method may be different for MB and dimuon triggered events in particular because of the number of tracks produced at mid-rapidity. This can explain the observed difference.

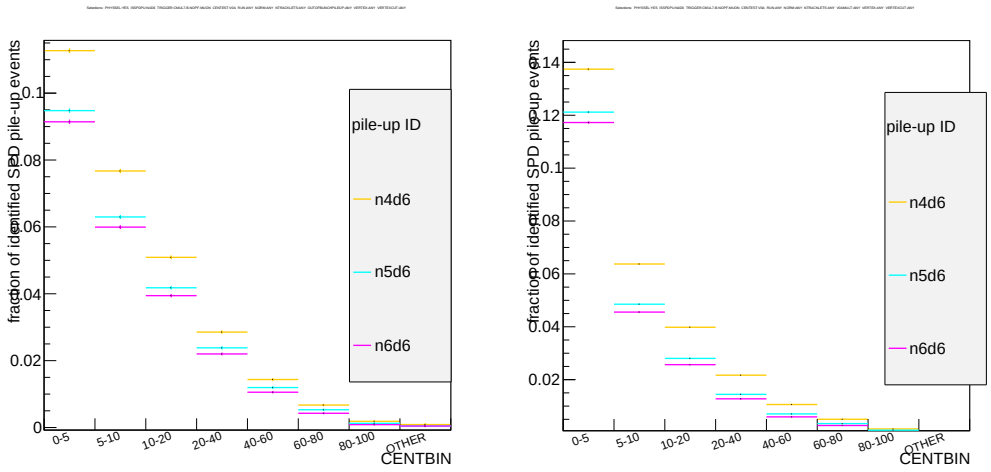

Figure 7.9. SPD pile-up fraction for dimuon triggered events as a function of the V0A event activity for p-Pb (left) and Pb-p (right).

7.4 Analysis details

The results presented in this chapter are extracted from the data sample described in Chapter 6. The same analysis technique is used.

In addition to the event selection described in Chapter 6, events were binned in event activity classes according to the V0A estimator for p-Pb or Pb-p and with ZNA (ZNC) estimator for p-Pb (Pb-p).

The J/ψ raw yields are corrected by acceptance and efficiency described in Chapter 6. No dependence of the detectors efficiency with the event activity is expected, therefore the same $A\epsilon$ value is used for different event activity classes. This assumption is based on the tracking efficiency studies as a function of multiplicity [200].

The event normalization has been checked as a function of the event activity for the V0A estimator, resulting in a flat dependence of the normalization factor with the event activity. The same behaviour was assumed for the ZN estimator.

7.4.1 pp reference at $\sqrt{s} = 5.02$ TeV

The pp reference is obtained using the same method as described in the previous chapter. The interpolated values of the $d^2\sigma_{\rm pp}/{\rm d}y{\rm d}p_{\rm T}$ of inclusive J/ψ at $\sqrt{s} = 5.02$ TeV are presented in Table 7.3 with the corresponding uncertainties.

Table 7.3. Interpolated $d^2\sigma_{\rm pp}/{\rm d}y{\rm d}p_{\rm T}$ of inclusive J/ψ at $\sqrt{s} = 5.02$ TeV. The first quoted systematic uncertainty is uncorrelated, the second one is correlated and the third one is partially correlated. The correlation is with $p_{\rm T}$ (i.e not y).

$p_{\rm T}$ range (GeV/c)	Interpolated $d^2\sigma_{\rm pp}/{\rm d}y{\rm d}p_{\rm T}$ (μb/(GeV/c))	
	$2.03 < y_{\rm cms} < 3.53$	$2.96 < y_{\rm cms} < 4.46$
0-1	0.624±0.036±0.032±0.025	0.490±0.029±0.026±0.017
1-2	1.197±0.064±0.062±0.046	0.892±0.048±0.046±0.030
2-3	0.980±0.051±0.051±0.039	0.693±0.036±0.036±0.025
3-4	0.579±0.032±0.030±0.022	0.388±0.021±0.020±0.012
4-5	0.294±0.017±0.015±0.008	0.187±0.011±0.010±0.004
5-6	0.156±0.011±0.008±0.005	0.094±0.007±0.005±0.002
6-8	0.057±0.005±0.003±0.003	0.032±0.003±0.002±0.002

7.4.2 Signal extraction

The J/ψ raw yield extraction as a function of the V0A event activity is carried out as described in Chapter 6. For the ZN estimator few changes were applied to the J/ψ raw yield extraction procedure:

- New tests were added: the width of the ψ(2S) was fixed to the width of the J/ψ with a factor of 0.9, 1.0 and 1.1.
- The NA60 function was changed by a new formulation which better scales with the invariant mass. NA60CB2 function was replaced by the new NA60 function.
- An additional systematic uncertainty of 2% related to the tails definition was added to the final results. This uncertainty is estimated when varying the tails obtained for different p_{T} intervals [217].

The results of the signal extraction procedure for p-Pb and Pb-p integrated over the event activity, for the highest and the lowest ZN event activity classes are presented in Appendix A. Signal-to-background ratio estimated in a 3σ interval around the J/ψ mass peak does not go below 0.97, providing a clear visible J/ψ signal in all the intervals under study.

7.5 p_{T} distribution and $< p_T >$ extraction for inclusive J/ψ

7.5.1 Extraction of $< p_T >$ and $< p_T^2 >$

Fig.7.10 shows the p_{T} distributions of $d^2\sigma_{\mathrm{pPb}}/\mathrm{d}y\mathrm{d}p_{\mathrm{T}}$ for p-Pb (top) and Pb-p (bottom) for different V0A event activity classes. Calculation of $\langle p_{\mathrm{T}} \rangle$ and its corresponding uncertainties is based on these p_{T} distributions. The procedure is divided into 3 steps:

1 $\langle p_{\mathrm{T}} \rangle$ calculation

2 calculation of the statistical uncertainty

3 calculation of the systematic uncertainty

1st step: To obtain the $\langle p_{\mathrm{T}} \rangle$ in the range $[0; p_{\mathrm{T}}^{\mathrm{max}}]$, the p_{T} dependence of $d^2\sigma_{\mathrm{pPb}}/\mathrm{d}y\mathrm{d}p_{\mathrm{T}}$ is fitted with a function $f(p_{\mathrm{T}})$. The statistical and the uncorrelated systematic uncertainties of the p_{T}-dependent cross sections are quadratically combined when performing the fit. Then, the $\langle p_{\mathrm{T}} \rangle$ is computed as:

$$\langle p_{\mathrm{T}} \rangle = \frac{\int_0^{p_{\mathrm{T}}^{\mathrm{max}}} p_{\mathrm{T}} f(p_{\mathrm{T}})\, \mathrm{d}p_{\mathrm{T}}}{\int_0^{p_{\mathrm{T}}^{\mathrm{max}}} f(p_{\mathrm{T}})\, \mathrm{d}p_{\mathrm{T}}} \tag{7.5}$$

In an ideal case, $p_{\mathrm{T}}^{\mathrm{max}}$ should be equal to infinity. In a real experiment due to the limited statistics, the range of integration is also limited. Assuming that the J/ψ cross section p_{T}-dependence outside of the range $[0; p_{\mathrm{T}}^{\mathrm{max}}]$ follows the

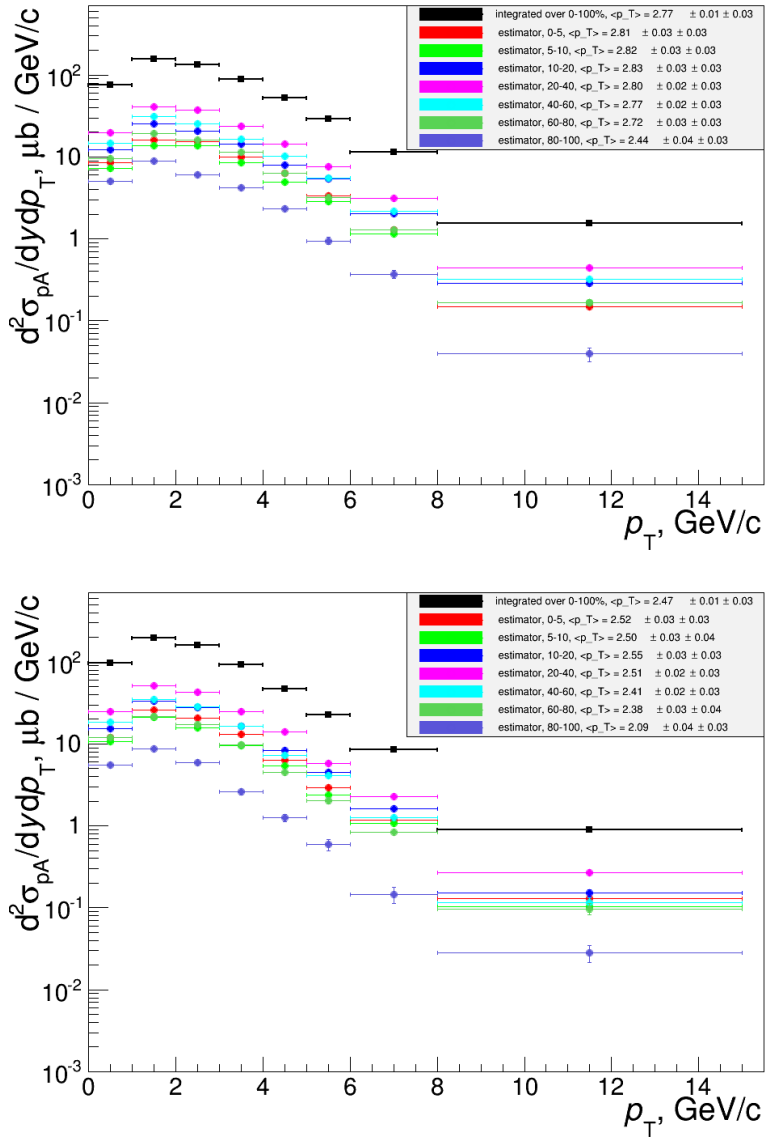

Figure 7.10. $d^2\sigma_{\mathrm{pPb}}/\mathrm{d}y\mathrm{d}p_{\mathrm{T}}$ as a function of p_{T} for different V0A event activity classes in p-Pb (top) and Pb-p (bottom).

distribution of the fit function, one can estimate the contribution of the range $[p_{\rm T}^{\rm max};\infty]$ to the $\langle p_{\rm T}\rangle$.

In this analysis, the following function is used to parametrize the $p_{\rm T}$ dependence:

$$f(p_{\rm T}) = C\frac{p_{\rm T}}{(1+(p_{\rm T}/p_0)^2)^n} \tag{7.6}$$

For $p_{\rm T}^{\rm max}$, three values were used: 8 GeV/c (the upper limit of the J/ψ pp analysis), 15 GeV/c (the upper limit of this analysis) and 1000 GeV/c (for $p_{\rm T}^{\rm max} = \infty$). It was seen that there is 3-5% difference between the results obtained with $p_{\rm T}^{\rm max} = 8$ GeV/c and with $p_{\rm T}^{\rm max} = 15$ GeV/c, while the latter results are very similar to the results obtained with $p_{\rm T}^{\rm max} = \infty$. Indeed, the cross-section at forward rapidity integrated over $0-15$ GeV/c represent 99.9% of the total cross-section (if one considers the fitted function). This allows to consider 15 GeV/c as a correct upper limit to extract the $p_{\rm T}$. However in the result, the range of integration is always specified.

Since the exact position of the bin centers is not known a priori, the ROOT option I is used when fitting the $p_{\rm T}$ -dependence of $d^2\sigma_{\rm pPb}/{\rm d}y{\rm d}p_{\rm T}$ (see Tables 7.4, 7.5). This option uses the integral of each bin when fitting.

The value obtained from the procedure described above correspond to the extracted $\langle p_{\rm T}\rangle$.

2nd step: The fit of $d^2\sigma_{\rm pPb}/{\rm d}y{\rm d}p_{\rm T}$ is then repeated using only the statistical uncertainties. Then using the fit function (7.6), a contour plot of 1σ on the parameters p_0 and n was obtained (the parameter C is fixed since it just affects the overall normalization not the $\langle p_{\rm T}\rangle$). To produce the contour plot, 2000 random points were generated. The $\langle p_{\rm T}\rangle$ was computed using (7.5) with these values of p_0 and n. A histogram was filled with this $\langle p_{\rm T}\rangle$ values. The statistical uncertainty on $\langle p_{\rm T}\rangle$ was then taken as the largest difference between the mean value obtained in the first step and the positions of the two peaks at the edge of the histogram mentioned above (Fig. 7.11).

3rd step: Finally, following the step 2, the fit of $d^2\sigma_{\rm pPb}/{\rm d}y{\rm d}p_{\rm T}$ was repeated using only the uncorrelated systematic uncertainties with $p_{\rm T}$. The obtained uncertainty is the systematic uncertainty on $\langle p_{\rm T}\rangle$. Note that the systematic uncertainties evaluated on $\langle p_{\rm T}\rangle$ are partially correlated with the event activity. The systematic uncertainties on the signal extraction and pile-up uncertainties are uncorrelated while the other systematics are considered as correlated.

The procedure described above is illustrated in Fig. 7.11.

For the $\langle p_{\rm T}^2\rangle$ calculation the procedure is similar to the one applied for the $\langle p_{\rm T}\rangle$ but with the following definition:

$$\langle p_{\rm T}^2\rangle = \frac{\int_0^{p_{\rm T}^{\rm max}} p_{\rm T}^2 f(p_{\rm T})\,{\rm d}p_{\rm T}}{\int_0^{p_{\rm T}^{\rm max}} f(p_{\rm T})\,{\rm d}p_{\rm T}} \tag{7.7}$$

Table 7.4. J/ψ $d^2\sigma_{\mathrm{pPb}}/\mathrm{d}y\mathrm{d}p_{\mathrm{T}}$ in p-Pb as a function of p_{T} (row) and event activity (column). The first quoted uncertainty is statistical and the second represents the uncorrelated systematic uncertainty.

p_{T} range	J/ψ $d^2\sigma_{\mathrm{pPb}}/\mathrm{d}y\mathrm{d}p_{\mathrm{T}}$ (μb/(GeV/c))							
	Event activity classes in percent							
(GeV/c)	0-100%	0-5%	5-10%	10-20%	20-40%	40-60%	60-80%	80-100%
0-1	76 ± 2 ± 4	8.5 ± 0.6 ± 0.6	7.3 ± 0.6 ± 0.5	12.2 ± 0.6 ± 0.7	20 ± 1 ± 1	14.6 ± 0.7 ± 0.8	9.5 ± 0.5 ± 0.5	5.1 ± 0.3 ± 0.3
1-2	156 ± 3 ± 8	16.2 ± 0.7 ± 0.9	13.8 ± 0.7 ± 0.7	25 ± 1 ± 1	41 ± 1 ± 2	31 ± 1 ± 2	19 ± 1 ± 1	8.9 ± 0.4 ± 0.5
2-3	134 ± 2 ± 7	15.3 ± 0.7 ± 0.8	13.9 ± 0.7 ± 0.8	20 ± 1 ± 1	37 ± 1 ± 2	25 ± 1 ± 1	16.3 ± 0.6 ± 0.9	6.1 ± 0.4 ± 0.4
3-4	89 ± 2 ± 5	9.9 ± 0.5 ± 0.6	8.5 ± 0.5 ± 0.5	14.4 ± 0.6 ± 0.8	24 ± 1 ± 1	16.5 ± 0.6 ± 0.9	11.5 ± 0.5 ± 0.7	4.2 ± 0.3 ± 0.2
4-5	52 ± 1 ± 3	6.3 ± 0.4 ± 0.4	4.9 ± 0.3 ± 0.2	8.0 ± 0.4 ± 0.5	14.2 ± 0.6 ± 0.8	10.1 ± 0.4 ± 0.5	6.3 ± 0.3 ± 0.4	2.3 ± 0.2 ± 0.1
5-6	29 ± 1 ± 1	3.4 ± 0.2 ± 0.2	2.9 ± 0.2 ± 0.1	5.5 ± 0.3 ± 0.3	7.6 ± 0.3 ± 0.4	5.5 ± 0.3 ± 0.3	3.2 ± 0.2 ± 0.2	0.95 ± 0.10 ± 0.05
6-8	11.5 ± 0.2 ± 0.6	1.30 ± 0.08 ± 0.08	1.15 ± 0.08 ± 0.07	2.0 ± 0.1 ± 0.1	3.2 ± 0.1 ± 0.2	2.2 ± 0.1 ± 0.1	1.28 ± 0.08 ± 0.07	0.37 ± 0.05 ± 0.02
8-15	1.56 ± 0.05 ± 0.08	0.148 ± 0.007 ± 0.009	0.17 ± 0.01 ± 0.01	0.29 ± 0.02 ± 0.02	0.44 ± 0.02 ± 0.03	0.32 ± 0.02 ± 0.02	0.17 ± 0.01 ± 0.01	0.039 ± 0.008 ± 0.003

where the fit function $f(p_{\mathrm{T}})$ is the same as in (7.6). The corresponding uncertainties are evaluated as for the $\langle p_{\mathrm{T}} \rangle$.

The same procedure is performed for calculating the $\langle p_{\mathrm{T}} \rangle$ value in pp at $\sqrt{s_{\mathrm{NN}}} = 5.02$ TeV using the interpolated p_{T}-dependence of $d^2\sigma_{\mathrm{pp}}/\mathrm{d}y\mathrm{d}p_{\mathrm{T}}$ from [218] (see Table 7.3). However all the uncertainties are quadratically combined for this calculation.

In Table 7.6 the results on $\langle p_{\mathrm{T}} \rangle$ and $\langle p_{\mathrm{T}}^2 \rangle$ are summarized for p-Pb and Pb-p data as well as for pp interpolated data, with different p_{T}-ranges (e.g. different $p_{\mathrm{T}}^{\mathrm{max}}$ used in (7.5) and (7.7)).

The $\langle p_{\mathrm{T}} \rangle$ and $\langle p_{\mathrm{T}}^2 \rangle$ values for the pp data at $\sqrt{s} = 2.76$ TeV and $\sqrt{s} = 7$ TeV were also extracted in order to compare the results of the present analysis with the published ones [54]. The results are presented in Table 7.7. The difference of the order of $\sqrt{2.3}$ in both statistical and systematic uncertainties

Table 7.5. J/ψ $d^2\sigma_{\mathrm{pPb}}/\mathrm{d}y\mathrm{d}p_{\mathrm{T}}$ distribution in Pb-p in μb/(GeV/c) as a function of p_{T} (row) and event activity (column). The first quoted uncertainty is statistical and the second represents the uncorrelated systematic uncertainty.

p_{T} range	J/ψ $d^2\sigma_{\mathrm{pPb}}/\mathrm{d}y\mathrm{d}p_{\mathrm{T}}$ (μb/(GeV/c))							
	Event activity classes in percent							
(GeV/c)	0-100%	0-5%	5-10%	10-20%	20-40%	40-60%	60-80%	80-100%
0-1	97 ± 2 ± 7	12.1 ± 0.8 ± 0.9	10.7 ± 0.8 ± 0.8	15 ± 1 ± 1	25 ± 1 ± 2	18 ± 1 ± 1	12.0 ± 0.7 ± 0.9	5.5 ± 0.4 ± 0.4
1-2	197 ± 3 ± 14	26 ± 1 ± 2	21 ± 1 ± 1	33 ± 1 ± 2	52 ± 1 ± 4	35 ± 1 ± 2	22 ± 1 ± 2	8.7 ± 0.5 ± 0.7
2-3	159 ± 2 ± 11	21 ± 1 ± 2	16 ± 1 ± 1	28 ± 1 ± 2	43 ± 1 ± 3	29 ± 1 ± 2	17 ± 1 ± 1	6.0 ± 0.3 ± 0.4
3-4	92 ± 2 ± 6	13.1 ± 0.7 ± 0.9	9.5 ± 0.6 ± 0.6	16 ± 1 ± 1	25 ± 1 ± 2	17 ± 1 ± 1	9.8 ± 0.4 ± 0.7	2.6 ± 0.2 ± 0.2
4-5	47 ± 1 ± 3	6.4 ± 0.4 ± 0.5	5.5 ± 0.4 ± 0.4	8.3 ± 0.4 ± 0.6	14.0 ± 0.5 ± 1.0	7.2 ± 0.4 ± 0.5	4.5 ± 0.3 ± 0.3	1.3 ± 0.1 ± 0.1
5-6	22 ± 1 ± 1	2.9 ± 0.2 ± 0.2	2.4 ± 0.2 ± 0.2	4.4 ± 0.2 ± 0.3	5.8 ± 0.3 ± 0.4	4.1 ± 0.2 ± 0.3	2.1 ± 0.2 ± 0.1	0.59 ± 0.09 ± 0.04
6-8	8.5 ± 0.2 ± 0.6	1.19 ± 0.08 ± 0.09	1.07 ± 0.09 ± 0.08	1.6 ± 0.1 ± 0.1	2.3 ± 0.1 ± 0.2	1.27 ± 0.09 ± 0.09	0.85 ± 0.07 ± 0.08	0.15 ± 0.03 ± 0.01
8-15	0.89 ± 0.04 ± 0.07	0.13 ± 0.01 ± 0.01	0.10 ± 0.01 ± 0.01	0.15 ± 0.02 ± 0.01	0.27 ± 0.02 ± 0.02	0.12 ± 0.02 ± 0.01	0.10 ± 0.02 ± 0.01	0.028 ± 0.007 ± 0.002

for $\langle p_{\mathrm{T}} \rangle$ and $\langle p_{\mathrm{T}}^2 \rangle$ between the published results and the new calculations comes from a different evaluation of the uncertainties in [54] where in the second and third step a contour plot of 2.3σ was used instead of 1σ.

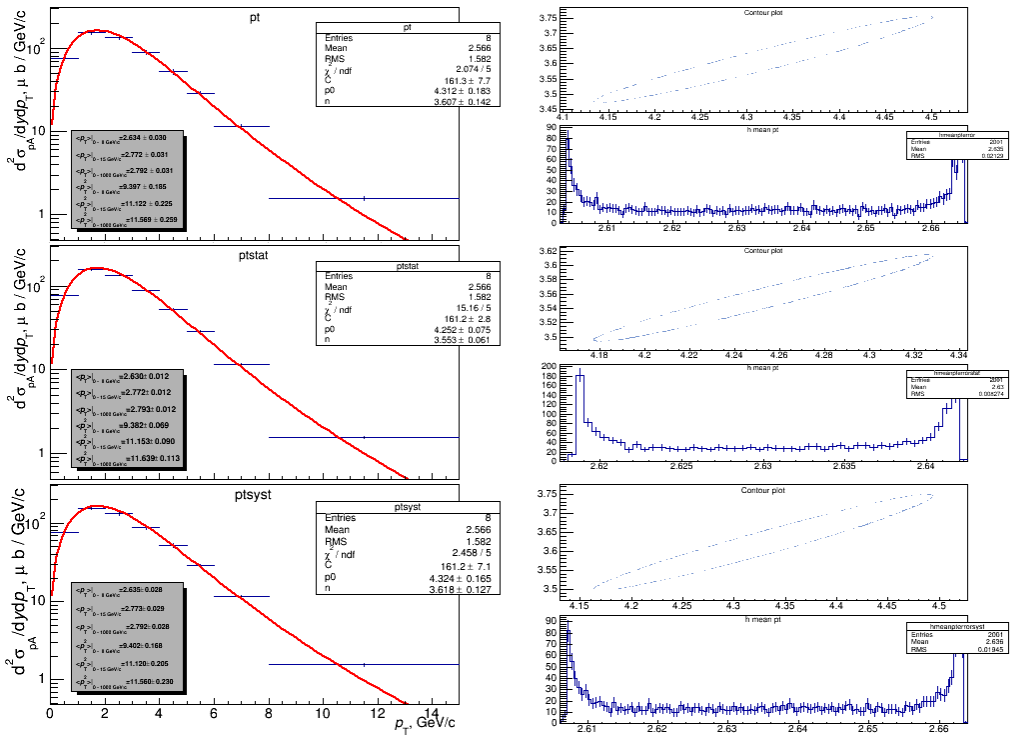

Figure 7.11. Example of $\langle p_{\mathrm{T}} \rangle$ calculation procedure for p-Pb at forward rapidity integrated over the event activity. Three rows of plots represent the fitting procedure performed considering the total uncertainties on the $d^2\sigma_{\mathrm{pp}}/\mathrm{d}y\mathrm{d}p_{\mathrm{T}}$ distribution (top row), only the statistical uncertainties (middle row) and only the systematic uncertainties (bottom row). The right two plots in each row show the 1σ contour plot on the parameters p_0 and n (top right plot in each row) and the corresponding histogram with $\langle p_{\mathrm{T}} \rangle$ values (bottom right plot in each row) used for the evaluation of the uncertainty (see text for details). The same procedure is used for $\langle p_{\mathrm{T}}^2 \rangle$ calculation.

Table 7.6. $\langle p_{\mathrm{T}} \rangle$ and $\langle p_{\mathrm{T}}^2 \rangle$ summary. First quoted uncertainty is statistical and second one is systematic. See text for details.

System	y_{cms} range	event activity	0-$p_{\mathrm{T}}^{\mathrm{max}}$, GeV/$c$	$\langle p_{\mathrm{T}} \rangle$, GeV/$c$	$\langle p_{\mathrm{T}}^2 \rangle$, (GeV/$c$)^2
pp	[2.96; 4.46]	0–100%	0–8	2.30 ± 0.03	7.33 ± 0.20
pp	[2.96; 4.46]	0–100%	0–15	2.37 ± 0.04	8.18 ± 0.30
pp	[2.96; 4.46]	0–100%	0–1000	2.38 ± 0.04	8.35 ± 0.40
pp	[2.03; 3.53]	0–100%	0–8	2.42 ± 0.04	8.06 ± 0.22
pp	[2.03; 3.53]	0–100%	0–15	2.52 ± 0.04	9.28 ± 0.40
pp	[2.03; 3.53]	0–100%	0–1000	2.53 ± 0.05	9.60 ± 0.62
p–Pb	[-4.46; -2.96]	0–100%	0–8	2.40 ± 0.01 ± 0.03	7.87 ± 0.06 ± 0.19
p–Pb	[-4.46; -2.96]	0–100%	0–15	2.47 ± 0.01 ± 0.03	8.73 ± 0.08 ± 0.21
p–Pb	[-4.46; -2.96]	0–100%	0–1000	2.48 ± 0.01 ± 0.03	8.87 ± 0.08 ± 0.21
p–Pb	[-4.46; -2.96]	0–5%	0–8	2.43 ± 0.03 ± 0.03	8.08 ± 0.17 ± 0.20
p–Pb	[-4.46; -2.96]	0–5%	0–15	2.51 ± 0.03 ± 0.03	9.04 ± 0.20 ± 0.22
p–Pb	[-4.46; -2.96]	0–5%	0–1000	2.52 ± 0.03 ± 0.03	9.20 ± 0.22 ± 0.22
p–Pb	[-4.46; -2.96]	5–10%	0–8	2.41 ± 0.03 ± 0.04	7.99 ± 0.19 ± 0.20
p–Pb	[-4.46; -2.96]	5–10%	0–15	2.50 ± 0.03 ± 0.04	9.02 ± 0.23 ± 0.24
p–Pb	[-4.46; -2.96]	5–10%	0–1000	2.51 ± 0.03 ± 0.04	9.23 ± 0.27 ± 0.25
p–Pb	[-4.46; -2.96]	10–20%	0–8	2.48 ± 0.02 ± 0.04	8.30 ± 0.14 ± 0.20
p–Pb	[-4.46; -2.96]	10–20%	0–15	2.55 ± 0.03 ± 0.04	9.16 ± 0.17 ± 0.22
p–Pb	[-4.46; -2.96]	10–20%	0–1000	2.55 ± 0.03 ± 0.04	9.27 ± 0.19 ± 0.22
p–Pb	[-4.46; -2.96]	20–40%	0–8	2.43 ± 0.02 ± 0.03	8.04 ± 0.10 ± 0.18
p–Pb	[-4.46; -2.96]	20–40%	0–15	2.51 ± 0.02 ± 0.03	8.97 ± 0.14 ± 0.21
p–Pb	[-4.46; -2.96]	20–40%	0–1000	2.51 ± 0.02 ± 0.03	9.12 ± 0.15 ± 0.22
p–Pb	[-4.46; -2.96]	40–60%	0–8	2.35 ± 0.02 ± 0.03	7.50 ± 0.12 ± 0.18
p–Pb	[-4.46; -2.96]	40–60%	0–15	2.40 ± 0.02 ± 0.03	8.16 ± 0.15 ± 0.20
p–Pb	[-4.46; -2.96]	40–60%	0–1000	2.41 ± 0.02 ± 0.03	8.24 ± 0.16 ± 0.19
p–Pb	[-4.46; -2.96]	60–80%	0–8	2.30 ± 0.03 ± 0.03	7.32 ± 0.15 ± 0.19
p–Pb	[-4.46; -2.96]	60–80%	0–15	2.37 ± 0.03 ± 0.03	8.19 ± 0.21 ± 0.24
p–Pb	[-4.46; -2.96]	60–80%	0–1000	2.38 ± 0.03 ± 0.03	8.38 ± 0.25 ± 0.28
p–Pb	[-4.46; -2.96]	80–100%	0–8	2.04 ± 0.04 ± 0.03	5.88 ± 0.19 ± 0.15
p–Pb	[-4.46; -2.96]	80–100%	0–15	2.09 ± 0.04 ± 0.03	6.45 ± 0.28 ± 0.17
p–Pb	[-4.46; -2.96]	80–100%	0–1000	2.09 ± 0.04 ± 0.03	6.59 ± 0.34 ± 0.18
p–Pb	[2.03; 3.53]	0–100%	0–8	2.63 ± 0.01 ± 0.03	9.40 ± 0.07 ± 0.17
p–Pb	[2.03; 3.53]	0–100%	0–15	2.77 ± 0.01 ± 0.03	11.12 ± 0.09 ± 0.20
p–Pb	[2.03; 3.53]	0–100%	0–1000	2.79 ± 0.01 ± 0.03	11.57 ± 0.11 ± 0.23
p–Pb	[2.03; 3.53]	0–5%	0–8	2.69 ± 0.03 ± 0.03	9.69 ± 0.19 ± 0.20
p–Pb	[2.03; 3.53]	0–5%	0–15	2.81 ± 0.03 ± 0.03	11.13 ± 0.21 ± 0.23
p–Pb	[2.03; 3.53]	0–5%	0–1000	2.82 ± 0.03 ± 0.03	11.34 ± 0.21 ± 0.23

System	y_{cms} range	event activity	0-$p_{\mathrm{T}}^{\mathrm{max}}$, GeV/$c$	$\langle p_{\mathrm{T}} \rangle$, GeV/$c$	$\langle p_{\mathrm{T}}^2 \rangle$, (GeV/$c$)^2
p–Pb	[2.03; 3.53]	5–10%	0–8	2.67 ± 0.03 ± 0.03	9.63 ± 0.20 ± 0.19
p–Pb	[2.03; 3.53]	5–10%	0–15	2.82 ± 0.04 ± 0.03	11.56 ± 0.28 ± 0.24
p–Pb	[2.03; 3.53]	5–10%	0–1000	2.85 ± 0.04 ± 0.03	12.11 ± 0.38 ± 0.28
p–Pb	[2.03; 3.53]	10–20%	0–8	2.67 ± 0.03 ± 0.03	9.68 ± 0.16 ± 0.18
p–Pb	[2.03; 3.53]	10–20%	0–15	2.84 ± 0.03 ± 0.03	11.75 ± 0.21 ± 0.24
p–Pb	[2.03; 3.53]	10–20%	0–1000	2.87 ± 0.03 ± 0.03	12.43 ± 0.29 ± 0.32
p–Pb	[2.03; 3.53]	20–40%	0–8	2.65 ± 0.02 ± 0.03	9.51 ± 0.12 ± 0.17
p–Pb	[2.03; 3.53]	20–40%	0–15	2.80 ± 0.02 ± 0.03	11.33 ± 0.16 ± 0.23
p–Pb	[2.03; 3.53]	20–40%	0–1000	2.82 ± 0.02 ± 0.03	11.83 ± 0.21 ± 0.31
p–Pb	[2.03; 3.53]	40–60%	0–8	2.62 ± 0.02 ± 0.03	9.35 ± 0.14 ± 0.17
p–Pb	[2.03; 3.53]	40–60%	0–15	2.77 ± 0.02 ± 0.03	11.23 ± 0.18 ± 0.22
p–Pb	[2.03; 3.53]	40–60%	0–1000	2.80 ± 0.02 ± 0.03	11.83 ± 0.24 ± 0.26
p–Pb	[2.03; 3.53]	60–80%	0–8	2.60 ± 0.03 ± 0.03	9.14 ± 0.15 ± 0.17
p–Pb	[2.03; 3.53]	60–80%	0–15	2.72 ± 0.03 ± 0.03	10.63 ± 0.20 ± 0.20
p–Pb	[2.03; 3.53]	60–80%	0–1000	2.73 ± 0.03 ± 0.03	10.95 ± 0.25 ± 0.23
p–Pb	[2.03; 3.53]	80–100%	0–8	2.36 ± 0.04 ± 0.03	7.65 ± 0.20 ± 0.16
p–Pb	[2.03; 3.53]	80–100%	0–15	2.44 ± 0.04 ± 0.03	8.59 ± 0.28 ± 0.18
p–Pb	[2.03; 3.53]	80–100%	0–1000	2.45 ± 0.04 ± 0.03	8.78 ± 0.34 ± 0.18

Table 7.7. $\langle p_{\mathrm{T}} \rangle$ and $\langle p_{\mathrm{T}}^2 \rangle$ summary for pp collisions at $\sqrt{s_{\mathrm{NN}}} = 2.76$ TeV and 7 TeV compared to the published values from [54]. First quoted uncertainty is statistical and the second one is systematic. See text details.

$\sqrt{s_{\mathrm{NN}}}$, TeV	0-$p_{\mathrm{T}}^{\mathrm{max}}$, GeV/$c$	$\langle p_{\mathrm{T}} \rangle$, GeV/$c$	$\langle p_{\mathrm{T}}^2 \rangle$, (GeV/$c$)^2	source
2.76	0–8	2.28 ± 0.07 ± 0.04	7.06 ± 0.40 ± 0.22	published
2.76	0–8	2.28 ± 0.04 ± 0.03	7.06 ± 0.26 ± 0.13	new
2.76	0–15	2.32 ± 0.05 ± 0.02	7.50 ± 0.40 ± 0.14	new
2.76	0–1000	2.32 ± 0.05 ± 0.02	7.53 ± 0.44 ± 0.15	new
7	0–8	2.44 ± 0.09 ± 0.06	8.32 ± 0.50 ± 0.35	published
7	0–8	2.45 ± 0.06 ± 0.04	8.36 ± 0.35 ± 0.24	new
7	0–15	2.60 ± 0.08 ± 0.06	10.33 ± 0.82 ± 0.73	new
7	0–1000	2.65 ± 0.10 ± 0.10	11.45 ± 1.31 ± 1.99	new

7.5.2 SPD pile-up effect on $< p_T >$ extraction

The effect of pile-up on the $\langle p_{\mathrm{T}} \rangle$ using different options of the SPD pile-up tagging method was studied. One option was chosen to quantify the pile-up effect on the extracted signal and $\langle p_{\mathrm{T}} \rangle$.

The p_{T} dependent cross sections are shown in Fig.7.12 when removing events tagged as SPD pile-up events.

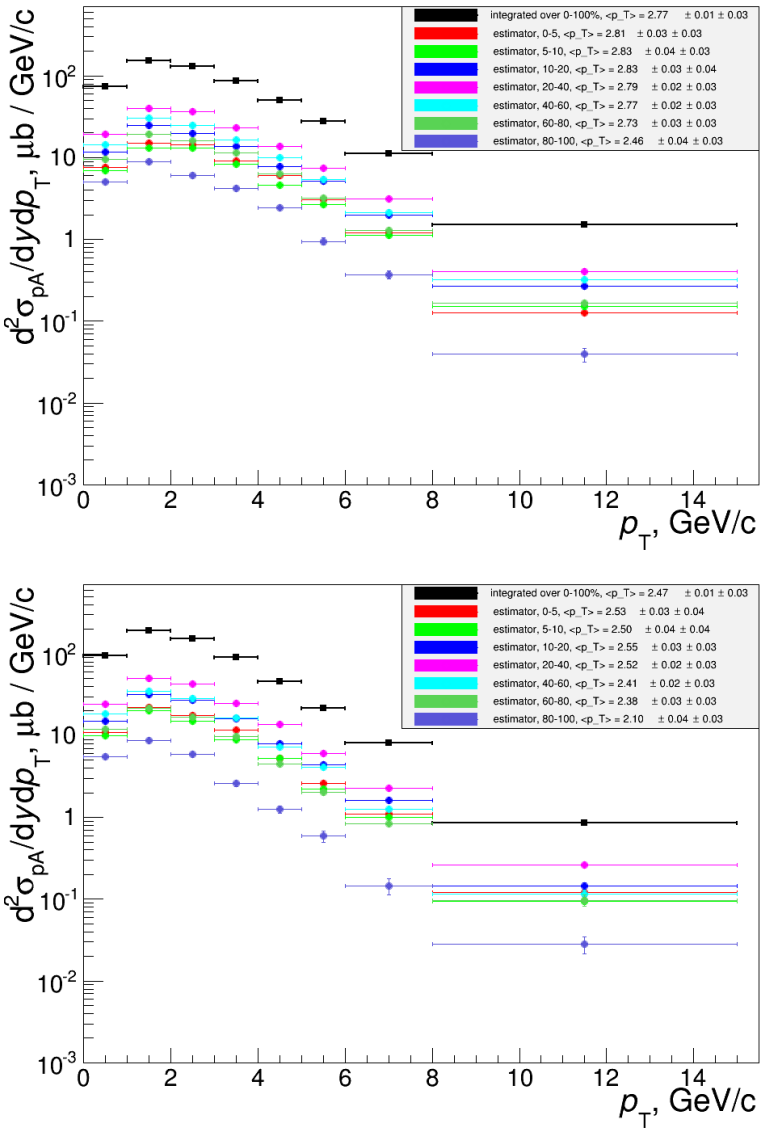

Figure 7.12. $d^2\sigma_{\mathrm{pPb}}/\mathrm{d}y\mathrm{d}p_{\mathrm{T}}$ as a function of p_{T} for different V0A event activity classes in p-Pb (top) and Pb-p (bottom), with SPD pile-up cut: $n = 5$, $d = 6mm$

Procedures of calculation of $\langle p_{\mathrm{T}} \rangle$ described in the previous section were performed for each V0A event activity bins. The result is shown in Fig. 7.13, for both p-Pb and Pb-p with $n = 5$, $d = 6mm$ SPD pile-up cut and without pile-up cut.

Removing or not the SPD pile-up events does not affect the $\langle p_{\mathrm{T}} \rangle$ values. The difference between $\langle p_{\mathrm{T}} \rangle$ calculated with and without pile-up cut could be considered as an additional systematic uncertainty uncorrelated with the the event activity classes. However it was not included in the final results since its effect on the $\langle p_{\mathrm{T}} \rangle$ and $\langle p_{\mathrm{T}}^2 \rangle$ is negligible compared to the statistical and systematic uncertainties.

7.6 Systematic uncertainties

The systematic uncertainties evaluations for the p_{T} distributions are similar to those described in the Section 6.8.

For the $\langle p_{\mathrm{T}} \rangle$ extraction, the systematics include uncertainties on the signal extraction, MC parametrization, tracking, trigger and matching efficiency.

Tab.7.8 shows the sharing between the uncorrelated, the correlated and the partially correlated systematic uncertainties for different results.

The main difference with respect to the previous analysis is the new observable, event activity. The dependence of the systematic uncertainties on this observable is discussed below.

Such components of the systematic uncertainty as BR uncertainty, Glauber uncertainty on T_{pPb}, uncertainty from the luminosity and all different types of uncertainties on the $\sigma_{\mathrm{pp}}^{\mathrm{J}/\psi}$ do not depend on the event activity due to their nature. No dependence of the detectors efficiency with the event activity is expected, therefore the same $A\epsilon$ value is used for different event activity classes. Corresponding systematic uncertainties on the matching, trigger and tracking efficiency thus also do not depend on the event activity.

Signal extraction systematic uncertainty is dependent on the event activity by its definition. The same stands for the MC inputs. F_{norm} systematic uncertainty was considered as dependent on the event activity. In this way, it better reflects the fact that the ZN event activity distribution is not completely flat. Model uncertainty on T_{pPb} also depends on the event activity since it is based on T_{pPb} from different hypotheses, estimated in each event activity class.

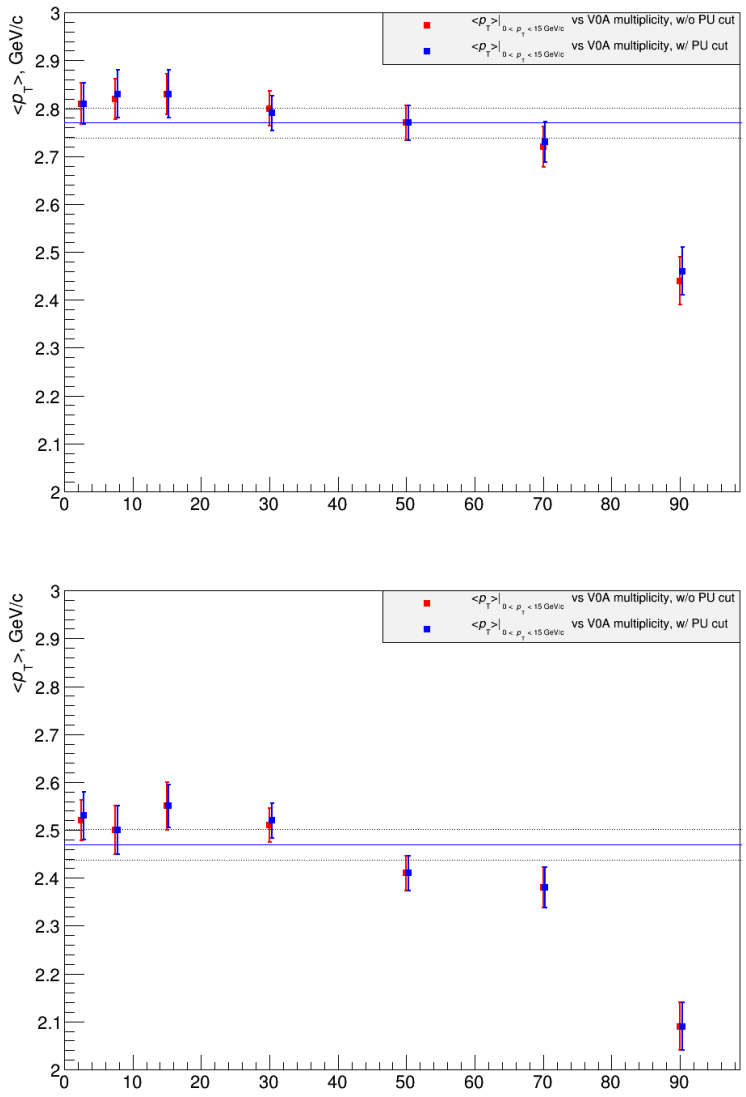

Figure 7.13. $\langle p_{\mathrm{T}} \rangle$ as a function of the V0A event activity in p-Pb (top) and Pb-p (bottom). Blue (Red) points correspond to the calculations with SPD pile-up cut (without SPD pile-up cut).

Table 7.8. Summary on the systematic uncertainties.

Source	Q_{pPb} vs event activity	$d^2\sigma_{\mathrm{pPb}}/\mathrm{d}y\mathrm{d}p_{\mathrm{T}}$ vs p_{T} in event activity bins	Q_{pPb} vs p_{T} in event activity
BR	global	global	global
Glauber uncertainty on the T_{pPb}		—	
Corr. unc. on $\sigma_{pp}^{J\psi}$		—	
Model uncertainty on T_{pPb}	uncorrelated	—	Partially correlated
Signal extraction	uncorrelated		
F_{Norm}			
Acc. inputs			
Part. corr. unc. on $\sigma_{pp}^{J\psi}$	Correlated in p-Pb or Pb-p, but partially correlated when considering the two periods together	—	Partially correlated
Uncorr. unc. on $\sigma_{pp}^{J\psi}$		—	uncorrelated
matching		uncorrelated	
trigger efficiency			
tracking			
luminosity		global	global in p-Pb or Pb-p, but partially correlated when considering the two periods together

Chapter 8

Results

This chapter presents the results of the analyses described in the two previous chapters. These results include the J/ψ nuclear modification factor as a function of rapidity, as a function of the event activity and as a function of both p_{T} and the event activity, as well as the forward-to-backward ratio as a function of rapidity and p_{T} in p-Pb collisions. From the p_{T} and event activity dependence, I also extracted the $\langle p_{\mathrm{T}} \rangle$ and $\langle p_{\mathrm{T}}^2 \rangle$ as a function of the event activity. Results of other ALICE analyses, where I was involved, are also presented in this chapter: the p_{T} dependence of the J/ψ nuclear modification factor and the ψ(2S) production measurements in p-Pb collisions. The results are compared to the theoretical models described in Chapter 3. Finally the p-Pb measurements allow an estimation of the contribution of the CNM to the Pb-Pb measurements and this is also discussed.

8.1 p_{T} and y dependence of the J/ψ production

The results on cross section, nuclear modification factor and forward-to-backward ratio are presented below. As stated previously, the following convention was defined: the rapidity is defined according to the proton beam direction. The muon spectrometer provides access to positive rapidity in p-Pb and negative in Pb-p. This is motivated by the x value of the probed gluon in the nucleus. In p-Pb configuration (corresponding to positive rapidity results), the Pb beam is coming from the muon spectrometer side and the J/ψ detected in the muon spectrometer are produced from gluons in the Pb beam with x values of the order of $5 \cdot 10^{-5}$, while in Pb-p configuration (corresponding to negative rapidity results), x values of the gluons probed in the Pb beam are of the order of $2 \cdot 10^{-2}$. The results presented in this chapter are published in [219]. In the following we will use p-Pb (Pb-p) to denote the forward (backward) rapidity configuration.

8.1.1 Inclusive J/ψ cross section measurement

8.1.1.1 Inclusive J/ψ cross section integrated over $p_{\rm T}$ and y

The integrated cross sections are given in Tab.8.1. The uncorrelated systematics include the uncertainties on tracking, trigger, matching and on the MC parametrization. The systematic uncertainties on signal extraction, branching ratio, CINT7-CMUL7 normalization and the MB cross section are either fully or partially correlated between the backward and forward rapidity results. The quadratic sum of these uncertainties is quoted as partially correlated.

$y_{\rm cms}$ range	σ_{int} (μb)	systematic uncertainties (μb)	
		uncorrelated	partially correlated
$[-4.46; -2.96]$	966 ± 8	70	31
$[2.03; 3.53]$	886 ± 6	48	30

Table 8.1. Inclusive J/ψ cross section integrated over rapidity and $p_{\rm T}$ in two rapidity ranges for $0 \leq p_{\rm T} \leq 15$ GeV/c.

8.1.1.2 Rapidity dependence of the inclusive J/ψ cross section

The rapidity dependence of the inclusive J/ψ cross section in p-Pb collisions is presented in Fig.8.1 and is given in Tab.8.2 where 6 intervals in rapidity are defined. A significant y dependence of the inclusive J/ψ production in p-Pb collisions is found. The J/ψ cross section increases towards the lower $|y_{\rm cms}|$. The J/ψ cross section is larger at backward than at forward rapidity by $\sim 20\%$. The pp cross section interpolated at $\sqrt{s_{\rm NN}} = 5.02$ TeV and scaled by the Pb-nucleus atomic mass number, is shown with its derived uncertainties as a blue band. At backward rapidity the J/ψ cross section in p-Pb collisions is similar to the scaled pp cross section while at forward rapidity the J/ψ p-Pb cross section is smaller than the scaled pp one.

A comparison of the ALICE measurements with the LHCb data [220] is presented in Fig.8.2. A good agreement is reached for $y_{\rm cms} \geq 2.5$ and $y_{\rm cms} \leq -3$ while the ALICE data points are systematically higher with respect to those of LHCb for $y_{\rm cms} < 2.5$ and $y_{\rm cms} > -3$ by $\sim$10%. Both measurements are however in agreement within 1σ.

8.1.2 Inclusive J/ψ nuclear modification factor

8.1.2.1 $p_{\rm T}$ and y integrated $R_{\rm pPb}$

The inclusive J/ψ $R_{\rm pPb}$ measured by ALICE at $\sqrt{s_{\rm NN}} = 5.02$ TeV and integrated in the range $-4.46 \leq y_{\rm cms} \leq -2.96$ ($2.03 \leq y_{\rm cms} \leq 3.53$) and for

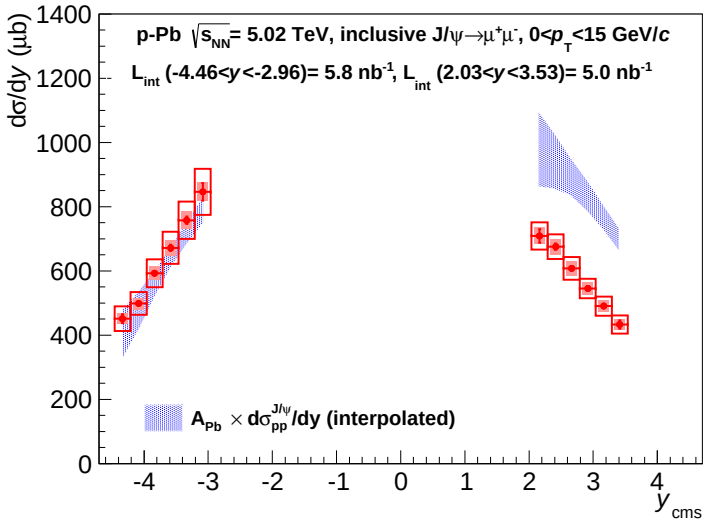

Figure 8.1. Rapidity dependence of the inclusive J/ψ cross section. The error bars correspond to the statistical uncertainties, the open boxes to the uncorrelated and the shaded boxes to the partially correlated systematic uncertainties. The bands are the inclusive J/ψ cross section obtained with an interpolation procedure as described in Section 6.7 and scaled by the Pb-nucleus atomic mass number. From [219].

$0 \leq p_{\mathrm{T}} \leq 15$ GeV/c is shown in Fig.8.3 and presented in Tab.8.3. The uncorrelated systematics (open boxes) include the normalization, matching, trigger, tracking and MC parametrization uncertainties. The partially correlated systematics (shaded boxes) with the collision system include the uncertainty on the yield extraction and the pp reference. Finally the fully correlated uncertainty (grey box at unity) includes the uncertainty on the nuclear overlap function.

y_{cms} range	$\frac{d\sigma}{dy}$ (μb)	systematic uncertainies (μb)	
		partially correlated	uncorrelated
$[-4.46; -4.21]$	457 ± 14	15	39
$[-4.21; -3.96]$	504 ± 9	17	36
$[-3.96; -3.71]$	599 ± 9	20	44
$[-3.71; -3.46]$	680 ± 10	23	51
$[-3.46; -3.21]$	767 ± 12	25	59
$[-3.21; -2.96]$	856 ± 28	28	72
$[2.03; 2.28]$	721 ± 22	24	44
$[2.28; 2.53]$	687 ± 11	23	40
$[2.53; 2.78]$	618 ± 8	21	37
$[2.78; 3.03]$	554 ± 8	19	31
$[3.03; 3.28]$	498 ± 9	17	31
$[3.28; 3.53]$	440 ± 13	15	29

Table 8.2. Rapidity dependence of the cross section for the inclusive J/ψ production for $0 \leq p_{\mathrm{T}} \leq 15$ GeV/c.

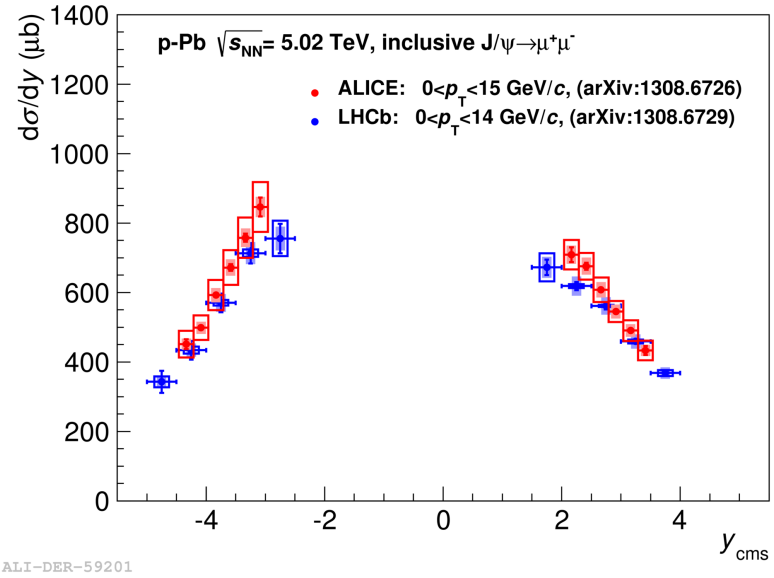

Figure 8.2. Rapidity dependence of the inclusive J/ψ cross section for ALICE (red points) and LHCb (blue points). The error bars correspond to the statistical uncertainties, the open boxes to the uncorrelated and the shaded boxes to the partially correlated systematic uncertainties. The LHCb inclusive cross section has been obtained summing contributions from B feed down and prompt J/ψ [220].

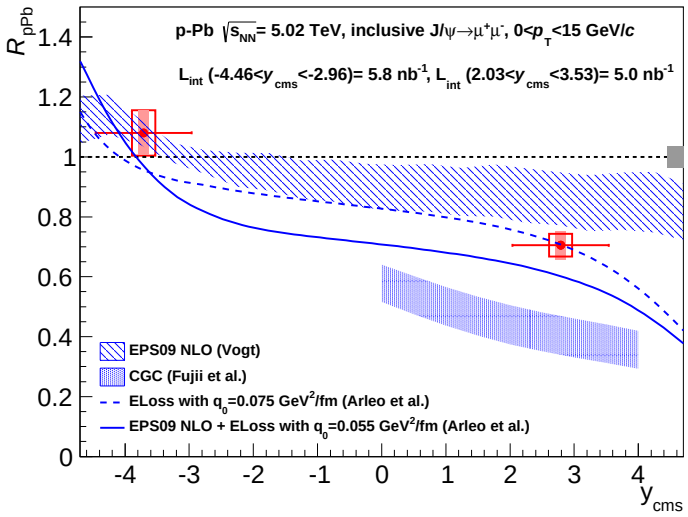

Figure 8.3. Integrated R_{pPb} in p-Pb ($y \geq 0$) and Pb-p ($y \leq 0$). The error bars correspond to the statistical uncertainties, the open boxes to the uncorrelated systematic uncertainties, the shaded boxes around the point to the partially correlated systematic uncertainties and the box around $R_{\mathrm{pPb}} = 1$ to the size of the correlated systematic uncertainties. Theoretical predictions: EPS09 NLO [221], CGC [125], coherent parton energy loss model [133]. From [219].

The results are compared to theoretical predictions of the following models: NLO CEM calculation with the EPS09 shadowing parametrization [221], model including coherent parton energy loss contribution [133] either in addition to EPS09 shadowing or as the only nuclear effect, CGC-based model[1]

[1]It is assumed in the presented CGC-based model that the quark pair produced from dense small-x gluons in the nuclear target bounds into a quarkonium outside the target.

combined with a CEM production model [125]. Both shadowing and coherent parton energy loss models describe well the data within the experimental uncertainties, while the CGC-based prediction overestimates the J/ψ suppression. Theoretical uncertainties of the EPS09 NLO model are related to the EPS09 shadowing parametrization and to the mass and scale uncertainties on the cross section. The band for the CGC corresponds to the uncertainty from the choice of the parton saturation scale and of the charm quark mass. The parameter q_0 is the transport coefficient defined in (3.10). None of the models includes a suppression related to the break-up of the $c\bar{c}$ pair. It allows to conclude that the inclusive J/ψ production in p-Pb collisions at the LHC energies can be reproduced by the models without the nuclear absorption contribution.

Theoretical predictions are done for the prompt J/ψ (direct J/ψ plus contribution from ψ(2S) and χ_c decays) while the ALICE measurements are for the inclusive J/ψ production (prompt J/ψ plus non-prompt contribution from B-decays). However it was shown by LHCb that the $p_{\rm T}$-integrated non-prompt J/ψ fraction is small: 7.1% at $\sqrt{s_{\rm NN}} = 2.76$ TeV in pp collisions in the kinematic range $2 < y_{\rm cms} < 4.5$, $p_{\rm T} < 12$ GeV/c [222] and 9.8% at $\sqrt{s_{\rm NN}} = 7$ TeV in pp collisions for $2 < y_{\rm cms} < 4.5$, $p_{\rm T} < 14$ GeV/c [223]. The difference between the inclusive and the prompt $R_{\rm pPb}$ stays within uncertainties for a very large range of $R_{\rm pPb}^{\rm non-prompt}$, from almost complete suppression ($R_{\rm pPb}^{\rm non-prompt} = 0.2$) to a strong enhancement ($R_{\rm pPb}^{\rm non-prompt} = 1.3$) [219]. This is true for the forward and backward rapidity regions.

$y_{\rm cms}$	$R_{\rm pPb}$	systematic uncertainties		
		partially correlated	uncorrelated	fully correlated
$[-4.46; -2.96]$	1.08 ± 0.01	0.03	0.09	0.07
$[2.03; 3.53]$	0.70 ± 0.01	0.03	0.05	0.05

Table 8.3. Integrated nuclear modification factor for inclusive J/ψ production for $0 \leq p_{\rm T} \leq 15$ GeV/c.

8.1.2.2 Rapidity dependence of $R_{\rm pPb}$

The inclusive J/ψ $R_{\rm pPb}$ was measured for six intervals in rapidity in each period of data taking as shown in Fig.8.4 and given in Tab.8.4.

Large uncertainties at the edges of the rapidity ranges correspond to the large uncertainty of the interpolated pp cross section extrapolated outside the y-range $2.5 < |y_{\rm cms}| < 4$ (see details in Section 6.7). The $R_{\rm pPb}$ is consistent with a constant at backward rapidity. The models described above are also shown.

An assumption of dilute-dense colliding system applies only in the positive rapidity region ($y > 0$), especially for pp , which is needed in the denominator of the $R_{\rm pPb}$ [125].

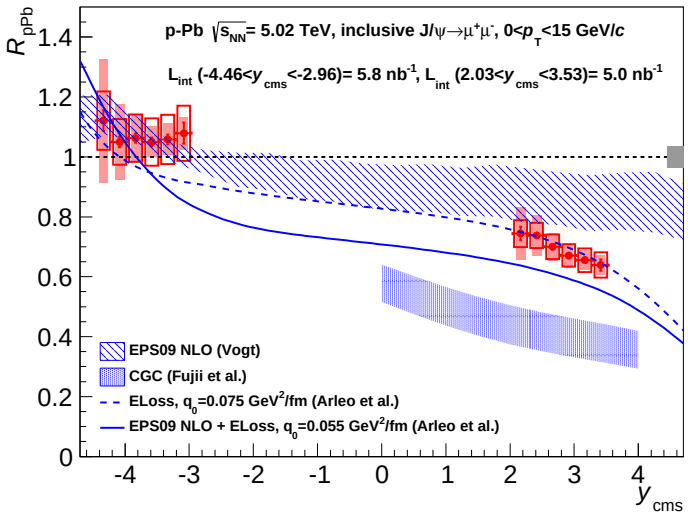

Figure 8.4. R_{pPb} as a function of rapidity in p-Pb collisions. The error bars correspond to the statistical uncertainties, the open boxes to the uncorrelated, the shaded boxes around the point to the partially correlated and the box around $R_{\mathrm{pPb}} = 1$ to the correlated systematic uncertainties. The models are the same as in Fig.8.3. From [219].

Both calculations of the energy loss model well describe the data within the experimental uncertainties while they predict a steeper behaviour of R_{pPb} at backward rapidity. At forward rapidity both configurations agree with the data in both the shape and the amplitude of R_{pPb}. EPS09 NLO model also shows a fair agreement with the experimental measurements but slightly overestimates the R_{pPb} at forward rapidity. CGC-based model significantly underestimates the measured R_{pPb} at forward rapidity for the full rapidity range.

$y_{\rm cms}$	$R_{\rm pPb}$	systematic uncertainties (μb)	
		uncorrelated	partially correlated
$[-4.46; -4.21]$	1.12 ± 0.04	0.18	0.09
$[-4.21; -3.96]$	1.05 ± 0.02	0.12	0.05
$[-3.96; -3.71]$	1.06 ± 0.02	0.10	0.02
$[-3.71; -3.46]$	1.05 ± 0.02	0.09	0.02
$[-3.46; -3.21]$	1.06 ± 0.02	0.09	0.03
$[-3.21; -2.96]$	1.08 ± 0.04	0.10	0.03
$[2.03; 2.28]$	0.74 ± 0.02	0.06	0.07
$[2.28; 2.53]$	0.74 ± 0.01	0.06	0.05
$[2.53; 2.78]$	0.70 ± 0.01	0.05	0.02
$[2.78; 3.03]$	0.67 ± 0.01	0.05	0.02
$[3.03; 3.28]$	0.65 ± 0.01	0.05	0.02
$[3.28; 3.53]$	0.64 ± 0.02	0.05	0.02

Table 8.4. Rapidity dependence of the nuclear modification factor for inclusive J/ψ production for $0 \leq p_{\rm T} \leq 15$ GeV/c.

8.1.3 Forward to Backward ratio

In order to cancel out the pp interpolated cross section and its associated systematic uncertainties, the forward to backward ratio $R_{\rm FB}$ is defined:

$$R_{\rm FB}(2.96 \leq y_{\rm cms} \leq 3.53) = \frac{Y^{\rm pPb}_{\rm J/\psi}(\Delta p_{\rm T}, 3.43 \leq y_{\rm lab} \leq 4)}{Y^{\rm Pbp}_{\rm J/\psi}(\Delta p_{\rm T}, -3.07 \leq y_{\rm lab} \leq -2.5)}. \tag{8.1}$$

In this ratio, the nuclear overlap function $T_{\rm pPb}$ also cancels out. This ratio is defined in the common rapidity range $2.96 \leq y_{\rm cms} \leq 3.53$ which corresponds to a rapidity range of $3.43 \leq y_{\rm lab} \leq 4$ in p-Pb and of $-3.07 \leq y_{\rm lab} \leq -2.5$ in Pb-p. Due to the reduced y-range used for the $R_{\rm FB}$ calculation, the statistics is reduced by a factor ~ 3. It should be also noted, that even if a theoretical model shows a good agreement with the measured $R_{\rm FB}$, it does not necessary mean that it also describes correctly the corresponding invariant yields in both rapidity ranges. In particular, it can be the case for the models which globally overestimate/underestimate the nuclear modification factors.

8.1.3.1 $p_{\rm T}$ and y integrated $R_{\rm FB}$

The inclusive J/ψ $R_{\rm FB}$ in p-Pb collisions at $\sqrt{s_{\rm NN}} = 5.02$ TeV measured in the range $2.96 \leq y_{\rm cms} \leq 3.53$ and $0 \leq p_{\rm T} \leq 15$ GeV/c is 0.60 ± 0.01(stat.) $\pm$ 0.06(syst.). The systematic uncertainties uncorrelated between p-Pb and Pb-p data samples (tracking, matching and trigger efficiency, normalization, MC

input) have been quadratically combined. The signal extraction uncertainties have been calculated directly from the ratio of the number of J/ψ. The total uncertainty on the R_{FB} ratio is dominated by the tracking efficiency uncertainty.

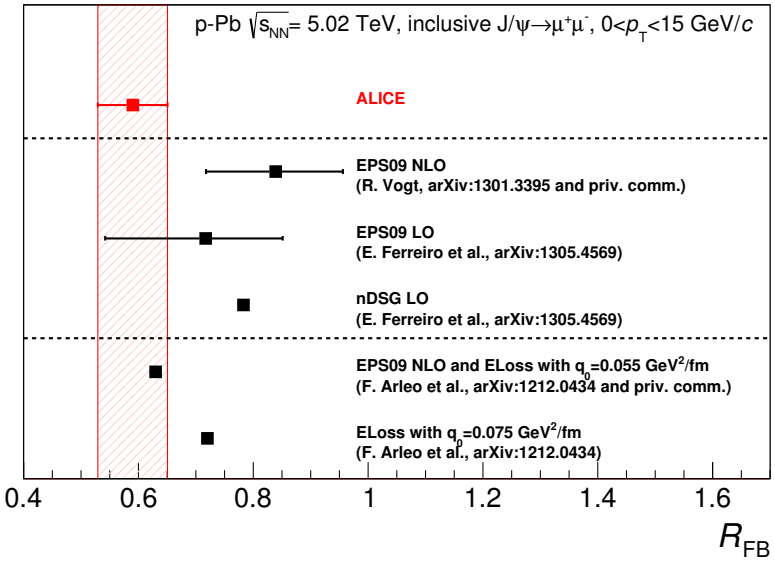

Figure 8.5. R_{FB} integrated over p_{T} and y . The experimental error bar corresponds to the statistical and systematic uncertainties added in quadrature. The uncertainties on the shadowing calculations are given when available. See text for details. From [219].

In Fig.8.5 the R_{FB} is compared to theoretical predictions from the models described above. CGC-based model results are not presented since it gives prediction only at forward rapidity. One additional model, based on the LO approach, implementing $2 \rightarrow 2$ kinematics ($gg \rightarrow \mathrm{J}/\psi g$) and using either the EPS09 or the nDSG shadowing parametrization [224], is shown in the figure. The model including both energy loss and shadowing predicts a value consistent with the data within the experimental uncertainties. Pure shadowing or pure energy loss model seem to overestimate the R_{FB} ratio, except the EPS09 LO model which has a larger theoretical uncertainty which fully includes the measured R_{FB} with its total experimental uncertainty.

8.1.3.2 Transverse momentum dependence of the R_{FB} ratio

The transverse momentum dependence of inclusive J/ψ R_{FB} measured in p-Pb collisions at $\sqrt{s_{\mathrm{NN}}} = 5.02$ TeV, integrated in the range $2.96 \leq y_{\mathrm{cms}} \leq 3.53$ is shown in Fig.8.6 and is given in Tab.8.5 for 10 intervals in p_{T}. An increase of the R_{FB} from 0.62 to 0.95 is seen with increasing p_{T}.

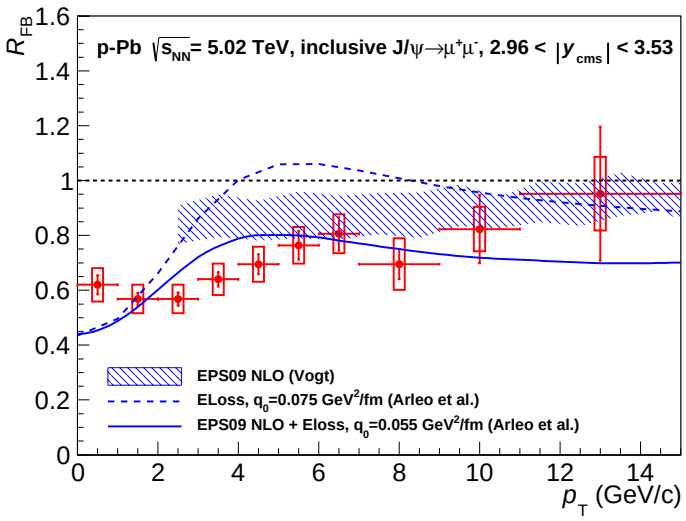

Figure 8.6. R_{FB} as a function of p_{T}. The error bars correspond to the statistical uncertainties, the open boxes to the uncorrelated systematic uncertainties. From [219].

It is compared to two models with the energy loss contribution [225] and to the EPS09 NLO model [221]. The energy loss model is in fair agreement with the data, when including the shadowing contribution. Pure shadowing model is in agreement with the data for $p_{\mathrm{T}} > 5$ GeV/c, while at lower p_{T} ($2.5 < p_{\mathrm{T}} < 5$ GeV/c) it predicts a higher R_{FB} ratio than seen in the data.

8.1.3.3 Rapidity dependence of R_{FB}

The rapidity dependence of inclusive J/ψ R_{FB} measured in p-Pb collisions at $\sqrt{s_{\mathrm{NN}}} = 5.02$ TeV in the rapidity range $2.96 \leq y_{\mathrm{cms}} \leq 3.53$ is shown in

y_{cms}	R_{FB}	systematic uncertainty
$[0;1]$	0.62 ± 0.04	0.06
$[1;2]$	0.57 ± 0.02	0.05
$[2;3]$	0.57 ± 0.02	0.05
$[3;4]$	0.64 ± 0.03	0.06
$[4;5]$	0.70 ± 0.04	0.06
$[5;6]$	0.76 ± 0.05	0.07
$[6;7]$	0.81 ± 0.06	0.07
$[7;9]$	0.70 ± 0.06	0.09
$[9;11]$	0.82 ± 0.13	0.08
$[11;15]$	0.95 ± 0.24	0.13

Table 8.5. p_{T} dependence of the R_{FB} for inclusive J/ψ production for $2.96 \leq y_{\mathrm{cms}} \leq 3.53$.

Fig.8.7 and is given in Tab.8.6 for three rapidity bins. In this narrow y-range it shows almost no rapidity dependence. The rapidity dependence of the models which are consistent with the integrated R_{FB}, show also a fair agreement with the y dependence of the R_{FB}. The energy loss model including the shadowing contribution predicts a slight decrease of the R_{FB} with the increase of y. This behaviour is also in fair agreement with the data within the experimental uncertainties. Other models also predict a slight decrease of the R_{FB} with the increase of y. However the large theoretical uncertainties do not allow to conclude more.

y_{cms}	R_{FB}	systematic uncertainty
$[2.96;3.15]$	0.58 ± 0.03	0.06
$[3.15;3.34]$	0.60 ± 0.03	0.05
$[3.34;3.53]$	0.61 ± 0.03	0.06

Table 8.6. Rapidity dependence of the R_{FB} for inclusive J/ψ production for $0 \leq p_{\mathrm{T}} \leq 15$ GeV/c.

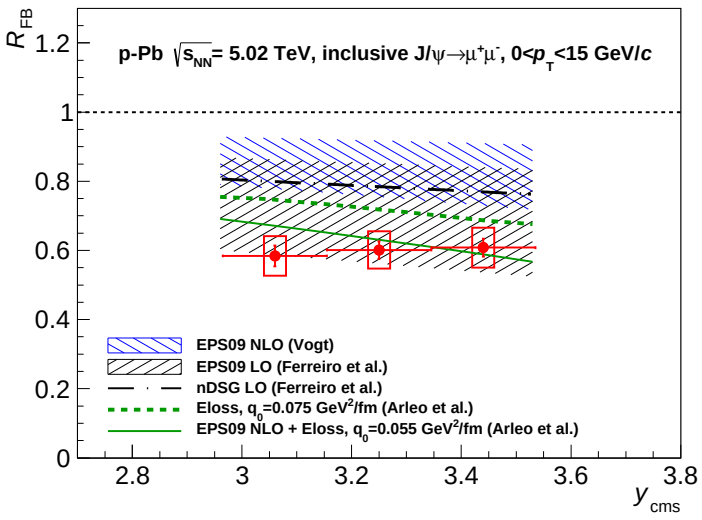

Figure 8.7. R_{FB} as a function of y . The error bars correspond to the statistical uncertainties, the open boxes to the uncorrelated systematic uncertainties. From [219].

8.2 J/ψ production as a function of the event activity

In the following, the results of the event activity dependence analysis are presented: the $p_{\rm T}$ dependence of the cross sections, $\langle p_{\rm T}\rangle$ and $\langle p_{\rm T}^2\rangle$, and $Q_{\rm pPb}$ as a function of the event activity. The ZN and the V0A centrality estimators were used for this analysis. Most of the official preliminary ALICE results are performed using the ZN estimator, while the V0A estimator results are mostly presented for comparison. The $\langle p_{\rm T}\rangle$ and $\langle p_{\rm T}^2\rangle$ results as a function of the V0A event activity are official ALICE preliminary results first presented in [226, 227]. In the V0A analysis, systematics from pile-up events are not considered.

8.2.1 Cross-section as a function of $p_{\rm T}$ for different event activity classes

In Fig.8.8 the $d^2\sigma^{\rm J/\psi}_{\rm pPb}/{\rm d}y{\rm d}p_{\rm T}$ as a function of $p_{\rm T}$ for different ZN event activity classes are shown for forward (top) and backward (bottom) rapidity. All the cross sections are normalized by the width of the event activity interval. Boxes represent the uncorrelated systematic uncertainties while the bars are the statistical uncertainties.

For comparison, the same figures are shown in Fig.8.9 for the V0A estimator. A visible difference is seen between the results obtained with the V0A and with the ZN estimators. In particular, the amplitude $d^2\sigma^{\rm J/\psi}_{\rm pPb}/{\rm d}y{\rm d}p_{\rm T}$ in the largest event activity class (0-5%) is higher for the V0A estimator than for the ZN estimator, while the lowest event activity class (80-100%) shows the opposite: the amplitude of $d^2\sigma^{\rm J/\psi}_{\rm pPb}/{\rm d}y{\rm d}p_{\rm T}$ is lower for the V0A estimator than for the ZN estimator.

8.2.2 The J/ψ $< p_T >$ as a function of the V0A event activity.

The results of the J/ψ $\langle p_{\rm T}\rangle$ dependence as a function of the V0A event activity are presented in Fig.8.10. Green points correspond to the J/ψ $\langle p_{\rm T}\rangle$ measured in pp at $\sqrt{s}$ =2.76 TeV and 7 TeV from [205]. These pp values were calculated in the $p_{\rm T}$ range $[0; 8]$ GeV/c. At forward rapidity, the J/ψ $\langle p_{\rm T}\rangle$ values are equal or higher than the pp ones. At backward rapidity, the J/ψ $\langle p_{\rm T}\rangle$ in p-Pb collisions for all the V0A event activity classes higher than 80-100%, is of the order of the J/ψ $\langle p_{\rm T}\rangle$ in pp . In the V0A event activity class 80-100% at backward rapidity, the J/ψ $\langle p_{\rm T}\rangle$ in p-Pb collisions is lower than the pp one. This is not expected (the J/ψ $\langle p_{\rm T}\rangle$ in p-Pb collisions should be either equal

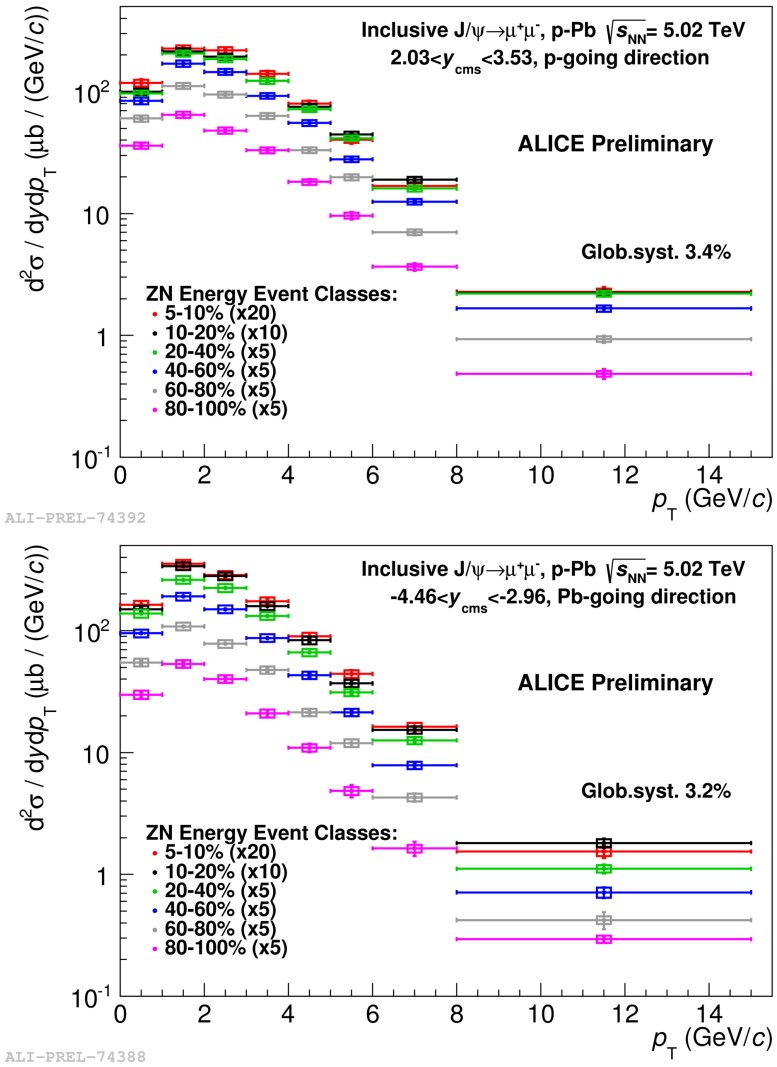

Figure 8.8. $d^2\sigma^{J/\psi}_{\mathrm{pPb}}/\mathrm{d}y\mathrm{d}p_{\mathrm{T}}$ as a function of p_{T} for different ZN event activity classes in p-Pb (top) and Pb-p (bottom). From [228].

or higher than pp) but this can be explained by the V0A event activity determination: the events selected by the V0A estimator in this class can have different characteristics (i.e. $\langle N\mathrm{coll}\rangle$) with respect to the pp collisions.

The J/ψ $\langle p_{\mathrm{T}}\rangle$ decreases towards lower event activity at forward and backward rapidity. The J/ψ $\langle p_{\mathrm{T}}\rangle$ was also measured for the V0A event activity interval $80-90\%$. The values of the J/ψ $\langle p_{\mathrm{T}}\rangle = 2.46 \pm 0.04 \pm 0.03$ ($\langle p_{\mathrm{T}}\rangle = 2.11 \pm 0.04 \pm 0.03$) in p-Pb (Pb-p) are similar to the values measured in the V0A event activity class $80-100\%$: $\langle p_{\mathrm{T}}\rangle = 2.44 \pm 0.04 \pm 0.03$ ($\langle p_{\mathrm{T}}\rangle = 2.09 \pm 0.04 \pm 0.03$) in p-Pb (Pb-p). It may be an indication of some

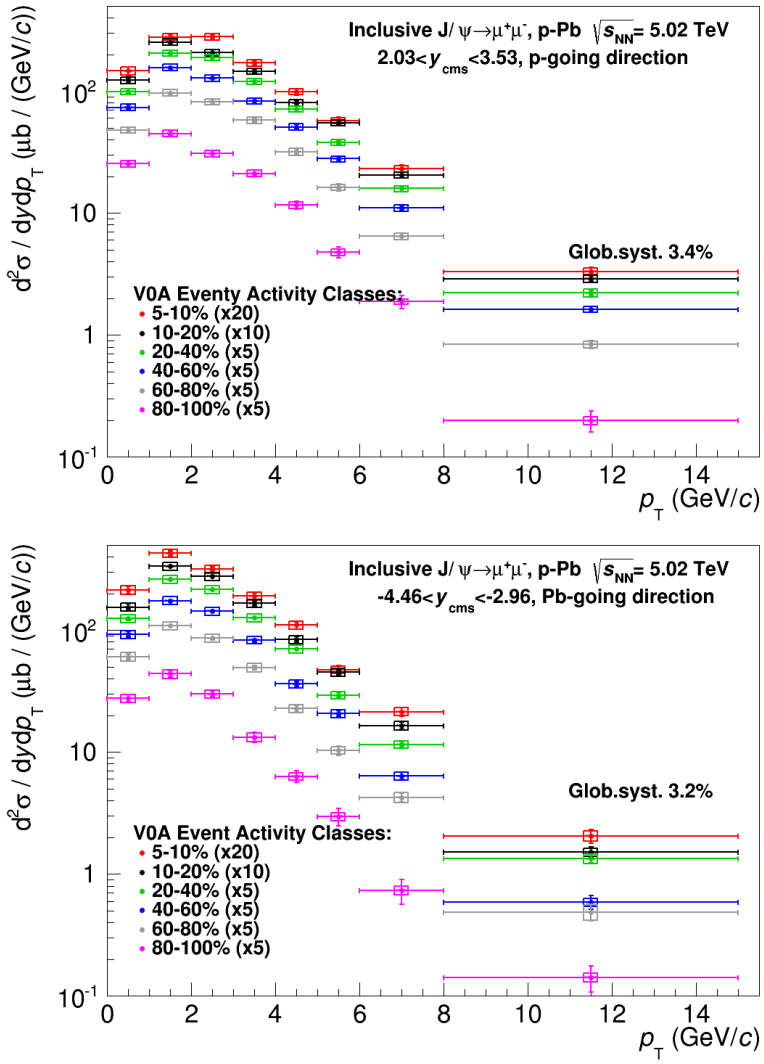

Figure 8.9. $d^2\sigma^{J/\psi}_{pPb}/dydp_T$ as a function of p_T for different V0A event activity classes in p-Pb (top) and Pb-p (bottom).

bias in the V0A event activity class 80-100%.

In Fig.8.11 $\Delta\langle p_T^2\rangle^{J/\psi}_{pPb}$ is shown as a function of the V0A event activity for forward (top) and backward (bottom) rapidity. $\Delta\langle p_T^2\rangle^{J/\psi}_{pPb}$ is defined as the difference between the $\langle p_T^2\rangle^{J/\psi}_{pPb}$ and $\langle p_T^2\rangle^{J/\psi}_{pp}$ at the same energy and in the same rapidity range. The $\langle p_T^2\rangle^{J/\psi}_{pp}$ values given in Tab.7.6 are common to all the V0A event activity classes in p-Pb. For that reason, the total uncertainty on the $\langle p_T^2\rangle^{J/\psi}_{pp}$ value is considered as fully correlated and is shown as a color box around zero. $\Delta\langle p_T^2\rangle^{J/\psi}_{pPb}$ increases with the V0A event activity. This can

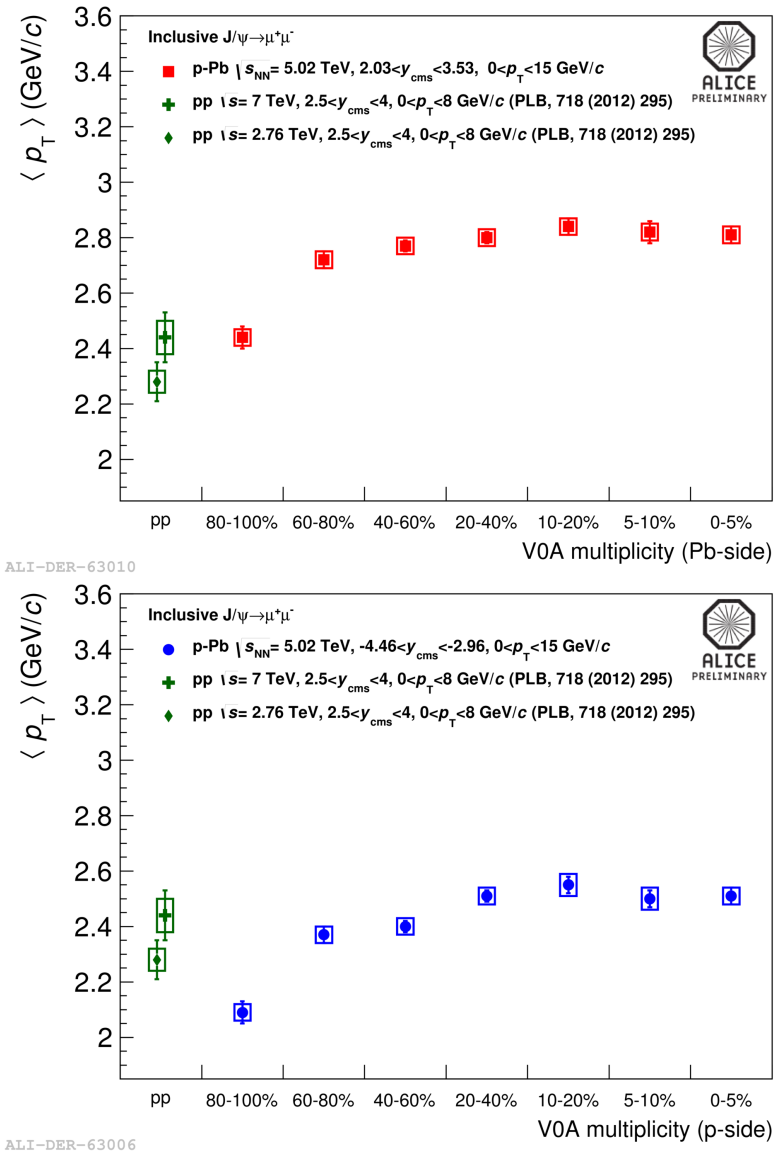

Figure 8.10. The J/ψ $\langle p_{\mathrm{T}} \rangle$ as a function of the V0A event activity in p-Pb (top) and Pb-p (bottom). Error bars represent statistical uncertainty, boxes represent systematic uncertainty. From [227].

be an indication of the multiple parton scattering in the initial nucleus state (the so-called Cronin effect). However the shadowing effect that deplete the J/ψ of low p_{T} leads to the same trend of $\Delta\langle p_{\mathrm{T}}^2 \rangle_{\mathrm{pPb}}^{\mathrm{J}/\psi}$. In the smallest V0A event activity class (80-100%) the p-Pb results are lower than the pp ones at the same energy and rapidity range, but this is significant only at backward rapidity. As explained earlier, this can be a result of the possible bias in this

V0A event activity class or of the different event characteristics.

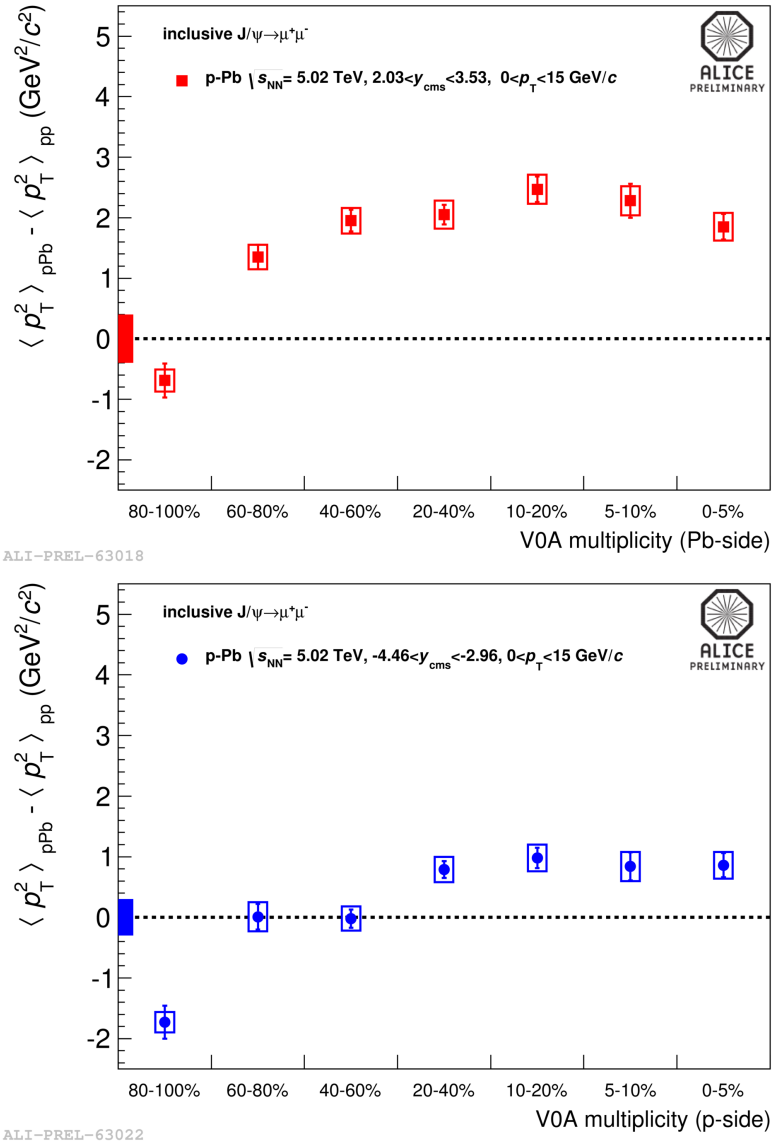

Figure 8.11. The V0A event activity dependence of $\Delta\langle p_{\mathrm{T}}^2\rangle_{\mathrm{pPb}}^{\mathrm{J}/\psi}$ for forward (top) and backward (bottom) rapidity. The boxes around zero represent the uncertainties of $\langle p_{\mathrm{T}}^2\rangle_{\mathrm{pp}}^{\mathrm{J}/\psi}$. From [226, 227].

8.2.3 The J/ψ $< p_T >$ as a function of the ZN event activity

In this section, the J/ψ $\langle p_{\rm T} \rangle$ is shown as a function of the ZN event activity. The J/ψ $\langle p_{\rm T} \rangle$ dependence on the ZN event activity is presented in Fig. 8.12 for p-Pb (red) and Pb-p (blue). $\Delta\langle p_{\rm T}^2 \rangle_{\rm pPb}^{\rm J/\psi}$ increases with the ZN event activity as it was also seen in Fig.8.11 for the V0A estimator. The pp results at $\sqrt{s} = 2.76$ and 7 TeV [205] are also added for comparison. A visible difference is seen compared to the V0A studies, especially in the lowest event activity classes where the J/ψ $\langle p_{\rm T} \rangle$ in the ZN case is higher than the one obtained for the V0A estimator. The difference is also visible in the top panel of Fig.8.13 where the $\Delta\langle p_{\rm T}^2 \rangle_{\rm pPb}^{\rm J/\psi}$ is shown as a function of the ZN event activity. In the event activity selection with ZN, the lowest event activity class is similar to pp. This is not observed with the V0A estimator indicating a different event activity selection with the two estimators at low event activity.

In the bottom panel of Fig.8.13 the $\Delta\langle p_{\rm T}^2 \rangle_{\rm pPb}^{\rm J/\psi}$ is presented as a function of $N_{\rm coll}^{\rm mult}$ (see the correspondence between the ZN event activity and $N_{\rm coll}^{\rm mult}$ in Tab.7.1). It is compared to the $\Delta\langle p_{\rm T}^2 \rangle_{\rm dAu}^{\rm J/\psi}$ PHENIX results [139] as a function of $N_{\rm coll}$ for d-Au collisions at $\sqrt{s_{\rm NN}} = 200$ GeV. The $p_{\rm T}$ broadening is the same for all rapidities at RHIC energies and at backward rapidity at LHC energies. Only for the forward rapidity at LHC, the $p_{\rm T}$ broadening is larger. It should be noted that there is no direct correspondence between the $N_{\rm coll}^{\rm mult}$ and the $N_{\rm coll}$ due to the unknown level of bias in the $N_{\rm coll}$ determination for the ZN event activity classes. This can slightly shift the data points along the $N_{\rm coll}$ axis.

8.2.4 $Q_{\rm pPb}^{\rm J/\psi}$ as a function of the event activity

In Fig.8.14 $Q_{\rm pPb}^{\rm J/\psi}$ as a function of the V0A event activity is shown for p-Pb (red) and Pb-p (blue) using $T_{\rm pPb}^{\rm V0A}$ from the column 2 of Table 7.2. At forward rapidity $Q_{\rm pPb}^{\rm J/\psi}$ decreases for the higher event activity classes and at backward rapidity $Q_{\rm pPb}^{\rm J/\psi}$ is consistent with unity except for the lowest and highest event activity classes.

In the top panel of Fig.8.15 $Q_{\rm pPb}^{\rm J/\psi}$ as a function of the ZN event activity is shown for p-Pb (red) and Pb-p (blue). At forward rapidity, $Q_{\rm pPb}$ decreases towards the higher multiplicity collisions while at backward rapidity $Q_{\rm pPb}^{\rm J/\psi}$ is consistent with unity in the full event activity range. The results for the V0A estimator are consistent with those for the ZN estimator, except for the smallest event activity class (80-100%). This is another hint of different event characteristic selection with V0A and ZN in the event activity class 80-100%.

In the bottom panel of Fig.8.15 the same results as in the top panel are shown as a function of $N_{\rm coll}^{\rm mult}$. The correspondence between the ZN event

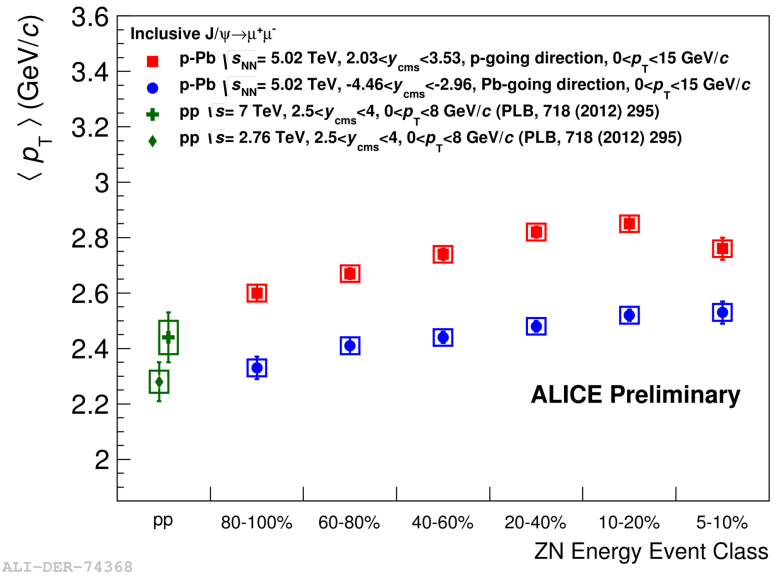

Figure 8.12. The J/ψ $\langle p_{\mathrm{T}} \rangle$ as a function of the ZN event activity. Error bars represent statistical uncertainty, boxes represent systematic uncertainty

activity and the $N_{\mathrm{coll}}^{\mathrm{mult}}$ values is discussed above. The $N_{\mathrm{coll}}^{\mathrm{mult}}$ dependence of Q_{pPb} is compared to the predictions given in private communications by the authors of the papers on EPS09 NLO [229] (striped bands) and coherent parton energy loss model [225] (shaded bands). Blue data points and theoretical lines correspond to the backward rapidity range while red points and lines are the results for forward rapidity range. The dashed lines in the theoretical bands correspond to the central values, the bands are the corresponding uncertainties.

The predictions of the EPS09 NLO model should be considered as preliminary and the uncertainties on the corresponding curves are taken from the centrality-integrated predictions made for [219]. The EPS09 NLO and the energy loss models calculations are genuine predictions made before the release of the ALICE measurements. The EPS09 NLO model describes well $Q_{\mathrm{pPb}}^{\mathrm{mult}}$ for the J/ψ at backward rapidity but significantly overestimates it at forward rapidity. The energy loss model shows a good agreement with $Q_{\mathrm{pPb}}^{\mathrm{mult}}$ for the J/ψ at forward rapidity and for small $N_{\mathrm{coll}}^{\mathrm{mult}}$ at backward rapidity. For high $N_{\mathrm{coll}}^{\mathrm{mult}}$ at backward rapidity the energy loss model underestimates $Q_{\mathrm{pPb}}^{\mathrm{mult}}$ for the J/ψ . The theoretical predictions are made for the N_{coll} dependence of the prompt J/ψ production, while the ALICE results are for the $N_{\mathrm{coll}}^{\mathrm{mult}}$ dependence of the inclusive J/ψ production. The effect from the non-prompt contribution of the J/ψ production to the nuclear modification factor is expected to be small as it was discussed in Section 8.1.2.1. As explained earlier, there is no direct correspondence between the $N_{\mathrm{coll}}^{\mathrm{mult}}$ and the N_{coll}. It can slightly shift the data

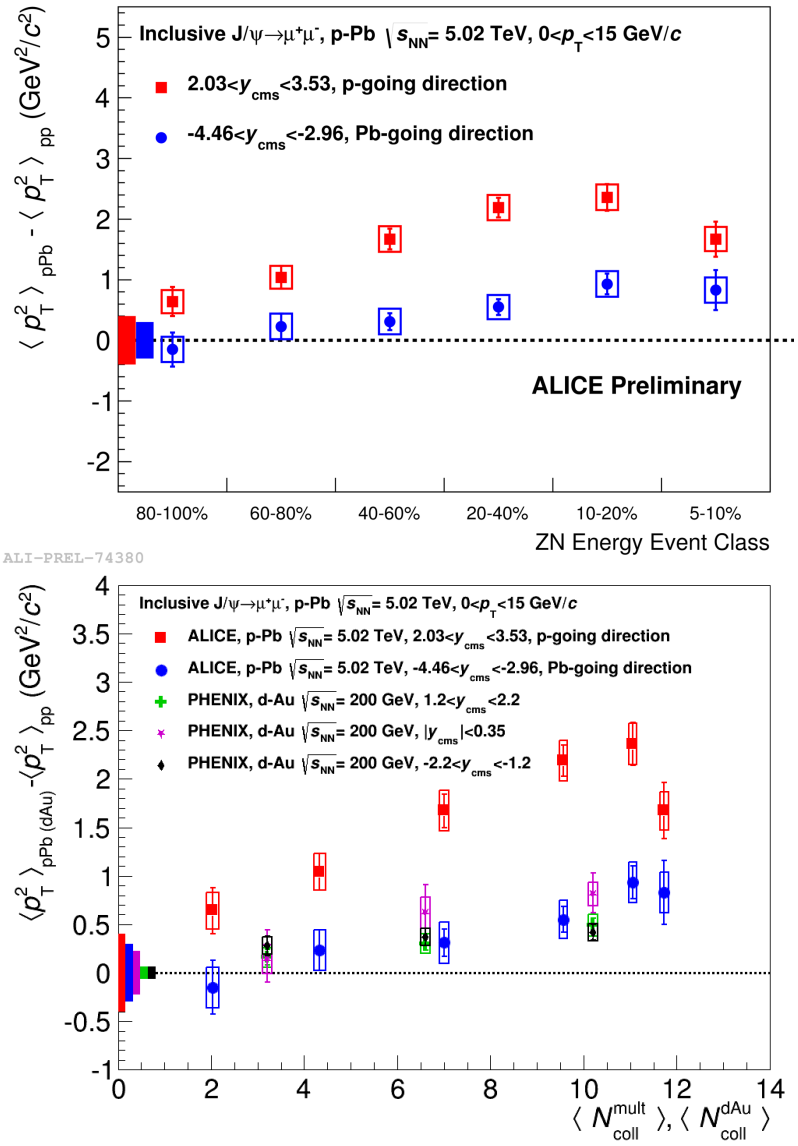

Figure 8.13. Top: The ZN event activity dependence of $\Delta\langle p_{\mathrm{T}}^2\rangle_{\mathrm{pPb}}^{\mathrm{J}/\psi}$. Bottom: $\Delta\langle p_{\mathrm{T}}^2\rangle_{\mathrm{pPb}}^{\mathrm{J}/\psi}$ ALICE results as a function of $N_{\mathrm{coll}}^{\mathrm{mult}}$ at $\sqrt{s_{\mathrm{NN}}} = 5.02$ TeV compared to the $\Delta\langle p_{\mathrm{T}}^2\rangle_{\mathrm{dAu}}^{\mathrm{J}/\psi}$ PHENIX results [139] vs N_{coll} for d-Au collisions at $\sqrt{s_{\mathrm{NN}}} = 200$ GeV. Data points are shown in colors: red (ALICE, forward y), blue (ALICE, backward y), green (PHENIX, forward y), purple (ALICE, mid-y), black (PHENIX, backward y). The color boxes around zero represent the uncertainties of $\langle p_{\mathrm{T}}^2\rangle_{\mathrm{pp}}^{\mathrm{J}/\psi}$ for the results with the same color. From [228].

points along the N_{coll} axis. Also the amplitude of $Q_{\mathrm{pPb}}^{\mathrm{mult}}$ can slightly vary since it is obtained from $N_{\mathrm{coll}}^{\mathrm{mult}}$. However the amplitude of the forward-to-backward

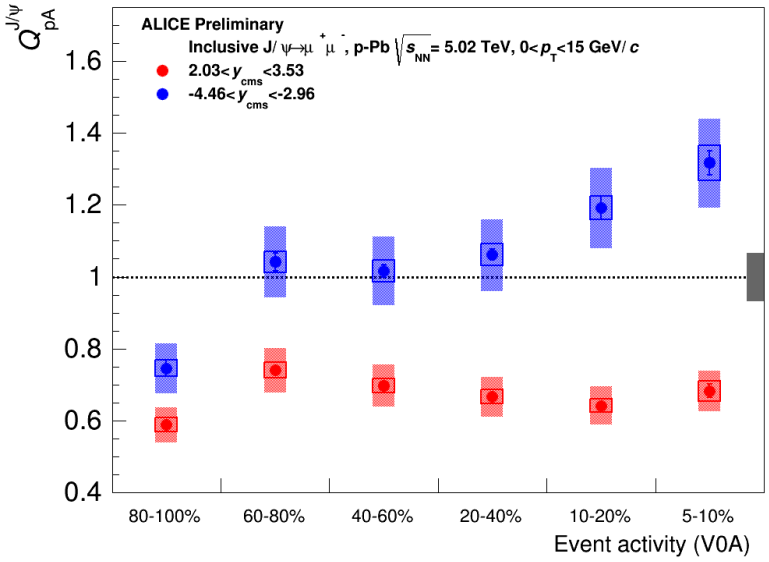

Figure 8.14. $Q_{\mathrm{pPb}}^{\mathrm{J}/\psi}$ as a function of the V0A event activity for p-Pb (red) and Pb-p (blue) using obtained using $T_{\mathrm{pPb}}^{\mathrm{V0A}}$ from the column 2 of Table 7.2.

ratio does not suffer from the bias in the $N_{\mathrm{coll}}^{\mathrm{mult}}$ determination and can be used to better constrain the models even if the N_{coll} coordinates of the R_{FB} can also slightly move along the N_{coll} axis.

8.2.5 $Q_{\mathrm{pPb}}^{\mathrm{J}/\psi}$ as a function of the J/ψ p_{T} for different event activity classes

$Q_{\mathrm{pPb}}^{\mathrm{J}/\psi}$ is shown in Fig.8.16 for p-Pb (top) and Pb-p (bottom) as a function of the J/ψ p_{T} for three different V0A event activity classes: 5-10% (red), 40-60% (black) and 80-100% (blue). The bars are the statistical uncertainties, the open boxes represent the uncorrelated and the shaded boxes denote the partially correlated systematic uncertainties. Grey box at unity is the global uncertainty. At forward rapidity, the $Q_{\mathrm{pPb}}^{\mathrm{J}/\psi}$ dependence on the J/ψ p_{T} is similar in shape and in amplitude for two V0A event classes: 5-10% and 40-60%. $Q_{\mathrm{pPb}}^{\mathrm{J}/\psi}$ in this two classes increases with the J/ψ p_{T}, while $Q_{\mathrm{pPb}}^{\mathrm{J}/\psi}$ in the V0A event activity class 80-100% is consistent with no dependence on the J/ψ p_{T}. At backward rapidity, $Q_{\mathrm{pPb}}^{\mathrm{J}/\psi}$ increases with the J/ψ p_{T} for the class 5-10%, and decreases with the J/ψ p_{T} for the class 80-100%, while for the class 40-60% it is consistent with unity for the full p_{T} range.

In Fig.8.17 $Q_{\mathrm{pPb}}^{\mathrm{J}/\psi}$ is shown for p-Pb (left) and Pb-p (right) as a function of the J/ψ p_{T} for three different ZN event activity classes. $Q_{\mathrm{pPb}}^{\mathrm{J}/\psi}$ as a function of

the J/ψ $p_{\rm T}$ in different event activity classes shows a similar behaviour for the event activity classes 5-10% and 40-60% as for the V0A estimator. A significant difference between the two estimators is seen for the event activity class 80-100%: for the ZN estimator it is consistent with unity for the full $p_{\rm T}$ range at forward rapidity (except at $p_{\rm T}$ = 2.5 GeV/c) and backward rapidity. This shows again that the results obtained with the V0A estimator are similar to those of the ZN estimator for the event activity higher than 80%. For the event activity class 80-100% a possible bias or different event characteristic with the V0A estimator gives different results with the V0A estimator as compared to the ZN one.

In the next figure (Fig.8.18), the $Q_{\rm pPb}^{\rm J/\psi}$ results as a function of the J/ψ $p_{\rm T}$ are shown separately in three ZN event activity classes. In the 80-100% ZN event activity class, $Q_{\rm pPb}^{\rm J/\psi}$ at forward and backward rapidity are quite similar and are consistent with unity. At larger event activity, the difference increases: $Q_{\rm pPb}$ differs from unity, it decreases in p-Pb and increases in Pb-p.

$Q_{\rm pPb}^{\rm J/\psi}$ is expected to be equal to unity in the ZN event activity class 80-100%. Indeed this class corresponds to the most peripheral events which are expected to give the same results as in pp collisions. Looking at Fig.8.18, one can conclude that the ZN estimator results agree with this hypothesis. The ZN event activity estimator seems to be a very good estimator of the centrality dependence.

In summary, the results with the ZN estimator indicate a strong $p_{\rm T}$ dependence of $Q_{\rm pPb}^{\rm J/\psi}$ for large event activity, while for small event activity, $Q_{\rm pPb}^{\rm J/\psi}$ is consistent with unity in the full $p_{\rm T}$ range.

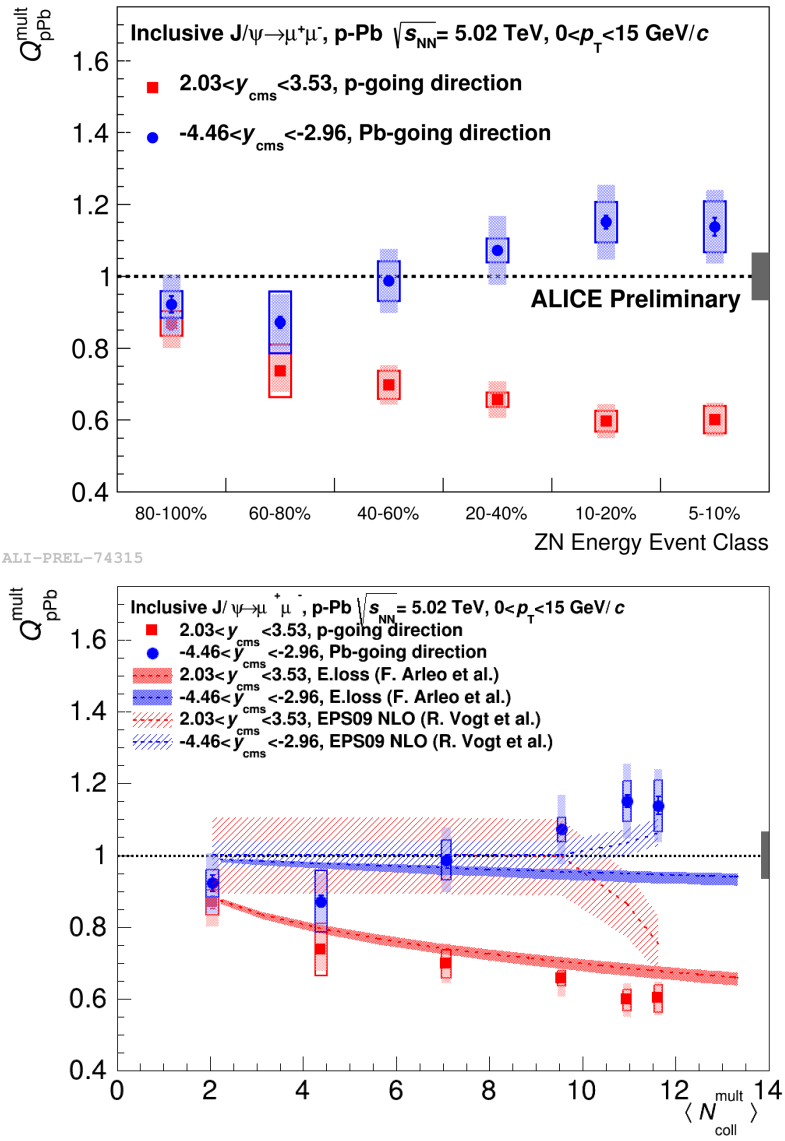

Figure 8.15. $Q_{\mathrm{pPb}}^{\mathrm{mult}}$ for the J/ψ as a function of the ZN event activity (top, from [228]) and of the $N_{\mathrm{coll}}^{\mathrm{mult}}$ (bottom) for forward (red) and backward (blue) rapidity. Vertical errors represent the statistical uncertainties, shaded boxes around the points the partially correlated uncertainties and open boxes around the points the uncorrelated uncertainties. Grey box at unity is the global uncertainty. The theoretical predictions in the right panel are from the private communications with the authors of the papers on EPS09 LO [229] (striped bands) and coherent parton energy loss model [225] (shaded bands). The dashed lines in the theoretical bands correspond to the central values, the bands are the corresponding uncertainties.

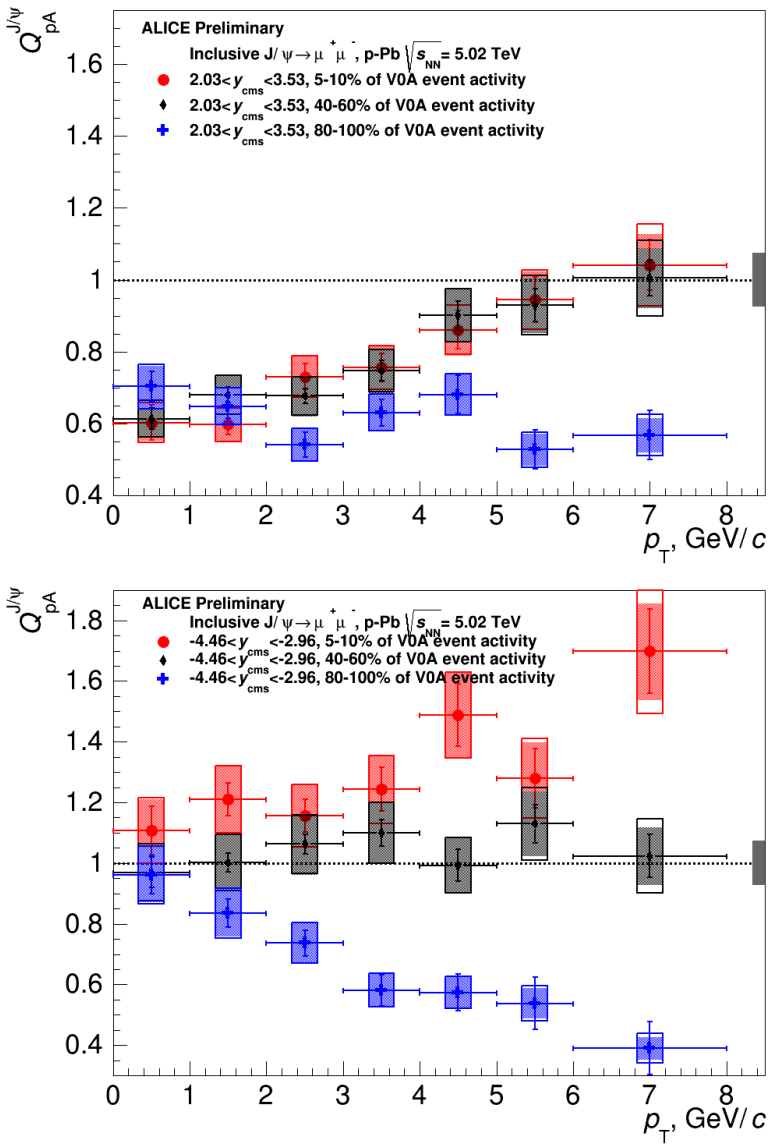

Figure 8.16. $Q_{\mathrm{pPb}}^{\mathrm{J}/\psi}$ as a function of the J/ψ p_{T} for three different V0A event activity classes: 5-10% (red), 40-60% (black)) and 80-100% (blue) in p-Pb (top) and Pb-p (bottom).

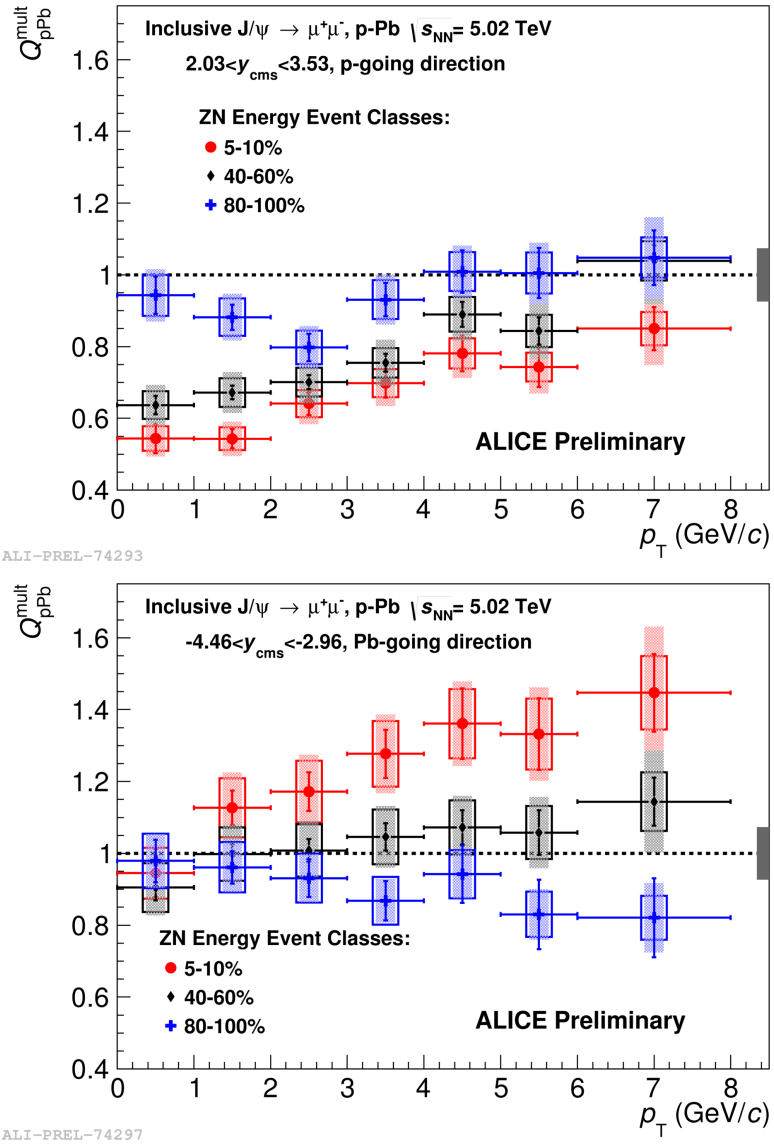

Figure 8.17. Q_{pPb} as a function of the J/ψ p_{T} in p-Pb (top) and Pb-p (bottom) for 3 different ZN event activity classes: 5-10% (red), 40-60% (black) and 80-100% (blue). Lines: statistical uncertainties, open boxes: uncorrelated uncertainties (signal extraction, matching, trigger, tracking, MC inputs, normalization), shaded boxes: partially correlated uncertainties (uncorrelated and partially correlated uncertainties on pp cross section, T_{pPb} model uncertainty, pile-up). Grey box: global uncertainties (correlated uncertainty on pp cross section, BR, T_{pPb} Glauber uncertainty).

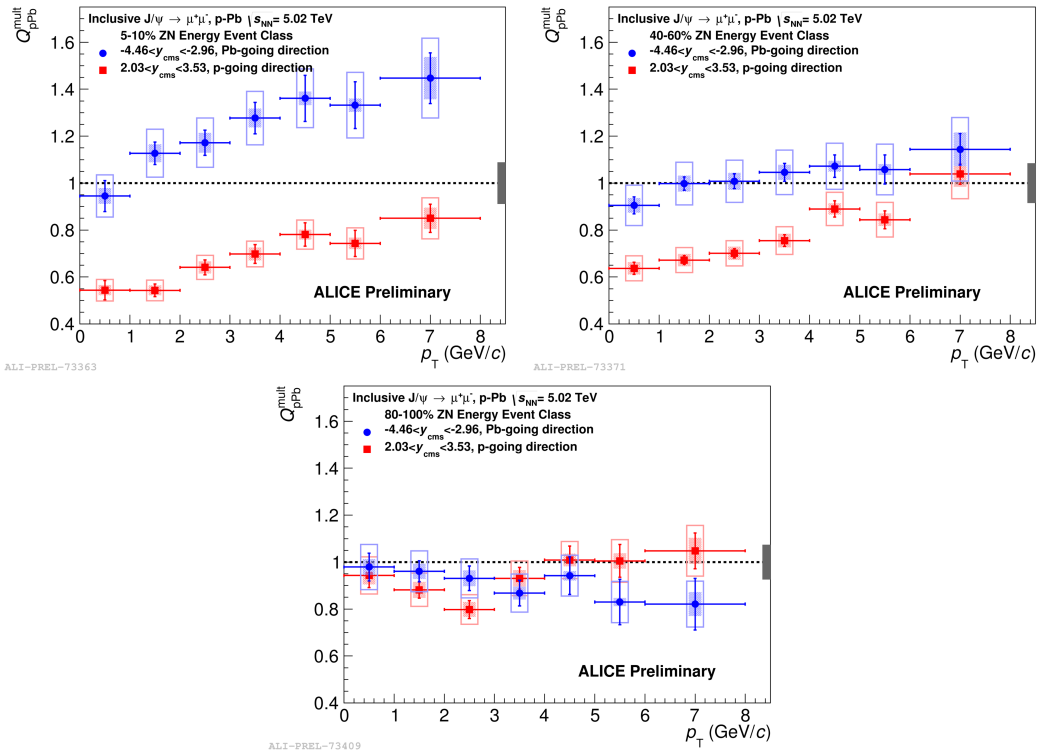

Figure 8.18. Q_{pPb} vs p_{T} separately in three different bins in ZN event activity: largest (top left panel), intermediate (top right panel) and smallest (bottom panel) event activity in p-Pb (red) and Pb-p (blue). Lines: statistical uncertainties, open boxes: uncorrelated uncertainties (signal extraction, matching, trigger, tracking, MC inputs, normalization, uncorrelated uncertainty on pp cross section), shaded boxes: partially correlated uncertainties (partially correlated uncertainty on pp cross section, luminosity). Grey box: global uncertainties (correlated uncertainty on pp cross section, BR, T_{pPb} Glauber uncertainty, T_{pPb} model uncertainty, pile-up).

8.3 Other ALICE p-Pb results

In addition to the results presented In Section 8.1 and Section 8.2, other p-Pb measurements related to the charmonium production at $\sqrt{s_{\rm NN}} = 5.02$ TeV are available from ALICE. They include the $p_{\rm T}$-dependence of the J/ψ production integrated over y and the event activity, both in dimuon and dielectron decay channels, the ψ(2S) production in the dimuon decay channel.

Fig.8.19 shows the $p_{\rm T}$-dependence of $R_{\rm pPb}^{\rm J/\psi}$ at backward (top left), mid (top right) and forward (bottom) rapidities. They are compared to theoretical predictions from the EPS09 NLO [221], CGC [125] and coherent parton energy loss model [225]. The uncertainties of the models were already discussed, except the uncertainties in the coherent parton energy loss model (not shown in the previous results). They include a variation of both the q_0 parameter and the parametrization of the production cross section.[1] The EPS09 NLO calculations reproduce fairly well the $p_{\rm T}$-dependence $R_{\rm pPb}^{\rm J/\psi}$ for $p_{\rm T} > 2.5$ GeV/c in all the three rapidity intervals. The coherent parton energy loss model predictions including the EPS09 NLO shadowing contribution improve the agreement however it predicts a steeper $p_{\rm T}$-dependence at low $p_{\rm T}$ than seen in the data at forward rapidity. This leads to a slight overestimation of the J/ψ suppression for $p_{\rm T} < 1$ GeV/c at forward rapidity. The pure coherent parton energy loss model has a less predictive power. It overestimates the J/ψ suppression for $p_{\rm T} <2$ GeV/c at backward rapidity and for $p_{\rm T} < 1$ GeV/c at forward rapidity and underestimates it for $p_{\rm T} > 3$ GeV/c at forward rapidity, while it agrees with the mid-rapidity experimental results in the full $p_{\rm T}$ range. Finally the CGC model was compared to the data at mid and forward rapidity. While it is in agreement with the data for $p_{\rm T} > 1$ GeV/c at mid-y, it systematically underestimates $R_{\rm pPb}^{\rm J/\psi}$ at forward rapidity.

The ψ(2S) results usually suffer from much lower statistics than in the corresponding J/ψ analysis. One of the main reasons for that is a much lower branching ratio of the ψ(2S) dimuon decay than the one of the J/ψ dimuon decay: B.R.$_{\psi(2S)\to\mu^+\mu^-} = (0.77 \pm 0.08)\%$ compared to B.R.$_{\rm J/\psi\to\mu^+\mu^-} = (5.93 \pm 0.06)\%$. In addition, about 59.5% of the ψ(2S) decay into the J/ψ [194]. Apart from that, ALICE was able to perform the differential ψ(2S) studies in p-Pb collisions. The main results of this analysis are presented below. Fig.8.20 shows the ratios B.R.$_{\psi(2S)\to\mu^+\mu^-}\sigma^{\psi(2S)}$/B.R.$_{\rm J/\psi\to\mu^+\mu^-}\sigma^{\rm J/\psi}$ of ψ(2S) and J/ψ cross sections for backward and forward rapidity in p-Pb at $\sqrt{s_{\rm NN}} = 5.02$ TeV. They are compared to the ALICE pp results at $\sqrt{s_{\rm NN}} = 7$ TeV, $2.5 < y_{\rm cms} < 4$ [231] due to the absence of the pp results in the same kinematic conditions as in p-Pb. The p-Pb ratios for both rapidity ranges are significantly lower than those for pp .

[1] When the model considers both energy loss and EPS09 NLO, since the uncertainty on EPS09 NLO is the dominant one, only this one is considered.

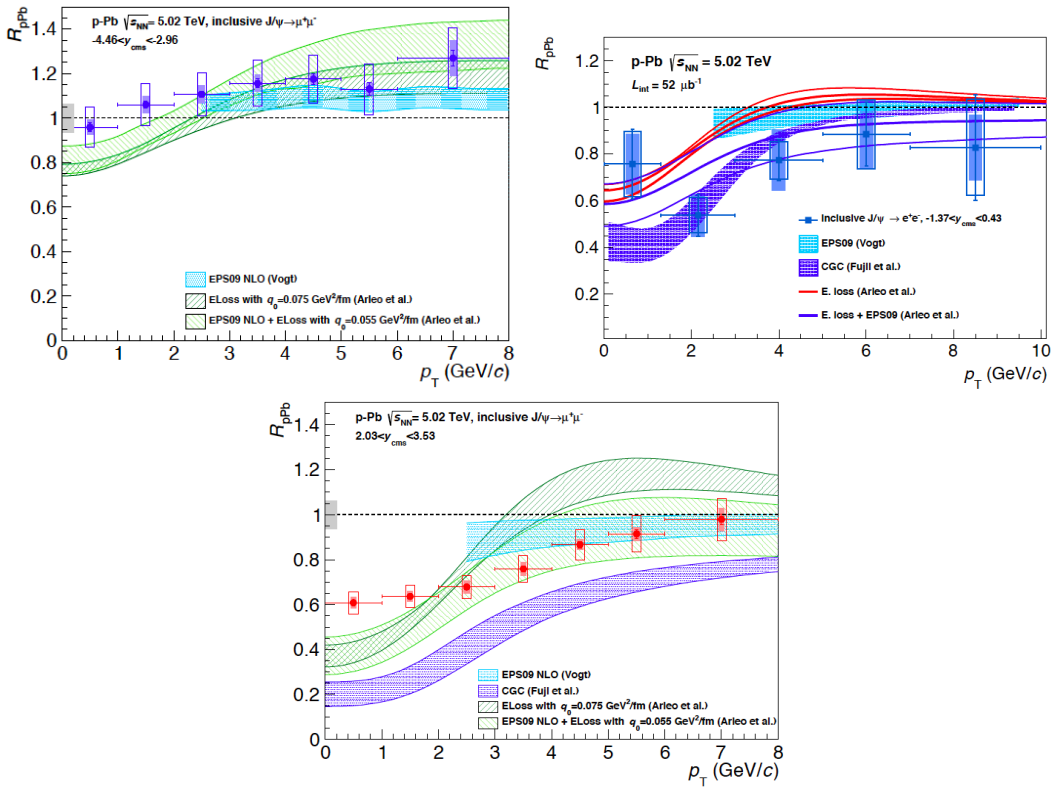

Figure 8.19. $R_{\mathrm{pPb}}^{\mathrm{J}/\psi}$ vs p_{T} at backward (top left), mid (top right) and forward (bottom) rapidities. Error bars are the statistical uncertainties, while the open boxes are the uncorrelated uncertainties and the shaded boxes represent the partially correlated uncertainties (partially correlated uncertainty on pp cross section, luminosity). Grey box: global uncertainties. Theoretical predictions: EPS09 NLO [221], CGC [125], coherent parton energy loss model [225]. From [230].

Dividing p-Pb results to those from pp one obtains a useful observable, double-ratio $\left[\sigma_{\psi(2S)}/\sigma_{\mathrm{J}/\psi}\right]_{\mathrm{pPb}} / \left[\sigma_{\psi(2S)}/\sigma_{\mathrm{J}/\psi}\right]_{\mathrm{pp}}$, which allows to directly compare the relative suppression of the two states between various experiments. Fig.8.21 shows such a comparison between the ALICE p-Pb measurements at $\sqrt{s_{\mathrm{NN}}}$ = 5.02 TeV and the d-Au PHENIX data at $\sqrt{s_{\mathrm{NN}}}$ =200 GeV [233]. The ALICE results are obtained by division of the p-Pb results at $\sqrt{s_{\mathrm{NN}}}$ = 5.02 TeV to the pp results at $\sqrt{s_{\mathrm{NN}}}$ = 7 TeV (see Fig.8.20). The possible dependence of the $\sigma^{\psi(2S)}/\sigma^{\mathrm{J}/\psi}$ on the $\sqrt{s_{\mathrm{NN}}}$ and y was estimated in pp collisions. This effect was estimated to be smaller than 8% and was added as an additional systematic uncertainty to the ratio. Finally, it is seen that the ψ(2S) is more suppressed than the J/ψ for the ALICE results both at backward and forward rapidity and for the PHENIX measurements at mid-y. The level of this suppression is

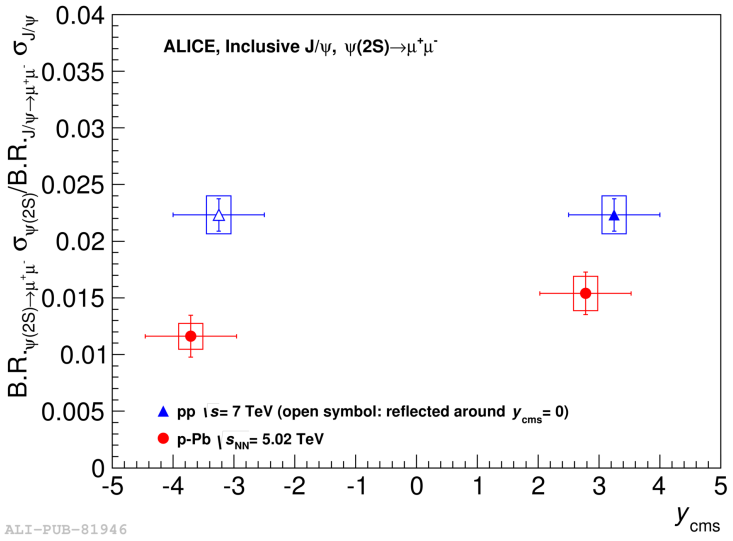

Figure 8.20. The ratios $\text{B.R.}_{\psi(2S)\to\mu^+\mu^-}\sigma^{\psi(2S)}/\text{B.R.}_{\text{J}/\psi\to\mu^+\mu^-}\sigma^{\text{J}/\psi}$ of the ψ(2S) and the J/ψ cross sections for backward and forward rapidity in p-Pb at $\sqrt{s_{\text{NN}}} = 5.02$ TeV, compared to the pp results at $\sqrt{s_{\text{NN}}} = 7$ TeV [231]. The horizontal bars represent the width of the corresponding rapidity ranges, the vertical bars are statistical uncertainties, the boxes correspond to the systematic uncertainties. From [232].

similar for both ALICE and PHENIX results within uncertainties.

It should be mentioned that CMS measured slightly higher double-ratios for the $\Upsilon(nS)$ states at rapidity $y_{\text{cms}} < |1.93|$ [234]:

$$\begin{aligned} \frac{\Upsilon(2S)/\Upsilon(1S)|_{pPb}}{\Upsilon(2S)/\Upsilon(1S)|_{pp}} &= 0.83 \pm 0.05\,(stat.) \pm 0.05\,(syst.), \\ \frac{\Upsilon(3S)/\Upsilon(1S)|_{pPb}}{\Upsilon(3S)/\Upsilon(1S)|_{pp}} &= 0.71 \pm 0.08\,(stat.) \pm 0.09\,(syst.). \end{aligned} \tag{8.2}$$

However within uncertainties the CMS results for the $\Upsilon(nS)$ states are compatible with the $\left[\sigma_{\psi(2S)}/\sigma_{\text{J}/\psi}\right]_{\text{dAu}} / \left[\sigma_{\psi(2S)}/\sigma_{\text{J}/\psi}\right]_{\text{pp}}$ measured by RHIC at midrapidity. This can be an indication of the similar effects for both charmonia and bottomonia.

Fig.8.22 shows the comparison between the $R_{\text{pPb}}^{\psi(2S)}$ (red) and the $R_{\text{pPb}}^{\text{J}/\psi}$ (blue) for backward and forward rapidity, integrated over p_{T}, y and the event activity. The ψ(2S) nuclear modification factor is calculated by combining $R_{\text{pPb}}^{\text{J}/\psi}$ with the double ratio shown above:

$$R_{\text{pPb}}^{\psi(2S)} = R_{\text{pPb}}^{\text{J}/\psi} \cdot \frac{\sigma_{\text{pPb}}^{\text{J}/\psi}}{\sigma_{\text{pPb}}^{\psi(2S)}} \cdot \frac{\sigma_{\text{pp}}^{\psi(2S)}}{\sigma_{\text{pp}}^{\text{J}/\psi}} \tag{8.3}$$

The theoretical predictions shown in the plot correspond to J/ψ. In the

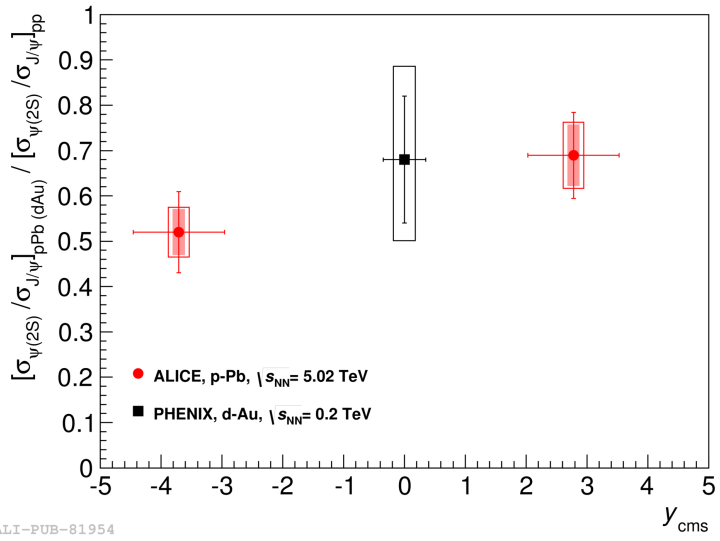

Figure 8.21. Double ratios $\left[\sigma_{\psi(2S)}/\sigma_{\mathrm{J}/\psi}\right]_{\mathrm{pPb\,(dAu)}}$ / $\left[\sigma_{\psi(2S)}/\sigma_{\mathrm{J}/\psi}\right]_{\mathrm{pp}}$ for p-Pb ALICE (red) and d-Au PHENIX (black) results. The horizontal bars represent the width of the corresponding rapidity ranges, the vertical bars are statistical uncertainties. For ALICE points, the boxes correspond to the uncorrelated systematic uncertainties, while the shaded boxes denote the correlated uncertainties. Open box for the PHENIX point includes various sources of systematic uncertainties combined in quadrature. From [232].

coherent parton energy loss model the predictions for J/ψ are identical to those for ψ(2S). For the EPS09 NLO, the calculations predict a larger $R_{\mathrm{pPb}}^{\psi(2S)}$ than the $R_{\mathrm{pPb}}^{\mathrm{J}/\psi}$ by 2-3%. Such predictions are in strong disagreement with the data where a significant difference, up to $\sim$ 2 times at backward y, is seen in the J/ψ and ψ(2S) suppression.

The p_{T}-dependence of $R_{\mathrm{pPb}}^{\psi(2S)}$ (red) is compared to $R_{\mathrm{pPb}}^{\mathrm{J}/\psi}$ (blue) for backward (top panel) and forward (bottom panel) rapidity is shown in Fig.8.23. The $R_{\mathrm{pPb}}^{\psi(2S)}$ is calculated using (8.3). The $R_{\mathrm{pPb}}^{\psi(2S)}$ shows a strong suppression with almost no p_{T}-dependence at forward rapidity. At backward rapidity, a hint of a decreasing trend of the ψ(2S) suppression towards hight p_{T} is seen. The ψ(2S) is systematically more suppressed than the J/ψ, as it was for the p_{T}-integrated case.

Finally the ZN event activity dependence of the ψ(2S) production is shown in Fig.8.24 for backward and forward y. $Q_{\mathrm{pPb}}^{\psi(2S)}$ is compared $Q_{\mathrm{pPb}}^{\mathrm{J}/\psi}$. $Q_{\mathrm{pPb}}^{\psi(2S)}$ shows a strong suppression, increasing towards the largest ZN event activity class. At forward rapidity, this decreasing trend is similar to the one of $Q_{\mathrm{pPb}}^{\mathrm{J}/\psi}$. At backward rapidity, the ψ(2S) suppression has completely different ZN event

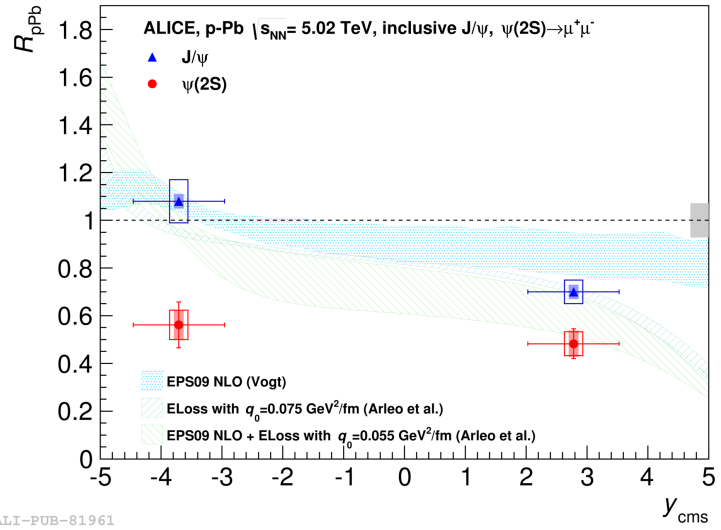

Figure 8.22. Comparison between the $R_{\mathrm{pPb}}^{\psi(2S)}$ (red) and the $R_{\mathrm{pPb}}^{\mathrm{J}/\psi}$ (blue) for backward and forward rapidity, integrated over p_{T}, y and the event activity. The horizontal bars represent the width of the corresponding rapidity ranges, the vertical bars are statistical uncertainties, the boxes correspond to the uncorrelated and the shaded boxes stand for the partially correlated systematic uncertainties. A grey box at unity is the uncertainty fully correlated between the J/ψ and the ψ(2S). From [232].

activity dependence with respect to the one of the J/ψ. This difference reaches a factor $\sim$ 4 at the largest event activity class (5-20%), pointing to some additional final state effects suppressing the most weakly bound ψ(2S).

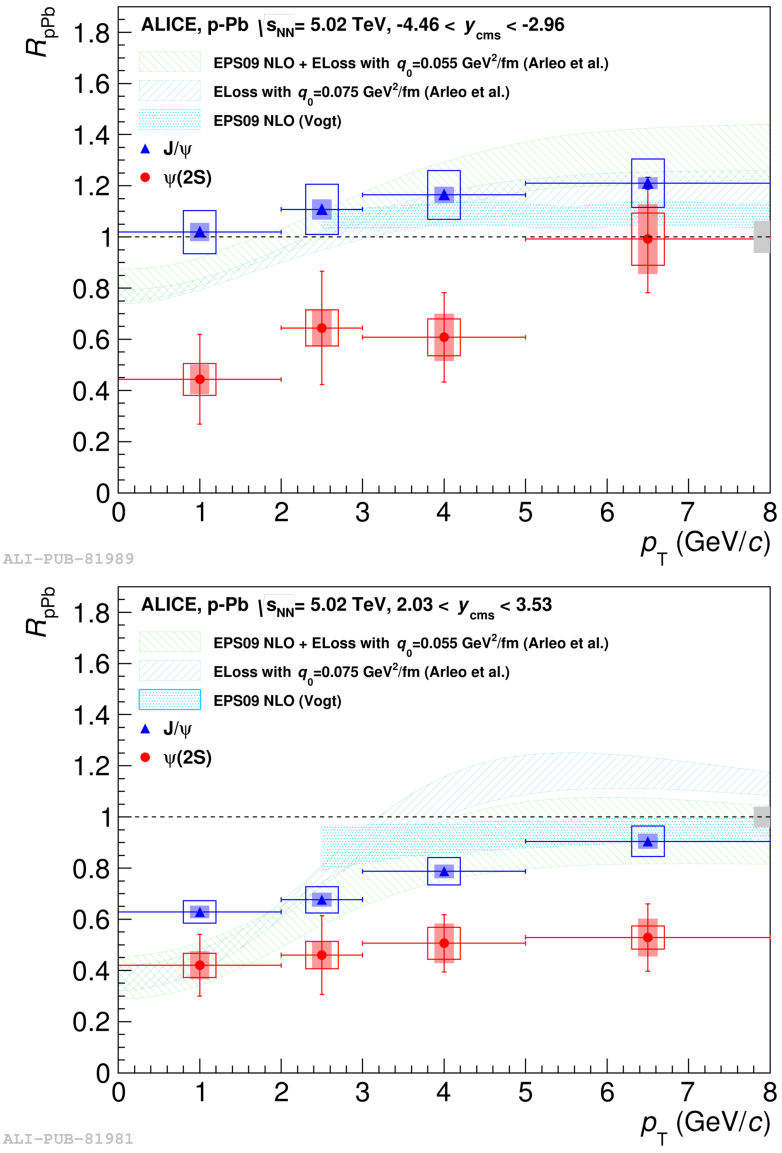

Figure 8.23. The p_{T}-dependence of the $R_{\mathrm{pPb}}^{\psi(2S)}$ (red) compared to the $R_{\mathrm{pPb}}^{\mathrm{J}/\psi}$ (blue) for backward (top panel) and forward (bottom panel) rapidity. The horizontal bars represent the width of the corresponding rapidity ranges, the vertical bars are statistical uncertainties, the boxes correspond to the uncorrelated and the shaded boxes stand for the partially correlated systematic uncertainties. The grey boxes at unity are the uncertainties fully correlated between J/ψ and ψ(2S). From [232].

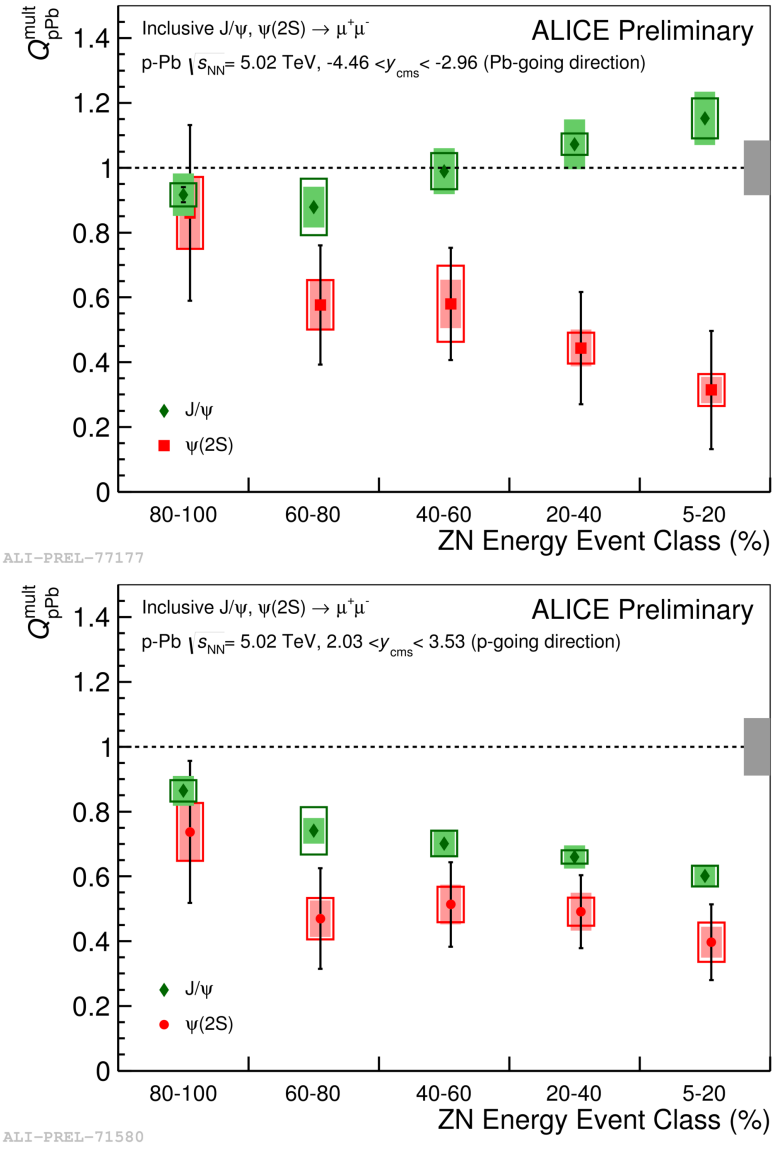

Figure 8.24. ZN event activity dependence of the ψ(2S) (red) production for backward (top panel) and forward (bottom panel) rapidity compared to the J/ψ results (green). The horizontal bars represent the width of the corresponding rapidity ranges, the vertical bars are statistical uncertainties, the boxes correspond to the uncorrelated and the shaded boxes stand for the partially correlated systematic uncertainties. The grey boxes at unity are the uncertainties fully correlated between the J/ψ and the ψ(2S). From [235].

8.4 From p-Pb to Pb-Pb: theory vs experiment

One of the main motivations for the studies of p-Pb collisions is to quantify the CNM effects and, if possible, to extrapolate them to Pb-Pb collisions. An estimation of the CNM effects in Pb-Pb collisions from the p-Pb measurements can be made if one assumes that:

- The J/ψ production mechanism is $g + g \rightarrow$ J/ψ. In this process the J/ψ kinematics defines entirely the nucleon longitudinal momentum fractions, $x_{1,2}$, carried by the two initial gluons. It allows then to compare the gluon x in the nucleus in p-Pb collisions at $\sqrt{s_{\rm NN}} = 5.02$ TeV to the one in Pb-Pb collisions at $\sqrt{s_{\rm NN}} = 2.76$ TeV. The x values are close but not equal (within 10%).

- Shadowing is the dominant cold nuclear matter effect. This hypothesis is in agreement with the integrated over event activity analysis. In that case the first approximation of CNM effects on $R_{\rm Pb-Pb}$ can be obtained as a product of $R^{\rm forward}_{\rm pPb} \times R^{backward}_{\rm pPb}$, where $R^{\rm forward}_{\rm pPb}$ ($R^{\rm backward}_{\rm pPb}$) is the nuclear modification factor at forward (backward) rapidity.

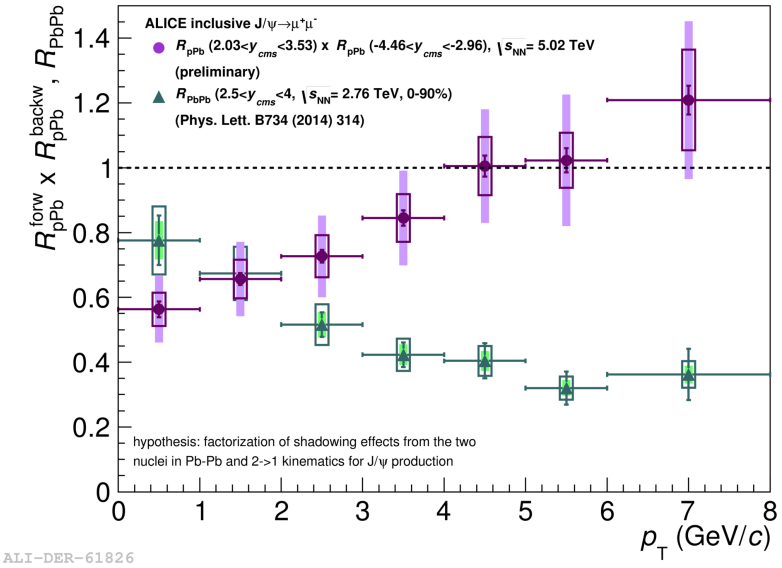

Figure 8.25. $R_{\rm Pb-Pb}$ and $R^{\rm forward}_{\rm pPb} \times R^{backward}_{\rm pPb}$ as a function of the J/ψ $p_{\rm T}$. The bars correspond to statistical uncertainties, shaded areas represent the partially correlated and the open boxes stand for the uncorrelated systematic uncertainties. N.B. A mistype is made in the Pb-Pb reference (should be Phys. Lett. B743 instead of Phys. Lett. B734). From [226].

The product $R_{\rm pPb}^{\rm forward} \times R_{\rm pPb}^{backward}$ integrated over $p_{\rm T}$, y and the event activity gives $0.75 \pm 0.10 \pm 0.12$ [219] (the first uncertainty is the quadratical combination of statistical and uncorrelated systematic uncertainties, the second one is the linear combination of the correlated uncertainties), which is larger than $R_{\rm Pb-Pb} = 0.57 \pm 0.01 \pm 0.09$ [236]. Such a difference could be an indication that the J/ψ suppression in Pb-Pb collisions cannot be ascribed to CNM effects only. However, no strong conclusion can be made due to the large size of uncertainties.

This comparison is presented differentially as a function of the J/ψ $p_{\rm T}$ in Fig.8.25. The Pb-Pb points are taken from [236] and the $R_{\rm Pb-Pb}$ is calculated in the centrality range 0-90%. For $p_{\rm T} > 3$ GeV/c, the extrapolated CNM effect is small and the $R_{\rm pPb}^{\rm forward} \times R_{\rm pPb}^{backward}$ is consistent with unity. At lower $p_{\rm T}$ the suppression in Pb-Pb collisions is similar to the one estimated from CNM effect alone. This can be explained by a superposition of the hot nuclear matter effects in this region and it thus could be an indication of the regeneration. A large J/ψ suppression at hight $p_{\rm T}$ in Pb-Pb collisions with respect to the pp case, which cannot be explained by the CNM effects, indicates that at high $p_{\rm T}$ hot nuclear matter effects become dominant.

Similar estimations were also made for the mid-y results (Fig.8.26) where $R_{\rm PbPb}$ is compared to $\left(R_{\rm pPb}^{{\rm mid}y}\right)^2$. $R_{\rm Pb-Pb}$ at mid-y is calculated in the centrality range 0-40%. Similar conclusion can be made as for the forward rapidity. For $p_{\rm T} > 7$ GeV/c, the extrapolated CNM effect is small, while at lower $p_{\rm T}$ (3 GeV/c $< p_{\rm T} <$ 6 GeV/c) it increases allowing to ascribe the J/ψ suppression in Pb-Pb collisions to this effect alone (in sense that hot nuclear matter effects compensate each other). However at even smaller $p_{\rm T}$ ($p_{\rm T} < 3$ GeV/c) the extrapolated CNM effect is seen, while $R_{\rm Pb-Pb}$ is consistent with unity. This can be explained by the superposition of the CNM effect with the contribution from the re-combination of $c\bar{c}$ pairs [236] in hot medium.

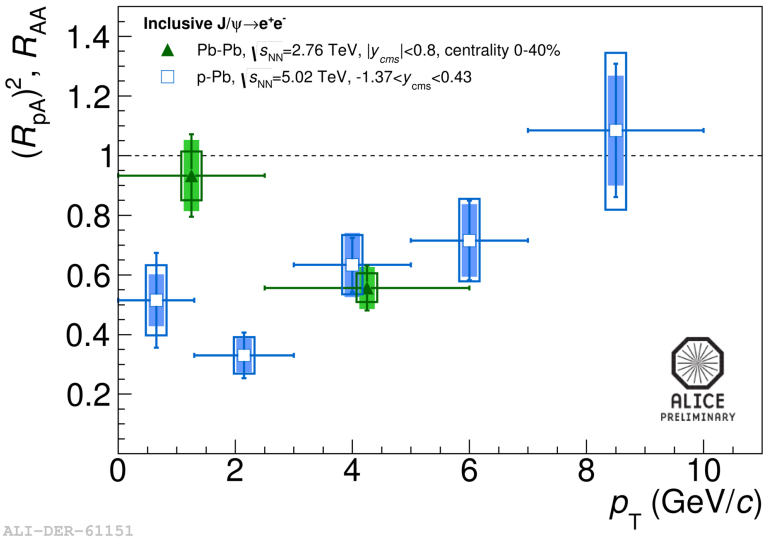

Figure 8.26. $R_{\mathrm{Pb-Pb}}$ and $\left(R_{\mathrm{pPb}}^{\mathrm{mid}y}\right)^2$ vs p_{T}. The bars correspond to statistical uncertainties, shaded areas represent the partially correlated and the open boxes stand for the uncorrelated systematic uncertainties. From [226].

Conclusions and outlooks

This thesis has presented a detailed study of the J/ψ production in p-Pb collisions at $\sqrt{s_{\rm NN}}$ = 5.02 TeV with the ALICE Muon Spectrometer at the LHC. The analysis is based on the data of the p-Pb run performed at the LHC in the beginning of 2013. The work presented in this thesis can be divided in three main parts.

In the first part of the thesis (Chapters 1, 2 and 3) I studied the theoretical background of the J/ψ production. The J/ψ production plays an important role in the understanding of fundamental processes in heavy-ion collisions. In nucleus-nucleus collisions there are two types of effects affecting the J/ψ production: hot and cold nuclear matter (CNM) effects. Since they cannot be distinguished properly in nucleus-nucleus collisions, nucleon-nucleus collisions are used to quantify the CNM effects, providing a reference of the CNM effects for nucleus-nucleus collisions. Different models of the CNM effects are described. They include gluon shadowing, gluon saturation, nuclear absorption and coherent parton energy loss models.

The second part of the thesis (Chapters 4 and 5) describes my work related to the preparation of the J/ψ production studies in the ALICE Collaboration. This work included the participation in shifts during data taking of the pilot p-Pb run in 2012 and of the p-Pb run in 2013 and the tuning of the corresponding MC generator. In cooperation with the author of this generator, we found and corrected several bugs in the beta version and implemented in the code a function of scaling of the charmonia and bottomonia cross sections. This generator allowed to estimate the production rates and to prepare the required framework for the real data analysis. I also compared the results of the generator to the real data from the pilot p-Pb run.

The third part of the thesis (Chapters 6, 7 and 8) is devoted to the data analysis with my personal contribution. It includes the studies of the J/ψ and ψ(2S) production in p-Pb collisions at the LHC with the ALICE muon spectrometer. This work consists of three main analyses:

- $p_{\rm T}$ and y dependence of the J/ψ production;
- event activity and $p_{\rm T}$ dependence of the J/ψ production;
- ψ(2S) production studies.

I contributed mainly to the first two analyses but I also performed some analysis steps in the third one. My contribution included the full signal extraction procedure and the final estimation of the physical observables. In addition I made a major contribution to the pile-up effect estimation.

The result of this work yielded in four ALICE internal analyses notes where I was one of the co-authors. Two corresponding ALICE papers are already published: "J/ψ production and nuclear effects in p-Pb collisions at $\sqrt{s_{\rm NN}} = 5.02$ TeV" [219], where I was chosen as a member of the paper committee, and "Suppression of ψ(2S) production in p-Pb collisions at $\sqrt{s_{\rm NN}} = 5.02$ TeV" [232]. Two other ALICE papers are in preparation: "Event activity dependence of inclusive J/ψ production in p-Pb collisions at $\sqrt{s_{\rm NN}} = 5.02$ TeV", where I am a member of the paper committee, and "Event activity dependence of ψ(2S) production in p-Pb collisions at $\sqrt{s_{\rm NN}} = 5.02$ TeV".

The measurements of the $p_{\rm T}$ and y dependence of the J/ψ production allowed to study p-Pb collisions in different kinematic domains. An asymmetric J/ψ suppression is seen as a function of rapidity. While at backward rapidity the J/ψ production is similar to the one in pp collisions scaled by the number of binary collisions, strong CNM effects are seen at forward rapidity (where x values are smaller). A strong $p_{\rm T}$ dependence was also observed in for the J/ψ suppression in p-Pb collisions. CNM effects were found to play less significant role at high $p_{\rm T}$ since the particles with high $p_{\rm T}$ interact less time with the cold nuclear matter than those with smaller $p_{\rm T}$ values.

The measurements of the event activity dependence of the J/ψ production allowed to study p-Pb collisions from another angle focusing on geometrical properties of the collision. Different centrality estimators were used for these studies. A strong event activity dependence of the J/ψ suppression was measured in this analysis. At the smallest event activity, corresponding to the most peripheral collisions, the measurements show no CNM effects on the J/ψ production. Large event activity events corresponding to the most central collisions show strong CNM effects. This can be ascribed to the much lower density of the nuclear matter affecting the J/ψ production in the most peripheral collisions with respect to the most central collisions.

The comparison of the presented results with theoretical models shows that the CGC-based model including the CEM as a J/ψ production model fails to describe the J/ψ production at forward rapidity while it is in fair agreement with the $p_{\rm T}$-dependence of the J/ψ production at mid rapidity. Probably the failure of this model is related to the wrong tuning of the intrinsic J/ψ production model. Some recent improvements to the model with a change of the CEM to NRQCD show good results for pp collisions [237] and will be probably extended to p-Pb collisions.

The shadowing model based on the EPS09 NLO parametrization shows a good agreement with the event activity and the rapidity dependence of the

J/ψ production at backward y, while it underestimates its suppression and does not describe the $N_{\rm coll}$ dependence at forward rapidity. It is also in fair agreement with the $p_{\rm T}$ dependence of the J/ψ production for all the rapidity intervals considered in this analysis, for $p_{\rm T} > 3$ GeV/c.

The coherent parton energy loss model seems to be very promising. When including the contribution from shadowing, it shows a fair agreement with almost all the presented results within the experimental uncertainties. However this model predicts a steeper behaviour of the y dependence of the J/ψ nuclear modification factor at backward rapidity. Its configuration without shadowing contribution also slightly underestimates the enhancement of the J/ψ production at backward rapidity at the largest event activity, while it provides a good description of forward rapidity results in the full event activity range. The $p_{\rm T}$-dependence of the J/ψ production is well described by the coherent parton energy loss model including the shadowing contribution at all rapidities for $p_{\rm T} > 1$ GeV/c, while the pure energy loss model does not describe well these data, except for the results at backward rapidity for $p_{\rm T} > 2$ GeV/c where a fair agreement is seen with the data.

Finally, the ψ(2S) production studies were performed using the same analysis technique as for the J/ψ. Indeed, the J/ψ analysis includes also the ψ(2S) one since the signal extraction is carried out on the same invariant mass distributions. In addition, universal fitting functions which include simultaneously signal functions for both ψ(2S) and J/ψ were used. Due to much lower statistics for the ψ(2S) analysis as compared to the J/ψ one, the final uncertainty for the ψ(2S) results is much larger. But it was possible to perform some interesting studies of the ψ(2S) production including the ratio between the ψ(2S) and J/ψ production yields.

Despite the success of some theoretical predictions for J/ψ production there is one puzzle which is not resolved by the existing theoretical models: the difference between the suppression of the J/ψ and ψ(2S) production, not expected by the existing models.

In order to better constrain the models, two improvements of the present analysis can be done. First, one can reduce one of the main contributors to the systematic uncertainty: the pp reference. This reduction can be achieved by performing the pp collisions at the same energy as the p-Pb collisions. Secondly, one can study the prompt J/ψ production instead of the inclusive J/ψ production used in the ALICE J/ψ analysis. The Muon Forward Tracker (MFT) [238] will allow to track the muons from B-hadrons decays and thus, separate the prompt and non-prompt J/ψ. The MFT project was approved by the LHC Comittee (LHCC) in 2013 and it will be ready for the data taking in 2019.

Appendix A

Signal extraction of J/ψ

Fig. A.1 and A.2 show the examples of the signal extraction procedure for p-Pb and Pb-p in different rapidity intervals, integrated over p_{T} and the event activity.

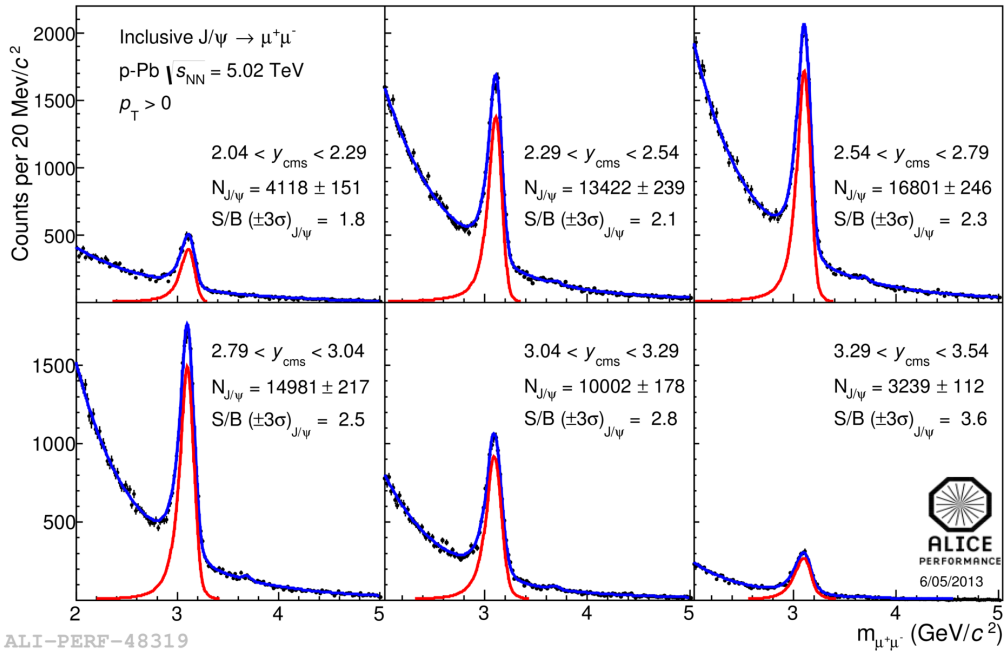

Figure A.1. Examples of the signal extraction in p-Pb with Pol2×Exp + NA60CB2 fit for different y intervals integrated over p_{T} and the event activity.

Fig. A.3 and A.4 show the examples of the signal extraction procedure for p-Pb and Pb-p in the common rapidity range (for the R_{FB} calculations) in different p_{T} intervals, integrated over the event activity.

Fig. A.5 and A.6 show the examples of the signal extraction procedure for

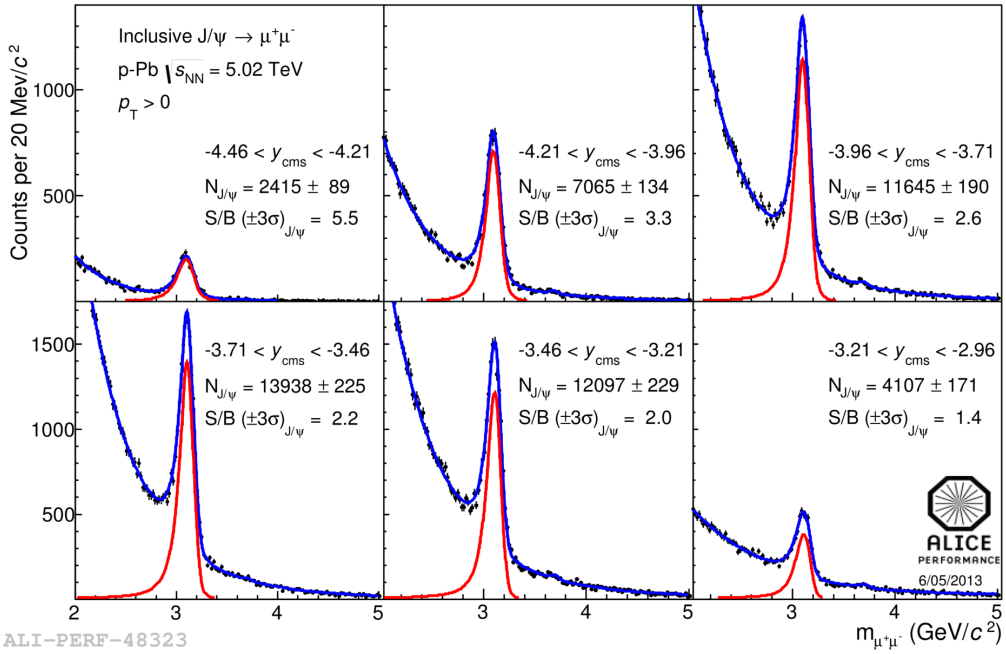

Figure A.2. Examples of the signal extraction in Pb-p with Pol2×Exp + NA60CB2 fit for different y intervals integrated over p_{T} and the event activity.

p-Pb and Pb-p in different V0A event activity classes, integrated over p_{T} and y.

Fig. A.7, A.8, A.9, A.10, A.11 and A.12 represent the examples of the signal extraction procedure for p-Pb and Pb-p integrated over the event activity, for the highest and the lowest ZN event activity classes.

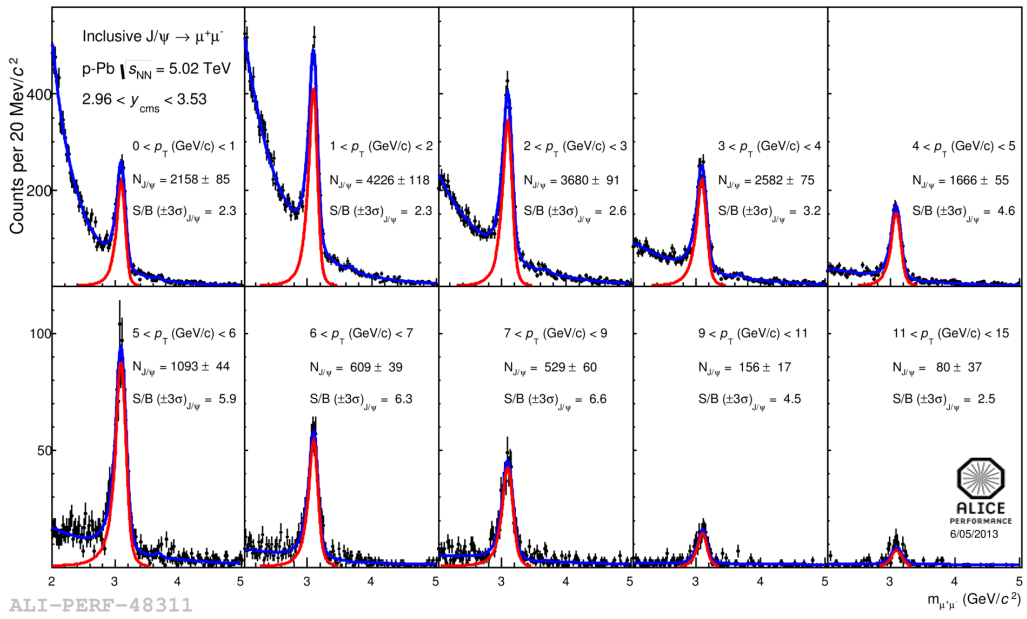

Figure A.3. Examples of the signal extraction in p-Pb with Pol2×Exp + NA60CB2 fit in the rapidity range $2.96 < y_{\rm cms} < 3.53$ in different $p_{\rm T}$ intervals, integrated over the event activity.

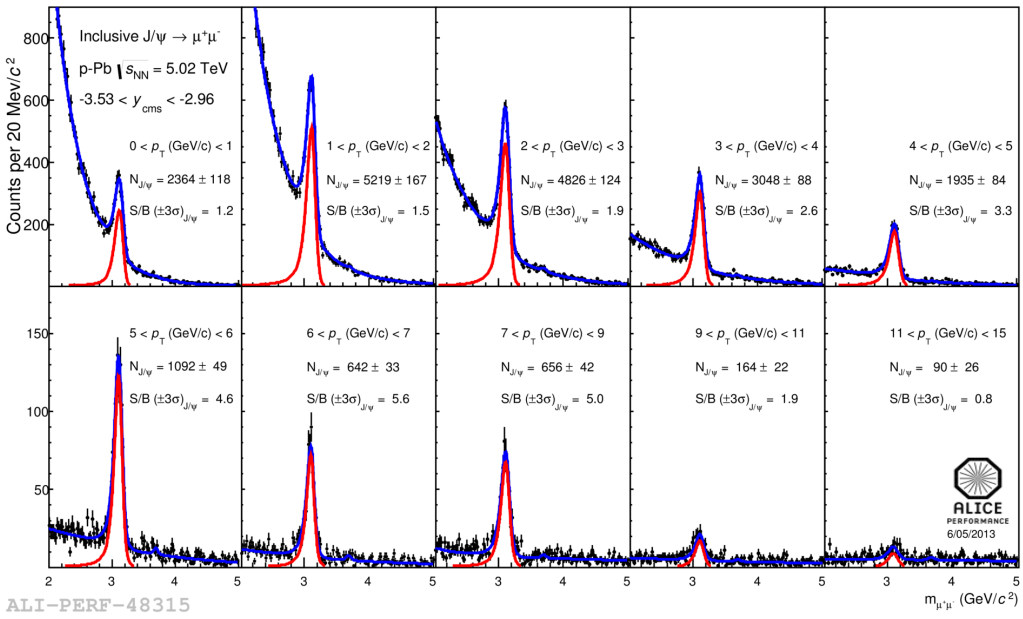

Figure A.4. Examples of the signal extraction in Pb-p with Pol2×Exp + NA60CB2 fit in the rapidity range $-3.53 < y_{\mathrm{cms}} < -2.96$ in different p_{T} intervals, integrated over the event activity.

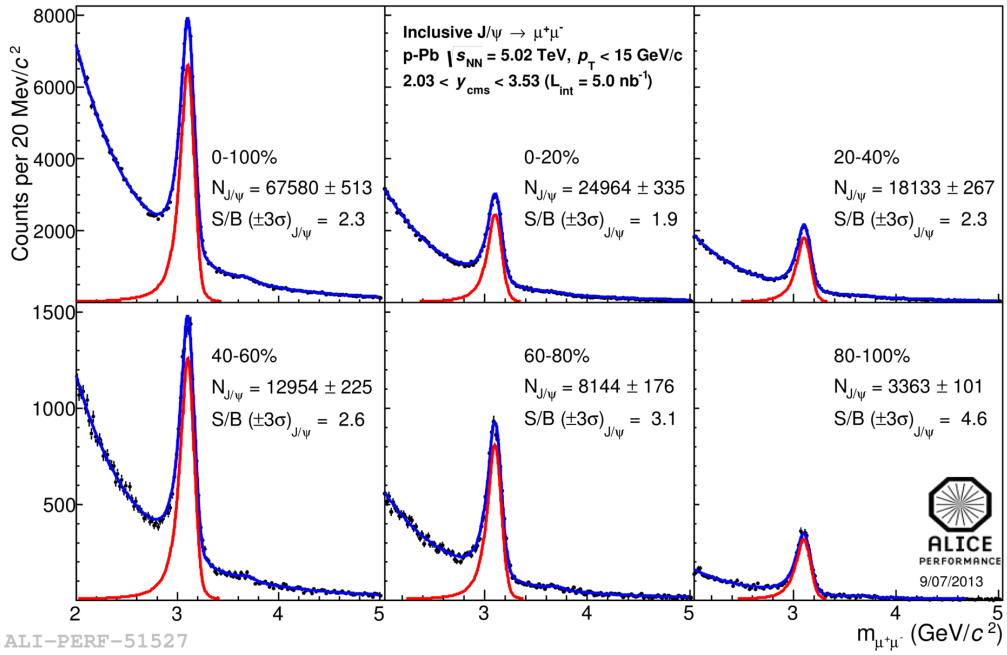

Figure A.5. Examples of the signal extraction in p-Pb with Pol2×Exp + NA60CB2 fit in different V0A event activity classes, integrated over p_{T} and y.

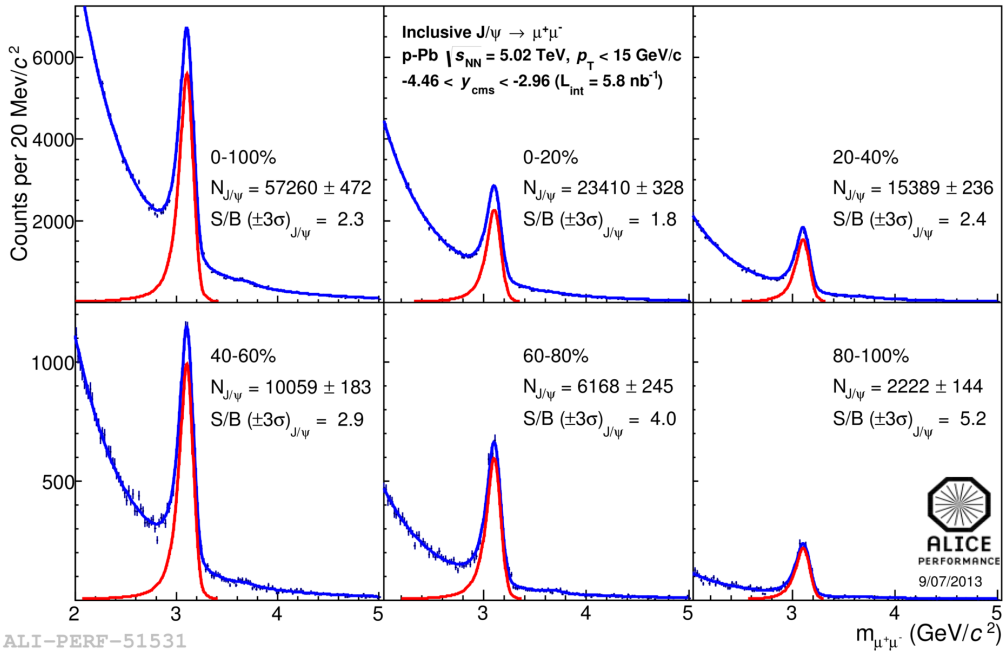

Figure A.6. Examples of the signal extraction in Pb-p with Pol2×Exp + NA60CB2 fit in different V0A event activity classes, integrated over p_{T} and y.

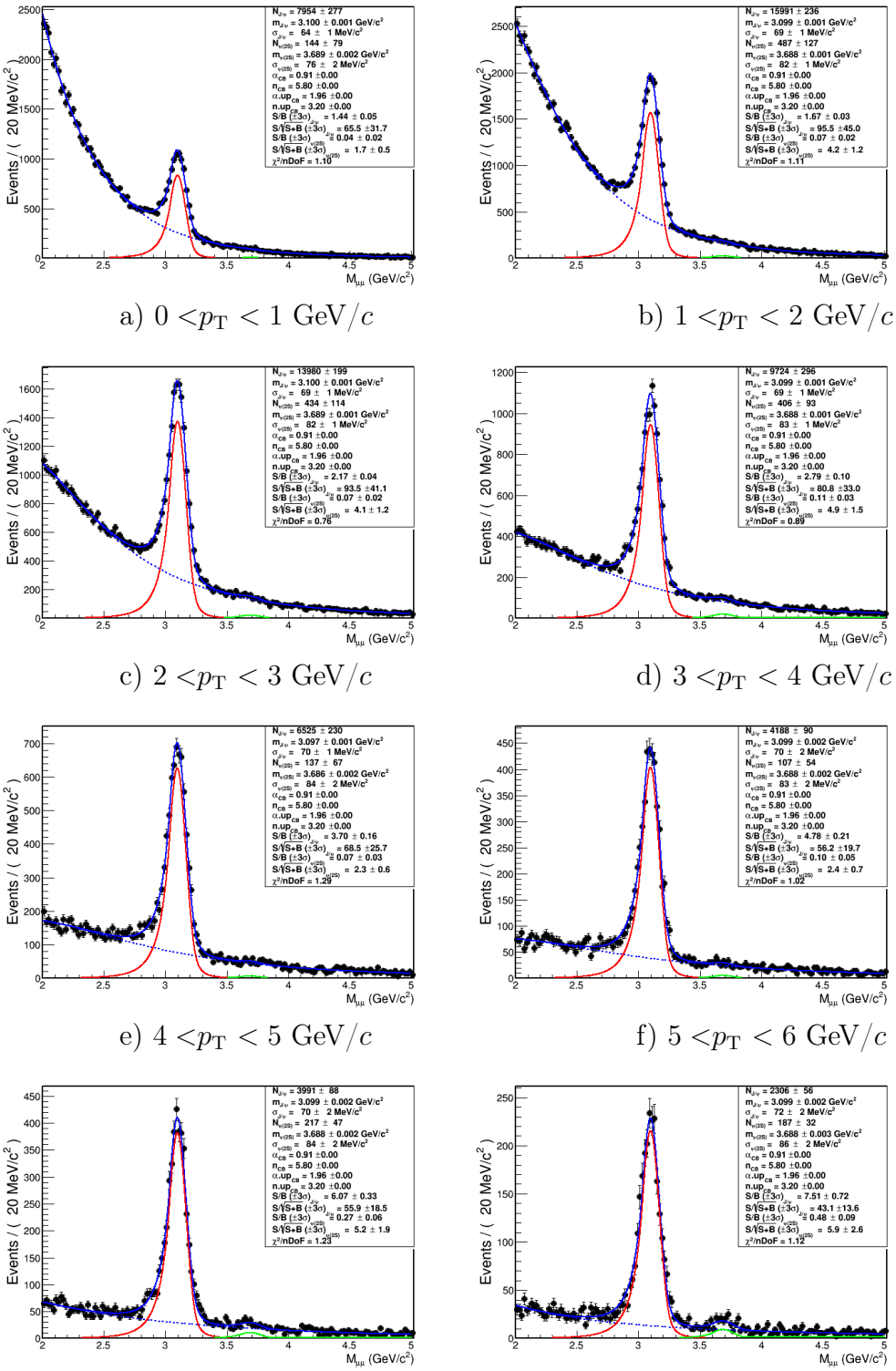

a) $0 < p_{\mathrm{T}} < 1$ GeV/c b) $1 < p_{\mathrm{T}} < 2$ GeV/c

c) $2 < p_{\mathrm{T}} < 3$ GeV/c d) $3 < p_{\mathrm{T}} < 4$ GeV/c

e) $4 < p_{\mathrm{T}} < 5$ GeV/c f) $5 < p_{\mathrm{T}} < 6$ GeV/c

g) $6 < p_{\mathrm{T}} < 8$ GeV/c h) $8 < p_{\mathrm{T}} < 15$ GeV/c

Figure A.7. Examples of the signal extraction in p-Pb with VWG + CB2 fit for different p_{T} intervals integrated over the event activity.

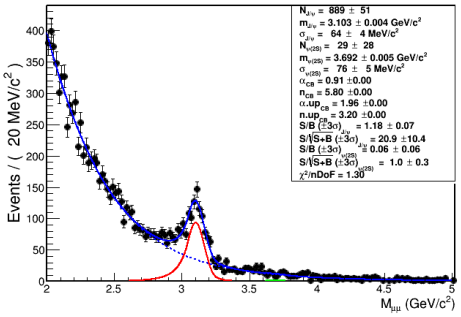

a) 0 <$p_{\rm T}$ < 1 GeV/c

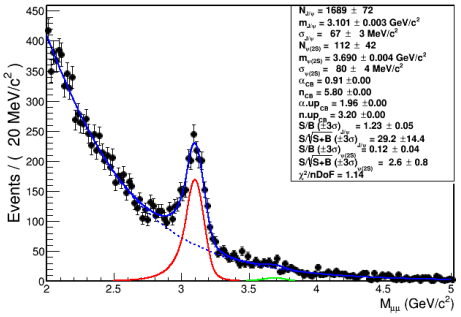

b) 1 <$p_{\rm T}$ < 2 GeV/c

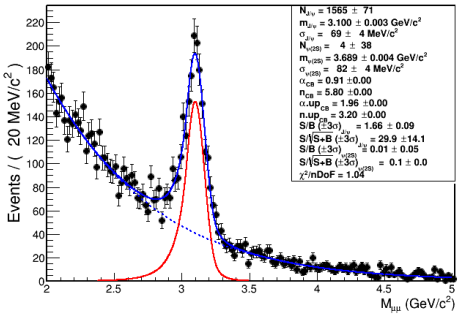

c) 2 <$p_{\rm T}$ < 3 GeV/c

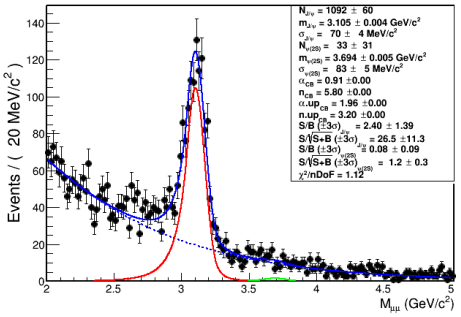

d) 3 <$p_{\rm T}$ < 4 GeV/c

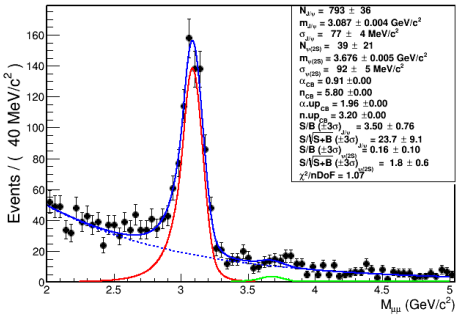

e) 4 <$p_{\rm T}$ < 5 GeV/c

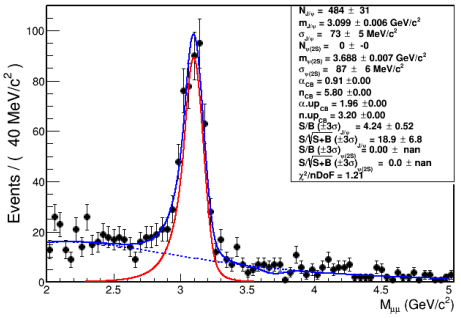

f) 5 <$p_{\rm T}$ < 6 GeV/c

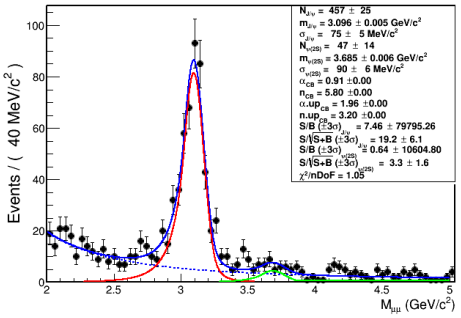

g) 6 <$p_{\rm T}$ < 8 GeV/c

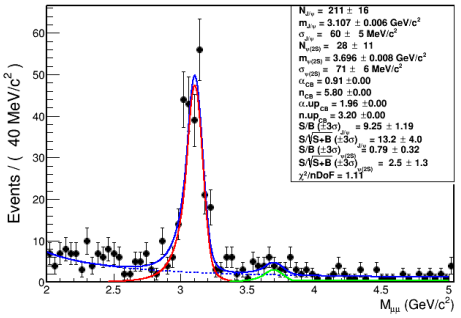

h) 8 <$p_{\rm T}$ < 15 GeV/c

Figure A.8. Examples of the signal extraction in p-Pb with VWG + CB2 fit for different $p_{\rm T}$ intervals for the ZN event activity class 0-5%.

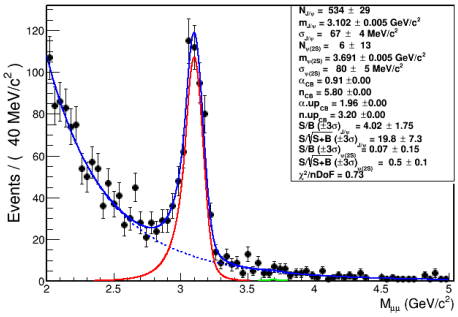

a) $0 < p_{\mathrm{T}} < 1$ GeV/c

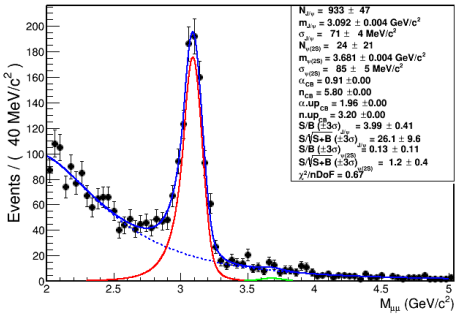

b) $1 < p_{\mathrm{T}} < 2$ GeV/c

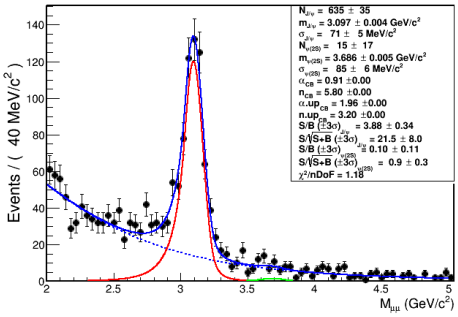

c) $2 < p_{\mathrm{T}} < 3$ GeV/c

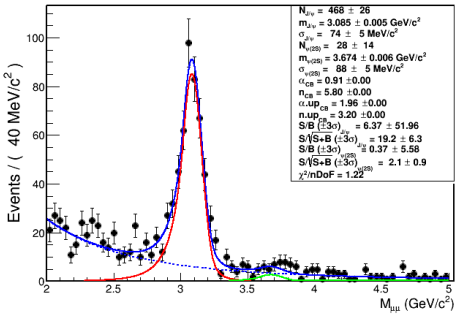

d) $3 < p_{\mathrm{T}} < 4$ GeV/c

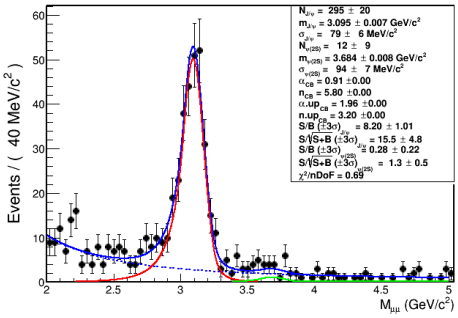

e) $4 < p_{\mathrm{T}} < 5$ GeV/c

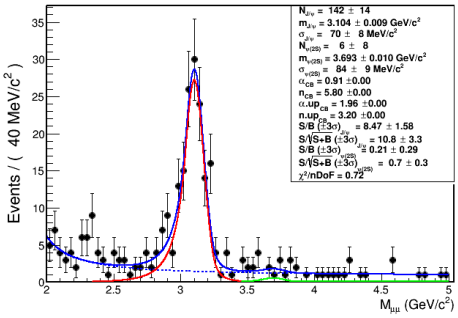

f) $5 < p_{\mathrm{T}} < 6$ GeV/c

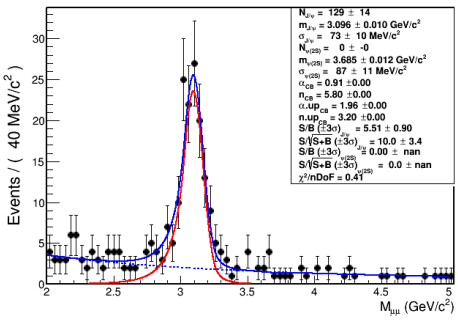

g) $6 < p_{\mathrm{T}} < 8$ GeV/c

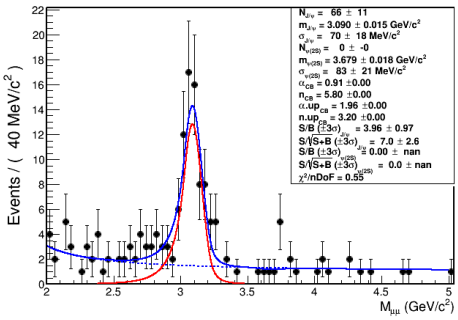

h) $8 < p_{\mathrm{T}} < 15$ GeV/c

Figure A.9. Examples of the signal extraction in p-Pb with VWG + CB2 fit for different p_{T} intervals for the ZN event activity class 80-100%.

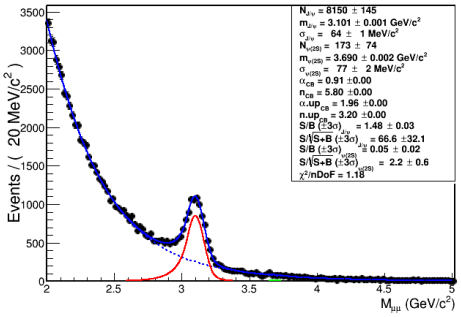

a) 0 <$p_{\rm T}$ < 1 GeV/c

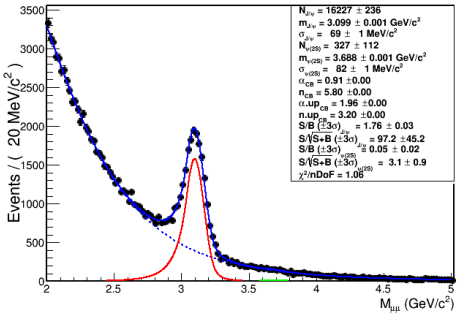

b) 1 <$p_{\rm T}$ < 2 GeV/c

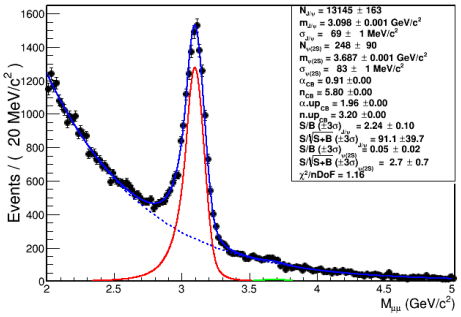

c) 2 <$p_{\rm T}$ < 3 GeV/c

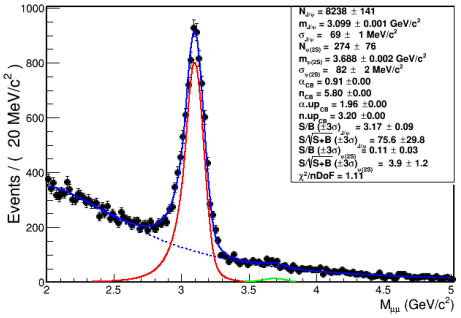

d) 3 <$p_{\rm T}$ < 4 GeV/c

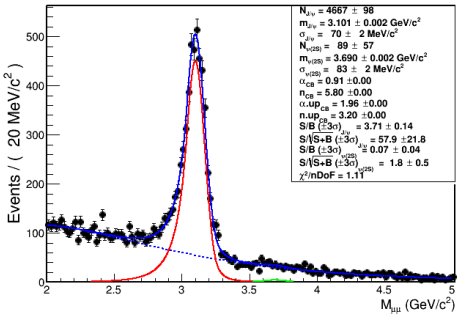

e) 4 <$p_{\rm T}$ < 5 GeV/c

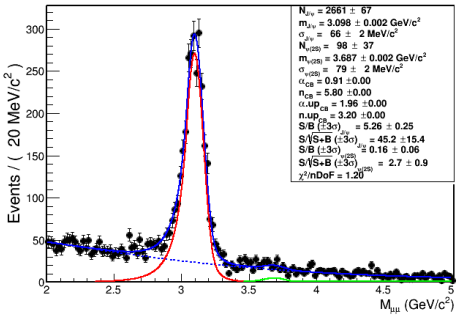

f) 5 <$p_{\rm T}$ < 6 GeV/c

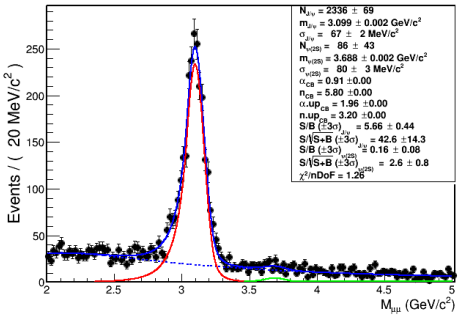

g) 6 <$p_{\rm T}$ < 8 GeV/c

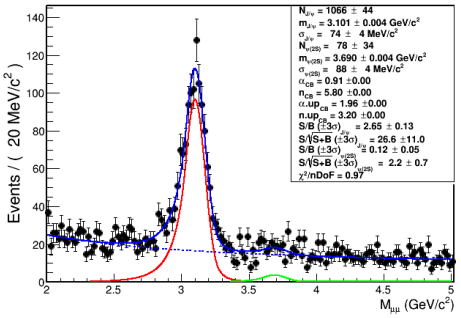

h) 8 <$p_{\rm T}$ < 15 GeV/c

Figure A.10. Examples of the signal extraction in Pb-p with VWG + CB2 fit for different $p_{\rm T}$ intervals integrated over the event activity.

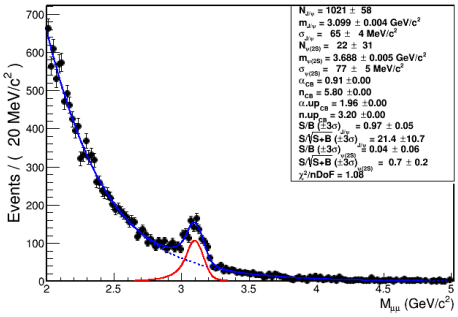

a) $0 < p_{\mathrm{T}} < 1$ GeV/c

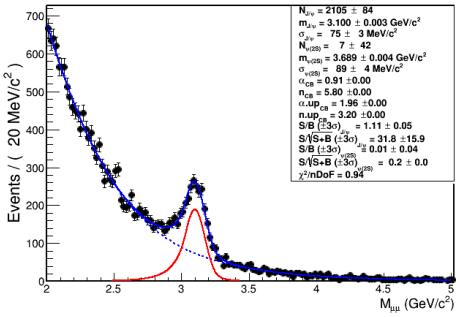

b) $1 < p_{\mathrm{T}} < 2$ GeV/c

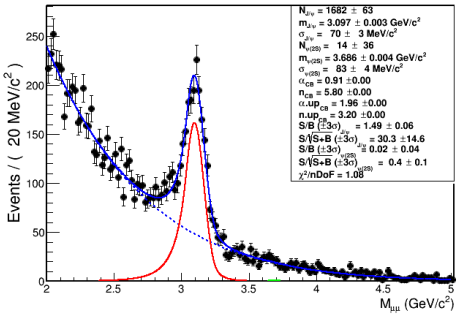

c) $2 < p_{\mathrm{T}} < 3$ GeV/c

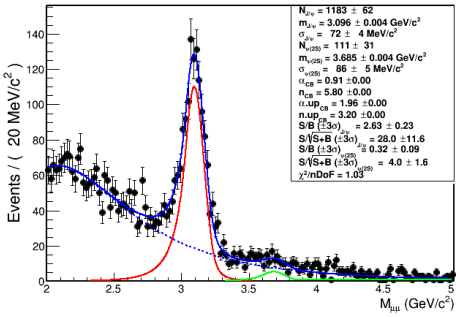

d) $3 < p_{\mathrm{T}} < 4$ GeV/c

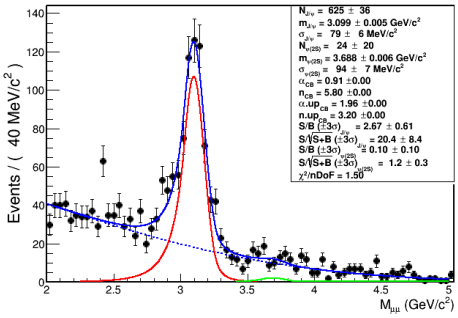

e) $4 < p_{\mathrm{T}} < 5$ GeV/c

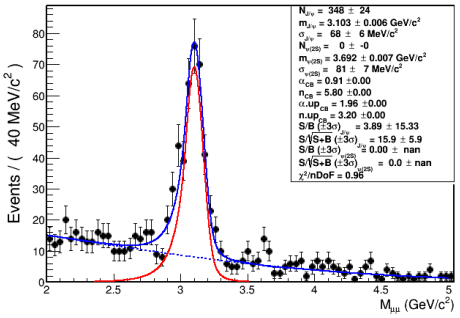

f) $5 < p_{\mathrm{T}} < 6$ GeV/c

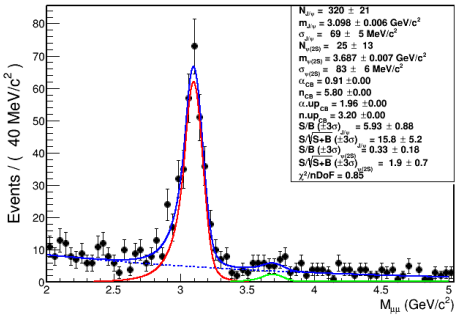

g) $6 < p_{\mathrm{T}} < 8$ GeV/c

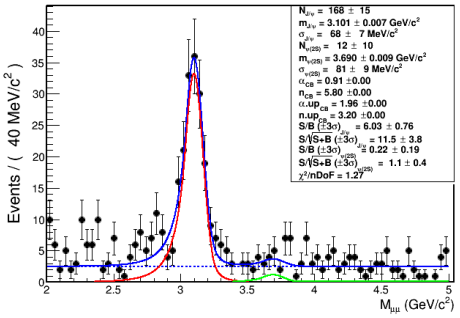

h) $8 < p_{\mathrm{T}} < 15$ GeV/c

Figure A.11. Examples of the signal extraction in Pb-p with VWG + CB2 fit for different p_{T} intervals for the ZN event activity class 0-5%.

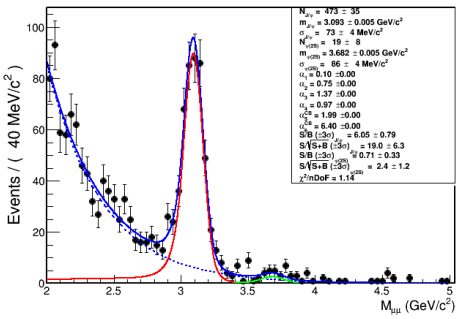

a) 0 <$p_{\rm T}$ < 1 GeV/c

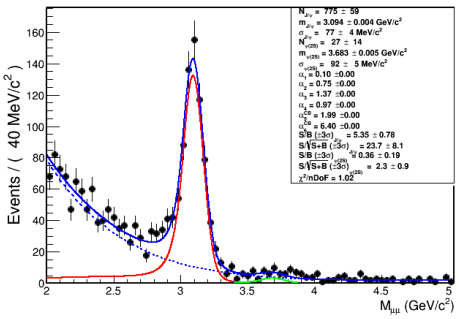

b) 1 <$p_{\rm T}$ < 2 GeV/c

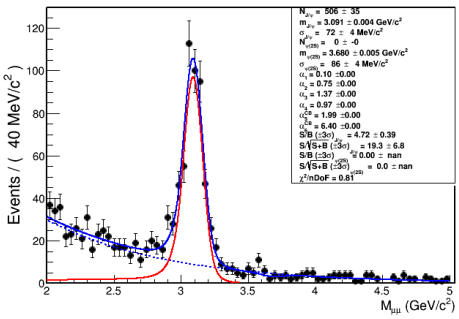

c) 2 <$p_{\rm T}$ < 3 GeV/c

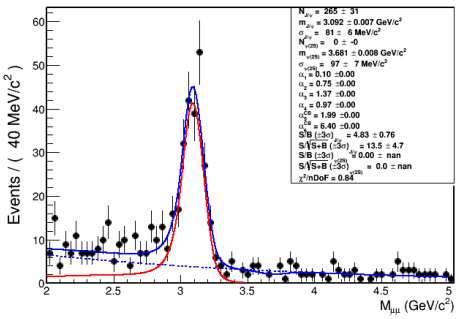

d) 3 <$p_{\rm T}$ < 4 GeV/c

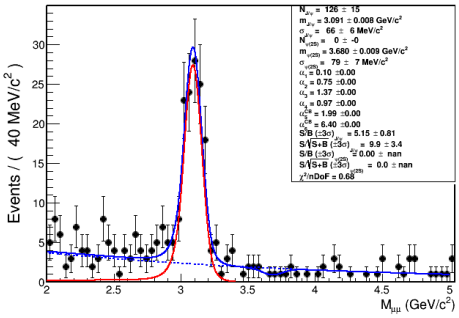

e) 4 <$p_{\rm T}$ < 5 GeV/c

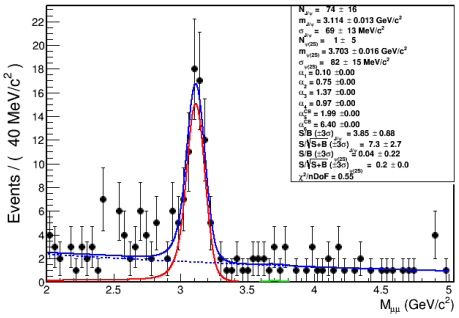

f) 5 <$p_{\rm T}$ < 6 GeV/c

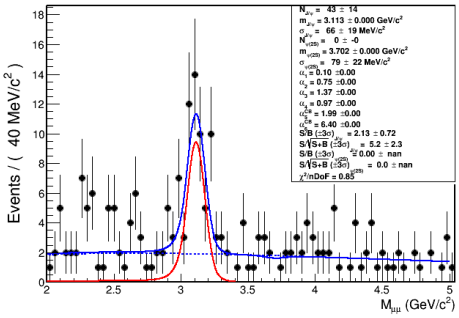

g) 6 <$p_{\rm T}$ < 8 GeV/c

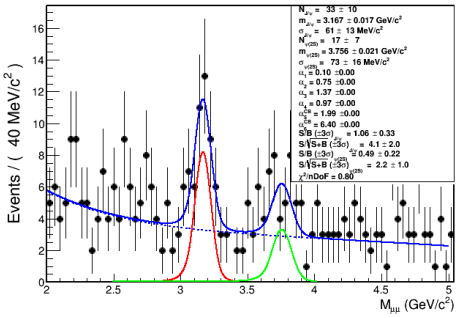

h) 8 <$p_{\rm T}$ < 15 GeV/c

Figure A.12. Examples of the signal extraction in Pb-p with Pol2xExp + NA60 fit for different $p_{\rm T}$ intervals for the ZN event activity class 80-100%.

Appendix B

Functions used for the signal extraction

The following functions were used for the signal extraction. In all of them only x, σ, N are left free when fitting the data, while all the other parameters are fixed from the corresponding pure J/ψ MC simulations.

B.1 CB2 function

An extended Crystal Ball Function is defined as follows:

$$f(x; N, \bar{x}, \sigma, \alpha, \alpha', n, n') = N \cdot \begin{cases} \exp\left(-\frac{(x-\bar{x})^2}{2\sigma^2}\right) & , -\alpha < \frac{x-\bar{x}}{\sigma} < \alpha' \\ A \cdot \left(B - \frac{x-\bar{x}}{\sigma}\right)^{-n} & , \frac{x-\bar{x}}{\sigma} \leq -\alpha \\ C \cdot \left(D + \frac{x-\bar{x}}{\sigma}\right)^{-n} & , \frac{x-\bar{x}}{\sigma} \geq -\alpha' \end{cases} , \quad \text{(B.1)}$$

where

$$\begin{aligned} A &= \left(\frac{n}{|\alpha|}\right)^n \cdot \exp\left(-\frac{|\alpha|^2}{2}\right) \\ B &= \frac{n}{|\alpha|} - |\alpha| \\ C &= \left(\frac{n'}{|\alpha'|}\right)^{n'} \cdot \exp\left(-\frac{|\alpha'|^2}{2}\right) \\ D &= \frac{n'}{|\alpha'|} - |\alpha'| \end{aligned}$$

B.2 NA60 function

The NA60 function was first used in one PhD thesis of the NA60 Collaboration [127].

$$f(x; N, \bar{x}, \sigma, x_1, x_2, p_1, ..., p_6) = N \cdot \exp\left(-\frac{(x-\bar{x})^2}{2\sigma^2_{NA60}}\right), \quad \text{(B.2)}$$

where

$$\sigma_{NA60} = \begin{cases} \sigma \cdot \left(1 + (p_1(x_1 - x))^{p_2 - p_3\sqrt{x_1 - x}}\right) & , x < x_1 \\ \sigma & , x_1 \leq x < x_2 \\ \sigma \cdot \left(1 + (p_4(x_1 - x))^{p_5 - p_6\sqrt{x - x_2}}\right) & , x \geq x_2 \end{cases}$$

B.3 NA60CB2 function

The NA60CB2 function is a combination of the two previous functions where NA60 function was used for the left tail, CB2 function was used for the right tail. The core is the same in both functions and was not modified.

B.4 New formulation of NA60 function

Variables $x_{1,2}$ can be redefined via $\bar{x}$: $x_{1,2} = a_{1,2} \cdot \bar{x}$. Then a new formulation of the NA60 function can be proposed [239]:

$$f(x; N, \bar{x}, \sigma, t_1, t_2, p_1, ..., p_6) = N \cdot \exp\left(-\frac{1}{2}\left(\frac{t}{t_0}\right)^2\right), \tag{B.3}$$

where

$$t = \frac{x - \bar{x}}{\sigma}$$

and

$$t_0 = \begin{cases} 1 + (p_1(t_1 - t))^{p_2 - p_3\sqrt{t_1 - t}} & , t < t_1 \\ 1 & , t_1 \leq t < t_2 \\ 1 + (p_4(t - t_2))^{p_5 - p_6\sqrt{t - t_2}} & , t \geq t_2 \end{cases}$$

This formulation is equivalent to the formulation on the previous slide, provided that one replaces the old formulation parameters, obtained from the fit to MC J/ψ signal, by the parameters for the new formulation, using the following prescription:

$$
\begin{aligned}
t_1 &= (x_1^{\mathrm{MC}} - \bar{x}^{\mathrm{MC}})/\sigma^{\mathrm{MC}} = (a_1 - 1) \cdot \bar{x}^{\mathrm{MC}}/\sigma^{\mathrm{MC}}, \\
t_2 &= (x_2^{\mathrm{MC}} - \bar{x}^{\mathrm{MC}})/\sigma^{\mathrm{MC}} = (a_2 - 1) \cdot \bar{x}^{\mathrm{MC}}/\sigma^{\mathrm{MC}}, \\
p_1^{\mathrm{new}} &= \sigma^{\mathrm{MC}} \cdot p_1^{\mathrm{old}}, \\
p_2^{\mathrm{new}} &= p_2^{\mathrm{old}}, \\
p_3^{\mathrm{new}} &= \sqrt{\sigma^{\mathrm{MC}}} \cdot p_3^{\mathrm{old}}.
\end{aligned}
$$

Values of $x_{1,2}^{\mathrm{MC}}, \bar{x}^{\mathrm{MC}}$ and σ^{MC} are fixed with the old formulation of NA60 from the corresponding MC simulations.

List of Figures

List of Tables

References

1. **E598 Collaboration** , J. Aubert *et al.*, "Experimental Observation of a Heavy Particle J," *Phys.Rev.Lett.* **33** (1974) 1404–1406. 17, 18

2. **SLAC-SP-017 Collaboration** , J. Augustin *et al.*, "Discovery of a Narrow Resonance in e+ e- Annihilation," *Phys.Rev.Lett.* **33** (1974) 1406–1408. 17

3. A. Mocsy, P. Petreczky, and M. Strickland, "Quarkonia in the Quark Gluon Plasma," *Int.J.Mod.Phys.* **A28** (2013) 1340012, `arXiv:1302.2180 [hep-ph]`. 19, 209

4. H. Satz, "Colour deconfinement and quarkonium binding," *J.Phys.* **G32** (2006) R25, `arXiv:hep-ph/0512217 [hep-ph]`. 19

5. S. Okubo, "Phi meson and unitary symmetry model," *Phys.Lett.* **5** (1963) 165–168. 20

6. G. Zweig, "An SU(3) model for strong interaction symmetry and its breaking. Version 2,". 20

7. J. Iizuka, "Systematics and phenomenology of meson family," *Prog.Theor.Phys.Suppl.* **37** (1966) 21–34. 20

8. H. Fritzsch, "Producing Heavy Quark Flavors in Hadronic Collisions: A Test of Quantum Chromodynamics," *Phys.Lett.* **B67** (1977) 217. 20

9. F. Halzen, "CVC for Gluons and Hadroproduction of Quark Flavors," *Phys.Lett.* **B69** (1977) 105. 20

10. R. Vogt, "J/ψ production and suppression," *Phys.Rept.* **310** (1999) 197–260. 20

11. **Quarkonium Working Group** , N. Brambilla *et al.*, "Heavy quarkonium physics," *CERN YELLOW REPORT* (2004) , `arXiv:hep-ph/0412158 [hep-ph]`. 21, 22, 25, 26, 209

12. M. Einhorn and S. Ellis, "Hadronic Production of the New Resonances: Probing Gluon Distributions," *Phys.Rev.* **D12** (1975) 2007. 21

13. S. Ellis, M. B. Einhorn, and C. Quigg, "Comment on Hadronic Production of Psions," *Phys.Rev.Lett.* **36** (1976) 1263. 21

14. C. Carlson and R. Suaya, "Hadronic Production of psi/J Mesons," *Phys.Rev.* **D14** (1976) 3115. 21

15. C.-H. Chang, "Hadronic Production of J/ψ Associated With a Gluon," *Nucl.Phys.* **B172** (1980) 425–434. 21

16. E. L. Berger and D. L. Jones, "Inelastic Photoproduction of J/psi and Upsilon by Gluons," *Phys.Rev.* **D23** (1981) 1521–1530. 21

17. N. Brambilla, S. Eidelman, B. Heltsley, R. Vogt, G. Bodwin, *et al.*, "Heavy quarkonium: progress, puzzles, and opportunities," *Eur.Phys.J.* **C71** (2011) 1534, arXiv:1010.5827 [hep-ph]. 21, 43, 211

18. G. A. Schuler, "Quarkonium production and decays," *Phys.Rept.* (1994) , arXiv:hep-ph/9403387 [hep-ph]. 21

19. P. Artoisenet, J. Lansberg, and F. Maltoni, "Hadroproduction of J/ψ and Υ in association with a heavy-quark pair," *Phys.Lett.* **B653** (2007) 60–66, arXiv:hep-ph/0703129 [HEP-PH]. 21, 23

20. J. M. Campbell, F. Maltoni, and F. Tramontano, "QCD corrections to J/psi and Upsilon production at hadron colliders," *Phys.Rev.Lett.* **98** (2007) 252002, arXiv:hep-ph/0703113 [HEP-PH]. 21, 23

21. P. Artoisenet, J. M. Campbell, J. Lansberg, F. Maltoni, and F. Tramontano, "Υ Production at Fermilab Tevatron and LHC Energies," *Phys.Rev.Lett.* **101** (2008) 152001, arXiv:0806.3282 [hep-ph]. 21, 23, 26

22. G. T. Bodwin, E. Braaten, and G. P. Lepage, "Rigorous QCD analysis of inclusive annihilation and production of heavy quarkonium," *Phys.Rev.* **D51** (1995) 1125–1171, arXiv:hep-ph/9407339 [hep-ph]. 22

23. G. T. Bodwin, E. Braaten, and J. Lee, "Comparison of the color-evaporation model and the NRQCD factorization approach in charmonium production," *Phys.Rev.* **D72** (2005) 014004, arXiv:hep-ph/0504014 [hep-ph]. 22, 25

24. G. T. Bodwin, X. Garcia i Tormo, and J. Lee, "Factorization theorems for exclusive heavy-quarkonium production," *Phys.Rev.Lett.* **101** (2008) 102002, arXiv:0805.3876 [hep-ph]. 23

25. G. T. Bodwin, X. Garcia i Tormo, and J. Lee, "Factorization in exclusive quarkonium production," *Phys.Rev.* **D81** (2010) 114014, arXiv:1003.0061 [hep-ph]. 23

26. **CDF Collaboration** , H. B. Jensen, "The Collider Detector at Fermilab (CDF)," *IEEE Trans.Nucl.Sci.* **33** (1986) 40–45. 23

27. T. Group, "Design Report Tevatron 1 project,". 23

28. **CDF Collaboration** , F. Abe *et al.*, "J/ψ and $\psi(2S)$ production in $p\bar{p}$ collisions at $\sqrt{s} = 1.8$ TeV," *Phys.Rev.Lett.* **79** (1997) 572–577. 23, 26, 209

29. **CDF Collaboration** , F. Abe *et al.*, "Production of J/ψ mesons from χ_c meson decays in $p\bar{p}$ collisions at $\sqrt{s} = 1.8$ TeV," *Phys.Rev.Lett.* **79** (1997) 578–583. 23, 26, 209

30. . Kramer, Michael, "Quarkonium production at high-energy colliders," *Prog.Part.Nucl.Phys.* **47** (2001) 141–201, arXiv:hep-ph/0106120 [hep-ph]. 23, 24, 209

31. E. Braaten, D. Kang, J. Lee, and C. Yu, "Optimal spin quantization axes for the polarization of dileptons with large transverse momentum," *Phys.Rev.* **D79** (2009) 014025, arXiv:0810.4506 [hep-ph]. 25

32. S. P. Baranov, "Highlights from the $k_{\rm T}$ factorization approach on the quarkonium production puzzles," *Phys.Rev.* **D66** (2002) 114003. 25, 27, 209

33. E. Braaten, B. A. Kniehl, and J. Lee, "Polarization of prompt J/ψ at the Tevatron," *Phys.Rev.* **D62** (2000) 094005, arXiv:hep-ph/9911436 [hep-ph]. 27, 209

34. **CDF Collaboration** , A. Abulencia *et al.*, "Polarization of J/ψ and ψ_{2S} mesons produced in $p\bar{p}$ collisions at $\sqrt{s} = 1.96$-TeV," *Phys.Rev.Lett.* **99** (2007) 132001, arXiv:0704.0638 [hep-ex]. 27, 209

35. H. Hahn, E. Forsyth, H. Foelsche, M. Harrison, J. Kewisch, *et al.*, "The RHIC design overview," *Nucl.Instrum.Meth.* **A499** (2003) 245–263. 26

36. **PHENIX Collaboration** , S. Aronson, "The PHENIX experiment at RHIC,". 26

37. **STAR Collaboration** , J. Harris, "The STAR experiment at the relativistic heavy ion collider," *Nucl.Phys.* **A566** (1994) 277C–285C. 26

38. **STAR Collaboration** , B. Abelev *et al.*, "J/psi production at high transverse momentum in p+p and Cu+Cu collisions at s(NN)**1/2 = 200GeV," *Phys.Rev.* **C80** (2009) 041902, arXiv:0904.0439 [nucl-ex]. 26, 27, 28, 210

39. G. C. Nayak, M. X. Liu, and F. Cooper, "Color octet contribution to high $p_T J/\psi$ production in pp collisions at $\sqrt{s}$ = 500-GeV and 200-GeV at RHIC," *Phys.Rev.* **D68** (2003) 034003, arXiv:hep-ph/0302095 [hep-ph]. 26

40. H. S. Chung, C. Yu, S. Kim, and J. Lee, "Polarization of prompt J/psi in proton-proton collisions at RHIC," *Phys.Rev.* **D81** (2010) 014020, arXiv:0911.2113 [hep-ph]. 27, 28, 29, 209

41. **PHENIX Collaboration** , C. L. da Silva, "Quarkonia measurement in p+p and d+Au collisions at s**(1/2) = 200- GeV by PHENIX Detector," *Nucl.Phys.* **A830** (2009) 227C–230C, arXiv:0907.4696 [nucl-ex]. 28, 209

42. J. Lansberg, "QCD corrections to J/psi polarisation in pp collisions at RHIC," *Phys.Lett.* **B695** (2011) 149–156, arXiv:1003.4319 [hep-ph]. 27, 28, 29, 210

43. **PHENIX Collaboration** , A. Adare *et al.*, "J/ψ production versus transverse momentum and rapidity in p^+p collisions at $\sqrt{s}$ = 200-GeV," *Phys.Rev.Lett.* **98** (2007) 232002, arXiv:hep-ex/0611020 [hep-ex]. 27, 28, 210

44. C. Lam and W.-K. Tung, "A Systematic Approach to Inclusive Lepton Pair Production in Hadronic Collisions," *Phys.Rev.* **D18** (1978) 2447. 27

45. O. S. Bruning, P. Collier, P. Lebrun, S. Myers, R. Ostojic, *et al.*, "LHC Design Report. 1. The LHC Main Ring,". 29, 67

46. O. Buning, P. Collier, P. Lebrun, S. Myers, R. Ostojic, *et al.*, "LHC Design Report. 2. The LHC infrastructure and general services,". 29, 67

47. M. Benedikt, P. Collier, V. Mertens, J. Poole, and K. Schindl, "LHC Design Report. 3. The LHC injector chain,". 29, 67

48. **ATLAS Collaboration** , G. Aad *et al.*, "The ATLAS Experiment at the CERN Large Hadron Collider," *JINST* **3** (2008) S08003. 29, 69

49. **CMS Collaboration** , S. Chatrchyan *et al.*, "The CMS experiment at the CERN LHC," *JINST* **3** (2008) S08004. 29, 69

50. **ALICE Collaboration** , K. Aamodt *et al.*, "The ALICE experiment at the CERN LHC," *JINST* **3** (2008) S08002. 29, 69, 81, 212

51. **LHCb Collaboration** , J. Alves, A. Augusto *et al.*, "The LHCb Detector at the LHC," *JINST* **3** (2008) S08005. 29, 69

52. **CMS Collaboration** , S. Chatrchyan *et al.*, "J/ψ and ψ_{2S} production in pp collisions at $\sqrt{s} = 7$ TeV," *JHEP* **1202** (2012) 011, arXiv:1111.1557 [hep-ex]. 30

53. **LHCb collaboration** , R. Aaij *et al.*, "Production of J/ψ and Υ mesons in pp collisions at $\sqrt{s} = 8$ TeV," *JHEP* **1306** (2013) 064, arXiv:1304.6977 [hep-ex]. 30

54. **ALICE Collaboration** , B. Abelev *et al.*, "Inclusive J/ψ production in pp collisions at $\sqrt{s} = 2.76$ TeV," *Phys.Lett.* **B718** (2012) 295–306, arXiv:1203.3641 [hep-ex]. 30, 122, 143, 144, 147, 222

55. **ATLAS Collaboration** , G. Aad *et al.*, "Measurement of the differential cross-sections of inclusive, prompt and non-prompt J/ψ production in proton-proton collisions at $\sqrt{s} = 7$ TeV," *Nucl.Phys.* **B850** (2011) 387–444, arXiv:1104.3038 [hep-ex]. 30

56. **CMS Collaboration** , V. Khachatryan *et al.*, "Prompt and non-prompt J/ψ production in pp collisions at $\sqrt{s} = 7$ TeV," *Eur.Phys.J.* **C71** (2011) 1575, arXiv:1011.4193 [hep-ex]. 31, 210

57. **LHCb Collaboration** , R. Aaij *et al.*, "Measurement of the ratio of prompt χ_c to J/ψ production in pp collisions at $\sqrt{s} = 7$ TeV," *Phys.Lett.* **B718** (2012) 431–440, arXiv:1204.1462 [hep-ex]. 31, 210

58. T. A. collaboration, "Measurement of χ_{c1} and χ_{c2} production with $\sqrt{s} = 7$ TeV pp collisions at ATLAS,". 31, 32, 210

59. **CMS Collaboration** , S. Chatrchyan *et al.*, "Measurement of the relative prompt production rate of chi(c2) and chi(c1) in pp collisions at $\sqrt{s} = 7$ TeV," *Eur.Phys.J.* **C72** (2012) 2251, arXiv:1210.0875 [hep-ex]. 32, 210

60. L. Bianchi, "J/ψ polarization in pp collisions at $\sqrt{s} = 7$ TeV with the ALICE muon spectrometer at the LHC," *PhD thesis* (2012) . 30, 77, 81, 212

61. M. Butenschoen and B. A. Kniehl, "J/psi polarization at Tevatron and LHC: Nonrelativistic-QCD factorization at the crossroads," *Phys.Rev.Lett.* **108** (2012) 172002, arXiv:1201.1872 [hep-ph]. 33, 210

62. C. Wong, "Introduction to high-energy heavy ion collisions,". 35, 36

63. T. Matsui and H. Satz, "J/ψ Suppression by Quark-Gluon Plasma Formation," *Phys.Lett.* **B178** (1986) 416. 35, 36

64. H. Reeves, "Big Bang nucleosynthesis and the quark - hadron phase transition," *Phys.Rept.* **201** (1991) 335–354. 35

65. M. Lamont, "Neutral Strange Particle Production in Ultra-Relativistic Heavy Ion collisions at $\sqrt{s_{\rm NN}} = 130$ GeV," *PhD thesis* (2002) . 37, 210

66. Y. Aoki, Z. Fodor, S. Katz, and K. Szabo, "The QCD transition temperature: Results with physical masses in the continuum limit," *Phys.Lett.* **B643** (2006) 46–54, `arXiv:hep-lat/0609068 [hep-lat]`. 37

67. M. Cheng, N. Christ, S. Datta, J. van der Heide, C. Jung, *et al.*, "The QCD equation of state with almost physical quark masses," *Phys.Rev.* **D77** (2008) 014511, `arXiv:0710.0354 [hep-lat]`. 37

68. Y. Aoki, S. Borsanyi, S. Durr, Z. Fodor, S. D. Katz, *et al.*, "The QCD transition temperature: results with physical masses in the continuum limit II.," *JHEP* **0906** (2009) 088, `arXiv:0903.4155 [hep-lat]`. 37

69. A. Bazavov, T. Bhattacharya, M. Cheng, N. Christ, C. DeTar, *et al.*, "Equation of state and QCD transition at finite temperature," *Phys.Rev.* **D80** (2009) 014504, `arXiv:0903.4379 [hep-lat]`. 37

70. M. Cheng, S. Ejiri, P. Hegde, F. Karsch, O. Kaczmarek, *et al.*, "Equation of State for physical quark masses," *Phys.Rev.* **D81** (2010) 054504, `arXiv:0911.2215 [hep-lat]`. 37

71. **HotQCD Collaboration** , A. Bazavov and P. Petreczky, "First results on QCD thermodynamics with HISQ action," *PoS* **LAT2009** (2009) 163, `arXiv:0912.5421 [hep-lat]`. 37

72. **HotQCD collaboration** , A. Bazavov and P. Petreczky, "Deconfinement and chiral transition with the highly improved staggered quark (HISQ) action," *J.Phys.Conf.Ser.* **230** (2010) 012014, `arXiv:1005.1131 [hep-lat]`. 37

73. **HotQCD Collaboration** , A. Bazavov and P. Petreczky, "Chiral transition and deconfinement transition in QCD with the highly improved staggered quark (HISQ) action," *Phys.Part.Nucl.Lett.* **8** (2011) 860–864, `arXiv:1009.4914 [hep-lat]`. 37

74. **Wuppertal-Budapest Collaboration** , S. Borsanyi *et al.*, "Is there still any T_c mystery in lattice QCD? Results with physical masses in the continuum limit III," *JHEP* **1009** (2010) 073, arXiv:1005.3508 [hep-lat]. 37

75. S. Borsanyi, G. Endrodi, Z. Fodor, A. Jakovac, S. D. Katz, *et al.*, "The QCD equation of state with dynamical quarks," *JHEP* **1011** (2010) 077, arXiv:1007.2580 [hep-lat]. 37

76. H. Satz, "Charm and beauty in a hot environment," arXiv:hep-ph/0602245 [hep-ph]. 38, 221

77. P. Braun-Munzinger and J. Stachel, "(Non)thermal aspects of charmonium production and a new look at J / psi suppression," *Phys.Lett.* **B490** (2000) 196–202, arXiv:nucl-th/0007059 [nucl-th]. 38

78. R. L. Thews, M. Schroedter, and J. Rafelski, "Enhanced J/ψ production in deconfined quark matter," *Phys.Rev.* **C63** (2001) 054905, arXiv:hep-ph/0007323 [hep-ph]. 38

79. X. Zhao and R. Rapp, "Transverse Momentum Spectra of J/ψ in Heavy-Ion Collisions," *Phys.Lett.* **B664** (2008) 253–257, arXiv:0712.2407 [hep-ph]. 38, 40, 42, 211

80. P. P. Bhaduri, P. Hegde, H. Satz, and P. Tribedy, "An Introduction to the Spectral Analysis of the QGP," *Lect.Notes Phys.* **785** (2010) 179–197, arXiv:0812.3856 [hep-ph]. 38, 40, 210

81. K. Zhou, N. Xu, and P. Zhuang, "Quarkonium Production and Medium Effects in High Energy Nuclear Collisions," arXiv:1309.7520 [nucl-th]. 38

82. M. L. Mangano, P. Nason, and G. Ridolfi, "Heavy quark correlations in hadron collisions at next-to-leading order," *Nucl.Phys.* **B373** (1992) 295–345. 39, 210

83. **ALICE Collaboration** , B. Abelev *et al.*, "Measurement of charm production at central rapidity in proton-proton collisions at $\sqrt{s} = 2.76$ TeV," *JHEP* **1207** (2012) 191, arXiv:1205.4007 [hep-ex]. 39, 210

84. **NA50 Collaboration** , M. Abreu *et al.*, "Anomalous J / psi suppression in Pb - Pb interactions at 158 GeV/c per nucleon," *Phys.Lett.* **B410** (1997) 337–343. 40

85. **NA50 Collaboration** , B. Alessandro *et al.*, "A New measurement of J/psi suppression in Pb-Pb collisions at 158-GeV per nucleon," *Eur.Phys.J.* **C39** (2005) 335–345, arXiv:hep-ex/0412036 [hep-ex]. 40

86. **NA50 Collaboration** , B. Alessandro *et al.*, "J/psi and psi-prime production and their normal nuclear absorption in proton-nucleus collisions at 400-GeV," *Eur.Phys.J.* **C48** (2006) 329, arXiv:nucl-ex/0612012 [nucl-ex]. 40

87. D. Kharzeev, C. Lourenco, M. Nardi, and H. Satz, "A Quantitative analysis of charmonium suppression in nuclear collisions," *Z.Phys.* **C74** (1997) 307–318, arXiv:hep-ph/9612217 [hep-ph]. 40

88. C. Lourenco, "Open questions in quarkonium and electromagnetic probes," *Nucl.Phys.* **A783** (2007) 451–460, arXiv:nucl-ex/0612014 [nucl-ex]. 41, 211

89. **PHENIX Collaboration** , A. Adare *et al.*, "J/ψ suppression at forward rapidity in Au+Au collisions at $\sqrt{s_{NN}} = 200$ GeV," *Phys.Rev.* **C84** (2011) 054912, arXiv:1103.6269 [nucl-ex]. 40, 42, 211

90. X. Zhao and R. Rapp, "Forward and midrapidity charmonium production at RHIC," *Eur.Phys.J.* **C62** (2009) 109–117, arXiv:0810.4566 [nucl-th]. 40, 42, 211

91. A. Collaboration, "Differential studies of inclusive J/ψ and ψ(2S) production at forward rapidity in Pb-Pb collisions at $\sqrt{s_{\rm NN}} =$ 2.76 TeV," *Publication in preparation* (2014) . 44, 45, 46, 211

92. X. Zhao and R. Rapp, "Medium Modifications and Production of Charmonia at LHC," *Nucl.Phys.* **A859** (2011) 114–125, arXiv:1102.2194 [hep-ph]. 44

93. Y.-p. Liu, Z. Qu, N. Xu, and P.-f. Zhuang, "J/psi Transverse Momentum Distribution in High Energy Nuclear Collisions at RHIC," *Phys.Lett.* **B678** (2009) 72–76, arXiv:0901.2757 [nucl-th]. 44

94. E. Ferreiro, "Charmonium dissociation and recombination at LHC: Revisiting comovers," *Phys.Lett.* **B731** (2014) 57–63, arXiv:1210.3209 [hep-ph]. 44

95. **P. Shukla for CMS collaboration** , P. Shukla, "Overview of quarkonia and heavy flavour measurements by CMS," arXiv:1405.3810 [nucl-ex]. 44, 47, 211

96. **CMS Collaboration** , S. Chatrchyan *et al.*, "Indications of suppression of excited Υ states in PbPb collisions at $\sqrt{S_{NN}} = 2.76$ TeV," *Phys.Rev.Lett.* **107** (2011) 052302, arXiv:1105.4894 [nucl-ex]. 46

97. **CMS Collaboration** , S. Chatrchyan *et al.*, "Observation of sequential Upsilon suppression in PbPb collisions," *Phys.Rev.Lett.* **109** (2012) 222301, arXiv:1208.2826 [nucl-ex]. 46, 48, 211

98. M. Arneodo, "Nuclear effects in structure functions," *Phys.Rept.* **240** (1994) 301–393. 50, 51, 211

99. **H1 Collaboration** , C. Berger *et al.*, "Letter of intent for an experiment at HERA: H1 Collaboration,". 52

100. **ZEUS Collaboration** , K. Edwards *et al.*, "ZEUS, A DETECTOR FOR HERA: LETTER OF INTENT,". 52

101. A. Cooper-Sarkar and C. Gwenlan, "Comparison and combination of ZEUS and H1 PDF analyses: HERA - LHC workshop proceedings," arXiv:hep-ph/0508304 [hep-ph]. 52, 211

102. K. Eskola, H. Paukkunen, and C. Salgado, "EPS09: A New Generation of NLO and LO Nuclear Parton Distribution Functions," *JHEP* **0904** (2009) 065, arXiv:0902.4154 [hep-ph]. 53, 54, 55, 62, 211

103. K. Eskola, V. Kolhinen, and P. Ruuskanen, "Scale evolution of nuclear parton distributions," *Nucl.Phys.* **B535** (1998) 351–371, arXiv:hep-ph/9802350 [hep-ph]. 53

104. S. Forte and G. Watt, "Progress in the Determination of the Partonic Structure of the Proton," *Ann.Rev.Nucl.Part.Sci.* **63** (2013) 291–328, arXiv:1301.6754 [hep-ph]. 54

105. Y. L. Dokshitzer, "Calculation of the Structure Functions for Deep Inelastic Scattering and e+ e- Annihilation by Perturbation Theory in Quantum Chromodynamics.," *Sov.Phys.JETP* **46** (1977) 641–653. 54

106. V. Gribov and L. Lipatov, "Deep inelastic e p scattering in perturbation theory," *Sov.J.Nucl.Phys.* **15** (1972) 438–450. 54

107. G. Altarelli and G. Parisi, "Asymptotic Freedom in Parton Language," *Nucl.Phys.* **B126** (1977) 298. 54

108. G. Curci, W. Furmanski, and R. Petronzio, "Evolution of Parton Densities Beyond Leading Order: The Nonsinglet Case," *Nucl.Phys.* **B175** (1980) 27. 54

109. W. Furmanski and R. Petronzio, "Singlet Parton Densities Beyond Leading Order," *Phys.Lett.* **B97** (1980) 437. 54

110. R. K. Ellis, W. J. Stirling, and B. Webber, "QCD and collider physics," *Camb.Monogr.Part.Phys.Nucl.Phys.Cosmol.* **8** (1996) 1–435. 54

111. E. Kuraev, L. Lipatov, and V. S. Fadin, "The Pomeranchuk Singularity in Nonabelian Gauge Theories," *Sov.Phys.JETP* **45** (1977) 199–204. 54

112. I. Balitsky and L. Lipatov, "The Pomeranchuk Singularity in Quantum Chromodynamics," *Sov.J.Nucl.Phys.* **28** (1978) 822–829. 54

113. V. S. Fadin and L. Lipatov, "BFKL pomeron in the next-to-leading approximation," *Phys.Lett.* **B429** (1998) 127–134, arXiv:hep-ph/9802290 [hep-ph]. 54

114. F. Gelis, E. Iancu, J. Jalilian-Marian, and R. Venugopalan, "The Color Glass Condensate," *Ann.Rev.Nucl.Part.Sci.* **60** (2010) 463–489, arXiv:1002.0333 [hep-ph]. 55

115. D. Kharzeev and K. Tuchin, "Signatures of the color glass condensate in J/psi production off nuclear targets," *Nucl.Phys.* **A770** (2006) 40–56, arXiv:hep-ph/0510358 [hep-ph]. 55, 57, 62, 65

116. D. Triantafyllopoulos, "The Color Glass Condensate and some applications," *Acta Phys.Polon.Supp.* **5** (2012) 1155–1162, arXiv:1209.3183 [hep-ph]. 56, 212

117. B. A. Meredith, "A Study of Nuclear Effects using Forward-Rapidity Hadron Production and Di-Hadron Angular Correlations in $\sqrt{s_{NN}} = 200$ GeV d+Au and p+p Collisions with the PHENIX Detector at RHIC," *PhD thesis* (2011) . 56

118. H. Kowalski, T. Lappi, and R. Venugopalan, "Nuclear enhancement of universal dynamics of high parton densities," *Phys.Rev.Lett.* **100** (2008) 022303, arXiv:0705.3047 [hep-ph]. 56

119. D. Kharzeev and K. Tuchin, "Open charm production in heavy ion collisions and the color glass condensate," *Nucl.Phys.* **A735** (2004) 248–266, arXiv:hep-ph/0310358 [hep-ph]. 57, 62

120. K. Tuchin, "Heavy quark production from color glass condensate at RHIC," *J.Phys.* **G30** (2004) S1167–S1170, arXiv:hep-ph/0402298 [hep-ph]. 57

121. E. Levin, M. Ryskin, Y. Shabelski, and A. Shuvaev, "Heavy quark production in semihard nucleon interactions," *Sov.J.Nucl.Phys.* **53** (1991) 657. 57

122. D. Kharzeev, E. Levin, and K. Tuchin, "Nuclear modification of the J/ψ transverse momentum distributions in high energy pA and AA collisions," *Nucl.Phys.* **A924** (2014) 47–64, arXiv:1205.1554 [hep-ph]. 57

123. F. Dominguez, D. Kharzeev, E. Levin, A. Mueller, and K. Tuchin, "Gluon saturation effects on the color singlet J/Psi production in high energy dA and AA collisions," *Phys.Lett.* **B710** (2012) 182–187, arXiv:1109.1250 [hep-ph]. 57

124. H. Fujii, F. Gelis, and R. Venugopalan, "Quark pair production in high energy pA collisions: General features," *Nucl.Phys.* **A780** (2006) 146–174, arXiv:hep-ph/0603099 [hep-ph]. 57

125. H. Fujii and K. Watanabe, "Heavy quark pair production in high energy pA collisions: Quarkonium," *Nucl.Phys.* **A915** (2013) 1–23, arXiv:1304.2221 [hep-ph]. 57, 157, 158, 179, 180, 216, 218

126. Z.-B. Kang, Y.-Q. Ma, and R. Venugopalan, "Quarkonium production in high energy proton-nucleus collisions: CGC meets NRQCD," *JHEP* **1401** (2014) 056, arXiv:1309.7337 [hep-ph]. 57

127. R. Shahoyan, "J/psi and psi-prime production in 450 GeV pA interactions and its dependence on the rapidity and xF," *PhD thesis* (2001) . 58, 102, 205

128. **NA50 Collaboration** , B. Alessandro *et al.*, "Charmonium production and nuclear absorption in p A interactions at 450-GeV," *Eur.Phys.J.* **C33** (2004) 31–40. 58

129. C. Lourenco, R. Vogt, and H. K. Woehri, "Energy dependence of J/psi absorption in proton-nucleus collisions," *JHEP* **0902** (2009) 014, arXiv:0901.3054 [hep-ph]. 59, 212

130. A. Accardi, F. Arleo, W. Brooks, D. D'Enterria, and V. Muccifora, "Parton Propagation and Fragmentation in QCD Matter," *Riv.Nuovo Cim.* **32** (2010) 439–553, arXiv:0907.3534 [nucl-th]. 59

131. D. d'Enterria, "Jet quenching," arXiv:0902.2011 [nucl-ex]. 59

132. F. Arleo, S. Peigné, and T. Sami, "Revisiting scaling properties of medium-induced gluon radiation," *Phys.Rev.* **D83** (2011) 114036, arXiv:1006.0818 [hep-ph]. 59, 60

133. F. Arleo and S. Peigné, "Heavy-quarkonium suppression in p-A collisions from parton energy loss in cold QCD matter," *JHEP* **1303** (2013) 122, arXiv:1212.0434 [hep-ph]. 60, 64, 65, 157, 216

134. F. Arleo and S. Peigné, "J/ψ suppression in p-A collisions from parton energy loss in cold QCD matter," *Phys.Rev.Lett.* **109** (2012) 122301, arXiv:1204.4609 [hep-ph]. 60, 61

135. R. Baier, Y. L. Dokshitzer, A. H. Mueller, S. Peigne, and D. Schiff, "Radiative energy loss and p(T) broadening of high-energy partons in nuclei," *Nucl.Phys.* **B484** (1997) 265–282, arXiv:hep-ph/9608322 [hep-ph]. 60

136. K. J. Golec-Biernat and M. Wusthoff, "Saturation effects in deep inelastic scattering at low Q**2 and its implications on diffraction," *Phys.Rev.* **D59** (1998) 014017, arXiv:hep-ph/9807513 [hep-ph]. 61

137. **NuSea Collaboration** , M. Leitch *et al.*, "Measurement of J / psi and psi-prime suppression in p-A collisions at 800-GeV/c," *Phys.Rev.Lett.* **84** (2000) 3256–3260, arXiv:nucl-ex/9909007 [nucl-ex]. 61

138. **PHENIX Collaboration** , A. Adare *et al.*, "Cold Nuclear Matter Effects on J/ψ Yields as a Function of Rapidity and Nuclear Geometry in Deuteron-Gold Collisions at $\sqrt{s_{NN}} = 200$ GeV," *Phys.Rev.Lett.* **107** (2011) 142301, arXiv:1010.1246 [nucl-ex]. 61, 62, 64, 212

139. **PHENIX Collaboration** , A. Adare *et al.*, "Transverse-Momentum Dependence of the J/ψ Nuclear Modification in d+Au Collisions at $\sqrt{s_{NN}} = 200$ GeV," *Phys.Rev.* **C87** no. 3, (2013) 034904, arXiv:1204.0777 [nucl-ex]. 61, 63, 170, 172, 212, 217

140. R. Vogt, "Shadowing and absorption effects on J/psi production in dA collisions," *Phys.Rev.* **C71** (2005) 054902, arXiv:hep-ph/0411378 [hep-ph]. 62, 65

141. D. de Florian and R. Sassot, "Nuclear parton distributions at next-to-leading order," *Phys.Rev.* **D69** (2004) 074028, arXiv:hep-ph/0311227 [hep-ph]. 63

142. E. Ferreiro, F. Fleuret, J. Lansberg, N. Matagne, and A. Rakotozafindrabe, "Centrality, Rapidity, and Transverse-Momentum Dependence of Gluon Shadowing and Antishadowing on J/ψ Production in dAu Collisions at $\sqrt{s}$=200 GeV," *Few Body Syst.* **53** (2012) 27–36, arXiv:1201.5574 [hep-ph]. 64

143. B. Kopeliovich, I. Potashnikova, and I. Schmidt, "J/Ψ production in nuclear collisions: Theoretical approach to measuring the transport coefficient," *Phys.Rev.* **C82** (2010) 024901, arXiv:1006.3042 [nucl-th]. 64

144. B. Kopeliovich, I. Potashnikova, and I. Schmidt, "Nuclear suppression of J/Psi: from RHIC to the LHC," *Nucl.Phys.* **A864** (2011) 203–212, arXiv:1012.5648 [hep-ph]. 64

145. J. Cronin, H. J. Frisch, M. Shochet, J. Boymond, R. Mermod, *et al.*, "Production of Hadrons with Large Transverse Momentum at 200-GeV, 300-GeV, and 400-GeV," *Phys.Rev.* **D11** (1975) 3105. 64

146. **HERA-B Collaboration** , I. Abt *et al.*, "Kinematic distributions and nuclear effects of J/psi production in 920-GeV fixed-target proton-nucleus collisions," *Eur.Phys.J.* **C60** (2009) 525–542, arXiv:0812.0734 [hep-ex]. 64

147. **CERN** , "Latest update in the search for the Higgs boson." https://indico.cern.ch/event/197461/, 2012. 67

148. **ATLAS Collaboration** , G. Aad *et al.*, "Observation of a new particle in the search for the Standard Model Higgs boson with the ATLAS detector at the LHC," *Phys.Lett.* **B716** (2012) 1–29, arXiv:1207.7214 [hep-ex]. 67

149. **CMS Collaboration** , S. Chatrchyan *et al.*, "Observation of a new boson at a mass of 125 GeV with the CMS experiment at the LHC," *Phys.Lett.* **B716** (2012) 30–61, arXiv:1207.7235 [hep-ex]. 67

150. **CERN** , "LHC: the guide." http://cds.cern.ch/record/1165534/files/CERN-Brochure-2009-003-Eng.pdf, 2009. 68, 212

151. M. Bajko, F. Bertinelli, N. Catalan Lasheras, S. Claudet, P. Cruikshank, *et al.*, "Report of the task force on the incident of 19th September 2008 at the LHC,". 69

152. **ALICE Collaboration** , F. Carminati *et al.*, "ALICE: Physics performance report, volume I," *J.Phys.* **G30** (2004) 1517–1763. 69

153. **ALICE Collaboration** , B. Alessandro *et al.*, "ALICE: Physics performance report, volume II," *J.Phys.* **G32** (2006) 1295–2040. 69

154. http://aliceinfo.cern.ch/Public/en/Chapter2/Chap2Experiment-en.html. 71, 212

155. **ALICE Collaboration** , G. Dellacasa *et al.*, "ALICE technical design report of the inner tracking system (ITS),". 70

156. **ALICE Collaboration** , G. Dellacasa *et al.*, "ALICE: Technical design report of the time projection chamber,". 70

157. J. Wiechula, "Inbetriebnahme und Kalibrierung der ALICE-TPC (Commissioning and Calibration of the ALICE-TPC)," *PhD thesis* (2008) . 72, 212

158. **ALICE Collaboration** , "ALICE Transition Radiation Detector Technical Design Report,". 70

159. `http://aliceinfo.cern.ch/Public/en/Chapter2/Chap2_TOF.html`. 73, 212

160. **ALICE Collaboration** , G. Dellacasa *et al.*, "ALICE technical design report of the time-of-flight system (TOF),". 72

161. **ALICE Collaboration** , P. Cortese *et al.*, "ALICE: Addendum to the technical design report of the time of flight system (TOF),". 72

162. **ALICE Collaboration** , "ALICE Technical Design Report of the High Momentum Particle Identification Detector,". 72

163. `http://alice-hmpid.web.cern.ch/alice-hmpid/`. 74, 212

164. **ALICE Collaboration** , G. Dellacasa *et al.*, "ALICE technical design report of the photon spectrometer (PHOS),". 73

165. **ALICE Collaboration** , "ALICE Technical Design Report of the Electromagnetic Calorimeter,". 74

166. A. Fernandez, E. Gamez, G. Herrera, R. Lopez, M. Martinez, *et al.*, "ACORDE a Cosmic Ray Detector for ALICE," *Nucl.Instrum.Meth.* **A572** (2007) 102–103, `arXiv:physics/0606051 [physics]`. 74

167. **ALICE Collaboration** , "ALICE Technical Design Report of the Photon Multiplicity Detector,". 74

168. **ALICE Collaboration** , "ALICE: Addendum to the technical design report of the Photon Multiplicity Detector (PMD),". 74

169. **ALICE Collaboration** , P. Cortese *et al.*, "ALICE technical design report on forward detectors: FMD, T0 and V0,". 75

170. **ALICE Collaboration** , G. Dellacasa *et al.*, "ALICE technical design report of the zero degree calorimeter (ZDC),". 75

171. **ALICE Collaboration** , "ALICE technical design report of the dimuon forward spectrometer,". 76

172. **ALICE Collaboration** , "Addendum to the ALICE Technical Design Report of the Dimuon Forward Spectrometer,". 76

173. L. Valencia Palomo, "Inclusive J/ψ production measurement in Pb-Pb collisions at $\sqrt{s_{\rm NN}} = 2.76$ TeV with the ALICE Muon Spectrometer," *PhD thesis* (2013) . 78, 82, 83, 212

174. **ALICE Collaboration** , N. Bastid *et al.*, "Test Experiment for the Beam Shielding in ALICE,". 79

175. **ALICE Collaboration** , V. Chambert, "The electronics of ALICE dimuon tracking chambers,". 81, 212

176. Cynthia Hadjidakis *private communication* . 82, 212

177. **ALICE Collaboration** , R. Arnaldi *et al.*, "The ALICE dimuon trigger: Overview and electronics prototypes," *Nucl.Instrum.Meth.* **A456** (2000) 126–131. 83

178. **ALICE Collaboration** , R. Arnaldi *et al.*, "A dual threshold technique to improve the time resolution of resistive plate chambers in streamer mode," *Nucl.Instrum.Meth.* **A457** (2001) 117–125. 83

179. **ALICE Collaboration** , R. Arnaldi *et al.*, "Study of the resistive plate chambers for the ALICE dimuon arm," *Nucl.Instrum.Meth.* **A456** (2000) 73–76. 83

180. H. Bengtsson, "The Lund Monte Carlo for High p_T Physics," *Comput.Phys.Commun.* **31** (1984) 323. 87

181. F. Bossu, Z. C. del Valle, A. de Falco, M. Gagliardi, S. Grigoryan, *et al.*, "Phenomenological interpolation of the inclusive J/psi cross section to proton-proton collisions at 2.76 TeV and 5.5 TeV," `arXiv:1103.2394 [nucl-ex]`. 87, 93, 117

182. R. Glauber, "Cross-sections in deuterium at high-energies," *Phys.Rev.* **100** (1955) 242–248. 87

183. V. Franco and R. Glauber, "High-energy deuteron cross-sections," *Phys.Rev.* **142** (1966) 1195–1214. 87

184. W. Czyz and L. Lesniak, "ELASTIC AND ALMOST ELASTIC SCATTERING OF HIGH-ENERGY PROTONS FROM DEUTERIUM,". 88

185. A. Bialas, M. Bleszynski, and W. Czyz, "Multiplicity Distributions in Nucleus-Nucleus Collisions at High-Energies," *Nucl.Phys.* **B111** (1976) 461. 88

186. M. L. Miller, K. Reygers, S. J. Sanders, and P. Steinberg, "Glauber modeling in high energy nuclear collisions," *Ann.Rev.Nucl.Part.Sci.* **57** (2007) 205–243, arXiv:nucl-ex/0701025 [nucl-ex]. 88, 89, 213

187. D. G. d'Enterria, "Hard scattering cross-sections at LHC in the Glauber approach: From pp to pA and AA collisions," arXiv:nucl-ex/0302016 [nucl-ex]. 89

188. K. Eskola, R. Vogt, and X. Wang, "Nuclear overlap functions," *Int.J.Mod.Phys.* **A10** (1995) 3087–3090. 89

189. X.-N. Wang and M. Gyulassy, "HIJING: A Monte Carlo model for multiple jet production in pp, pA and AA collisions," *Phys.Rev.* **D44** (1991) 3501–3516. 91, 128

190. M. Cacciari, M. Greco, and P. Nason, "The P(T) spectrum in heavy flavor hadroproduction," *JHEP* **9805** (1998) 007, arXiv:hep-ph/9803400 [hep-ph]. 92, 115, 117, 214

191. **ALICE Collaboration** , S. Grigoryan and A. de Falco, "Capabilities of the ALICE Muon Spectrometer to measure quarkonia production in Pb-Pb collisions at 5.5 TeV." https://edms.cern.ch/file/938944/1/ALICE-INT-2008-016.pdf, 2008. 92

192. B. Alver, M. Baker, C. Loizides, and P. Steinberg, "The PHOBOS Glauber Monte Carlo," arXiv:0805.4411 [nucl-ex]. 93

193. **ALICE Collaboration** , B. Abelev *et al.*, "Pseudorapidity density of charged particles p-Pb collisions at $\sqrt{s_{NN}} = 5.02$ TeV," *Phys.Rev.Lett.* **110** (2013) 032301, arXiv:1210.3615 [nucl-ex]. 94

194. **Particle Data Group** , J. Beringer *et al.*, "Review of Particle Physics (RPP)," *Phys.Rev.* **D86** (2012) 010001. 99, 104, 123, 179

195. **ALICE Collaboration** , B. B. Abelev *et al.*, "Measurement of visible cross sections in proton-lead collisions at $\sqrt{s_{NN}} = 5.02$ TeV in van der Meer scans with the ALICE detector," arXiv:1405.1849 [nucl-ex]. 99, 101

196. B. Abelev *et al.*, "Pseudorapidity density of charged particles p-Pb collisions at $\sqrt{s}$ =5.02 TeV," *Phys.Rev.Lett. 110 (2013) 032301* (2013) . 100, 123

197. **ALICE Collaboration** , B. Abelev *et al.*, "J/ψ polarization in *pp* collisions at $\sqrt{s} = 7$ TeV," *Phys.Rev.Lett.* **108** (2012) 082001, arXiv:1111.1630 [hep-ex]. 107, 120

198. **LHCb Collaboration** , R. Aaij *et al.*, "Measurement of J/ψ polarization in *pp* collisions at $\sqrt{s} = 7$ TeV," *Eur.Phys.J.* **C73** (2013) 2631, arXiv:1307.6379 [hep-ex]. 107, 120

199. **CMS Collaboration** , S. Chatrchyan *et al.*, "Measurement of the prompt J/ψ and ψ(2S) polarizations in pp collisions at $\sqrt{s} = 7$ TeV," *Phys.Lett.* **B727** (2013) 381–402, arXiv:1307.6070 [hep-ex]. 107, 120

200. Javier Martin Blanco *private communication* . 107, 122, 139, 214

201. **ALICE Collaboration** , L. Aphecetche *et al.*, "Luminosity determination for the J/$\psi \to \mu^+\mu^-$ analysis in pp interactions at $\sqrt{s} = 7$ TeV." https://cds.cern.ch/record/1388921/files/ALICE-Scientific-Note-2011-001.pdf, 2011. 112

202. **ALICE Collaboration, LHCb Collaboration** , "Reference *pp* cross-sections for J/ψ studies in proton-lead collisions at $\sqrt{s_{NN}} = 5.02$ TeV and comparisons between ALICE and LHCb results," *ALICE-PUBLIC-2013-002, LHCB-CONF-2013-013-002* (2013) . 114, 116, 117, 119, 214

203. **ALICE Collaboration** , I. Lakomov, "Inclusive J/ψ production in p-Pb collisions with ALICE at the LHC," *J.Phys.Conf.Ser.* **509** (2014) 012104, arXiv:1310.3139 [nucl-ex]. 114

204. R. Martinez Turtos, Z. Conesa del Valle, and D. Stocco, "Energy interpolation of J/ψ production cross section to s = 5.023 TeV: rapidity and transverse momentum dependence," *https://twiki.cern.ch/twiki/pub/ALICE/JPsipPb2013/JpsiInterpolationForpPb.pdf* (2013) . 114

205. **ALICE Collaboration** , B. Abelev *et al.*, "Inclusive J/ψ production in pp collisions at $\sqrt{s}$ =2.76 TeV ," *Phys. Lett. B718 (2012) 295-306* (2012) . 114, 165, 170

206. **ALICE Collaboration** , K. Aamodt *et al.*, "Rapidity and transverse momentum dependence of inclusive J/ψ production in pp collisions at $\sqrt{s} = 7$ TeV ," *Phys. Lett. B704 (2011) 442-455* (2011) . 114

207. M. Gluck, J. Owens, and E. Reya, "Gluon Contribution to Hadronic J/psi Production," *Phys.Rev.* **D17** (1978) 2324. 115, 117, 214

208. **ALICE Collaboration** , K. Aamodt *et al.*, "Rapidity and transverse momentum dependence of inclusive J/psi production in *pp* collisions at $\sqrt{s} = 7$ TeV," *Phys.Lett.* **B704** (2011) 442–455, arXiv:1105.0380 [hep-ex]. 121, 122

209. Marco Leoncino *private communication* . 122

210. Diego Stocco *private communication* . 122

211. **ALICE Collaboration** , B. Abelev *et al.*, "J/ψ suppression at forward rapidity in Pb-Pb collisions at $\sqrt{s_{NN}} = 2.76$ TeV," *Phys.Rev.Lett.* **109** (2012) 072301, arXiv:1202.1383 [hep-ex]. 122

212. Philippe Pillot *private communication* . 123

213. **ALICE Collaboration** , A. Toia, "ALICE Measurements in p-Pb Collisions: Charged Particle Multiplicity, Centrality Determination and implications for Binary Scaling," *Nucl.Phys.* **A926** (2014) 78–84, arXiv:1403.5143 [nucl-ex]. 126, 127, 214

214. F. Sikler, "Centrality control of hadron nucleus interactions by detection of slow nucleons," arXiv:hep-ph/0304065 [hep-ph]. 126

215. M. Gallio, C. Oppedisano, and E. Scomparin, "Slow nucleon detection with the ALICE ZDC to select centrality in pA collisions," *ALICE Internal Note* (2005) . 126

216. **ALICE Collaboration** , "Centrality determination and implication on particle production in p-Pb collisions at $\sqrt{S_{NN}} = 5.02$ TeV," *in preparation* (2014) . 127, 128

217. Hugo Pereira Da Costa *private communication* . 140

218. L. Aphecetche, R. Arnaldi, C. Hadjidakis, I. Lakomov, and E. Scomparin, "J/psi RpA versus pT in p-A collisions at $\sqrt{s_{\rm NN}} = 5.02$ TeV," *ALICE Analysis Note* (2013) . 143

219. **ALICE Collaboration** , B. B. Abelev *et al.*, "J/ψ production and nuclear effects in p-Pb collisions at $\sqrt{S_{NN}} = 5.02$ TeV," *JHEP* **1402** (2014) 073, arXiv:1308.6726 [nucl-ex]. 153, 155, 157, 158, 159, 161, 162, 164, 171, 187, 190, 216

220. **LHCb Collaboration** , R. Aaij *et al.*, "Study of J/ψ production and cold nuclear matter effects in *pPb* collisions at $\sqrt{s_{NN}} = 5$ TeV," *JHEP* **1402** (2014) 072, arXiv:1308.6729 [nucl-ex]. 154, 156, 216

221. J. Albacete, N. Armesto, R. Baier, G. Barnafoldi, J. Barrette, *et al.*, "Predictions for p+Pb Collisions at $\sqrt{s_{\rm NN}} = 5$ TeV," *Int.J.Mod.Phys.* **E22** (2013) 1330007 and priv.comm. with R. Vogt, `arXiv:1301.3395 [hep-ph]`. 157, 162, 179, 180, 216, 218

222. **LHCb collaboration** , R. Aaij *et al.*, "Measurement of J/ψ production in pp collisions at $\sqrt{s} = 2.76$ TeV," *JHEP* **1302** (2013) 041, `arXiv:1212.1045 [hep-ex]`. 158

223. **LHCb Collaboration** , R. Aaij *et al.*, "Measurement of J/ψ production in pp collisions at $\sqrt{s} = 7$ TeV," *Eur.Phys.J.* **C71** (2011) 1645, `arXiv:1103.0423 [hep-ex]`. 158

224. E. Ferreiro, F. Fleuret, J. Lansberg, and A. Rakotozafindrabe, "Impact of the Nuclear Modification of the Gluon Densities on J/ψ production in pPb collisions at $\sqrt{s_{NN}} = 5$ TeV," *Phys.Rev.* **C88** no. 4, (2013) 047901, `arXiv:1305.4569 [hep-ph]`. 161

225. F. Arleo, R. Kolevatov, S. Peigné, and M. Rustamova, "Centrality and $p_\perp$ dependence of J/ψ suppression in proton-nucleus collisions from parton energy loss," *JHEP* **1305** (2013) 155, `arXiv:1304.0901 [hep-ph]`. 162, 171, 175, 179, 180, 217, 218

226. **ALICE Collaboration** , C. Hadjidakis, "Quarkonium production in ALICE at the LHC," `arXiv:1405.1177 [hep-ex]`. 165, 169, 186, 188, 217, 219

227. **ALICE Collaboration** , I. Lakomov, "Multiplicity dependence of the J/ψ production in p-Pb collisions with ALICE at the LHC," *Poster at the conference "Hard Probes 2013"* . 165, 168, 169, 217

228. **ALICE Collaboration** , I. Lakomov, "Event activity dependence of inclusive J/ψ production in p-Pb collisions at $\sqrt{s} = 5.02$ TeV with ALICE at the LHC," *Proceedings of the conference "Quark Matter 2014"* (2014) . 166, 172, 175, 217

229. D. McGlinchey, A. Frawley, and R. Vogt, "Impact parameter dependence of the nuclear modification of J/ψ production in d+Au collisions at $\sqrt{S_{NN}} = 200$ GeV," *Phys.Rev.* **C87** no. 5, (2013) 054910, `arXiv:1208.2667 [nucl-th]`. 171, 175, 217

230. **ALICE Collaboration** , "Transverse momentum dependence of the inclusive J/ψ nuclear modification factor in p-Pb collisions at $\sqrt{s_{\rm NN}} =$ 5.02 TeV," *in preparation* (2014) . 180, 218

231. **ALICE Collaboration** , B. B. Abelev *et al.*, "Measurement of quarkonium production at forward rapidity in pp collisions at $\sqrt{s}$= 7 TeV," arXiv:1403.3648 [nucl-ex]. 179, 181, 218

232. **ALICE Collaboration** , B. B. Abelev *et al.*, "Suppression of ψ(2S) production in p-Pb collisions at $\sqrt{s_{\rm NN}}$ = 5.02 TeV," arXiv:1405.3796 [nucl-ex]. 181, 182, 183, 184, 190, 218, 219

233. **PHENIX Collaboration** , A. Adare *et al.*, "Nuclear Modification of ψ(2S) , χ_c and J/ψ Production in d-Au Collisions at $\sqrt{s_{\rm NN}}$=200 GeV," *Phys.Rev.Lett.* **111** no. 20, (2013) 202301, arXiv:1305.5516 [nucl-ex]. 180

234. **CMS Collaboration** , S. Chatrchyan *et al.*, "Event activity dependence of Y(nS) production in $\sqrt{s_{NN}}$=5.02 TeV pPb and $\sqrt{s}$=2.76 TeV pp collisions," *JHEP* **1404** (2014) 103, arXiv:1312.6300 [nucl-ex]. 181

235. **ALICE Collaboration** , R. Arnaldi, "Inclusive Psi(2S) production at forward rapidity in p-Pb and Pb-Pb collisions with ALICE at LHC," *Proceedings of the conference "Quark Matter 2014"* (2014) . 185, 219

236. **ALICE Collaboration** , B. B. Abelev *et al.*, "Centrality, rapidity and transverse momentum dependence of J/Ψ suppression in Pb-Pb collisions at $\sqrt{s_{\rm NN}}$=2.76 TeV," *Phys.Lett.* **743** (2014) 314–327, arXiv:1311.0214 [nucl-ex]. 187

237. Y.-Q. Ma and R. Venugopalan, "Comprehensive description of J/ψ production in proton-proton collisions at collider energies," arXiv:1408.4075 [hep-ph]. 190

238. **ALICE Collaboration** , "Addendum of the Letter Of Intent for the Upgrade of the ALICE Experiment: The Muon Forward Tracker,". 191

239. https://indico.cern.ch/event/259128/material/slides/0?contribId=0. 206